Design of a Resonator Enhanced Optical Dipole Trap for Fermionic Mixtures

diploma thesis in physics

by

Andreas Trenkwalder

submitted to the Faculty of Mathematics, Computer Science and Physics of the University of Innsbruck

in partial fulfillment of the requirements
for the degree of „Magister der Naturwissenschaften“

supervised by Univ.-Prof. Dr. Rudolf Grimm,
Institute of Experimental Physics,
Institute for Quantum Optics and Quantum Information
(IQOQI) of the Austrian Academy of Sciences

Innsbruck, May 2007

> There is grandeur in this view of life, with its several powers, having been originally breathed [..][a] into a few forms or into one; and that, whilst this planet has gone cycling on according to the fixed law of gravity, from so simple a beginning endless forms most beautiful and most wonderful have been, and are being, evolved.

Origin of Species (1859), Charles Darwin, [Dar59]

[a] In the 2^{nd} edition "by the Creator" was inserted here.

In memory of Martin Trenkwalder,
17.1.1922 - 26.12.2005.

We are missing your charming laughter and your lighthearted spirit.

Abstract

Our new experiment, which is built at the Institute for Quantum Optics and Quantum Information (IQOQI) of the Austrian Academy of Sciences, aims for the generation of heteronuclear Fermi-Fermi mixtures at ultracold temperatures; where heteronuclear Feshbach resonances should exist, with which the interaction strength could be tuned. Due to the Pauli exclusion principle heteronuclear molecules are much more stable than molecules made of bosons. Imbalanced mixtures with respect to atom number, mass difference, Fermi surfaces or confinement allow to test fundamental theories of many-body quantum systems, such as properties of heteronuclear mixtures at the BEC-BCS crossover. We will gain new insights and probably new behavior and new phases will be observed.

The newly designed machine gives us the versatility to generate not only mixtures of the fermionic species ^{6}Li, ^{40}K and ^{87}Sr, but of the bosonic isotopes as well. A novel three-species oven provides the atom beams, which are decelerated with a Zeeman slower and trapped within a custom-shaped glasscell in a three-color MOT. Using magnetic fields allows us to tune the interactions by Feshbach resonances while the mixture is held in an optical dipole trap which maintains stable trapping conditions. The first dipole trap used is a resonator enhanced optical dipole trap. It will create a large and deep trapping potential due to the power enhancement of the standing wave. Through evaporative cooling the temperature of ^{6}Li is lowered while the other elements can be sympathetically cooled with ^{6}Li. On the repulsive side of the Feshbach resonance heteronuclear molecules will be formed which can Bose condense.

The design of the resonator is the content of this thesis. A laser linewidth reduction to 10 kHz and the measurements of the losses of the resonator are presented. With the knowledge of the losses, the design was optimized. The measurements show that a power enhancement of three orders of magnitude can be reached. The resonator is nearly finished, but it is not yet integrated into the experiment. In a different optical dipole trap we have already created a $^6Li_2$ molecular BEC and have observed sympathetic cooling of ^{39,40}K by ^{6}Li. The next goal is the generation of a heteronuclear molecular BEC.

Zusammenfassung

In unserem neuen Experiment am Institut für Quantenoptik und Quanteninformation (IQOQI) der österreichischen Akademie der Wissenschaften, wollen wir ultrakalte, heteronukleare Mischungen fermionischer Atome herstellen. In den von uns gewählten Mischungen sollten heteronukleare Feshbach-Resonanzen existieren, mit denen die Wechselwirkungen individuell eingestellt werden können. Damit könnten auch Moleküle erzeugt werden, die aufgrund des Pauli-Prinzips wesentlich stabiler als bosonische Moleküle sind. Unser Ziel ist es, Mischungen zu erzeugen, die in ihrer Atomzahl, dem Massenverhältnis, den Fermienergieen oder im Fallenpotential unterschiedlich sind. Wir hoffen, fundamentale Fragen der Quantenphysik, im besonderen der Theorie vieler Teilchen, klären zu können. Vielleicht können wir neues Verhalten oder neue Zustände beobachten. Wir wollen die heteronuklearen Wechselwirkungen und Stöße im BEC-BCS Übergangsbereich genauer untersuchen.

Zu diesem Zweck haben wir ein neues Experiment aufgebaut, in dem wir Mischungen erzeugen werden, die aus den fermionischen Elementen ^{6}Li, ^{40}K und ^{87}Sr bestehen. Der vielseitige Aufbau lässt aber auch Mischungen zu, welche bosonische Isotope enthalten. Die Atomstrahlen kommen aus einem neu entwickelten drei-Elemente-Ofen, passieren einen Zeeman-Abbremser und werden innerhalb einer speziell geformten Glaszelle, mittels einer drei-Farben-MOT, gefangen. Die Feshbach-Resonanzen werden über Magnetfelder eingestellt. Um ein magnetfeldunabhängiges Potential und ebenso, um alle möglichen Spinzustände fangen zu können, laden wir das Gemisch in eine optische Dipolfalle. Dies erfolgt in mehreren Schritten, um eine möglichst große Teilchenzahl zu erreichen. Der erste davon ist eine Resonator verstärkte optische Dipolfalle, welche, durch die Verstärkungswirkung der Stehwelle im Resonator, ein besonders großes und tiefes Potential erlaubt. Die Temperatur der ^{6}Li-Atome wird durch Verdampfungskühlen bis zum degenerierten Fermigas verringert. Es ist möglich die anderen Atome dabei sympathetisch mitzukühlen. Unter Ausnutzung der Feshbach-Resonanzen wollen wir heteronukleare Moleküle herstellen, die dann auch Bose kondensiert werden können.

Der Aufbau des Resonators ist der Inhalt dieser Diplomarbeit. Im Rahmen dieser wird eine Linienbreitenreduktion des Resonatorlasers auf 10 kHz und die Messung der Verluste des Resonators beschrieben. Die genaue Kenntniss der Verluste erlaubt es die Parameter des Resonators zu optimieren um eine möglichst große Verstärkung zu erhalten. Die Messungen zeigen, dass ein Verstärkungsfaktor von 1000 erreicht werden sollte, doch der Aufbau konnte noch nicht abgeschlossen werden. Im Experiment wurde bereits ein $^6Li_2$ Molekül-BEC erzeugt und sympathetisches Kühlen von ^{39,40}K mit ^{6}Li wurde ebenfalls erfolgreich getestet. Das nächste Ziel ist die Erzeugung eines heteronuklearen Molekül-BEC.

Contents

Chapter 1

Introduction

1.1 Motivation

Even many years after quantum physics was developed, some questions remain to be answered, keeping physicists puzzling until today. Famous gedanken (thought) experiments, like the EPR paradox [EPR35, Boh35] still fascinate and animate controversial and exciting discussions. But, contrary to the early pioneers, who thought that it would never be possible to experimentally verify them [Sch52], such experiments can now be performed to proof the remarkable features of quantum physics, such as the EPR paradox [Bel64, AGR81], to be real.

One of the basic concepts of quantum physics [Sak94] is the wavefunction, which represents the probability[1] of finding a particle at a specific point in space. The time evolution of the wavefunction is described by the Schrödinger equation[2]. For this equation, there exist time independent solutions (with a time varying phase), called the states of the system, which have discrete energy levels[3]. For example, atoms have certain transition frequencies on which they can absorb and emit light. These frequencies correspond to the energy difference between discrete energy levels.

All kinds of particles can be divided into two fundamentally different categories, with either a symmetric or an anti-symmetric wavefunction, with respect to the exchange of two particles[4]. The first type is called bosons[5], with photons as their prominent representative. The second type of particles is called fermi-

[1] The wavefunction is the probability amplitude and its modulus square is the probability.
[2] Proposed in 1925 by Erwin Schrödinger, an Austrian physicist.
[3] The states are the eigenvectors with the energies as eigenvalues.
[4] Integer spin and half odd integer spin particles respectively.
[5] Named after the Indian physicist Satyendra Nath Bose. See also BEC below.

ons[6], to which electrons belong. If two equal fermions were in the same state and were placed at the same position[7], the wavefunctions would annihilate due to the anti-symmetry of the fermionic wave function. This means that equal fermions in the same state are not allowed to be placed at the same position, which is called the Pauli exclusion principle[8]. For neutron stars, it is thought that the Pauli exclusion leads to a "Pauli pressure" which balances the gravitational collapse. Another consequence of the Pauli exclusion is that equal fermions in the same internal state do not interact[9].

For bosons the situation is reversed. The wavefunctions add, so that the largest probability is to find two bosons at the same position. This led, in the mid-1920's, to the prediction of Einstein, on the inspiration by Satyendra Nath Bose, that a new phase of matter should exist, nowadays known as Bose-Einstein condensate (BEC) [Bos24, Ein24, Ein25]. In this phase, all bosons occupy the state with the lowest energy. That is the reason why it is called a degenerate gas. There the wavefunctions overlap, resulting in the particles behaving as an ensemble without individuality. Such a state is only reached at very low (ultracold) temperatures. It took 70 years until the first BEC could be achieved by Eric Cornell & Carl Wieman, Randall G. Hulet, and Wolfgang Ketterle in the year 1995 [AEM$^+$95, BSTH95, DMA$^+$95].

For fermions such a phase is impossible due to the Pauli exclusion principle. They can only stack up in a ladder of states, starting from the state with the lowest energy, followed by the state with the next higher energy, and so on, until all the fermions have filled up states with different energies. This is called the fermi sea or a degenerate fermi gas. Such a state was first observed 1999 in the group of Deborah S. Jin for ^{40}K [dMJ99] and 2001 in the groups of Randall G. Hulet [TSM$^+$01] and Christophe Salomon for ^{6}Li [SKC$^+$01].

In the field of ultracold physics, the so-called superfluidity is of large interest. In the year 1937 Pyotr L. Kapitza[10], John F. Allen and Don Misener discovered that, if liquid helium (^{4}He) is cooled below a certain temperature[11], it shows zero viscosity, zero entropy and infinite thermal conductivity [Kap38, AM38]. A medium having this properties is called a superfluid and has interesting behavior: it creeps out of any container if not sealed, and can support so-called vortices. Superfluidity can be explained by Bose-Einstein condensation for the bosonic isotope ^{4}He. The fermionic isotope ^{3}He shows also superfluidity, but at lower temperatures. Its behavior can be explained by the formation of so-called

[6]Named after the Italian physicist Enrico Fermi.
[7]This means, the wavefunctions overlap completely.
[8]Formulated by Wolfgang Pauli, an Austrian physicist.
[9]Scattering length equal zero for s-wave scattering and all even partial waves.
[10]Sometimes spelled as Pjotr Kapitsa
[11]This is called the lambda point, which is for ^{4}He at 2.18 K.

Cooper pairs, in a process obeying the same mechanism as described by the Bardeen-Cooper-Schrieffer (BCS) theory of superconductivity.

The interaction strength of bosons or fermions is magnetically tuneable by so-called Feshbach resonances[12]. It is possible to tune the interaction from attractive to repulsive, or even to zero. In the attractive regime, Cooper pairs are formed and, on the repulsive side, molecules. The transition region is called the BEC-BCS crossover.

Two-atom molecules consisting of fermions have bosonic character as well[13]. This allowed to obtain a molecular BEC of $^{40}K_2$ in 2003 in the group of Deborah S. Jin [GRJ03] and of $^6Li_2$ in the lithium experiment of our research group [JBA+03]. It turned out that at ultracold temperatures molecules composed of fermions are much more stable than molecules of bosons. This is a consequence of the Pauli exclusion principle which suppresses (s-wave) collisions.

In our newly designed fermionic-lithium-potassium-strontium-experiment (FeLiKx) we use the fermionic isotopes ^{6}Li, ^{40}K and ^{87}Sr. With these isotopes, and also with the bosonic isotopes, we generate different combinations of heteronuclear mixtures. Using Feshbach resonances we intend to create heteronuclear molecules. With them we will be able to study in detail the properties of the BEC-BCS crossover. The versatile design of the machine will allow a large variety of experiments.

The use of different atoms gives the possibility to individually tune the interaction strengths, the Fermi surfaces, the confinement, the mass ratios, the number ratio, etc. Unequal mixtures in any of those properties can be created, possibly leading to new superfluid phases (e.g. FFLO [FF64, LO64, CN04] or breached pair superfluidity [LW03, MGLW05]). Mediated pairing could also lead to novel behavior.

Beyond the study of fermionic systems we will investigate further areas. For example bose-fermi mixtures, which could reveal new features of quantum physics. The generation of ground-state heteronuclear molecules will open the field to new types of experiments: dipolar molecules could be used for quantum information processing, the change in collision properties and collective phenomena could be studied and BECs of dipolar molecules could show new properties. The chosen alkaline-earth strontium has some interesting features. Although it could be difficult to find magnetic Feshbach resonances its narrow intercombination line makes an optical Feshbach resonance feasible. It would give a large mass ratio in the mixture and has a rich energy structure with a metastable state.

[12]Named after Herman Feshbach, an American physicist. It is observed if the kinetic energy of the atoms becomes degenerate with a bound molecular state.

[13]This bosonic feature reduces the effect of Pauli exclusion.

Strontium also is not Bose condensed so far.

Applications of our results could include the understanding of high temperature superconductors and the behavior of neutron stars. Our experiment is an ideal model of fermionic systems, like quarks and gluons within the atoms nuclei. With this knowledge, one can test different theories which could rule out approaches, lead to extensions or the unification of different theories. For the generation of ground-state molecules new experimental tools have to be developed and further investigated: for example new Raman-schemes and coherent control of ro-vibrational molecular states (e.g. by dark states), etc.

In the FeLiKx experiment we could already produce $^6Li_2$ molecular BECs. The next major step we are working on is to obtain a heteronuclear BEC of ^{6}Li-^{40}K molecules. Sympathetic cooling of ^{39,40}K by ^{6}Li at the ^{6}Li Feshbach resonance was observed. We hope to obtain a heteronuclear molecular BEC soon, with which we will be able to explore the features of such a mixture in the region of the BEC-BCS crossover.

1.2 The experiment

The achievements in the field of ultracold physics, discussed in the previous section, did require the development of specific new experimental tools. The atoms have to be cooled and trapped simultaneously. The laser (light amplification by the stimulated emission of radiation) was invented in the late 1950's and is one of the most important developments with which cooling is performed to temperature regimes never thought to be reachable.

Cooling atoms means to reduce their velocity. But cold atoms alone are not sufficient for reaching BEC. The density must also be high. Therefore, the atoms have to be trapped as well. This is done in a first step by a combination of a magnetic quadrupole field together with a Doppler cooling scheme, which is called magneto-optical trap (MOT) [MvdS99].

The final temperature which can be reached by this method is limited to a few 100 μK since it involves resonant absorbtion-emission of photons which exert finite recoils to the atom. The corresponding recoil temperature, is still too high to obtain BEC in a MOT. Therefore, one had to develop different schemes of cooling and trapping, in which no resonant light is involved.

One of those is to trap the atoms in an off-resonant dipole trap which uses the dipolar force [GWO00]. The trapping laser induces a dipole moment of the atom by deforming the electron distribution. By focussing the laser tightly an intensity gradient is formed which exerts a force on the atom via the induced

dipole moment. If the laser is red-detuned the atom cloud deformation goes in-phase with the laser field and the force drives the atoms towards the intensity maximum. If the laser is blue detuned the electron cloud is out-of-phase with the field and the atoms are expelled to a region with lower intensity. Therefore, with a focussed and red-detuned laser trapping of the atoms in the intensity maximum can be achieved[14].

Cooling in a dipole trap is conveniently done by evaporative cooling. To force evaporation the potential depth of the trap is lowered, such that the hot atoms escape. By rethermalization of the remaining atoms, these are cooled efficiently [MvdS99][15]. This process needs a sufficient number of atoms to be in the trap, since many of them will be lost. Also a sufficiently large scattering rate and low enough trap loss is required, in order to be efficient. If this is not the case, one can use sympathetic cooling. A cooling agent is used, which can be cooled by evaporative cooling. By collisions with the cooling agent the second species in the trap is cooled. This requires a sufficiently large heteronuclear scattering length. By evaporative cooling the nK regime can be reached, where degenerate quantum gases can be formed if the density is sufficient large.

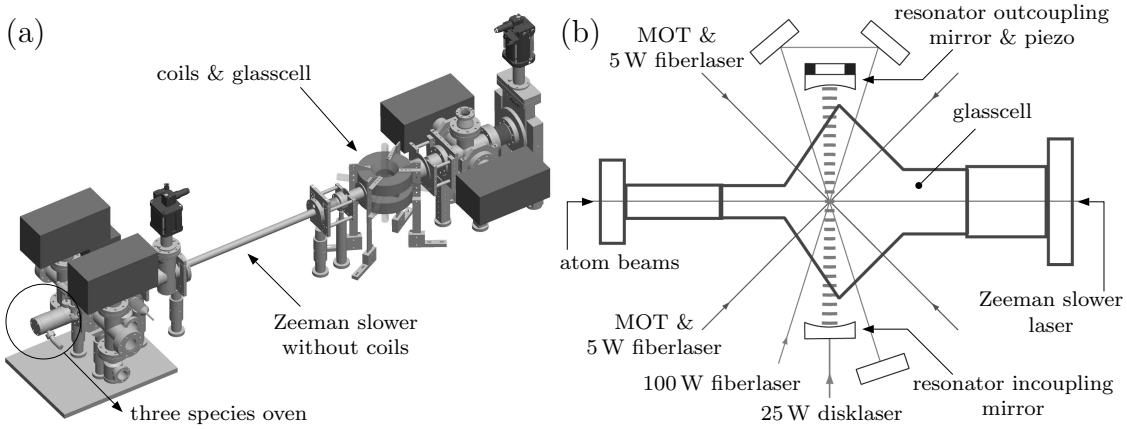

Figure 1.1: a) Experimental setup and b) glasscell with trapping laser beams.

In figure 1.1, the experimental setup for the FeLiKx experiment is shown. In the newly designed three-species oven we can heat up our elements individually. The part of the oven which contains the enriched (7%) ^{40}K is separated by valves which allows to exchange the source without opening the vacuum chamber. Microtubes (Ø 200 μm, L=12 mm, stainless steel) separate the individual sources from the rest of the vacuum chamber and provide collimation of the atom beam. They also allow us to use a very small amount of enriched potassium, which is very expensive (150 \$/mg). The atom beams then pass through two differential

[14] A different picture of the dipolar force is presented in section 3.4.5.

[15] Evaporative cooling of equal fermions requires to use a spin mixture, otherwise no rethermalization is possible due to the zero scattering length.

pumping stages and get decelerated by a Zeeman slower. The atoms are trapped at the center of a glasscell, shown in figure 1.1b).

In a first trapping step, our atoms are trapped in a three-color MOT. For this, three independent laser systems were set up. Since we want to tune our magnetic fields arbitrarily, we load the atoms from the MOT into optical dipole traps, which are independent of magnetic fields. The first of these will be a standing wave resonator dipole trap. This is a Fabry-Perot type (linear) cavity which enhances the 25 W input power by three orders of magnitude. The design of this trap, together with the necessary laser stabilization, are the contents of this thesis. Due to its deep potential, we can enlarge the beam size of the resonator to obtain a big overlap with the MOT and transfer a large fraction of atoms into the resonator. Additionally, the intensity of the resonator will be ramped down, resulting in a first evaporative cooling stage. The cold remaining atoms are then kept in a focussed 100 W dipole trap which is built in a crossed and retroreflected configuration[16], as shown in figure 1.1b). The depth of this trap will be ramped down as well and the remaining atoms will be transferred into two 5 W single focussed lasers beams. There, the final evaporation will be performed and quantum degeneracy should be reached. So far, only the 100 W laser serves as a dipole trap, but it was sufficient to obtain a molecular $^6Li_2$ BEC.

The design of the glasscell was developed in such a way that its walls are at Brewster's angle with respect to the resonator. This way the losses are minimized. Simultaneously, nearly ideal access for all the other laser beams is ensured. This is further discussed in section 3.4.1.

This thesis starts with the theoretical issues concerning Fabry-Perot type cavities. After this, some questions about servo controllers are discussed and laser noise is considered. In the experimental part, the laser used for the resonator is characterized and its linewidth stabilization is described. The measurement of the losses of the glasscell is presented. This was necessary for the design of the parameters of the resonator, which is performed in the last part. The resonator is nearly completed but it is not yet integrated into the experiment.

[16] Actually, the atoms are trapped only in the crossing of the 1^{st} and 3^{rd} beam, since otherwise we observed fast losses from the trap. See introduction to section 3.4.

Chapter 2

Theoretical part

For the design of a Fabry-Perot resonator and to achieve narrow linewidths by locking lasers to a cavity, it is necessary to understand the properties of a Fabry-Perot interferometer and laser light very well. Therefore, we want to establish some principles first. This chapter will be quite general and the content can be found in many books and articles. See references at the beginning of each chapter. Probably, the advanced reader may skip the theoretical part entirely and start immediately with the experimental part. Whenever questions arise one can always jump to the relevant theoretical section.

Here the focus was put on the section about the Fabry-Perot interferometer, since this thesis will deal mainly with such a configuration. In the literature its description often is only very briefly and partially or it is scattered over many chapters with diverse nomenclature and definitions. It may be useful having all basic ingredients in one chapter that should allow fast learning about Fabry-Perot type cavities for the novice as well as a fast reference for the more advanced reader. The majority of the equations are derived in detail, which should allow verification without difficulties. After reading this chapter one should have deeper insight how a Fabry-Perot resonator works and should be ready for designing one with the tools given here.

First the Gaussian beam and the ABCD law will be introduced, which describes such a beam passing through several optical elements. Then the basic features of a Fabry-Perot type cavity will be discussed. We will discuss the two main properties which are frequency discrimination and intensity enhancement. Both of these features will be used in the setup.

2.1 Gaussian beam and ABCD law

One of the main parts of a laser is the optical resonator, which is a Fabry-Perot type cavity, explained in section 2.2. It amplifies the light and forces the laser to emit at a certain wavelength. The mirrors have in nearly all cases planar and/or spherical shape, causing that the wavefronts of the laser light must have the same shape as the mirrors. In this section we will find that Gaussian beams have spherical wavefronts in the far field and planar wavefronts in the focus. Also they carry finite energy which makes Gaussian beams a physical solution, describing laser light very well. This is also true outside the cavity. The way a Gaussian beam is changed by passing optical elements is described by the ABCD law and using ray transfer matrices. We will see that higher modes of Gaussian beams exist and that they have different phases leading to mode dependent resonances of laser cavities. It makes sense to derive the properties of a Gaussian beam first. In this way one obtains all the formulas describing laser light inside and outside cavities [ST91, HW92, Sie86, KL66].

2.1.1 Gaussian beam

Starting with the Maxwell equations we will derive the wave equation which describes the propagation of light. By separating time and space dependencies in a complex ansatz we will arrive at the Helmholtz equation which, in the paraxial approximation, is solved by the Gaussian beam. The properties of the beam will be discussed briefly. This section follows mainly [ST91, Sie86].

The starting point are the Maxwell equations in their most general form:

$$\nabla \cdot \vec{D} = \rho \tag{2.1a}$$
$$\nabla \cdot \vec{B} = 0 \tag{2.1b}$$
$$\nabla \times \vec{E} = -\frac{\partial \vec{B}}{\partial t} \tag{2.1c}$$
$$\nabla \times \vec{H} = \vec{\jmath} + \frac{\partial \vec{D}}{\partial t} \tag{2.1d}$$

In table 2.1 the used quantities and relations which are useful in connection with the Maxwell equations are summarized.

Table 2.1: Units and definitions for the Maxwell equations (2.1) [Wik].

symbol	name	definition	SI units
$\vec{D}$	electric displacement field	$\epsilon_0\vec{E}+\vec{P}=(1+\chi_e)\epsilon_0\vec{E}=\epsilon\vec{E}$	$\frac{C}{m^2}=\frac{As}{m^2}$
$\vec{E}$	electric field	see $\vec{D}$	$\frac{V}{m}=\frac{N}{C}=\frac{kgm}{As^3}$
$\vec{P}$	polarization density	$\chi_e\epsilon_0\vec{E}$	$\frac{C}{m^2}=\frac{As}{m^2}$
χ_e	electric susceptibility	see $\vec{P}$	1
ϵ	electric permittivity	$(1+\chi_e)\epsilon_0=\epsilon_r\,\epsilon_0$	$\frac{F}{m}=\frac{C^2}{Jm}=\frac{A^2s^4}{kgm^3}$
ϵ_r	dielectric constant	$1+\chi_e$	1
$\vec{H}$	magnetic field	see $\vec{B}$	$\frac{A}{m}$
$\vec{B}$	magnetic flux density (magnetic field)	$\mu_0(\vec{H}+\vec{M})=(1+\chi_m)\mu_0\vec{H}=\mu\vec{H}$	$T=10^4G=\frac{kg}{As^2}$
$\vec{M}$	magnetisation density	$\chi_m\vec{H}$	$\frac{A}{m}$
χ_m	magnetic susceptibility	see $\vec{M}$	1
μ	magnetic permeability	$(1+\chi_m)\mu_0=\mu_r\,\mu_0$	$\frac{H}{m}=\frac{kgm}{A^2s^2}$
μ_r	relative permeability	$1+\chi_m$	1
n	refractive index	$\sqrt{\epsilon_r\,\mu_r}$	1
ρ	free electric charge density		$\frac{C}{m^3}=\frac{As}{m^3}$
$\vec{\jmath}$	free current density		$\frac{A}{m^2}$
c	vacuum speed of light	$2.99792458\times10^8\,(=\frac{1}{\sqrt{\epsilon_0\mu_0}})$	$\frac{m}{s}$
μ_0	permeability	$4\pi\times10^{-7}$	$\frac{H}{m}=\frac{kgm}{A^2s^2}$
ϵ_0	permittivity of free space	$\frac{1}{c^2\,\mu_0}=8.8541878176\times10^{-12}$	$\frac{F}{m}=\frac{C^2}{Jm}=\frac{A^2s^4}{kgm^3}$

The Maxwell equations (2.1) in vacuum ($\vec{P}=0,\vec{M}=0$) are:

$$\nabla\cdot\vec{E}=\frac{\rho}{\epsilon_0} \tag{2.2a}$$

$$\nabla\cdot\vec{B}=0 \tag{2.2b}$$

$$\nabla\times\vec{E}=-\frac{\partial\vec{B}}{\partial t} \tag{2.2c}$$

$$\nabla\times\vec{B}=\mu_0\vec{\jmath}+\frac{1}{c^2}\frac{\partial\vec{E}}{\partial t}\ . \tag{2.2d}$$

By applying the curl operator $\nabla\times$ to both sides of equation (2.2c), without free charges and currents ($\rho=0$ and $\vec{\jmath}=0$) one obtains:

$$\nabla\times(\nabla\times\vec{E})=-\nabla\times\frac{\partial\vec{B}}{\partial t}$$

$$\nabla(\nabla\cdot\vec{E})-\nabla^2\vec{E}=-\frac{\partial}{\partial t}\left(\nabla\times\vec{B}\right)$$

$$\Rightarrow\qquad \Delta\vec{E}\equiv\nabla^2\vec{E}=\frac{1}{c^2}\frac{\partial^2\vec{E}}{\partial t^2}\ , \tag{2.3}$$

where $\nabla \times (\nabla \times \vec{E}) = \nabla(\nabla \cdot \vec{E}) - \nabla^2 \vec{E}$ and equations (2.2d) and (2.2a) have been used for the charge and current free case. Equation (2.3) is the well known wave equation.

For simplicity, from now on, we will assume the electric field to propagate only within one plane, i.e. it is linearly polarized. For the free space case the electric field can always be decomposed into orthogonally polarized components, which can be treated independently. It is very useful to introduce a complex electric field $\tilde{E}$ for which the given wave equation is also valid. The physical meaningful quantity is the real part:

$$E = \mathrm{Re}\big[\tilde{E}\big] = \frac{1}{2}\left(\tilde{E} + \tilde{E}^*\right) \ . \tag{2.4}$$

But it is convenient to use the same notation for the complex electric field as for the real electric field. Therefore, the tilde will be dropped in the future. When calculating quantities one has to remember that the real part has to be used.

We use the ansatz

$$E(\vec{r}, t) = E(\vec{r}) \exp[i\omega t] \ , \tag{2.5}$$

where we introduced the spatial coordinate $\vec{r}$, time t and the angular frequency ω in radians per second. Inserting this into the wave equation gives the Helmholtz equation:

$$\left(\nabla^2 + k^2\right) E(\vec{r}) = 0 \ , \qquad \text{with } k \equiv \frac{\omega}{c} \ . \tag{2.6}$$

Here the wavenumber k appeared. The simplest solution to this equation is a plane wave:

$$E(\vec{r}, t) = E_0 \exp[\, i\,(\omega\, t - \vec{k} \cdot \vec{r})] \ , \tag{2.7}$$

where the wave vector $\vec{k}$ points into the direction of propagation of the wave and has as magnitude the wavenumber $\left|\vec{k}\right| = k$. E_0 is the amplitude of the wave. The spatial maxima at time t of this wave are separated by $\Delta r = \frac{2\pi}{k} \equiv \lambda$, which is the wavelength. Another solution to the Helmholtz equation is the spherical wave:

$$E(\vec{r}, t) = \frac{E_0}{r} \exp[\, i\,(\omega\, t - k\, r)] \ , \qquad \text{with } r \equiv \left|\vec{r}\right| \ . \tag{2.8}$$

The point at $r = 0$, where the electric field becomes infinite, is called the focus. This makes the spherical wave unphysical around this point.

A special case is the paraxial wave, where the wave is centered around an axis (z in our case) with only small amplitudes off this axis. Such a wave is described as a plane wave running along the z axis with an amplitude that depends on the x and y coordinates:

$$E(\vec{r}) = A(\vec{r}) \exp[-i\, k\, z\,] \ . \tag{2.9}$$

We assume that on a length scale of $\Delta z \approx \lambda$ the amplitude $A(\vec{r})$ of the paraxial wave varies slowly along the z axis, in comparison with both other axes, i.e.

$$\left|\frac{\partial^2 A}{\partial z^2}\right| \ll \left|\frac{\partial^2 A}{\partial x^2}\right| \quad , \quad \left|\frac{\partial^2 A}{\partial z^2}\right| \ll \left|\frac{\partial^2 A}{\partial y^2}\right| \, , \tag{2.10}$$

and

$$\left.\begin{array}{ll} (2.11a) & |\Delta A| \equiv \left|\frac{\partial A}{\partial z}\Delta z\right| = \left|\frac{\partial A}{\partial z}\lambda\right| = \frac{2\pi}{k}\left|\frac{\partial A}{\partial z}\right| \\ (2.11b) & |\Delta A| \ll |A| \end{array}\right\} \Rightarrow \left|\frac{\partial A}{\partial z}\right| \ll k|A| \, . \tag{2.12}$$

The derivative $\frac{\partial A}{\partial z}$ varies as well slowly along z:

$$\left.\begin{array}{l} |\Delta\Big(\frac{\partial A}{\partial z}\Big)| \equiv \left|\frac{\partial^2 A}{\partial z^2}\Delta z\right| = \left|\frac{\partial^2 A}{\partial z^2}\lambda\right| = \frac{2\pi}{k}\left|\frac{\partial^2 A}{\partial z^2}\right| \\ \qquad\qquad \overset{(2.12)}{\downarrow} \qquad\qquad\qquad\qquad\qquad\quad \overset{(2.11a)}{\downarrow} \\ |\Delta\Big(\frac{\partial A}{\partial z}\Big)| \ll \Delta\Big(k|A|\Big) = k|\Delta A| = 2\pi\left|\frac{\partial A}{\partial z}\right| \end{array}\right\} \Rightarrow \left|\frac{\partial^2 A}{\partial z^2}\right| \ll k\left|\frac{\partial A}{\partial z}\right| \, . \tag{2.13}$$

We insert the paraxial wave (2.9) into the Helmholtz equation (2.6) and neglect the term $\left|\frac{\partial^2 A}{\partial z^2}\right|$. This is justified with equations (2.10) to (2.13) and gives:

$$\begin{aligned} 0 &= \left(\nabla^2 + k^2\right) A(\vec{r})\boldsymbol{e}^{-i\,k\,z} \\ &= \left(\frac{\partial^2}{\partial x^2} + \frac{\partial^2}{\partial y^2} + \frac{\partial^2}{\partial z^2} + k^2\right) A(\vec{r})\boldsymbol{e}^{-i\,k\,z} \\ &= \left(\frac{\partial^2}{\partial x^2} + \frac{\partial^2}{\partial y^2}\right) A(\vec{r})\boldsymbol{e}^{-i\,k\,z} + \frac{\partial}{\partial z}\left(\frac{\partial A(\vec{r})}{\partial z}\boldsymbol{e}^{-i\,k\,z} - i\,kA(\vec{r})\boldsymbol{e}^{-i\,k\,z}\right) + k^2 A(\vec{r})\boldsymbol{e}^{-i\,k\,z} \\ &= \left(\frac{\partial^2}{\partial x^2} + \frac{\partial^2}{\partial y^2}\right) A(\vec{r})\boldsymbol{e}^{-i\,k\,z} + \underbrace{\frac{\partial^2 A(\vec{r})}{\partial z^2}\boldsymbol{e}^{-i\,k\,z}}_{\text{neglect this term}} - 2\,i\,k\frac{\partial A(\vec{r})}{\partial z}\boldsymbol{e}^{-i\,k\,z} + (-k^2 + k^2)A(\vec{r})\boldsymbol{e}^{-i\,k\,z} \\ &\approx \left(\frac{\partial^2}{\partial x^2} + \frac{\partial^2}{\partial y^2}\right) A(\vec{r})\boldsymbol{e}^{-i\,k\,z} - 2\,i\,k\frac{\partial A(\vec{r})}{\partial z}\boldsymbol{e}^{-i\,k\,z} \, . \end{aligned} \tag{2.14}$$

We get as result:

$$\left(\nabla_T^2 - 2\,i\,k\frac{\partial}{\partial z}\right) A(\vec{r}) \approx 0 \, , \qquad \text{with } \nabla_T^2 \equiv \frac{\partial^2}{\partial x^2} + \frac{\partial^2}{\partial y^2} \, . \tag{2.15}$$

This is known as the paraxial Helmholtz equation, which is valid for a wave varying slowly along the z axis.

A solution to this equation is:

$$A(\vec{r}) = \frac{A_1}{q(z)}\exp\left[-i\,k\,\frac{\rho^2}{2q(z)}\right] \, , \qquad \begin{array}{l} \text{with } \rho^2 \equiv x^2 + y^2 \\ \text{and } q(z) \equiv z + i\,z_0 \, , \end{array} \tag{2.16}$$

where we introduced the radius ρ and a complex number $q(z)$ which has a real part z and a constant complex part $i\,z_0$. This solution looks like the spherical wave (2.8) in the paraxial approximation where r is expanded in the following way:

$$\begin{aligned} r = \sqrt{x^2+y^2+z^2} &\approx z + \frac{x^2+y^2}{2z}\ , \\ \text{where } \sqrt{a+\epsilon} &\approx \sqrt{a}\left(1+\frac{\epsilon}{2a}\right)\ ,\ \text{with } \frac{\epsilon}{a} \ll 1 \text{ was used.} \end{aligned} \tag{2.17}$$

The radius r is replaced by $q(z)$, which is complex. Therefore, it is called the complex radius of curvature. Its complex nature gives rise to several features: at long distances from the focus the beam behaves like a spherical wave. Close to the focus it stays finite in diameter and the phase surfaces are nearly parallel. The intensity falls off in a Gaussian way along the transverse direction. Therefore, it is called a Gaussian beam. These features ensure that it can not carry infinite energy along the transverse direction and in the focus. This was not the case for the spherical wave, which makes therefore ansatz (2.16) more realistic.

We define two new real functions $w(z)$ and $r(z)$ in the following way:

$$\frac{1}{q(z)} \equiv \frac{1}{r(z)} - i\frac{\lambda}{\pi\, w(z)^2}\ , \tag{2.18}$$

and obtain the expressions for $r(q)$ and $w(q)$:

$$w(q)^2 = -\frac{\lambda}{\pi\,\mathrm{Im}\big[1/q(z)\big]} = \frac{\lambda\,\big|q(z)\big|^2}{\pi\,\mathrm{Im}\big[q(z)\big]}\ , \qquad \text{with } \frac{1}{q(z)} = \frac{1}{z+iz_0} = \frac{z-iz_0}{z^2+z_0^2}$$

$$w(q) = \sqrt{\frac{\lambda}{\pi}\frac{\big|q(z)\big|^2}{\mathrm{Im}\big[q(z)\big]}} \tag{2.19a}$$

$$r(q) = \frac{1}{\mathrm{Re}\big[1/q(z)\big]} = \frac{\big|q(z)\big|^2}{\mathrm{Re}\big[q(z)\big]}\ . \tag{2.19b}$$

To obtain the explicit expressions for $r(z)$ and $w(z)$ we insert $q(z) \equiv z + i\,z_0$:

$$w(z) = \sqrt{\frac{\lambda}{\pi}\frac{\big|q(z)\big|^2}{\mathrm{Im}\big[q(z)\big]}} = \sqrt{\frac{\lambda\,(z^2+z_0^2)}{\pi\,z_0}} = \sqrt{\frac{\lambda\,z_0}{\pi}}\sqrt{1+\left(\frac{z}{z_0}\right)^2}\ , \qquad \text{with } w_0^2 \equiv \frac{\lambda\,z_0}{\pi}$$

$$= w_0\sqrt{1+\left(\frac{z}{z_0}\right)^2} \tag{2.20a}$$

$$r(z) = \frac{\big|q(z)\big|^2}{\mathrm{Re}\big[q(z)\big]} = \frac{z^2+z_0^2}{z} = z\left(1+\left(\frac{z_0}{z}\right)^2\right)\ . \tag{2.20b}$$

The new parameter w_0 was defined in such a way that it corresponds to $w_0 \equiv w(z=0)$, i.e. the value at the focus. Rewriting $\frac{i}{q}$ in polar form and using (2.20) gives:

$$\begin{aligned}\frac{i}{q(z)} &= \Big|\frac{i}{q(z)}\Big| e^{i\zeta(z)} = \frac{1}{\big|z + i\,z_0\big|} e^{i\zeta(z)} = \frac{1}{\sqrt{z^2+z_0^2}} e^{i\zeta(z)} \;, \quad \text{with } \tan[\zeta(z)] \equiv \frac{z}{z_0} \\ &= \frac{1}{z_0\sqrt{1+(\frac{z}{z_0})^2}} e^{i\zeta(z)} = \frac{w_0}{z_0\, w(z)} e^{i\zeta(z)} \;. \end{aligned} \tag{2.21}$$

This expression was multiplied with i so that the introduced phase $\zeta(z)$ becomes zero for $z=0$. Inserting (2.18) and (2.21) into (2.16) gives with ansatz (2.9) and the definition $A_0 \equiv A_1/(iz_0)$ the complex electric field of the beam:

$$\begin{aligned} E(\vec{r}) = A_0 \frac{w_0}{w(z)} \exp\left[-\frac{\rho^2}{w(z)^2}\right] \exp\left[i\,\left(-k\,z - k\,\frac{\rho^2}{2r(z)} + \zeta(z)\right)\right] \;, \\ \text{with } \rho^2 \equiv x^2 + y^2 \;. \end{aligned} \tag{2.22}$$

The intensity is defined as the optical power per unit area [ST91]:

$$I(z,t) \equiv \epsilon_0\, c\, \left\langle Re(E(z,t))^2 \right\rangle_T \;, \tag{2.23}$$

where ϵ_0 is the permittivity of free space and the brackets $\langle\ \rangle_T$ denote averaging over a time period T since the sensor is usually slow in comparison with ω. Rewriting this expression in terms of the complex $E(z,t)$ and its complex conjugate $E^*(z,t)$ yields for linear polarized light:

$$\begin{aligned} I(z,t) &= \frac{\epsilon_0\, c}{4} \left\langle (E(z,t) + E^*(z,t))^2 \right\rangle_T \\ &= \frac{\epsilon_0\, c}{4} \left(\left\langle E^2(z,t) \right\rangle_T + \left\langle E^{*2}(z,t) \right\rangle_T + 2\left\langle E(z,t)\, E^*(z,t) \right\rangle_T \right) \\ &= \frac{\epsilon_0\, c}{2} \left\langle \big|E(z,t)\big|^2 \right\rangle_T \;, \end{aligned} \tag{2.24}$$

where the average of the squared electric field $\langle E^2(z,t)\rangle$ and $\langle E^{*2}(z,t)\rangle$ is zero and the cross terms are simply $E(z,t)\,E^*(z,t) = \big|E(z,t)\big|^2$. Using this equation and equation (2.22) for the electric field of a Gaussian beam gives:

$$I(\vec{r}) = I_0\, \frac{w_0^2}{w(z)^2} \exp\Big[-\frac{2\,\rho^2}{w(z)^2}\Big] \;, \qquad \begin{aligned} &\text{with } \rho^2 \equiv x^2 + y^2 \\ &\text{and } I_0 \equiv \frac{\epsilon_0\, c}{2} \big|A_0\big|^2 \;, \end{aligned} \tag{2.25}$$

where the maximum intensity I_0 was defined.

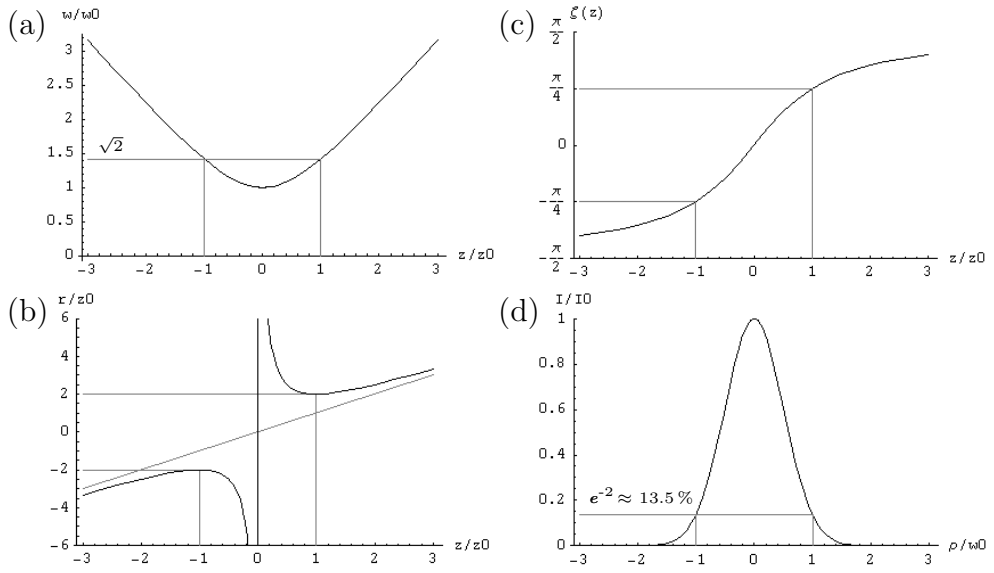

Figure 2.1: Gauss beam: a) beam radius $w(z)$, b) radius of curvature $r(z)$, c) Gouy phase $\zeta(z)$ and d) intensity profile $I(\rho)$.

We summarize previously introduced parameters and discuss them briefly afterwards, see figure 2.1:

$$z_0 = \frac{\pi}{\lambda} w_0^2 \tag{2.26a}$$

$$w(z) = w_0 \sqrt{1 + \left(\frac{z}{z_0}\right)^2} \tag{2.26b}$$

$$r(z) = z \left(1 + \left(\frac{z_0}{z}\right)^2\right) \tag{2.26c}$$

$$\zeta(z) = \arctan\left[\frac{z}{z_0}\right] \tag{2.26d}$$

$$\Theta_{div} = \frac{\lambda}{\pi\, w_0} \ . \tag{2.26e}$$

In equation (2.25) we see that for any z the intensity has a maximum at $\rho = 0$ of $I_0\,(\frac{w_0}{w(z)})^2$ and falls off by a factor of $1/\boldsymbol{e}^2 \approx 0.135$ at a radius $\rho = w(z)$. Therefore, $w(z)$ is called the beam radius. The beam has a focus (called the waist) at $z = \rho = 0$, where the intensity reaches its overall maximum and the beam radius its minimum w_0, called waist radius[1]. The distance $z = z_0$ at which the beam radius has grown to $\sqrt{2}\, w_0$ is called the Rayleigh range. For $z \gg z_0$ the beam radius is increasing linearly with $w(z) = \Theta_{div}\, z$, where Θ_{div} is called the angle of divergence. The important parameter $\zeta(z)$ is called the Gouy phase[2]

[1]Often the beam radius and the waist radius are confused.

[2]Named after the French physicist Louis Georges Gouy, who discovered 1890 that the phase of a Gaussian beam undertakes a phase shift of π when it passes through a focus [Gou90]. His name is sometimes misspelled as "Guoy", e.g. in [Sie86].

and gives the phase retardation of the Gaussian beam relative to a plane wave. Surfaces having the same phase have a radius of curvature which corresponds to $r(z)$. Far from the focus the radius of curvature corresponds to the distance from the focus $\left|r(z \gg z_0)\right| \approx z$ as it is the case for a spherical wave. The sign of $r(z)$ is positive for $z > 0$ and negative for $z < 0$, i.e. a negative sign tells us that the beam is converging and a positive sign means that the beam is diverging when going along the direction of the z axis.

The optical power within an area of radius ρ is obtained by integration:

$$\begin{aligned} P(\rho) &= \int_0^\rho I(r')\, 2\pi\rho'\, d\rho' \\ &= P_0\Big(1 - \exp\Big[-\frac{2\,\rho^2}{w(z)^2}\Big]\Big) \;, \qquad \text{with } P_0 \equiv \frac{I_0\,\pi\,w_0^2}{2} \;, \end{aligned} \tag{2.27}$$

where we introduced the total power of the beam P_0. More than 86 % of the power is inside a radius of $w(z)$ and more than 99.9 % of the power is within $2w(z)$.

In this section we have obtained the properties of the Gaussian beam, like waist radius, radius of curvature and the Gouy phase. The intensity profile and the power have been derived. In the next section we will learn that the Gaussian beam is the lowest mode of the family of Gauss-Hermite beams.

2.1.2 Higher modes and the M^2 factor

The Gaussian beam is not the only solution to the paraxial Helmholtz equation (2.15). There exist many other solutions, but we are mainly interested in modes which have, as the Gaussian beam, a spherical behavior far from the focus. Such solutions represent the field inside a cavity having spherical mirrors. They will show a phase factor, which is related to the Gouy phase, leading to certain resonance frequencies (section 2.2.5). In this section such solutions will be derived, mainly following [Sie86]. The number of higher order modes present in a Gaussian beam can be characterized by the M^2 parameter, which is discussed briefly [HW92].

The wave has to fulfill the paraxial Helmholtz equation (2.15), where we first separate the x and y dependency of $A(\vec{r}) = A_m(x,z)\,A_n(y,z)$ and then reformulate the paraxial Helmholtz equation for each axis independently:

$$\left(\frac{\partial^2}{\partial x^2} - 2\,i\,k\frac{\partial}{\partial z}\right) A_m(x,z) \approx 0 \;, \qquad \text{and similar for the } y \text{ axis.} \tag{2.28}$$

During the derivation of the Gaussian beam from the paraxial Helmholtz equation we used the solution (2.16). We modify this and use a more general

ansatz:

$$A_m(x,z) = A\Big[q(z)\Big]\, h_m\Big[\frac{x}{p(z)}\Big]\exp\Big[-i\,k\,\frac{x^2}{2q(z)}\Big]\ , \quad \text{similar for } A_n(y,z)\ , \tag{2.29}$$

where the quantities $A\big[q(z)\big]$, $h_m\big[\frac{x}{p(z)}\big]$, $h_n\big[\frac{y}{p(z)}\big]$ and $p(z)$ are unknown, and $q(z) = z + i\,z_0$ as before. Inserting this ansatz into equation (2.28) yields:

$$\begin{aligned} 0 &= \Big(\frac{\partial^2}{\partial x^2} - 2\,i\,k\frac{\partial}{\partial z}\Big) A\,h_m\,\boldsymbol{e}^{-i\,k\,\frac{x^2}{2q}} = \cdots \\ &= \frac{A}{p^2}\left(h_m'' - 2i\,k\,h_m'\,x\,\big(\frac{p}{q} - p'\big) - i\,k\frac{p^2}{q}\,h_m\big(1 + 2q\frac{A'}{A}\big)\right) \qquad (2.30a) \\ 0 &= h_m'' - 2i\,k\,h_m'\,x\,\big(\frac{p}{q} - p'\big) - i\,k\frac{p^2}{q}\,h_m\big(1 + 2q\frac{A'}{A}\big)\ , \qquad (2.30b) \end{aligned}$$

where $\frac{dq}{dz} = 1$ and the abbreviations $h_m' \equiv \frac{\partial h_m}{\partial(\frac{x}{p(z)})}$, $h_m'' \equiv \frac{\partial^2 h_m}{\partial(\frac{x}{p(z)})^2}$, $p' \equiv \frac{dp}{dz}$ and $A' \equiv \frac{\partial A}{\partial q(z)}$ were used. The dependencies were left out for brevity. Equation (2.30b) is related to the Hermite differential equation:

$$H_m'' - 2\frac{x}{p}H_m' + 2mH_m = 0\ , \qquad \text{with } m \text{ integer}, \tag{2.31}$$

where $H_m\big[\frac{x}{p(z)}\big]$ are the Hermite polynomials. For (2.30b) to become equal to (2.31) the following relations must be fulfilled:

$$\begin{aligned} \frac{2}{p} &\stackrel{!}{=} 2i\,k\,\big(\frac{p}{q} - p'\big) & \Rightarrow \quad \frac{dp}{dz} &\stackrel{!}{=} \frac{p}{q} + \frac{i}{k\,p} \qquad (2.32a) \\ 2m &\stackrel{!}{=} -i\,k\frac{p^2}{q}\,\big(1 + 2q\frac{A'}{A}\big) & \frac{2q}{A}\frac{dA}{dq} &\stackrel{!}{=} 2i\,m\,\frac{q}{k\,p^2} - 1\ . \qquad (2.32b) \end{aligned}$$

There are many ways to solve these equations, but usually one defines:

$$\frac{1}{p(z)} \equiv \frac{\sqrt{2}}{w(z)}\ , \tag{2.33}$$

and verifies that this fulfills equation (2.32a), with the relations of $w(q)$ and $r(q)$,

given in (2.19):

$$
\begin{aligned}
p(z) = \frac{w(z)}{\sqrt{2}} &= \sqrt{\frac{\lambda}{2\pi}\frac{\big|q(z)\big|^2}{\mathrm{Im}\big[q(z)\big]}} = \sqrt{\frac{w_0^2}{2z_0}\frac{\big|q(z)\big|^2}{z_0}} = \frac{1}{\sqrt{2}}\frac{w_0}{z_0}\big|q(z)\big| \\
\frac{dp}{dz} &= \frac{d}{dz}\frac{1}{\sqrt{2}}\frac{w_0}{z_0}\big|q\big| = \frac{w_0}{z_0\sqrt{2}}\frac{d}{dz}\sqrt{z^2+z_0^2} = \frac{w_0}{z_0\sqrt{2}}\frac{z}{\big|q\big|} \\
\frac{p}{q} &= \frac{1}{q}\frac{1}{\sqrt{2}}\frac{w_0}{z_0}\big|q\big| = \frac{w_0}{z_0\sqrt{2}}\frac{\big|q\big|^2}{q\,\big|q\big|} = \frac{w_0}{z_0\sqrt{2}}\frac{q^*}{\big|q\big|} \\
\frac{i}{k\,p} &= \frac{i}{k}\sqrt{2}\frac{z_0}{w_0\,\big|q\big|} = \frac{i\,\lambda\,z_0\sqrt{2}}{2\pi\,w_0\,\big|q\big|} = \frac{i\,w_0\,z_0}{z_0\sqrt{2}\,\big|q\big|} \\
\Rightarrow\quad \frac{p}{q} + \frac{i}{k\,p} &= \frac{w_0}{z_0\sqrt{2}}\frac{q^*}{\big|q\big|} + \frac{i\,w_0\,z_0}{z_0\sqrt{2}\,\big|q\big|} \\
&= w_0\frac{z - i\,z_0 + i\,z_0}{z_0\sqrt{2}\,\big|q\big|} = \frac{w_0\,z}{z_0\sqrt{2}\,\big|q\big|} \overset{!}{=} \frac{dp}{dz}\,. \qquad \checkmark \text{ ok.}
\end{aligned}
\tag{2.34}
$$

We search for a solution of the second equation (2.32b), which we first rewrite in terms of $q(z)$:

$$
\begin{aligned}
\frac{2q}{A}\frac{dA}{dq} &= 2i\,m\,\frac{q}{k\,p^2} - 1 = 2i\,m\,\frac{q}{k}\left(\sqrt{2}\frac{z_0}{w_0\,\big|q\big|}\right)^2 - 1 \\
&= 2i\,m\,\frac{\lambda}{2\pi}\,\frac{2\,z_0^2}{w_0^2}\frac{q}{q\,q^*} - 1 = 2i\,m\,\frac{z_0}{q^*} - 1 \qquad\qquad \Big|\frac{dq}{2q},\, z_0 = \frac{q-q^*}{2i} \\
\frac{dA}{A} &= \frac{2i\,m}{2q\,q^*}\frac{q-q^*}{2i}dq - \frac{dq}{2q} \qquad\qquad \Big|dq = dq^* \\
&= \frac{m}{2}\Big(\frac{dq^*}{q^*} - \frac{dq}{q}\Big) - \frac{dq}{2q}\,.
\end{aligned}
\tag{2.35}
$$

Integration gives:

$$
\begin{aligned}
\ln[A] &= \frac{m}{2}\Big(\ln[q^*] - \ln[q]\Big) - \frac{1}{2}\ln[q] + c = \ln\Big[\Big(\frac{q^*}{q}\Big)^{m/2} q^{-1/2}\Big] + c \quad \Big|e^{\wedge} \\
A\Big[q(z)\Big] &= A_m\left(\frac{1}{q}\right)^{1/2}\Big(\frac{q^*}{q}\Big)^{m/2}\,,
\end{aligned}
\tag{2.36}
$$

with A_m the integration constant. We insert equation (2.21)[3]:

$$\begin{aligned} \frac{1}{q} &= \frac{w_0}{i\, z_0\, w(z)} \boldsymbol{e}^{i\zeta(z)} = -\frac{i\, w_0}{z_0\, w(z)} \boldsymbol{e}^{i\zeta(z)} \\ \frac{q^*}{q} &= -\Big(\frac{q}{i}\Big)^* \frac{i}{q} = -\Big(\frac{z_0\, w(z)}{w_0} \boldsymbol{e}^{-i\zeta(z)}\Big)^* \frac{w_0}{z_0\, w(z)} \boldsymbol{e}^{i\zeta(z)} = -\boldsymbol{e}^{2i\zeta(z)} \\ \Rightarrow \quad A\Big[q(z)\Big] &= A_m \sqrt{\frac{i\, w_0}{z_0\, w(z)} \boldsymbol{e}^{i(2m+1)\zeta(z)}}\ , \end{aligned} \tag{2.37}$$

where the Gouy phase $\zeta(z)$ appeared again. This gives with equation (2.29):

$$\begin{aligned} A_m(x,z) &= A_m \sqrt{\frac{i\, w_0}{z_0\, w(z)} \boldsymbol{e}^{i(2m+1)\zeta(z)}}\, H_m\Big[\frac{x\sqrt{2}}{w(z)}\Big] \exp\Big[-i\, k\, \frac{x^2}{2\, q(z)}\Big] \\ A_n(y,z) &= A_n \sqrt{\frac{i\, w_0}{z_0\, w(z)} \boldsymbol{e}^{i(2n+1)\zeta(z)}}\, H_n\Big[\frac{y\sqrt{2}}{w(z)}\Big] \exp\Big[-i\, k\, \frac{y^2}{2\, q(z)}\Big]\ . \end{aligned} \tag{2.38}$$

The electric field becomes with the definitions $E_{mn} \equiv i A_m A_n / z_0$ and $\rho^2 \equiv x^2 + y^2$:

$$\begin{aligned} E(\vec{r}) &= A_m(x,z)\, A_n(y,z) \exp\big[-i\, k\, z\big] \\ &= E_{mn}\, \frac{w_0}{w(z)}\, H_m\Big[\frac{x\sqrt{2}}{w(z)}\Big]\, H_n\Big[\frac{y\sqrt{2}}{w(z)}\Big] \times \\ &\qquad \exp\Big[i(m+n+1)\zeta(z) - i\, k\, \frac{\rho^2}{2\, q(z)} - i\, k\, z\Big]\ . \end{aligned} \tag{2.39}$$

The term, which depends on the complex radius of curvature $q(z)$, can be decomposed into real and imaginary part, and equations (2.26) are inserted:

$$k\, \frac{\rho^2}{2\, q(z)} = k\, \frac{\rho^2}{2(z + i\, z_0)} = k\, \frac{\rho^2}{2}\, \frac{z - i\, z_0}{z^2 + z_0^2} \overset{(2.26)}{=} k\, \frac{\rho^2}{2\, r(z)} - i \frac{\rho^2}{w(z)^2}\ . \tag{2.40}$$

With this we obtain our final result [ST91, Sie86]:

$$E(\vec{r}) = E_{mn}\, \frac{w_0}{w(z)}\, H_m\Big[\frac{x\sqrt{2}}{w(z)}\Big]\, H_n\Big[\frac{y\sqrt{2}}{w(z)}\Big] \exp\Big[i\Phi(z) - \frac{\rho^2}{w(z)^2}\Big] \tag{2.41a}$$

$$\text{with} \qquad \Phi(z) \equiv (m+n+1)\zeta(z) - k\left(\frac{\rho^2}{2\, r(z)} + z\right)\ . \tag{2.41b}$$

This describes the family of so-called Gaussian-Hermite beams, which form a complete set of orthogonal solutions of the paraxial Helmholtz equation (2.15).

[3] In [Sie86] at this point a normalization is done, which is not entirely clear. Here we absorb these factors into the integration constant.

The different combinations of $\{m, n\}$ are called modes which are often abbreviated TEM_{mn} modes, standing for transversal electromagnetic. The Gaussian beam is exactly the TEM_{00} mode. The intensity of each mode is obtained by calculating $\left|E(\vec{r})\right|^2$, according to equation (2.24). The result is shown in figure 2.2b). In figure 2.2a) photos of the transmitted intensity of the resonator (see section 3) are shown.

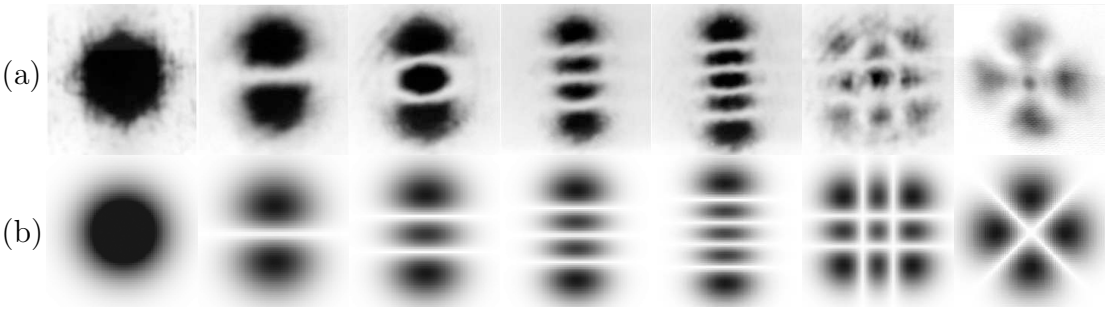

Figure 2.2: TEM modes of the Hermite-Gaussian beam. (a) photos (b) calculation. From left to right TEM_{00} to TEM_{04} and TEM_{22}. The rightmost mode probably is a TEM_{02}-TEM_{20} hybrid mode.

The first 6 modes are the TEM_{00} to TEM_{04} and TEM_{22} modes. The photos were taken with a glassplate inserted between the mirrors which caused the distorted boundaries. Nevertheless, one can clearly see that the modes agree very well with the Hermite-Gaussian modes. The 7^{th} mode, on the far right of figure 2.2, might be a hybrid mode where at the same time the TEM_{02} and the TEM_{20} mode were present. In this case the calculation was done by subtracting the electric fields of the two modes and taking the absolute square afterwards. The subtraction corresponds to a phase shift of π of the two fields[4]. If the fields were added, a circular profile would have emerged. On the photo, there is a maximum in the center which does not appear in the calculation. This central spot was always present, even when the cavity was scanned[5]. This indicates, that it was caused by the incoherent fraction of the laser light. This behavior was only observed with the 100 mW Nd:YAG laser, which was used for testing, but not for the ELS laser. In the other photos this spot is not visible, because the cavity was slightly misaligned, such that the spot was out of the view of the camera.

Our major motivation for doing this derivation was, to obtain the phase $\Phi(z)$ of the higher order modes in equation (2.41b). It is a very important result, which we will use in section 2.2.5 in order to obtain the resonance frequencies of the different Gauss-Hermite modes of a Fabry-Perot cavity.

[4]It is not clear where this phase shift should come from. Probably, from the orthogonality of the modes, which was not proven here.

[5]With the help of this spot it was easy to align the cavity.

As one can see from figure 2.2 the beam radius of the Hermite-Gaussian beam is minimal for the TEM_{00} mode, i.e. the Gaussian beam. The beam radius of the other modes is always larger and scales approximately with [HW92]:

$$w_m(z) = w_{00}(z)\sqrt{2\,m+1}\ , \tag{2.42}$$

where $w_{00}(z)$ is the beam radius for the Gaussian beam. The beam radius for the y axis is analogous with m replaced by n.

The beam quality of lasers is often specified by the M^2 parameter. It is qualitatively related to the deviation of the laser beam to a Gaussian TEM_{00} beam. Note the fact that for a Gaussian beam the product of the waist radius and the angle of divergence remains always constant. This can easily be seen from equations (2.26):

$$w_0\,\Theta_{div} = w_0\,\frac{\lambda}{\pi w_0} = \frac{\lambda}{\pi}\ . \tag{2.43}$$

If higher modes are present in the beam, the waist radius becomes larger: $\tilde{w}_0 > w_0$, as we saw in equation (2.42). The tilde should mark the waist radius of the beam having higher modes. The angle of divergence is defined in the far field by $\Theta_{div} = \frac{\lambda}{\pi w_0}$, equation (2.26e). It is largest for the TEM_{00} Gaussian beam and becomes smaller for higher modes. If higher modes are present in the beam the divergence is defined by the smallest mode of the beam, which is usually the TEM_{00} beam, while the waist is defined by the highest mode of the beam. Therefore, the product $\tilde{w}_0\tilde{\Theta}_{div}$ must be larger for a beam with higher modes than for a pure Gaussian beam. The fraction of these values is defined as the beam propagation (or beam quality) factor M^2:

$$M^2 \equiv \frac{\tilde{w}_0\,\tilde{\Theta}_{div}}{w_0\,\Theta_{div}} = \tilde{w}_0\,\tilde{\Theta}_{div}\,\frac{\pi}{\lambda} \geq 1\ . \tag{2.44}$$

It is 1 for a Gaussian TEM_{00} beam and larger 1 for the other modes. For further discussions see [HW92].

As was mentioned already, the Hermite-Gaussian family is not the only higher order solution of the paraxial Helmholtz equation. There are many others, but since the Gaussian-Hermite polynomials form a complete orthogonal set, all other solutions can be expanded in terms of these. One solution of interest are the Laguerre-Gaussian beams, which are obtained by writing the paraxial Helmholtz equation in cylindrical coordinates and performing a similar derivation as was done for Gaussian-Hermite beams. The result is [Sie86]:

$$\begin{aligned} A_{pm}(r,\theta,z) = &\sqrt{\frac{2p!}{(1+\delta_{0m})\pi(m+p)!}}\,\frac{\exp[i(2p+m+1)\zeta(z)]}{w(z)} \\ &\times\Big(\frac{r\sqrt{2}}{w(z)}\Big)L_p^m\Big[\frac{2r^2}{w(z)^2}\Big]\exp\Big[-ik\frac{r^2}{2q(z)}+im\theta\Big]\ . \end{aligned} \tag{2.45}$$

The L_p^m are the generalized Laguerre polynomials. This solution plays a role in systems having significant cylindrical symmetry. Nevertheless, the majority of laser systems effectively have rectangular symmetry. This is true even with circular mirrors, since it suffices having slightly tilted surfaces or Brewster plates for introducing rectangular asymmetry. Therefore, lasers are more often better described by Hermite-Gaussian beams than by Laguerre-Gaussian beams. Laguerre-Gaussian beams can be expanded in terms of Hermite-Gaussian beams and vice versa and the lowest order Laguerre-Gaussian beam is exactly the Gaussian TEM_{00} beam.

An interesting solution to the (not paraxial) Helmholtz equation (2.6) is the Bessel beam. It has the remarkable feature that the divergence is zero. See for example [DME87, Sch06a].

Concluding this section, it was shown that Hermite-Gaussian beams are valid solutions of the paraxial Helmholtz equation and that the Gaussian beam is the lowest order Hermite-Gaussian beam with the smallest waist. We were interested in the phase which gives the resonance frequencies of a Fabry-Perot cavity, as we will see later. The beam propagation factor M^2 was briefly introduced.

2.1.3 The ABCD law

A Gaussian beam propagating through different optical elements changes its properties, which can be described entirely by the ABCD law using ray transfer matrices. Some useful formulas will be given, allowing fast and simple application of the ABCD law. At the end of this section a few examples, like the glass-plate and lenses, will be discussed, which will be used in later chapters. Ray transfer matrices and the ABCD law are treated in many books, for example in [ST91, HW92].

We first describe light as a simple ray which is determined by its initial position y_1 and its slope y_1' (i.e. the tangent of the angle). These are written as the components of a 2×1 vector. The ray passing an optical element changes its position and slope to y_2 and y_2' respectively. In the paraxial limit, i.e. for small angles, this can be represented by a 2×2 matrix $M \equiv \left[\begin{smallmatrix} M_{1,1} & M_{1,2} \\ M_{2,1} & M_{2,2} \end{smallmatrix}\right]$. Such a matrix is called ray transfer matrix. With this notation the ray after passing the optical element can be calculated a follows:

$$\begin{pmatrix} y_2 \\ y_2' \end{pmatrix} = \begin{bmatrix} M_{1,1} & M_{1,2} \\ M_{2,1} & M_{2,2} \end{bmatrix} \cdot \begin{pmatrix} y_1 \\ y_1' \end{pmatrix} . \tag{2.46}$$

For every type of optical elements ray transfer matrices exist. In table 2.2 the important ones are given [ST91][6].

[6]These ray transfer matrices are different to those in [Sie86], since there the slopes y_i' are

Table 2.2: Ray transfer matrices.

optical element	ray matrix			beam path
free space	$M_{space}(L)$	$=$	$\begin{bmatrix} 1 & L \\ 0 & 1 \end{bmatrix}$	
thin lens	$M_{lens}(f)$	$=$	$\begin{bmatrix} 1 & 0 \\ -\frac{1}{f} & 1 \end{bmatrix}$	
planar mirror	M_{pm}	$=$	$\begin{bmatrix} 1 & 0 \\ 0 & 1 \end{bmatrix}$	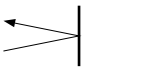
planar boundary	$M_{pb}(n_1, n_2)$	$=$	$\begin{bmatrix} 1 & 0 \\ 0 & \frac{n_1}{n_2} \end{bmatrix}$	
spherical mirror	$M_{sm}(r)$	$=$	$\begin{bmatrix} 1 & 0 \\ \frac{2}{r} & 1 \end{bmatrix}$	
spherical boundary	$M_{sb}(r, n_1, n_2)$	$=$	$\begin{bmatrix} 1 & 0 \\ -\frac{n_2-n_1}{n_2\, r} & \frac{n_1}{n_2} \end{bmatrix}$	

In the table the rays propagate always from left to right and the matrices correspond to the convex configuration. Therefore, caution must be applied when using these matrices, since the sign of the radius of the spherical boundary or mirror, which is denoted with r, or the focal length of the lens f may change sign for concave geometry and/or when the beam is propagating to the left. The refractive index before and after the boundary are denoted as n_1 and n_2 respectively. The slope of the reflected ray from the mirror is measured always in the direction of propagation[7]. For example for a beam inside a cavity having concave mirrors, the radius of the mirrors must be set with a minus sign. Also the beam changes direction on each reflection. It should be mentioned that the ray transfer matrix of the spherical mirror is the same as that of the thin lens with the focal length set to $f = -\frac{r}{2}$. When several optical elements are passed by the ray, the individual matrices have to be multiplied according to the usual rules of matrix multiplication, where the rightmost matrix corresponds to the first optical element. It is a general rule that the determinant of ray transfer matrices is always [ST91][6]:

$$\det[M] = \frac{n_1}{n_2} \ , \tag{2.47}$$

where n_1 and n_2 are the refractive index at the input and output respectively. Since the determinants of multiplied matrices is $\det[A \cdot B] = \det[A]\det[B]$, the

weighted by the refractive index $y_i' \equiv n_i \frac{dy_i}{dz}$. Therefore, the ray transfer matrix for e.g. a planar boundary in [Sie86] is simply the identity matrix. With this definition the determinant of each matrix (see below) would become always $\det[M] = 1$.

[7]It helps to regard the ray to propagate always to the right, even if it is reflected, then one can not be confused by this.

determinant of the matrix of a system, composed of several matrices, is defined by the initial and the final refractive indices inserted in equation (2.47).

The description of light as rays is often sufficient, but in reality laser light behaves like a Gaussian beam which has a waist and radius of curvature as we saw in section 2.1.1. There we related both quantities to the complex radius of curvature $q(z)$ by the definition (2.18) and calculated the waist and radius of curvature as a function of $q(z)$ in (2.19). When a Gaussian beam is passing an arbitrary optical element, described by a ray transfer matrix, it can be shown that the complex radius of curvature is changed in the following way [Sie86, HW92]):

$$q_2 = \frac{A\,q_1 + B}{C\,q_1 + D}\ , \qquad \begin{array}{l}\text{with } M = \left[\begin{smallmatrix} A & B \\ C & D \end{smallmatrix}\right] \text{ the ray matrix} \\ \text{of the optical system.}\end{array} \tag{2.48}$$

This is called the ABCD law, since the matrix elements are often called this way. Here q_1 and q_2 are the q's of the beam in front of and behind the optical element. The matrix M is the ray transfer matrix of the optical system derived.

It is cumbersome to apply this law by calculating first q_1 from the waist and radius of curvature and calculating q_2, from which the new waist and radius of curvature can be calculated. All of these steps imply complex arithmetics. In the case of a collimated beam at the input the radius of curvature is infinity which gives a purely complex q_{coll}:

$$q_{coll} = i\,\frac{\pi\,w_0^2}{\lambda} = i\,z_0\ . \tag{2.49}$$

In this case it is easier to perform the calculation with the ABCD law. The result for a general ray transfer matrix $M = \left[\begin{smallmatrix} A & B \\ C & D \end{smallmatrix}\right]$ is obtained from equation (2.48)[8]:

$$z_{02} = \mathrm{Im}\big[q_2\big] = z_{01}\,\frac{\det[M]}{z_{01}^2\,C^2 + D^2} \equiv \frac{\pi\,w_{focus}^2}{\lambda_2} \tag{2.50a}$$

$$z_{focus} = \mathrm{Re}\big[q_2\big] = \frac{z_{01}^2\,A\,C + B\,D}{z_{01}^2\,C^2 + D^2} \tag{2.50b}$$

$$w_2 = w_{01}\,\sqrt{A^2 + B^2/z_{01}^2} \tag{2.50c}$$

$$r_2 = \frac{z_{01}^2\,A^2 + B^2}{z_{01}^2\,A\,C + B\,D}\ . \tag{2.50d}$$

[8] In [HW92] equations (1.70) and (1.71), on page 47, are treating a similar case. There the ray transfer matrix is defined differently since it is assumed that on both sides the beam additionally propagates in free space by the distances z and z'. Effectively, equations (1.70) and (1.71) are the same as (2.50), except with the sign. In (1.70) the sign in front of the $A\,C\,Z_0^2$ term and the overall sign for $C \neq 0$ could not be verified.

Relation (2.47) for the determinant was inserted here. The variables defining the original collimated beam are w_{01} and $z_{01} = \frac{\pi w_{01}}{\lambda_1}$. The waist and radius of curvature at the output are w_2 and r_2 respectively. The distance from the output of the ray transfer matrix to the focus is z_{focus}[9]. If $z_{focus} > 0$ the beam is diverging. In this case the radius of curvature is positive as well ($r_2 > 0$). If both are negative the beam is converging. At the focus of the output beam the waist radius is denoted by w_{focus} and z_{02} corresponds to its Rayleigh range. The refractive index can change from input to output. This is taken into account by the different wavelengths in the different media labelled with $\lambda_i \equiv \lambda_0/n_i$, with λ_0 the vacuum wavelength and n_i the refractive index of the medium i. One has to be very careful not to mix up the different variables and keep in mind how they are defined.

We will show in some simple examples how to apply this law. The results will be useful later in this thesis. First we consider a collimated beam propagating in free space. We immediately obtain from equations (2.50):

$$M = \left[\begin{smallmatrix} 1 & z \\ 0 & 1 \end{smallmatrix}\right] \tag{2.51a}$$

$$w_{focus} = w_{01} \tag{2.51b}$$

$$z_{focus} = \mathrm{Im}\big[q_2\big] = z \tag{2.51c}$$

$$w_2 = w_{01}\sqrt{1 + z^2/z_{01}^2} \equiv w[z, w_{01}, \lambda] \tag{2.51d}$$

$$r_2 = z\Big(1 + \frac{z_{01}^2}{z^2}\Big) \equiv r[z, w_{01}, \lambda]\ . \tag{2.51e}$$

This is just the behavior of the Gaussian beam, similar as in equations (2.26). For later usage the functions $w[z, w_{01}, \lambda]$ and $r[z, w_{01}, \lambda]$ have been defined with λ being the wavelength in the medium, which is included in the Rayleigh range z_{01}.

A more interesting example is a planar boundary where the refractive index is changing from n_1 to n_2. We obtain with $M = M_{space}(z_2)\cdot M_{pb}(n_1, n_2)\cdot M_{space}(z_1)$:

$$M = \left[\begin{smallmatrix} 1 & z_1 + \frac{n_1}{n_2} z_2 \\ 0 & \frac{n_1}{n_2} \end{smallmatrix}\right] \tag{2.52a}$$

$$w_{focus} = w_{01} \tag{2.52b}$$

$$z_{focus} = z_1 \frac{n_2}{n_1} + z_2 \tag{2.52c}$$

$$w_2 = w\Big[z_1 \frac{n_2}{n_1} + z_2, w_{01}, \lambda_2\Big] \tag{2.52d}$$

$$r_2 = r\Big[z_1 \frac{n_2}{n_1} + z_2, w_{01}, \lambda_2\Big]\ . \tag{2.52e}$$

[9]This must not necessarily coincide with a real focus, but the beam behaves as if the focus and waist would have these values.

A diverging laser beam passing a planar boundary with $n_2 > n_1$ will propagate inside the medium the same way as if the focus was shifted by $z_1\left(\frac{n_2}{n_1} - 1\right)$ away from the boundary. Since at the boundary ($z_2 = 0$) the wavelength is changing, the beam radius is not changed whereas the radius of curvature is increased by a factor of $\frac{n_2}{n_1}$ [HW92].

If the beam passes a glassplate of thickness d the matrix is $M = M_{space}(z_2) \cdot M_{pb}(n_2, n_1) \cdot M_{space}(d) \cdot M_{pb}(n_1, n_2) \cdot M_{space}(z_1)$ and the result is [HW92]:

$$M = \begin{bmatrix} 1 & z_1+z_2+d\frac{n_1}{n_2} \\ 0 & 1 \end{bmatrix} \tag{2.53a}$$

$$w_{focus} = w_{01} \tag{2.53b}$$

$$z_{focus} = z_1 + z_2 + d\,\frac{n_1}{n_2} \tag{2.53c}$$

$$w_2 = w\left[z_1 + z_2 + d\,\frac{n_1}{n_2}, w_{01}, \lambda_1\right] \tag{2.53d}$$

$$r_2 = r\left[z_1 + z_2 + d\,\frac{n_1}{n_2}, w_{01}, \lambda_1\right] . \tag{2.53e}$$

This means that, when one sends a diverging laser beam through a glassplate of thickness d, the beam after the glassplate behaves as if the focus is shifted by $d\left(1 - \frac{n_1}{n_2}\right)$ closer to the glassplate than without the glassplate. This effect will change the waist of the resonator when the glasscell is inserted (section 3.4.6).

It is easy to calculate how the beam is changed by a lens. The matrix is $M = M_{lens}(f) \cdot M_{space}(z_1)$ and yields [HW92]:

$$M = \begin{bmatrix} 1 & z_1 \\ -\frac{1}{f} & 1-\frac{z_1}{f} \end{bmatrix} \tag{2.54a}$$

$$w_{focus} = \frac{w_{01}\, f}{\sqrt{z_{01}^2 + (z_1 - f)^2}} \tag{2.54b}$$

$$z_{focus} = -f\frac{z_{01}^2 + z_1(z_1 - f)}{z_{01}^2 + (z_1 - f)^2} \tag{2.54c}$$

$$\frac{1}{z_1} + \frac{1}{-z_{focus}} = \frac{1}{f} + \frac{z_{01}^2}{z_1(z_{01}^2 + z_1(z_1 - f))} . \tag{2.54d}$$

The negative sign in front of z_{focus} signifies that normally the beam behind the lens is converging. The last line corresponds to the well known lens equation from geometrical optics but with an additional term. This term becomes zero for $z_1 \gg z_{01}$, i.e. when the lens is far from the focus and the beam behaves like a spherical wave. From this result we can immediately derive the case for which the incoming beam is collimated ($z_1 = 0$) and write down the position and waist

of the focus [ST91]:

$$\left|z_{focus}\right| = \frac{f}{1+(f/z_{01})^2} \tag{2.55a}$$

$$w_{focus} = \frac{w_{01}}{\sqrt{1+(z_{01}/f)^2}} \ . \tag{2.55b}$$

The resulting waist in the focus is plotted in figure 2.3, labelled "precise". In order to obtain a certain waist radius of the focus we are solving equation (2.55b) for w_{01}:

$$w_{01} = \frac{f\,\lambda}{\pi\,\sqrt{2}\,w_{focus}}\sqrt{1 \pm \sqrt{1-\Big(\frac{2\,z_{0f}}{f}\Big)^2}} \ , \tag{2.56}$$

where $z_{0f} \equiv \frac{\pi\,w_{focus}^2}{\lambda}$ was inserted. The focal length f must fulfill $f \geq 2\,z_{0f}$, otherwise there is no real solution as can be seen from (2.56). This restriction comes from the fact that for a given f there exists a maximum $w_{focus}^{max} = \sqrt{\frac{f\,\lambda}{2\,\pi}}$ for $w_{01} = \sqrt{\frac{f\,\lambda}{\pi}}$ which can be calculated from equation (2.55b) and is seen in figure 2.3 on the curve labelled "precise". In the case $f \ll z_{01}$ equations (2.55) can be approximated by:

$$\begin{aligned} z_{focus} &\approx f \\ w_{focus} &\approx \frac{\lambda\,f}{\pi\,w_{01}} = \Theta_{div}\,f \ , \end{aligned} \tag{2.57}$$

where the angle of divergence was inserted. The approximate result is plotted in figure 2.3 and labelled "approx", for comparison with the precise curve. It seems that $f > 2\,z_{0f}$ and the condition for approximation $f \ll z_0$ are contradictiously, but they are not. This can be seen by rewriting the approximation condition in following way:

$$f \ll z_{01} = \frac{\pi\,w_{01}^2}{\lambda} \leq \frac{\pi}{\lambda}\Big(\frac{\lambda\,f}{\pi\,w_{focus}}\Big)^2 = \frac{f^2}{z_{0f}} \quad \Rightarrow \quad f \gg z_{0f} \ , \tag{2.58}$$

where we used the maximum result for w_{01} in equation (2.56). Another way of writing the approximation condition is:

$$\begin{aligned} f \ll z_{01} &= \frac{\pi\,w_{01}^2}{\lambda} \qquad \Big|\ \frac{\lambda}{\pi\,w_{01}} \\ w_{focus} \approx \frac{\lambda\,f}{\pi\,w_{01}} &\ll w_{01} \ . \end{aligned} \tag{2.59}$$

This means that, as long as the waist radius of the focus is much smaller than the beam radius at the lens, equation (2.57) is applicable. This is shown in graph 2.3.

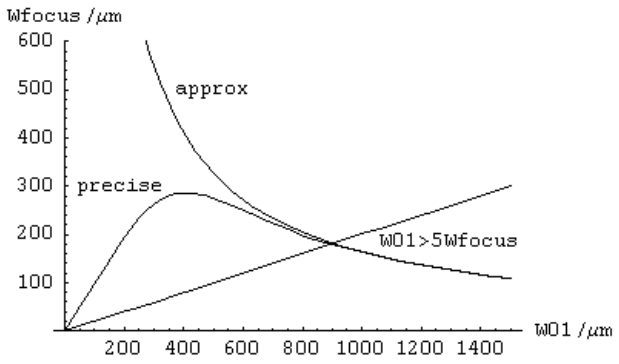

Figure 2.3: Waist at focus as a function of the waist at lens for focal length f=0.5 m. Precise and approximate results are plotted. A line with $w_{01} = 5\, w_{focus}$ is drawn, representing $w_{01} \gg w_{focus}$.

Equation (2.57) is very useful if one wants to measure the waist of a laser since it only depends on the wavelength and the focal length of the lens. As long as the position of the focus is in good agreement with the focal length this formula can be applied (this is just another formulation of previous condition for the approximation). For different lenses the angle of divergence is measured, which directly gives the waist of the laser.

In a similar way as before we can calculate a real (i.e. thick) plano-convex lens by the ray matrix $M_{PCX} = M_{pb}(n,1) \cdot M_{space}(d) \cdot M_{sb}(r,1,n) \cdot M_{space}(z_1)$, where the planar side is pointing away from the focus. Equations (2.50) yield:

$$w_{focus} = \frac{w_{01}\, f_{PCX}}{\sqrt{z_{01}^2 + (z_1 - f_{PCX})^2}} \tag{2.60a}$$

$$z_{focus} = -f_{PCX} \frac{z_{01}^2 + z_1(z_1 - f_{PCX})}{z_{01}^2 + (z_1 - f_{PCX})^2} + \frac{d}{n} \tag{2.60b}$$

$$\text{with} \quad f_{PCX} \equiv \frac{r}{n-1}\ . \tag{2.60c}$$

If the lens is turned around, i.e. the planar side points towards the focus, we get the same result, except that $z_1 \mapsto z_1 + \frac{d}{n}$ in the above equations. If we set the thickness $d = 0$, i.e. for a thin lens, both results agree exactly with equations (2.54) with the focal length determined by f_{PCX}. With these formulas one can easily calculate the focal length for a given wavelength and radius of curvature of a lens[10].

[10]In the datasheet of the lenses from Laser Component the radius of curvature and the focal lengths are listed for different wavelengths. If the focal length is calculated with equation (2.60c), the result agrees precisely with the values in the datasheet.

We have seen how the propagation of a Gaussian beam can be described by the ABCD law and how it is applied in the case of a collimated beam at the input. This law is very powerful and allows calculation of very complicated systems. Some examples have been presented, which will be useful later.

We have considered the Gaussian beam in previous sections, which normally describes laser beams very well. Also beams within cavities are described by Gaussian-Hermite modes as we will see later. The phase of these modes, which we derived here, will define the transversal resonance frequencies of cavities. We introduced ray transfer matrices and the ABCD law, which allow to describe how a Gaussian beam is changing when it is passing optical elements.

2.2 The Fabry-Perot interferometer

The Fabry-Perot interferometer (FPI) represents the core of the whole setup in this thesis. It consists of two high reflectivity mirrors, standing opposite to each other which is often called a "Fabry-Perot resonator" or simply a "cavity". This simple but powerful tool can be used as a stable frequency reference since its resonance frequencies and width depend only on the geometry and the reflectivity of the mirrors. This will be used in order to reduce the linewidth of a laser. Another feature of such a setup is its capability to store energy, which allows enhancement of the optical power inside the cavity. With this a deep and large trapping potential for our atoms will be produced. In this section the formulas, necessary for designing such a cavity will be derived.

The reflected and transmitted intensity of a FPI is calculated by interferences of plane waves. This reveals features, like resonances and power enhancement which are the essential properties of such a cavity. Further we will regard what happens inside the cavity. The power enhancement will be derived and how it can be maximized in the presence of losses. The waist inside the cavity is given by the geometry. But not all geometries lead to a stable operation of the resonator, which will be discussed in the last part [ST91, HW92, Sie86, GWO00, KL66].

2.2.1 Reflected and transmitted intensity

Here the reflected and transmitted intensity of a FPI with losses will be derived [Dem96, HW92]. The FPI is modelled as two mirrors, standing opposite to each other at a distance L. The inner sides of the mirrors are supplied with a

high reflectivity coating and reflection from the outer surfaces will be neglected[11]. See figure 2.4.

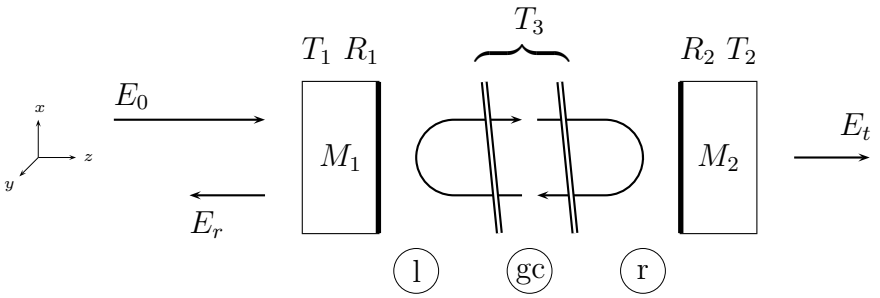

Figure 2.4: Scheme of a Fabry-Perot interferometer with a glassplate or glasscell (gc) inserted. Regions left (l) and right (r) of (gc) are labelled.

The reflectivity of the two mirrors is R_1 and R_2 and the transmittance is T_1 and T_2 respectively, where both variables are taken with respect to the intensity. In order to include losses we model the cavity with a glassplate placed between the mirrors. But it is tilted, so it does not reflect the incoupled light back to the first mirror. In this way it does not form another cavity[11]. But it does cause loss of intensity which is taken into account by the transmittance T_3[12]. The different regions left (l) and right (r) of the glassplate are labelled for later usage in 2.2.3, table 2.3. In our experiment the resonator is placed outside of the glasscell (see 1.2) which mainly causes the losses. The region inside this glasscell is labelled (gc) accordingly.

The half round-trip phase factor is defined by

$$\delta \equiv \frac{\omega\, L}{c} \ , \tag{2.61}$$

with c the speed of light. If the cavity is filled with a medium, one can substitute this constant by $c \mapsto \frac{c}{n}$ to include the refractive index n. In order to take into account an additional phase shift, caused by the glassplate, one can add a phase factor $\Phi_3 = d(n-1)$ to the definition: $\delta \mapsto \delta + \Phi_3$. Here d is the thickness and n the refractive index of the glassplate or glasscell.

The incoming electric field, travelling along the z axis is a plane wave, given in equation (2.7):

$$\vec{E}_0(\vec{z},t) = E_0\, \vec{e}_{x,y}\, \boldsymbol{e}^{\,i\left(\omega t - \vec{k}\cdot\vec{z}\right)} \ , \tag{2.62}$$

[11]By using a method described in [Mac86], one could also include the effect of additional surfaces within a matrix formalism.

[12]The symbol was chosen arbitrarily. Sometimes in the literature one finds a loss coefficient defined equivalent 1-T_3, but using a transmittance seemed to be straight forward here.

where E_0 is the amplitude of the incoming electric field, $\vec{e}_{x,y}$ gives the polarization direction in either x or y direction, t is the time, $\vec{k}$ is the associated wave vector with $k = \frac{2\pi}{\lambda} = \frac{\omega}{c}$. The angular frequency is denoted with $\omega = 2\pi f$, where f is the frequency given in Hertz. Assuming that the wave vector points along the z axis, allows to rewrite the inner product $\vec{k} \cdot \vec{z} = kz$ and from now on, we will assume linear polarization in one direction and neglect other directions.

With equation (2.24) the input intensity becomes from (2.62):

$$I_0 = \frac{\epsilon_0\, c}{2} \left\langle \left| E(z,t) \right|^2 \right\rangle_T = \epsilon_0\, c\, \frac{E_0^2}{2} \ , \tag{2.63}$$

which, due to the averaging, neither depend on time nor on space. Therefore, in the rest of this section the dependency of space and time will be omitted since it will average out everywhere outside the FPI.

Summing up the electric fields within the mirrors gives for the transmitted electric field of the FPI:

$$\begin{aligned} E_t &= E_0 \sum_{m=0}^{\infty} \sqrt{T_1 T_2}\, T_3^{(2m+1)/2}\, \boldsymbol{e}^{-i\,\delta(2m+1)}\, R_1^{m/2}\, R_2^{m/2}\, \boldsymbol{e}^{-i\,\pi\,2m} \\ &= E_0 \sqrt{T_1 T_2 T_3}\, \boldsymbol{e}^{-i\,\delta} \sum_{m=0}^{\infty} \left(T_3\, \boldsymbol{e}^{-i\,2\,\delta} \sqrt{R_1 R_2}\, \boldsymbol{e}^{-i\,2\pi} \right)^m \ . \end{aligned} \tag{2.64}$$

Using the geometric series

$$\sum_{m=0}^{\infty} q^m = \frac{1}{1-q} \ , \qquad \text{for} \quad \left|q\right| \le 1 \ , \tag{2.65}$$

and the fact that $\boldsymbol{e}^{-i\,2\pi} = 1$ the transmitted field is:

$$E_t = E_0\, \frac{\sqrt{T_1\, T_2\, T_3}\, \boldsymbol{e}^{-i\,\delta}}{1 - T_3 \sqrt{R_1 R_2}\, \boldsymbol{e}^{-i\,2\delta}} \ . \tag{2.66}$$

From this the transmitted intensity with equation (2.24) becomes

$$\begin{aligned} I_t &= \frac{\epsilon_0\, c}{2}\, E_0^2 \left| \frac{\sqrt{T_1\, T_2\, T_3}\, \boldsymbol{e}^{-i\,\delta}}{1 - T_3 \sqrt{R_1 R_2}\, \boldsymbol{e}^{-i\,2\delta}} \right|^2 \\ &= I_0\, \frac{T_1\, T_2\, T_3}{1 - 2\, T_3 \sqrt{R_1 R_2}\, \cos[2\delta] + R_1\, R_2\, T_3^2} \\ &= I_0\, \frac{T_1\, T_2\, T_3}{(1 - T_3 \sqrt{R_1 R_2})^2 + 2\, T_3 \sqrt{R_1 R_2}\, (1 - \cos[2\delta])} \\ &= I_0\, \frac{T_1\, T_2\, T_3}{(1-Z)^2 + 4\, Z \sin^2[\delta]} \ , \end{aligned} \tag{2.67}$$

where the initial intensity has been taken into account from equation (2.63). The identity $1-\cos[\alpha] = 2\sin^2[\alpha/2]$ has been used and the "effective reflectivity" Z has been defined as[13]:

$$Z \equiv T_3 \sqrt{R_1 R_2} \; . \tag{2.68}$$

If the mirrors are equal and no losses are present (i.e. $T = 1$), Z becomes simply the reflectivity of the mirrors $Z = R_1 = R_2 = R$. In the appendix, section 6.6, equation (6.37), we show an alternative way of calculating the transmitted electric field.

Following the same procedure as before the reflected electric field is:

$$\begin{aligned} E_r &= E_0 \left(\sqrt{R_1} + \sum_{m=0}^{\infty} T_1 \, T_3^{(2m+2)/2} \, \boldsymbol{e}^{-i\,\delta(2m+2)} \, R_1^{m/2} \, R_2^{(m+1)/2} \, \boldsymbol{e}^{-i\,\pi\,(2m+1)} \right) \\ &= E_0 \left(\sqrt{R_1} - T_1 \, T_3 \, \sqrt{R_2} \, \boldsymbol{e}^{-i\,2\,\delta} \sum_{m=0}^{\infty} \left(T_3 \, \boldsymbol{e}^{-i\,2\,\delta} \, \sqrt{R_1 R_2} \, \right)^m \right) \\ &= E_0 \left(\sqrt{R_1} - \frac{T_1 \, T_3 \, \sqrt{R_2} \, \boldsymbol{e}^{-i\,2\,\delta}}{1 - T_3 \, \sqrt{R_1 R_2} \, \boldsymbol{e}^{-i\,2\,\delta}} \right) \; . \end{aligned} \tag{2.69}$$

Note the missing phase jump of π at the first reflection whose origin stems from time reversal symmetry, which will be shown immediately.

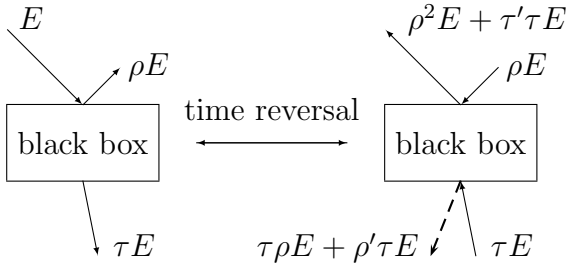

Figure 2.5: Time reversal symmetry causes a relative phase jump of π in reverse direction with respect to forward direction

In figure 2.5 the situation of an incoming electric field, entering a lossless medium ("black box"), is shown. The fields must be the same when time is reversed. This yields the requirements:

$$\begin{aligned} \rho^2 E + \tau' \tau E &\stackrel{!}{=} E \\ \tau \rho E + \rho' \tau E &\stackrel{!}{=} 0 \; , \end{aligned} \tag{2.70}$$

[13]The symbol Z is not commonly used, but was chosen following the impedance in electronics.

where the ρ and τ are the complex reflection and transmission coefficients in the forward direction (with respect to the electric fields) and ρ' and τ' denote the coefficients in backward direction. This requirement leads immediately to the result:

$$\begin{aligned} \rho^2 + \tau'\tau &\stackrel{!}{=} 1 \\ \rho' &\stackrel{!}{=} -\rho \ . \end{aligned} \tag{2.71}$$

These equations are called the Stokes relations and give the remarkable result that the reflected electric field is exactly the same in the reverse direction as in the forward direction but has an additional phase shift of π. This phase shift is the origin of our missing phase factor from before. The "black box" is the mirror in our case. We assumed in the calculation that if the light inside the cavity is reflected on the mirror it becomes phase shifted by π. According to the Stokes relations, if the light comes from outside the cavity it must get an additional phase shift of π, which results in a total phase shift of 2π. Therefore, the phase shift was set to zero for the first reflection. The Stokes relations are very general and are moreover true for complicated structures (like dielectric mirrors which consist of many layers) as long as there are no losses inside the media. Small losses will not alter the above relations too much (this would actually be the definition of small losses in this case).

With equations (2.69) and (2.24) the reflected intensity becomes:

$$\begin{aligned} I_r &= \frac{\epsilon_0\, c}{2}\, E_0^2 \Big| \frac{\sqrt{R_1}(1 - Z\, \boldsymbol{e}^{-i\,2\,\delta}) - T_1\, T_3\, \sqrt{R_2}\, \boldsymbol{e}^{-i\,2\,\delta}}{1 - Z\, \boldsymbol{e}^{-i\,2\,\delta}} \Big|^2 \\ &= I_0\, \frac{R_1((1-Z)^2 + 4\,Z \sin^2[\delta]) + T_1^2\, T_3^2\, R_2 - 2\,Z\,T_1\,(\cos[2\,\delta] - Z)}{(1-Z)^2 + 4\,Z \sin^2[\delta]} \\ &= I_0\, \frac{(\sqrt{R_1}\,(1-Z) - T_1\, T_3 \sqrt{R_2}\,)^2 + 4\,Z\, \sin^2[\delta]\,(T_1 + R_1)}{(1-Z)^2 + 4\,Z \sin^2[\delta]} \ . \end{aligned} \tag{2.72}$$

For the case of no losses (T_3=1) and equal mirrors ($R_1 = R_2$) it is convenient to rewrite the transmitted and reflected intensities, equations (2.67) and (2.72):

$$I_t = I_0\, \frac{1}{1 + (\frac{2\sqrt{R}}{1-R})^2\, \sin^2[\delta]} = I_0\, \frac{1}{1 + (\frac{2\,F}{\pi})^2\, \sin^2[\delta]} \tag{2.73a}$$

$$\text{with F} \equiv \frac{\pi\sqrt{R}}{1-R} \ .$$

$$I_r = I_0\, \frac{(\frac{2\sqrt{R}}{1-R})^2\, \sin^2[\delta]}{1 + (\frac{2\sqrt{R}}{1-R})^2\, \sin^2[\delta]} = I_0\, \frac{(\frac{2\,F}{\pi})^2\, \sin^2[\delta]}{1 + (\frac{2\,F}{\pi})^2\, \sin^2[\delta]} \tag{2.73b}$$

We have defined the new variable F, called finesse, which will proof to be very useful for characterizing the FPI. It will be discussed in the following section, where we will define it in a more general way, consistent with the definition given here. These equations (2.73) are called the Airy formulas. They are plotted in

figure 2.6 showing the reflection and transmission of the FPI as a function of δ for different mirror reflectivity.

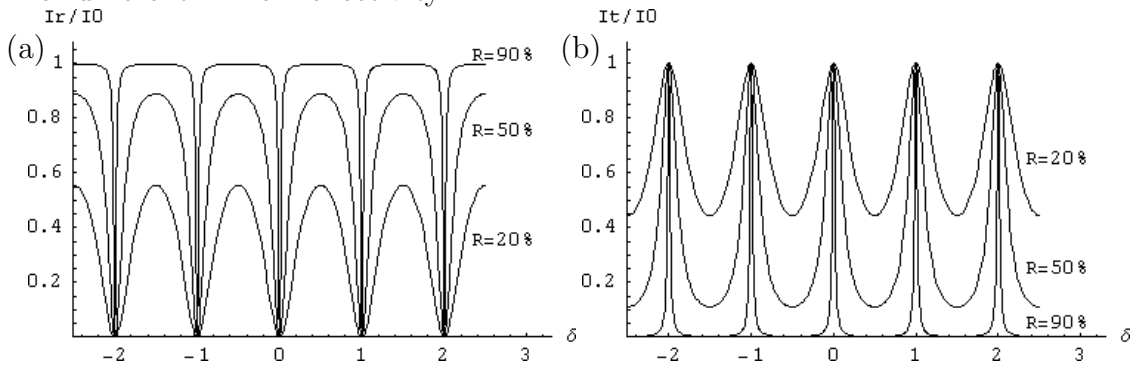

Figure 2.6: a) Reflection and b) transmission of the FPI given by equations (2.73) for $R_1 = R_2 = R$ and $T_3 = 1$.

We see that for certain frequencies the reflection becomes zero while the transmission becomes I_0, i.e. all the light passes the Fabry-Perot Interferometer. These so-called resonances are very useful as a frequency reference since they only depend on the geometry of the cavity, as will be shown in the next section.

Of course the energy conservation condition must be fulfilled which is given by $I_0 = I_r + I_t + I_{loss}^{total}$ where the total losses have been included. From this and the previous results the total losses can be derived:

$$\begin{aligned} I_{loss}^{total} = I_0 \frac{(1-Z)^2 - (\sqrt{R_1}\,(1-Z) - T_1\,T_3\sqrt{R_2}\,)^2}{(1-Z)^2 + 4\,Z\sin^2[\delta]} \times \\ \times \frac{-T_1\,T_2\,T_3 + 4\,Z\,\sin^2[\delta](1-T_1-R_1)}{(1-Z)^2 + 4\,Z\sin^2[\delta]} \end{aligned} \tag{2.74}$$

If one assumes no losses in the mirrors and inserts $T_1 = 1 - R_1$ and $T_2 = 1 - R_2$ in the previous formula then the losses due to T_3 are:

$$I_{loss}^{total} \approx I_0 \frac{T_1(1-T_3)(1+T_3\,R_2)}{(1-Z)^2 + 4\,Z\sin^2[\delta]} = \frac{(1-T_3)(1+T_3\,R_2)}{T_2\,T_3}\,I_t \tag{2.75}$$

It is convenient to define a loss coefficient S≡1-T_3, which is large when the losses are large[14]. In figure 2.7a) and b) we plot the losses of the FPI for different configurations. For δ approaching integer multiples of π, the losses are increased significantly. Further we see that the losses increase as well for higher reflectivity until a maximum is reached, after which they decrease rapidly. At first sight this seems contradictiously but this can be understood by the fact that the losses follow the transmitted intensity of the cavity, as given by equation (2.75). This

[14]There exists no common symbol for the loss coefficient. Sometimes it is S,L or α.

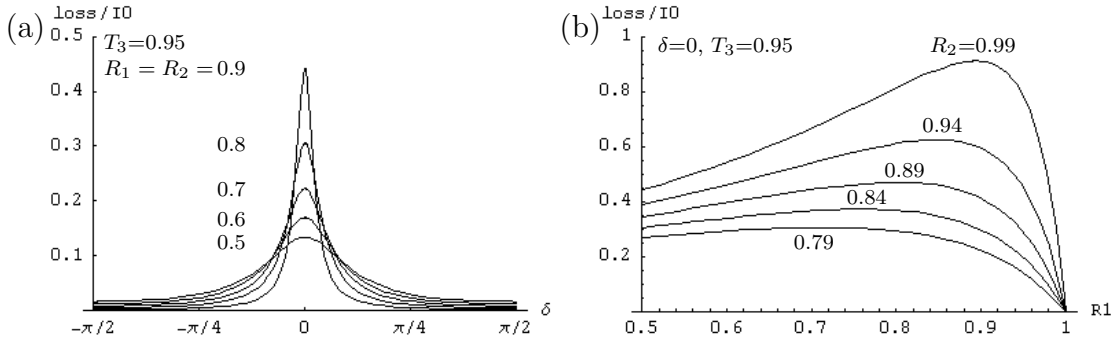

Figure 2.7: Losses of FPI as a function of a) δ and b) R_1. For each line either $R_1 = R_2$ or R_2 is altered in a) and b) respectively. The corresponding values are given. For both graphs T_3=0.95.

is large on resonance (see figure 2.6b) and for high reflectivity of the mirrors. For high reflectivity the power which can be coupled into the cavity decreases. Therefore, the losses are decreasing for the reflectivity approaching 100 %. If one would plot the losses divided over the transmitted intensity, one would obtain constant functions in both graphs, since this fraction does neither depend on R_1 nor on δ, as seen from equation (2.75). Another fact concerning the losses of the cavity must be mentioned. The sensitivity of the cavity to losses increases dramatically with increasing reflectivity of the mirrors. See figure 2.8. This

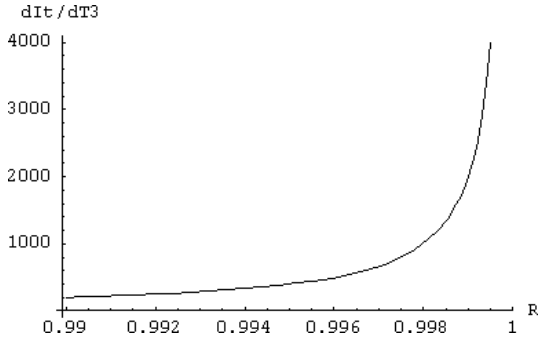

Figure 2.8: Sensitivity of losses of the FPI, equation (2.76), and I_0=1 W.

can be seen by deriving equation (2.67) by T_3 and setting $R_1 = R_2 = R$ and $T_1 = T_2 = 1 - R$:

$$\frac{dI_t}{dT_3} = I_0 \frac{1+R}{1-R} \,. \tag{2.76}$$

For the reflectivity approaching 1, the sensitivity becomes infinity. This comes from the fact, that each photon stays much longer inside the cavity and passes the region causing losses very often (see next sections). This implies, that with a FPI having high reflectivity one can measure very sensitively losses caused

by a medium inserted into the cavity. But on the other side, this means, that additional losses, caused for example by acoustic noise or other disturbances, have a much larger effect on high-reflectivity cavities, than on cavities having low reflectivity.

We have calculated the reflected and transmitted electric field of a Fabry-Perot interferometer. From the resulting intensity we derived the losses by using energy conservation. We saw that for certain frequencies the transmitted intensity becomes a maximum, which are the resonances of the cavity, discussed in detail in the next section.

2.2.2 FSR, FWHM and finesse

In this section the resonance condition and some of the important parameters characterizing a FPI will be derived. These are the spacing between adjacent longitudinal modes, the linewidth of the resonance peaks and the finesse. The cavity decay time and some line broadening effects will be discussed at the end.

From equations (2.67) and (2.72) in the previous section one sees immediately that for

$$\delta_m \stackrel{!}{=} m\,\pi \ , \qquad \text{with } m \text{ integer.} \tag{2.77}$$

the transmission is maximal whereas the reflection is minimal. With the definition of δ in (2.61) this gives a resonance condition for the frequency of the laser:

$$\begin{aligned} \omega_m &\stackrel{!}{=} m\,\frac{\pi\,c}{L} \\ f_m &\stackrel{!}{=} m\,\frac{c}{2\,L}\ , \end{aligned} \qquad \text{with } m \text{ integer.} \tag{2.78}$$

We have an infinite number of equally spaced resonances. The spacing is called the free spectral range (FSR) and is:

$$\mathrm{FSR} \equiv \frac{c}{2\,L}\ . \tag{2.79}$$

It is usually in the MHz or GHz range and is inversely proportional to the length of the cavity. For example, a cavity having L=150 mm has a FSR of 1 GHz. Solving the resonance condition for the length of the cavity we obtain:

$$L \stackrel{!}{=} m\,\frac{c}{2\,f_m} = m\,\frac{\lambda}{2}\ . \tag{2.80}$$

This means, that we can change the length of the cavity by half of the laser wavelength and jump by this from one resonance to the next. This intuitively

corresponds to the behavior of a standing wave. Therefore, these frequencies are called longitudinal frequencies or longitudinal modes of the resonator. In section 2.2.5 we will see that additional resonances appear due to the geometry of the resonator, which therefore are called transversal modes.

With equation (2.67) the maximum transmitted intensity becomes:

$$I_t^{max} = I_0 \, \frac{T_1 \, T_2 \, T_3}{(1-Z)^2} \; , \tag{2.81}$$

and the frequency of half maximum intensity is found by solving

$$\frac{I_t^{max}}{2} \stackrel{!}{=} I_0 \, \frac{T_1 \, T_2 \, T_3}{(1-Z)^2 + 4\,Z \sin^2[\frac{\pi}{\mathrm{FSR}} f_{1/2}]} \; , \tag{2.82}$$

which has the solution

$$f_{1/2} = \pm \, \frac{\mathrm{FSR}}{2\,\pi} \arccos\left[1 - \frac{(1-Z)^2}{2\,Z}\right] + \mathrm{FSR}\; m \; , \qquad \text{with } m \text{ integer.} \tag{2.83}$$

The width of the peak at half maximum intensity, which is commonly known as full-width-half-maximum (FWHM) is therefore:

$$\mathrm{FWHM} \equiv \frac{\mathrm{FSR}}{\pi} \arccos\left[1 - \frac{(1-Z)^2}{2\,Z}\right] \; . \tag{2.84}$$

The finesse (F) is defined as the ratio of the FSR over the FWHM and is therefore:

$$\mathrm{F} \equiv \frac{\mathrm{FSR}}{\mathrm{FWHM}} = \frac{\pi}{\arccos\left[1 - \frac{(1-Z)^2}{2\,Z}\right]} \; . \tag{2.85}$$

These expressions are precise but not so handy for daily work. Using the fact that in most cases Z is close to 1, which makes the term $\frac{(1-Z)^2}{2\,Z}$ small, allows a Taylor expansion in first order of

$$\arccos[1-\epsilon\,] = \sqrt{2\,\epsilon} + \mathcal{O}[\,\epsilon^{\,3/2}\,] \; , \qquad \text{with } \epsilon \ll 1 \; , \tag{2.86}$$

which gives for the arccos term:

$$\arccos\left[1 - \frac{(1-Z)^2}{2\,Z}\right] \approx \sqrt{2\frac{(1-Z)^2}{2\,Z}} = \frac{1-Z}{\sqrt{Z}} \; . \tag{2.87}$$

Using this approximation the precise result for the finesse given in equation (2.85) becomes the common expression given in literature. Losses are included within the coefficient T_3:

$$\mathrm{F} \approx \frac{\pi\,\sqrt{Z}}{1-Z} \; , \qquad \text{with } Z \equiv T_3\,\sqrt{R_1 R_2} \lesssim 1 \; . \tag{2.88}$$

For the approximate calculation of the FWHM one can use this result:

$$\mathrm{FWHM} = \frac{\mathrm{FSR}}{\mathrm{F}} \approx \frac{c}{2\,L}\frac{1-Z}{\pi\sqrt{Z}} \ . \tag{2.89}$$

We see that for Z approaching 1 the finesse becomes very large and the linewidth becomes small. We can make a Taylor expansion of the finesse for small losses of the cavity $S = 1 - T_3 \ll 1$:

$$\mathrm{F} = \frac{\pi\sqrt[4]{R_1 R_2}}{1-\sqrt{R_1 R_2}}\left(1 - \frac{1+\sqrt{R_1 R_2}}{1-\sqrt{R_1 R_2}}\,\frac{S}{2}\right) + \mathcal{O}[S^2] \ . \tag{2.90}$$

If there are losses inside the cavity they reduce the finesse and increase the linewidth. This effect can become very large for high reflectivity cavities, as already mentioned above.

Since it will be useful later we give here the inverse formula of equation (2.88), in order to calculate Z in dependence of the finesse:

$$Z = 1 + \frac{\pi}{\mathrm{F}}\left(\frac{\pi}{2\,\mathrm{F}} - \sqrt{1+\left(\frac{\pi}{2\,\mathrm{F}}\right)^2}\right) \ . \tag{2.91}$$

The unphysical solution, which has a "+" sign in front of the root, was left out since $0 < Z < 1$ must be fulfilled. For high reflectivity mirrors ($1 - Z \ll 1$) the finesse F becomes very large and can be approximated by a Taylor series expansion. The same we do for Z with the small quantity being $\frac{\pi}{2\,\mathrm{F}} \ll 1$:

$$\begin{aligned} \mathrm{F} &= \frac{\pi}{1-Z} - \frac{\pi}{2} - \frac{\pi}{8}(1-Z) + \mathcal{O}[(1-Z)^2] \\ Z &= 1 - \frac{\pi}{\mathrm{F}} + 2\Big(\frac{\pi}{2\,\mathrm{F}}\Big)^2 + \mathcal{O}\Big[\Big(\frac{\pi}{2\,\mathrm{F}}\Big)^3\Big] \ . \end{aligned} \tag{2.92}$$

One could also approximate the arccos term by

$$\arccos\left[1 - \frac{(1-Z)^2}{2\,Z}\right] \approx \big|\ln[Z]\big| \ , \tag{2.93}$$

which is valid for $Z \lesssim 1$. This would give for the finesse

$$\mathrm{F} \approx \frac{\pi}{\big|\ln[Z]\big|} \ , \tag{2.94}$$

which is sometimes given in literature. This approximation is not used any further in this thesis. Instead of the finesse one can also specify a cavity quality factor Q, which is defined as:

$$Q \equiv \frac{f_0}{\mathrm{FWHM}} = \frac{c}{\lambda}\frac{\mathrm{F}}{\mathrm{FSR}} = \frac{2\,L}{\lambda}\,\mathrm{F} \ . \tag{2.95}$$

The finesse can simply be measured by changing the length of the cavity by at least one FSR (=$\lambda/2$ of distance), by a piezo (piezo ceramic transducer), while recording the transmitted intensity. The fraction of the spacing between the TEM_{00} modes and the linewidth of them gives the finesse. This method is simple but has some disadvantages. Moving the piezo needs some time, during which the laser and the cavity must be stable. The piezo is not moving linearly and using a piezo in general causes mechanical instabilities. Another method would be to create sidebands on the laser light with an EOM and measure the linewidth relative to the spacing of the sidebands. This still needs a piezo, but the measurement time can be reduced since only the sideband spacing must be bridged by the piezo. If it is possible one could change the frequency of the laser instead of the length of the cavity. Maybe the most elegant method to measure the finesse of a cavity is to switch off the laser light fast and measure the decay time of the transmitted intensity. This time is directly related to the finesse, which we will derive immediately.

At time t after the laser was switched off, the transmitted intensity $I(t)$ can be expressed as a function of the transmitted intensity before one round trip $I(t-\Delta t)$, with $\Delta t = 2L/c$ the round trip time:

$$I(t) = I(t-\Delta t)\, T_3^2\, R_1\, R_2 = I(t-\Delta t)\, Z^2 \ . \tag{2.96}$$

The difference in intensity is:

$$\begin{aligned} \Delta I = I(t) - I(t-\Delta t) \ &= \ -I(t-\Delta t)(1-Z^2) \\ &= -I(t-\Delta t)(1-(1-\epsilon)^2) \\ &= -I(t-\Delta t)(1-(1-2\epsilon+\epsilon^2) \\ &\approx -I(t-\Delta t)\, 2\epsilon \ = -2\, I(t-\Delta t)\, (1-Z) \ , \end{aligned} \qquad \text{with } \epsilon \equiv 1-Z \ll 1 \ , \tag{2.97}$$

where only the linear term was kept. For small round trip time Δt this leads to the differential equation:

$$\begin{aligned} \dot{I}(t) &= \frac{dI}{dt} \approx \frac{\Delta I}{\Delta t} \\ \dot{I}(t) &\approx -2\, I(t)\, (1-Z) \frac{c}{2L} = -(1-Z)\frac{c}{L} I(t) \ . \end{aligned} \tag{2.98}$$

With the initial intensity $I(t=0) = I_0$ this has the solution:

$$\begin{aligned} I(t) &= I_0\, \boldsymbol{e}^{-(1-Z)\frac{c}{L}\, t} \\ &= I_0\, \boldsymbol{e}^{-t/\tau} \ , \end{aligned} \qquad \text{with } \tau \equiv \frac{L}{c\,(1-Z)} \ . \tag{2.99}$$

After the decay time τ the transmitted intensity has exponentially decreased by a factor $1/e \approx 0.368$. We can substitute Z by the finesse F using equation (2.91)

in the definition of τ:

$$\begin{aligned}\tau \equiv \frac{L}{c\,(1-Z)} &\overset{(2.91)}{\downarrow} -\frac{L\,\mathrm{F}}{c\,\pi\,\left(\frac{\pi}{2\,\mathrm{F}} - \sqrt{1+\left(\frac{\pi}{2\,\mathrm{F}}\right)^2}\,\right)} \\ &= \frac{L}{c}\left(\frac{\mathrm{F}}{\pi} + \frac{1}{2} + \frac{1}{4}\Big(\frac{\pi}{2\,\mathrm{F}}\Big) + \mathcal{O}\Big[\Big(\frac{\pi}{2\,\mathrm{F}}\Big)^3\Big]\right)\ .\end{aligned} \tag{2.100}$$

In the last step we have again performed a Taylor expansion in $\frac{\pi}{2\,\mathrm{F}}$. As already mentioned, from the measurement of the decay time the finesse can be obtained in an elegant way. This is especially true for high finesse cavities who have a relatively long decay time (1μs for F=10^4 and L=100mm). Such a measurement is often called a cavity ring-down measurement. An application is cavity ring-down spectroscopy (CRDS) where the losses inside a high finesse cavity are measured by the decay time. With this method small amounts of gases inside the cavity can be measured precisely. In the appendix, section 6.6 we have derived the same result, equation (6.40), in an alternative way. There the non-resonant case is included additionally, where in equation (6.42) the general time constant is calculated explicitly. These results correspond to the case where the input field is switched fast with respect to the cavity decay time. But the measurement in section 3.4.2, figure 3.15, showed that the input field could not be switched off fast enough. Therefore, in the appendix we calculated the ring-down time if the laser is switched off exponentially, which resulted in equation (6.47). In figure 6.2 an example is plotted.

With the decay time one can calculate how many round trips (N) in average each photon makes before escaping from the cavity. We obtain this by using the fact that for an exponential decay the mean time which each photon stays inside the cavity is τ:

$$\bar{T} = \frac{\int_0^\infty t\,\boldsymbol{e}^{-t/\tau}dt}{\int_0^\infty \boldsymbol{e}^{-t/\tau}dt} = \tau \tag{2.101a}$$

$$N = \frac{c}{2\,L}\,\bar{T} = \frac{c}{2\,L}\,\frac{L}{c\,(1-Z)} = \frac{1}{2(1-Z)} \tag{2.101b}$$

$$\text{Taylor:}\quad N = \frac{\mathrm{F}}{2\,\pi} + \frac{1}{4} + \frac{1}{8}\Big(\frac{\pi}{2\,\mathrm{F}}\Big) + \mathcal{O}\Big[\Big(\frac{\pi}{2\,\mathrm{F}}\Big)^3\Big]\ . \tag{2.101c}$$

Equation (2.100) was inserted and the same approximation as there was made. Another important parameter is the mean path length which the light propagates inside the cavity. This is the mean time each photon stays inside the cavity (2.100) multiplied by the speed of light:

$$\Delta l = c\,\bar{T} = \frac{L}{\pi}\mathrm{F}\ . \tag{2.102}$$

For our experiment it is important that the laser stays coherent within this length. Otherwise, the power enhancement described in the next section will not work

anymore, since it relies on the interference capability of the laser light. This will lead to a requirement of the laser linewidth, which will be derived in section 2.4.1.

So far we only considered the case for which the light incoming into the FPI is monochromatic. But lasers have some intrinsic linewidth which causes the measured linewidth of the FPI to be broadened. This can be expressed as the convolution of the Airy function I_t from equation (2.73) and the distribution function L of the Laser. This situation is described in the appendix (section 6.3). The convolution is defined as:

$$I_t(\omega) * L(\omega) \equiv \int_{-\infty}^{\infty} I_t(\omega')\, L(\omega - \omega')\, d\omega' \ . \tag{2.103}$$

If the laser has only one single frequency then $L(\omega)$ is the Dirac delta distribution and we get exactly the Airy function. For a Lorentzian distribution the Airy function can be approximated by a Lorentz function as well, resulting in a linewidth of the convolution which is the sum of both Lorentzian HWHM, as was shown in (6.25). If the laser is better described by a Gaussian curve the result is the Voigt profile for which no analytical solution exists (see equation (6.26) in the appendix). Therefore, a numerical calculation was done and the result is plotted in figure 2.9. The line profiles in 2.9a) are plotted for the case that the laser has twice the FWHM of the FPI $\delta = 2\delta_A$, where we used deltas for simplicity. The FWHM is given for different ratios of δ/δ_A in 2.9b). One can see that if one

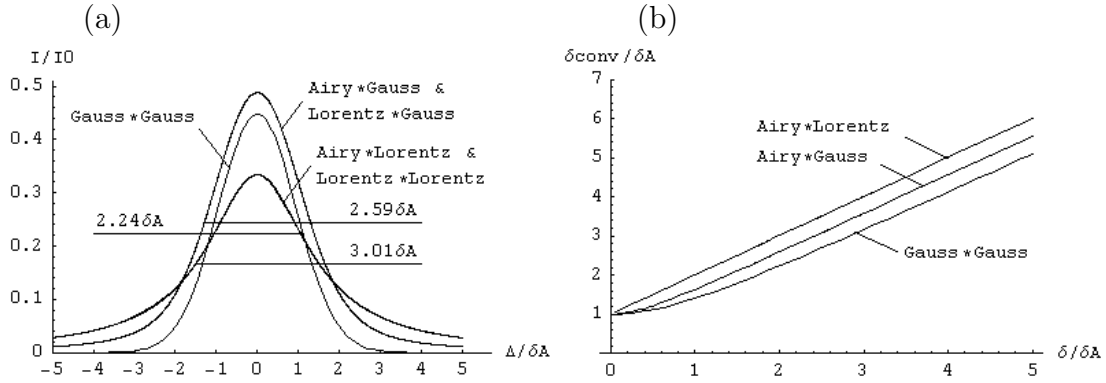

Figure 2.9: Numerical calculation of the convolution of the FPI-transmission with a laser having Gaussian or Lorentzian distribution. a) Lineshape for $\delta = 2\delta_A$. b) FWHM for different δ/δ_A.

approximates both, the cavity and the laser, as Gaussian (Lorentzian) curves one will obtain a lower (upper) boundary for the linewidth. The linewidth for two Gauss functions is derived in equation (6.23) and that of two Lorentz functions is derived in equation (6.25). In order to obtain the exact laser linewidth from the transmission curve of a FPI one has to know the linewidth of the FPI and assume a line profile for the Laser. Then one can determine from figure 2.9 the laser linewidth.

There exist other line broadening mechanisms, but we do not want to go into the details further. We only want to mention that, if the cavity or the laser is scanned faster than the cavity decay time this can cause interferences of the incoming light with the light stored in the cavity, causing an asymmetric line profile and oscillations of the transmitted intensity. Such a behavior was observed and is discussed in section 3.4.3.

We have seen that a Fabry-Perot type cavity has certain resonance frequencies which are predefined by the distance of the mirrors. The linewidth of the cavity is related to the finesse which is determined by the losses and the reflectivity of the mirrors. The finesse can be obtained by scanning the length of the cavity, or via the cavity decay time. We have discussed that the finite linewidth of the laser broadens the measured linewidth.

2.2.3 Power enhancement

In the previous section the light reflected and transmitted from the FPI was discussed. Now we want to consider what happens inside the cavity. Light bounces forwards and backwards between the mirrors and builds a standing wave by interference. The intensity shows maxima which are separated by $\lambda/2$ and in the maxima it is much higher than that of the incoming beam. This feature will be used in order to trap atoms by the dipolar force, mentioned in section 1.2 and further discussed in section 3.4.5. This intensity enhancement, or power enhancement, will be derived here for calculating and optimizing such a cavity in the following paragraph.

Starting from equation (2.81) for the maximum transmitted intensity, i.e. the case when the incoming light is in resonance with the FPI, the maximum intensity inside the cavity can be estimated from the maximum transmitted intensity by:

$$I_{max} \approx 4\,\frac{I_t^{max}}{T_2} = 4\,I_0\,\frac{T_1\,T_3}{(1-Z)^2}\ . \tag{2.104}$$

The factor of 4 takes into account that the electric fields interfere constructively, giving a factor of 2, which becomes 4 for the intensity. The power enhancement (A) is defined as the intensity in the maximum divided over the input intensity:

$$A \equiv \frac{I_{max}}{I_0} \approx \frac{4}{T_2}\,\frac{I_t^{max}}{I_0} = 4\,\frac{T_1\,T_3}{(1-Z)^2}\ . \tag{2.105}$$

Of course this is an estimation and, using the same procedure as in section 2.2.1, one can calculate the maximum intensity inside the FPI precisely. This is what we will do now. For this purpose the field inside the cavity is

calculated at a distance z to the first mirror. First we do this without losses:

$$\begin{aligned} E_{FPI}(z) &= E_0 \sum_{m=0}^{\infty} \sqrt{T_1}\, \boldsymbol{e}^{-i\,(\delta\,2m+\frac{\omega}{c}\,z)}\, R_1^{m/2}\, R_2^{m/2}\, \boldsymbol{e}^{-i\,\pi\,2m} + \\ &+ E_0 \sum_{m=0}^{\infty} \sqrt{T_1}\, \boldsymbol{e}^{-i\,(\delta\,(2m+1)+\frac{\omega}{c}\,(L-z))}\, R_1^{m/2}\, R_2^{(m+1)/2}\, \boldsymbol{e}^{-i\,\pi\,(2m+1)} \\ &= E_0\, \sqrt{T_1}\, \frac{\boldsymbol{e}^{-i\,\delta\,z/L} - \sqrt{R_2}\, \boldsymbol{e}^{-i\,\delta\,(2\,-z/L)}}{1-\sqrt{R_1 R_2}\, \boldsymbol{e}^{-i\,2\,\delta}}\ , \end{aligned} \tag{2.106}$$

where the definition of $\delta \equiv \frac{\omega\,L}{c}$ was used. From this the intensity becomes:

$$I_{FPI}(z) = I_0\, T_1\, \frac{(1-\sqrt{R_2}\,)^2 + 4\,\sqrt{R_2}\,\sin^2[\delta\,(1-z/L)]}{(1-\sqrt{R_1\,R_2}\,)^2 + 4\,\sqrt{R_1\,R_2}\,\sin^2[\delta]}\ . \tag{2.107}$$

Including losses is easy from this result. One has just to substitute, according to table 2.3, where the substitution rules are given for the different regions of the FPI, shown in figure 2.4. Considering different regions inside the FPI is necessary since it makes a difference at which position relative to the glassplate one wants to know the intensity. In the table was included also a row "glasscell", which is simply a region sitting between two glassplates. These glassplates have transmittance $\sqrt{T_3}$ each, so that the total transmittance of the glasscell is T_3.

Table 2.3: Replacement rules for including losses in equation (2.107). The regions refer to figure 2.4.

	region	$T_1 \mapsto$	$R_1 \mapsto$	$R_2 \mapsto$
(l)	left	T_1	R_1	$T_3^2\, R_2$
(r)	right	$T_1\, T_3$	$R_1\, T_3^2$	R_2
(gc)	glasscell	$T_1\, \sqrt{T_3}$	$R_1\, T_3$	$R_2\, T_3$

From equation (2.107) we calculate the intensity at the first mirror (I_1) and at the second mirror (I_2):

$$\begin{aligned} I_1 &= I_0\, T_1\, \frac{(1-T_3\,\sqrt{R_2}\,)^2 + 4\,T_3\,\sqrt{R_2}\,\sin^2[\delta]}{(1-Z)^2 + 4\,Z\,\sin^2[\delta]} \\ I_2 &= I_0\, T_1\, T_3\, \frac{(1-\sqrt{R_2}\,)^2}{(1-Z)^2 + 4\,Z\,\sin^2[\delta]}\ . \end{aligned} \tag{2.108}$$

Figure 2.10a) shows the intensity inside the cavity for different wavelengths and in 2.10b) it is plotted for different losses. In figure 2.10a) one can see, that the

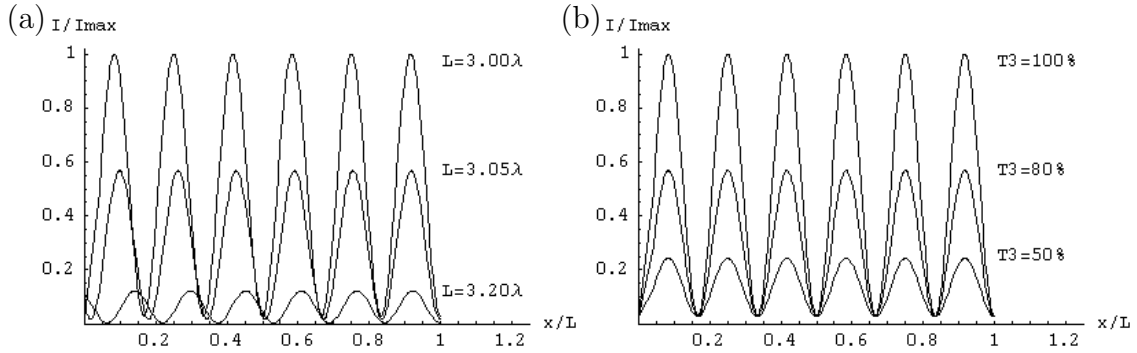

Figure 2.10: Standing wave inside FPI according to (2.107) for $R_1 = R_2$=0.5 . a) Without losses i.e. $T_3 = 1$ for $L = \{3.0\lambda, 3.05\lambda, 3.2\lambda\}$ and b) for $L = 3.0\lambda$ but for different losses $T_3 = \{1.0, 0.8, 0.5\}$.

intensity on the second mirror is always a minimum, but for the first mirror it is only a minimum on resonance.

On resonance, equation (2.78), the intensity (2.107) is maximized, but additionally we obtain maxima (minima) from the $\sin^2$ term in the nominator:

$$\begin{aligned} \sin^2[\delta\,(1 - z/L)] &\stackrel{!}{=} \begin{cases} 1 & \text{max.} \\ 0 & \text{min.} \end{cases} \quad \rightleftharpoons \\ \delta\,(1 - z/L) &\stackrel{!}{=} \begin{cases} \frac{\pi}{2}\,(2\,m + 1) & \text{max.} \\ \pi\,m & \text{min.} \end{cases} \quad \text{with } m \text{ integer.} \end{aligned} \tag{2.109}$$

With $\delta = \frac{\omega\,L}{c} = \frac{2\pi L}{\lambda}$ we obtain the maxima (minima) of the standing wave, which have a periodicity of $\lambda/2$:

$$\begin{aligned} z_{max} &\stackrel{!}{=} L - \frac{\lambda}{4}\,(2\,m + 1) \\ z_{min} &\stackrel{!}{=} L - \frac{\lambda}{2}\,m\ , \end{aligned} \qquad \text{with } m \text{ integer.} \tag{2.110}$$

On resonance the maximum and minimum intensities are as follows. Losses must be included as before, using table 2.3:

$$I_{FPI}^{max} = I_0\,T_1\,\frac{(1 + \sqrt{R_2}\,)^2}{(1 - \sqrt{R_1\,R_2}\,)^2} \tag{2.111a}$$

$$I_{FPI}^{min} = I_0\,T_1\,\frac{(1 - \sqrt{R_2}\,)^2}{(1 - \sqrt{R_1\,R_2}\,)^2}\ . \tag{2.111b}$$

Therefore, the power enhancement factors for the different regions are:

$$A_{FPI}^{(l)} = T_1 \frac{(1 + T_3 \sqrt{R_2}\,)^2}{(1-Z)^2} \tag{2.112a}$$

$$A_{FPI}^{(r)} = T_1 T_3 \frac{(1 + \sqrt{R_2}\,)^2}{(1-Z)^2}\ , \qquad \text{with } Z \equiv T_3 \sqrt{R_1 R_2}\ , \tag{2.112b}$$

$$A_{FPI}^{(gc)} = T_1 \sqrt{T_3} \frac{(1 + \sqrt{T_3 R_2}\,)^2}{(1-Z)^2}\ . \tag{2.112c}$$

These results are nearly the same as equation (2.105) when one assumes a large reflectivity of the second mirror $R_2 \approx 1$ which normally is the case. Therefore, the simpler relation, equation (2.105), can be used without loss of accuracy.

For equal mirrors ($R_1 = R_2 = R$) and without losses ($T_3 = 1$ and $T_{1,2} = 1 - R$) the power enhancement factor simplifies as follows, and we expand this in a Taylor series since $R \lesssim 1$:

$$\begin{aligned} A &= \frac{(1 + \sqrt{R_2}\,)^2}{1-R} \\ &= \frac{4}{1-R} - 2 - \frac{1-R}{4} + \mathcal{O}[(1-R)^2] \\ &\approx \frac{4}{1-R}\ . \end{aligned} \tag{2.113}$$

The factor 4 appears again as before. It is also possible to express the power enhancement approximately by the finesse. For this equation (2.91) is substituted into the previous result with $Z \mapsto R$. Then it is expanded in a series for $\epsilon \equiv \frac{\pi}{2\,\mathrm{F}^2}$ which usually is a very small number:

$$\begin{aligned} A = \frac{4}{1-R} &= \frac{4}{1 - 1 - \frac{\pi}{2\,\mathrm{F}^2}\,(\pi - \sqrt{\pi^2 + 4\,\mathrm{F}^2}\,)} \\ &= \frac{4}{-\epsilon\,(1 - \sqrt{1 - 2/\epsilon}\,)} \qquad \text{with } \epsilon \equiv \frac{\pi}{2\,\mathrm{F}^2} \ll 1 \\ &= \frac{4\,\mathrm{F}}{\pi} + 2 + \frac{\pi}{2\,\mathrm{F}} + \mathcal{O}[\mathrm{F}^{-1/3}] \\ \Rightarrow \qquad A &\approx 4\,\frac{\mathrm{F}}{\pi}\ . \end{aligned} \tag{2.114}$$

This result is useful for making a fast estimation of the power enhancement from a given finesse or vice versa. Since the finesse is strongly dependent of the losses of the cavity, this is true for the power enhancement as well.

The aim is to get as much power inside the cavity as possible. Therefore, the first mirror should have low reflectivity. But on the other hand the reflectivity

of both mirrors should be high for storing as much light as possible inside the cavity. Both demands are in contradiction, which requires to find the optimal compromise for the reflectivity of the first mirror. This value is simply obtained from equations (2.112) by setting the derivation with respect to R_1 to zero

$$0 \stackrel{!}{=} \frac{d}{dR_1} A \ . \tag{2.115}$$

This gives for all regions the so-called "impedance matching condition":

$$R_1^{opt} \stackrel{!}{=} R_2 \, T_3^2 \ . \tag{2.116}$$

With this the maximum power enhancement within the glasscell becomes:

$$A_{max}^{(gc)} = \sqrt{T_3} \, \frac{(1 + \sqrt{T_3 \, R_2} \,)^2}{1 - R_2 \, T_3^2} \ . \tag{2.117}$$

For the numerator expanded in both R_2 and T_3 close to one with keeping the first order of T_3 we obtain the same result as if we insert the optimum R_1^{opt} into equation (2.105):

$$A_{max} = 4 \, \frac{T_3}{1 - R_2 \, T_3^2} \ . \tag{2.118}$$

In figure 2.11 the power enhancement as a function of the entrance mirror reflection R_1 for different transmissions T_3 is plotted. One clearly sees that for

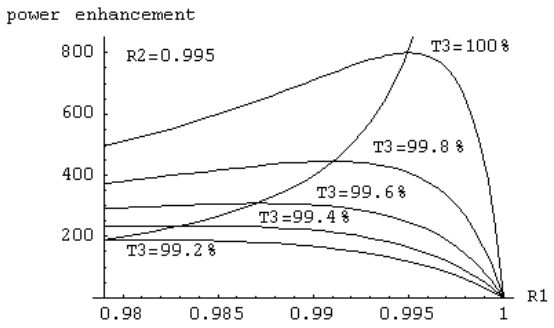

Figure 2.11: Power enhancement as a function of R_1 for $R_2 = 99.5\%$ and $T_3 = 99.2\% \ldots 100\%$.

R_1 approaching 1 the power enhancement falls off rapidly after the maximum. Therefore, the mirror reflectivity R_1 should be chosen close to the maximum R_1^{opt}, but the manufacturing tolerances should be such that they include mainly smaller reflectivity rather than higher.

In summary we have seen that the power enhancement strongly depends on the losses inside the cavity. It can be maximized by choosing the optimum reflectivity of the incoupling mirror according to the losses inside the FPI.

2.2.4 Resonator waist and mode matching

In the preceding sections we only considered plane waves, but as we know from section (2.1.1) a real laser beam has spatial components as waist and radius of curvature. There we saw that laser light in free space behaves like a Gaussian beam. When such a beam is sent into a cavity only the fraction of the incoming light can be amplified which has the same waist and radius of curvature as the light inside the cavity. The other fraction is changed on each round trip and decays rapidly. The cavity acts like a spatial filter (and also as a frequency filter as we saw in section 2.2.2) rejecting not matching light[15]. Therefore, it is desirable that the light inside the cavity is Gaussian. The way this is achieved will be presented here and in the next section. Another advantage in having Gaussian waves inside the cavity is that one can use spherical mirrors which are much easier to manufacture than other shapes. This is true with exception of the planar mirror, but a cavity of two planar mirrors is extremely sensitive of misalignment and it is also not "stable" as will be discussed in the next section. A cavity having one planar and a curved mirror does not have this disadvantages and is therefore the most common choice.

For our application as a resonator enhanced optical dipole trap the FPI is built of two curved mirrors, since we want to trap atoms in the focus of the resonator which has to be in the center of the glasscell (see introduction). For this application the waist of the light inside the resonator is a crucial parameter. On one hand it should be small in order to obtain a high intensity resulting in a deep trapping potential and on the other hand it should be large for trapping as many atoms as possible from the MOT. There exists an optimum value of the waist but it is difficult to predict since it depends on many parameter which we don't know exactly. For example the MOT temperature, densities, etc. This fact demanded an adjustable waist. In this section we describe how to calculate and adjust the waist by choosing the right mirror curvatures and distances between them.

For the light inside a FPI to be Gaussian it is necessary that the mirrors have the same radius of curvature $r(z)$ as the Gaussian beam. This ensures that the wavefronts are reflected back onto themselves so that after one round trip through the cavity the light has the same waist and radius of curvature as before (see section 2.2.5 for details). In the far field (i.e. $z \gg z_0$) the Gaussian beam is nearly spherical which allows using spherical mirrors. If one planar mirror is used, it has to be placed into the focus of the Gaussian beam (since the radius of curvature is infinite there). Under this condition the light can travel the same

[15] One can make a decomposition of the incoming light into a series of Gaussian-Hermite TEM modes and calculate the exact fraction which is accepted by the FPI, but this was not done, since it requires knowing the exact beam profile of the incoming beam.

path many times and only leaks out due to imperfect mirrors. In this context one often refers to the term "unstable" ("stable") which means that the shape of the beam is (is not) altered after one round trip.

Calculating the FPI with Gaussian beams is very simple. First a graph is given which shows the relation of the focus distance to the radius of curvature, calculated using equation (2.26c). We recognize the feature of the Gaussian

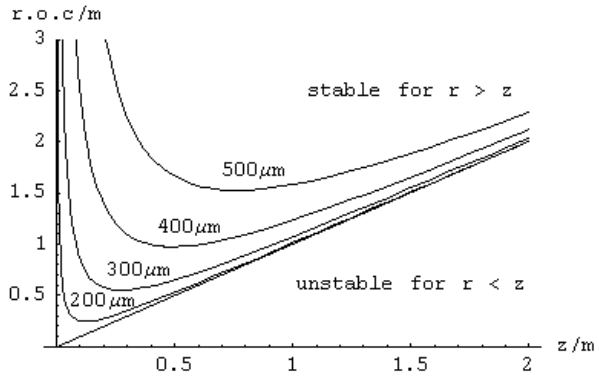

Figure 2.12: Radius of curvature (r.o.c.) as a function of the distance from the focus (z) and for different waists of the focus (in μm).

beam that the radius of curvature is infinite at the focus ($z = 0$), decreasing until a minimum value at $z = z_0$ of $r(z_0) = 2\,z_0$ and increasing afterwards again, becoming linear with z as $r(z \gg z_0) = z$. The radius of curvature reveals that around the focus the Gaussian beam behaves like a plane wave and far from the focus it behaves like a spherical wave. The graph also shows that a limit for the radius of curvature exists. It can not become smaller than z, as can be seen in equation (2.26c). If one positions the mirrors too far apart (i.e. when $L \geq 2r$ for equal mirrors) then light is still travelling between the mirrors but it is decaying because the light is not reflected onto itself as discussed before.

Figure 2.13 is one of the most useful for designing the resonator. It shows the result when solving equation (2.26c) for the waist:

$$w_0 = \sqrt{\frac{\lambda}{\pi}\sqrt{z(r-z)}} \tag{2.119}$$

In the figure the waist inside the resonator w_0 is plotted as a function of the distance from the focus z for different radii of curvature of the mirrors. The actual used mirrors are drawn with thick lines. Again we see the restriction of $z \leq qr$. The maximum value for the waist at $z = r/2$ is $w_0^{max} = \sqrt{\frac{\lambda r}{2\,\pi}}$. This configuration is called the "confocal configuration" since the focus of the resonator coincides

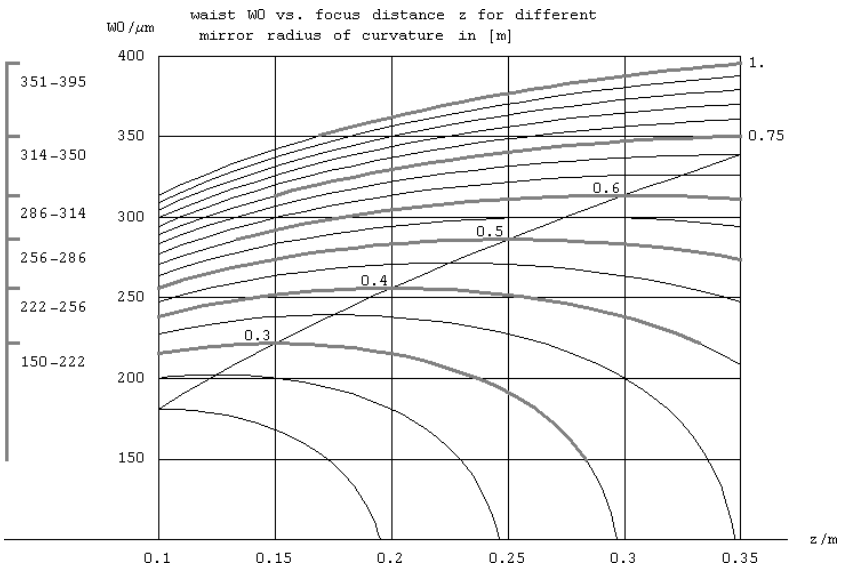

Figure 2.13: Waist inside resonator as a function of distance to focus for different radius of curvature. The thick lines correspond to the used mirrors in the setup and the markers and numbers on the left give the range of the waist of the corresponding mirror.

with the focus of the mirrors ($f_{mirror}^{spherical} = r/2$, see section 2.1.3). But this configuration should be avoided since there all modes of the FPI are overlapping, which is not useful for our application, as will be discussed in the next section (2.1.2). With this figure it is easy to select the correct mirrors for the required waist. The distances of the mirrors from the focus are obtained as well from this figure. If the mirrors are equal the distance between the mirrors is simply $L = 2z$ but in order to select two different mirrors the figure is plotted in dependence of z. In this case one selects the mirrors according to the desired waist and obtains the distance of the mirrors by adding the individual distances $L = \left|z_1\right| + z_2$. The absolute value was given here since we defined the origin of the z axis to coincide with the waist of the resonator. Consequently, the radius of curvature of the incoupling mirror is negative which is consistent with the definition of a negative radius of curvature of a converging Gaussian beam. For example for obtaining a waist of 300 μm, with radius of curvature of both mirrors of r=0.6 m a distance of the mirrors L=360 mm is needed for λ=1030 nm.

In figure 2.13 we saw how we can choose the mirrors and distances in order to get the desired waist inside the resonator. It is also possible to obtain the waist of the resonator from the figure if the mirror radii and the distances are given. Sometimes it is useful having a formula at hand which gives the waist of the resonator explicitly. We derive this formula by solving the following relations. The sign convention from before is used and the radius of the concave mirrors is

positive:

$$\begin{aligned} L \stackrel{!}{=} z_2 - z_1 \quad \& \quad r_1 \stackrel{!}{=} -z_1\big(1 + z_0^2/z_1^2\big) \quad \& \quad r_2 \stackrel{!}{=} z_2\big(1 + z_0^2/z_2^2\big) \\ \Rightarrow \qquad w_{FPI}^2 = \frac{\lambda}{\pi}\frac{\sqrt{-L(L-r_1)(L-r_2)(L-r_1-r_2)}}{\big|2\,L - r_1 - r_2\big|} \\ z_1 = -\frac{L(L-r_2)}{2L - r_1 - r_2} \quad \text{and} \quad z_2 = \frac{L(L-r_1)}{2L - r_1 - r_2} \end{aligned} \tag{2.120}$$

Obviously, the result could be complex, meaning that there is no Gaussian beam with such a geometry. This will be discussed in the next section. There we will get to know a simpler way of writing, equation (2.128).

In the last part of this section we want to discuss "mode matching". As we have said in the beginning of this section, that the light coupled into the cavity should have the same beam parameters as the light inside the cavity. A laser beam is well described by a Gaussian beam with a distinct beam waist, radius of curvature and focal position as parameters. We will show how to adjust those beam parameters appropriately, which is easily done with a lens (or several lenses). Basically, the focus of the lens should be at the position of the waist of the resonator and should have the same spot size. In section 2.1.3, equations (2.55), we saw already how a lens does focus a collimated beam and we obtained the waist at the lens in equation (2.56). One can use the approximation (2.57) as long as the requirement (2.58) is fulfilled. With these formulas it is possible to calculate the required lens and beam radius. Experimentally one can optimize the position of the lens by maximizing the transmitted intensity through the FPI.

We have so far only considered the incoupling lens but the incoming beam is altered by the incoupling mirror of the cavity. For a planar incoupling mirror the focus position is shifted, as was discussed for the beam deviation caused by a glassplate in section 2.1.3, equations (2.53). For a concave mirror the situation is slightly more complicated. Namely, not only the focal position is shifted, but the waist at the focus is changed as well. Using the ABCD law from section 2.1.3 we can calculate the deviation. It is easier when doing the calculation for the case of a beam coming outwards from the focus through the mirror. This is completely equivalent to the inverse propagation direction, see figure 2.14. The ray transfer matrix is $M = M_{pb}(n,1) \cdot M_{space}(d) \cdot M_{sb}(-r(z_1),1,n) \cdot M_{space}(z_1)$ (see table 2.2), where n and d are the refractive index and the thickness of the mirror substrate and z_1 is the distance from the resonator waist to the mirror. The radius of the mirror is equal to the radius of curvature of the beam $r(z_1)$, but must be inserted with negative sign into the ray transfer matrix. Using this ray transfer matrix

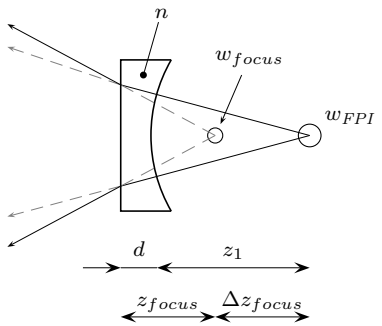

Figure 2.14: Beam deviation caused by incoupling mirror.

with equations (2.50) gives:

$$w_{focus} = w_{FPI}\sqrt{\frac{z_{01}^2 + z_1^2}{z_{01}^2 + n^2\, z_1^2}} \tag{2.121a}$$

$$z_{focus} = n\, z_1\, \frac{w_{focus}^2}{w_{FPI}^2} + \frac{d}{n} \tag{2.121b}$$

$$\Delta z_{focus} \equiv z_1 + d - z_{focus} = z_1\left(1 - n\frac{w_{focus}^2}{w_{FPI}^2}\right) + \frac{d}{n}(n-1)\ . \tag{2.121c}$$

Here the Rayleigh range of the FPI $z_{01} \equiv \frac{\pi\, w_{FPI}{}^2}{\lambda}$ was inserted. The beam after the mirror behaves the same way, as if it had a virtual focus at position z_{focus} with a virtual waist w_{focus}, while the real focus is at z_{FPI} and has waist w_{FPI}. This virtual focus is shifted by Δz_{focus}. If $\Delta z_{focus} \geq 0$ the focus is shifted closer to the mirror, otherwise it is farther from the mirror. This result is just the same if we used equation (2.60) of the plano-convex lens, and inserted $r = -r(z_1)$ from equation (2.26c) as the radius which is now concave. If one wants to couple a laser beam into the cavity it is easy to apply above formulas and calculate the virtual focus position and waist. The lens must then just be placed such that without the mirror the focus of the lens is at the position and has the waist of the virtual focus. In some situations, as for the resonator, it is necessary having the focus of the cavity to be at a certain position. In this case one needs another lens in order to have another degree of freedom, if one can not move the laser arbitrarily. This will be described in section 3.4.6. We continue the example from above (w_0=300 μm, r=0.6 m, L=360 mm, λ=1030 nm) and use a thickness of the incoupling mirror of d=2.5 mm and a refractive index of n=1.507 (BK7). We obtain a virtual waist of 255 μm which is shifted by 15 mm away from the real position of the focus further towards the outcoupling mirror (i.e. the distance from the lens to the virtual focus is larger than to the real focus)[16]. The

[16]In all calculations Δz was negative, what is surprising, since if one supposes that only the planar boundary changes the beam, then Δz should be positive. See equations (2.52) for a planar boundary in section 2.1.3, and figure 2.14.

relative deviation for the waist and the focus position are $\frac{w_{FPI}-w_{focus}}{w_{FPI}}$=15 % and $\frac{|\Delta z_{focus}|}{d+z_1}$=8 %. The deviations are quite large, which shows that the corrections are necessary to optimize the coupling efficiency into the cavity.

We have seen how the waist of the resonator can be adjusted by choosing the radius of curvature of the mirrors and by placing the mirrors at the appropriate positions. Coupling into the cavity is optimized with the help of an incoupling lens where we also regarded the deviation caused by the incoupling mirror.

2.2.5 Stability and TEM modes of the FPI

As we already saw in equation (2.120), not every geometry leads to a solution of a Gaussian beam travelling inside the cavity. In this section we will explore this issue more in detail and will find a criterion for the resonator to work. We learned in section 2.1.2 that a whole family of Gaussian-Hermite beams exists, which can be present inside a cavity as well. We will see here how these modes depend on the geometry of the FPI and we will see that they lead to additional resonance frequencies.

In the preceding section we have motivated, that the light inside the FPI can be described by a Gaussian beam, since far from the focus it behaves like a spherical wave which matches the spherical mirrors. But we did not proof this statement. For doing this we describe the propagation of the light inside the cavity by the ABCD law, which was introduced in the section 2.1.3. The matrix for one round trip inside the FPI is $M_{rt} = M_{sm}(-r_1) \cdot M_{space}(L) \cdot M_{sm}(-r_2) \cdot M_{space}(L) \equiv \left[\begin{smallmatrix} A & B \\ C & D \end{smallmatrix}\right]$ with the ray matrices from table 2.2 where the concave radii r_1 and r_2 (both > 0) of the two mirrors and the distance between the mirrors L are inserted. The condition that the light is trapped can be expressed from the ABCD law (2.48) as:

$$q_{rt} \stackrel{!}{=} \frac{A\,q_{rt} + B}{C\,q_{rt} + D} \;, \tag{2.122}$$

i.e. the beam is not changed after one round trip. The solution is given by

$$\begin{aligned} q_{rt} &= \frac{A - D \pm \sqrt{(A-D)^2 + 4\,B\,C}}{2\,C} \\ &= \frac{L(L-r_2) \pm \sqrt{L(L-r_1)(L-r_2)(L-r_1-r_2)}}{r_1 + r_2 - 2\,L} \;, \end{aligned} \tag{2.123}$$

where the entries of the matrix M_{rt} were inserted. This complex radius of curvature q_{rt} must have an imaginary part, otherwise, the waist is not defined by equation (2.19a). Therefore, the number below the square root must be negative:

$$L(L-r_1)(L-r_2)(L-r_1-r_2) < 0 \;, \tag{2.124}$$

This condition resulted already from equation (2.120). In order to discuss it more in detail, we distinguish between following cases:

case 1: $(L-r_1)(L-r_2)<0$ requires that $(L-r_1-r_2)>0$, which is never fulfilled, since either r_1 or r_2 is smaller than L from the first inequality. Therefore, this case must be ruled out.

case 2: if $(L-r_1)(L-r_2)>0$ then $(L-r_1-r_2)<0$ must be fulfilled. We have two possibilities: r_1 and r_2 are both larger than L which gives always $(L-r_1-r_2)<0$. Or r_1 and r_2 are both smaller than L, which needs to be considered more closely. This is done by rewriting the second inequality:

$$\begin{array}{rcll} L-r_1-r_2 & < & 0 & /*L \\ L^2-L(r_1+r_2) & < & 0 & \\ (L-r_1)(L-r_2)-r_1\,r_2 & < & 0 & /-r_1\,r_2 \\ (L-r_1)(L-r_2) & < & r_1\,r_2\ . & \end{array} \tag{2.125}$$

Thus, we can reformulate case 2, where simultaneously case 1 is excluded:

$$\begin{array}{rcccll} 0 & < & (L-r_1)(L-r_2) & < & r_1\,r_2 & /\frac{1}{r_1\,r_2} \\ 0 & < & (L/r_1-1)(L/r_2-1) & < & 1 & \\ 0 & < & (1-L/r_1)(1-L/r_2) & < & 1\ . & \end{array} \tag{2.126}$$

With the introduction of the g parameter we obtain the so-called resonator stability criterion:

$$0<g_1\,g_2<1 \qquad \text{with } g_{1,2}\equiv(1-L/r_{1,2})\ . \tag{2.127}$$

Only for geometries of the FPI, which fulfill this criterion, the light inside is like a Gaussian beam. These geometries are called "stable", in contrary to "unstable" geometries, which do not fulfill inequality (2.127). Here the term "stabile" ("unstable") means that the beam does not (does) change after one round trip. It does not mean mechanical stability in this case. In figure 2.15 the different regions for which this criterion is fulfilled, are shown as a function of g_1 and g_2 (shaded area). In addition, in this figure several configurations of interest are marked and their names and schematic representations are given. The planar-planar configuration (a) is exactly at the boundary of the stability diagram and does not fulfill the stability criterion (2.127) from above. But this does not necessarily mean that there is no stable wave possible inside this configuration, it only means that the beam is not Gaussian. Also inside laser cavities one often uses an unstable configuration since this gives a larger waist inside the active medium but at the cost of a larger divergence [Dem96]. The second configuration of interest is the symmetrical confocal geometry (b) where the radii and distances are equal. This is a very common setup since the modes inside the cavity all overlap in frequency resulting in a good coupling efficiency. This configuration is also at the edge of the stability diagram and will be discussed further below.

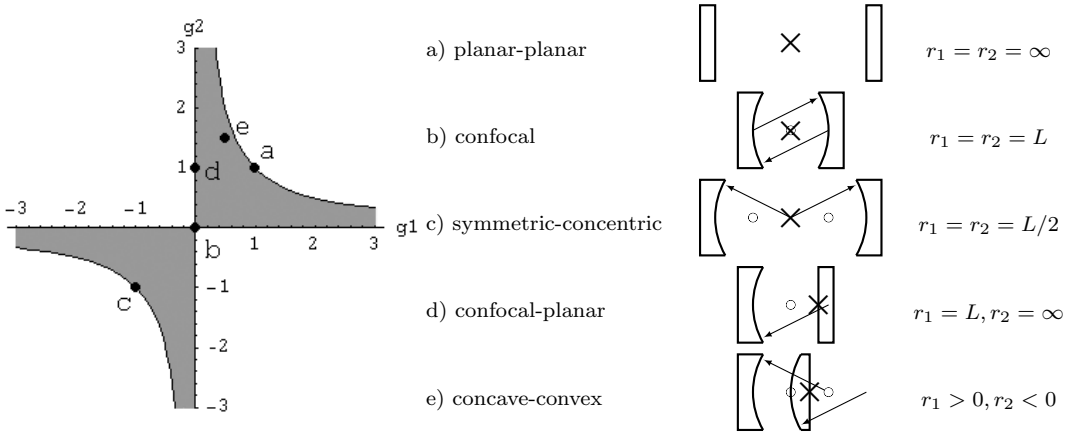

Figure 2.15: Stability diagram of different resonator configurations. Stable regions are shaded. The symbol $\times$ refers to the waist of the resonator and $\circ$ corresponds to the focus of the concave mirrors with $f = r/2$. The arrows $\rightarrow$ correspond to the radius of curvature r_1 and r_2 of the mirrors.

In the previous section we derived equation (2.120), giving the waist of the resonator. We can rewrite this in a more common form in terms of the g_i's [HW92, ST91, Sie86][17]:

$$\begin{aligned} w_{FPI}^2 &= L\frac{\lambda}{\pi}\frac{\sqrt{g_1\,g_2(1-g_1\,g_2)}}{\left|g_1+g_2-2\,g_1\,g_2\right|} \\ z_1 &= -L\frac{(1-g_1)g_2}{g_1+g_2-2\,g_1\,g_2} \\ z_2 &= L\frac{(1-g_2)g_1}{g_1+g_2-2\,g_1\,g_2}\ . \end{aligned} \tag{2.128}$$

We have seen that several geometries of a cavity are possible which all support Gaussian beams (inside the stability regime). Now we consider the resonance condition 2.78 which was derived in section 2.2.2. This was derived for planar mirrors and plane waves. We have to modify this, since the phase of the Gaussian beam is different to that of the plane wave, which will lead to additional resonances. The difference of the phase between a plane wave and of a Gaussian beam is derived in section 2.1.2, equation (2.41b). We repeat it again:

$$\Phi(z) = -k\,z - k\,\frac{\rho^2}{2r(z)} + (m+n+1)\zeta(z)\ , \tag{2.129}$$

[17]The formulas given by [Sie86] use the same sign convention, but the result for z_1 seems having the wrong sign (they even state that z_1 is negative but with their formula it is not).

with $\rho^2 \equiv x^2 + y^2$, and $\zeta(z) \equiv \arctan\left[\frac{z}{z_0}\right]$ is the Gouy phase, defined in equation 2.26d, section 2.1.1. The phase accumulated on one round trip along the axis ($\rho = 0$) is $k\,2L = \frac{\omega}{c}\,2L \equiv \frac{2\pi f}{\mathrm{FSR}}$, with FSR the free spectral range. To that we have to add the phase shift originating from the Gouy phase difference, which is two times the Gouy phase at the mirror positions $\Delta\zeta \equiv \zeta(z_2) - \zeta(z_1)$[18]. We require for the resonance that the phase is a multiple of 2π and can write down the resonance frequencies:

$$\begin{aligned} &\Delta\Phi(2L) = -\frac{2\pi f_{\ell mn}}{\mathrm{FSR}} + (m+n+1)\,2\,\Delta\zeta(z) \stackrel{!}{=} 2\pi\,\ell \qquad \text{with } \ell,m,n \text{ integer,} \\ &\Rightarrow\ f_{\ell mn} = \mathrm{FSR}\left(\ell + (m+n+1)\frac{\Delta\zeta}{\pi}\right) \qquad \mathrm{FSR} \equiv \frac{c}{2L},\ \Delta\zeta \equiv \zeta(z_2) - \zeta(z_1) \end{aligned} \tag{2.130}$$

We obtain again the resonance frequencies which coincide with the ones derived in equation (2.78) for $\Delta\zeta = 0$. But now we get additional frequencies. We see that Gauss-Hermite modes, given in equation (2.41a) and identified by m and n, have different resonance frequency with a frequency spacing related to the Gouy phase difference by $\Delta f_{trans} = \mathrm{FSR}\frac{\Delta\zeta}{\pi}$, which depends of the geometry of the resonator. Modes with equal m+n are degenerate.

The term $\Delta\zeta$ can be rewritten as is shown in the appendix 6.1, equation (6.5):

$$\Delta\zeta \equiv \zeta(z_2) - \zeta(z_1) = \arccos\left[\pm\sqrt{g_1\,g_2}\right]\,, \tag{2.131}$$

where the plus sign refers to the upper right quadrant ($g_1, g_2 > 0$) and the minus to the lower left quadrant.

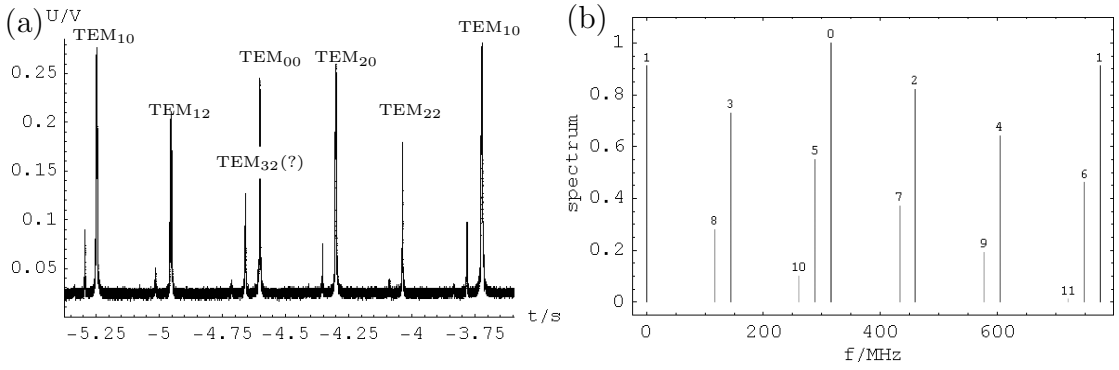

Figure 2.16: a) Transmitted intensity when the cavity length is changed and b) calculation of the measured spectrum.

In figure 2.16 we give an example of how the spectrum of a resonator looks like when the length is changed by a piezo. The left graph (a) shows a measurement of the photodiode signal detecting the transmission of the cavity. The

[18]The Gouy phase difference $\Delta\zeta$ is calculated with the sign convention for the z_i's.

cavity was slightly misaligned so that the TEM_{10} mode was maximized. The finesse is around 230, the distance of the mirrors is L≈190 mm and the linewidth (FWHM) was approximately 3 MHz. The nearest mode to the TEM_{10} mode was about 8 MHz separated. The different TEM modes are clearly visible up to $m + n = 11$. Modes up to the TEM_{32} could be identified on a TV camera with the last one only with the help of the calculation which is given in the right graph (b). The calculation was done with equation (2.130) and (2.131) for L=193.2 mm (FSR=776 MHz) with $R_1 = R_2$ =150 mm. The numbers correspond to the sum $m + n$. The calculation agrees very well with the measurement.

Figure 2.17 shows how the spectrum of a cavity is changed around the confocal configuration (L=r_1=r_2=150 mm) for different TEM_{mn} modes (numbers in plot are m+n). Exactly at the confocal configuration (dL=0) the modes become

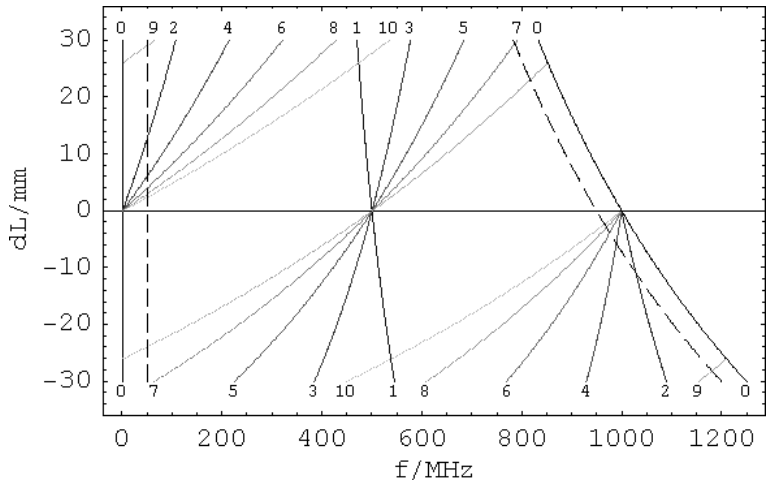

Figure 2.17: Frequencies of the first 10 transversal TEM_{mn} modes of a cavity around confocal configuration. The numbers correspond to m+n. One FSR=1 GHz is drawn with the mirror distance is varied by dL=± 30 mm around L=150 mm. $r_1 = r_2$=150 mm.

degenerate resulting in two peaks, one consisting of the even and the other of the odd modes. The two peaks are separated by FSR/2. Since the length of the cavity is never exactly the radius of the mirrors, the modes are always slightly shifted leading to a broader and asymmetric linewidth. Therefore, if one wants to use a FPI with a small linewidth as possible one should not use the confocal configuration. We see from figure 2.17 that for the drawn geometry one should increase or decrease the distance of the mirrors by about 14 mm in order to have the higher modes separated by more than 50 MHz (dashed line).

Summarizing the section about the Fabry-Perot interferometer we derived how the reflected and transmitted intensity shows longitudinal resonance frequencies which only depend on the geometry of the cavity. We saw how losses inside the cavity broaden the linewidth of the resonances and we introduced some of

the characteristic parameters describing the cavity such as the finesse. Another important feature of such a setup is the power enhancement which gives very high intensities at the waist of the cavity. This is the purpose of the whole setup. We learned how light can be coupled efficiently into the cavity by a lens. The geometry of the resonator leads to stable or unstable operating conditions and to higher Gaussian-Hermite modes which give rise to additional transversal resonance frequencies.

2.3 The servo control loop

Laser stabilization means, controlling the emitted frequency and the intensity. The frequency often has to be within a certain range. For example in order to drive a resonant transition of an atom. Not only the frequency itself is important, the linewidth and the frequency stability (frequency noise) have to be controlled as well. In this thesis a linewidth reduction is presented, where the emitting linewidth of the laser is reduced by more than two orders of magnitude. The intensity noise will be reduced as well, but this is not done so far.

In order to stabilize the laser frequency, several methods have been developed. Basically, the actual value of the frequency has to be measured and from this an error signal is obtained, which corresponds to the difference between the actual value and desired value of the frequency. This error signal is zero if the measured value coincides with the desired one and changes the sign from one side to the other. The slope of change is very important since if it is large, small deviations can be detected. The error signal could in principle directly act on the laser, but usually one uses in between a so-called servo control loop, which can give a much better performance if designed appropriately. In this section we will describe such a servo control loop in general. The application for the laser linewidth reduction is treated in section 3.3.

For mathematical modelling of a servo control loop a theory was developed, called control theory. Here we only want to look at one basic idea how to control a quantity. This idea is feedback, which means that the output of the system is monitored and the system is then influenced appropriately to give the desired output. Feedback is part of everyday life, for example the iris of the human eye is adapting itself to the intensity of light shining onto the retina [Bec05]. Electronic devices have been designed which allow easy application of feedback. They usually consist of different parts which can be separated into a proportional part (P), an integral part (I) and a differential part (D). Together they are called a PID controller (a typical design is found in table 3.3a).

In the first section we will consider feedback in general and the transfer

function will be introduced [Bec05, HTY99]. In the second section methods of measuring the transfer function will be presented, allowing to design an adequate PID. Finally, we will discuss the transfer function of piezo resonances and time-lag. Some solutions will be presented for overcoming such behavior.

2.3.1 Feedback and the transfer function

Here we are first describing the basic ideas of feedback briefly. After this we will show how the transfer function of the system can be measured which gives enough information to design the PID which matches the requirements.

The transfer function $G(s)$ of a system, with $s \equiv i\,\omega$, describes the response $y(s)$ of the system to an input signal $u(s)$:

$$G(s) \equiv \frac{y(s)}{u(s)} \ . \tag{2.132}$$

This is symbolized in figure 2.18. The signals can be complex numbers in order

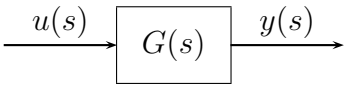

Figure 2.18: Definition of the transfer function.

to describe amplitude and phase simultaneously. Therefore, the transfer function is generally a complex function. A good way of plotting the transfer function is the so-called Bode plot. It consists of two plots, one of the amplitude of the transfer function which is also called the gain and the other of the phase of the transfer function, both plotted versus frequency.

We want to control the output of the system $y(s)$ in such a way that it approaches as well as possible the value $r(s)$. This is in most cases a constant number, as the frequency of a laser. The control of this output is done by comparing the output with the set value and adjusting the input signal $u(s)$ in dependence of $e(s) = r(s) - y(s)$, which is the so-called error signal. Therefore, we produce a feedback of the actual system output onto the system. This is called a feedback loop. We show this situation in figure 2.19. The error signal $e(s)$ is zero when the output equals the set value. The subtraction is easily done with an differential amplifier. Also an amplification could be done at this step, which will be considered later. The input of the system is set in dependence of the error signal. This is described by the transfer function of the controller $H(s) \equiv \frac{u(s)}{e(s)}$. The controller is usually some kind of PID controller. We can write down the

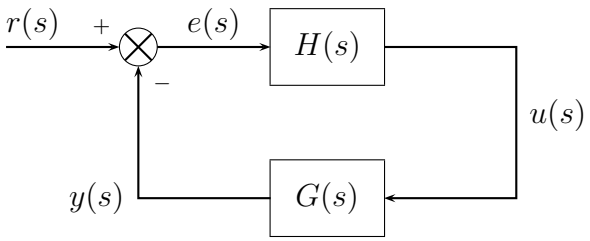

Figure 2.19: Feedback loop

equation of the "closed-loop" response of the system:

$$\begin{aligned} y(s) = u(s)\,G(s) = e(s)\,H(s)\,G(s) &= \big(r(s) - y(s)\big)\,H(s)\,G(s) \\ \Rightarrow \qquad y(s) &= \frac{H(s)\,G(s)}{1 + H(s)\,G(s)}\,r(s) \equiv A_{cl}\,r(s)\ , \end{aligned} \tag{2.133}$$

where the factor A_{cl} is called the closed loop gain and the quantity $A_{ol} \equiv H(s)\,G(s)$ is called the open loop gain. If the open loop gain is very large $A_{ol} \gg 1$, the output signal will follow the set value nearly exactly $y(s) \approx r(s)$. This means that for high closed loop gain the transfer function of the system $G(s)$ does not affect the output of the system anymore, which is the first advantage of using feedback. For example temperature drifts, hysteresis effects and nonlinearities do not affect the output of the system. The price for this is that the total gain of the system is reduced $A_{cl} < A_{ol}$. This means that we have to provide a larger input signal for obtaining the same output than without feedback. Considering the time response of the output signal, in [Bec05] it is shown, that the cutoff frequency of the system is increased by $\omega' = \omega_0(1 + H_p)$ with H_p the gain of the proportional part of the controller. This means that the system dynamics can be increased by feedback, which is the second advantage of feedback. On the other side feedback causes that sensor noise $\xi(t)$, which disturbs the error signal $e = r - \xi(t) - y$, is amplified by the high closed loop gain. Therefore, a trade-off exists between high tracking accuracy of the output signal to the set value and low sensor noise amplification.

Another issue is the stability of the feedback. If the open loop gain becomes $H(s)\,G(s) = -1$, the denominator in equation (2.133) becomes zero and the output of the system becomes "infinite". This means that the feedback does not compensate disturbances. It even amplifies them and the output starts to oscillate. Such a behavior must be avoided. This is done by designing the controller and/or the system in such a way that the open loop gain is smaller than one for the frequency where the open loop phase becomes larger than 180°. To achieve this, it is helpful to draw a Bode plot of the open loop gain $H(s)\,G(s)$.

The frequency, where the open loop gain becomes zero is often called the bandwidth of the system (plus controller). At this frequency the noise of the

stabilized signal $y(s)$, and consequently of the error signal $e(s)$, is increased. This so-called "servo bump" can be recorded with a spectrum analyzer[19]. It comes from the fact that disturbances at frequencies close to the bandwidth of the system need longer time until they are damped (due to the small phase margin), causing the noise spectrum to be increased in the range where the phase is close to 180° and the gain is larger one. For an ideally adjusted controller it should be small, but it can be still visible. During optimization of the controller one can simply increase the gain and obtain by the position of the servo bump the bandwidth. It can be seen on an oscilloscope as well, as the frequency where the system starts to oscillate if the gain is increased.

We have discussed in this section the basic properties of a simple feedback loop. We have seen that a feedback loop with high gain is not affected by the system transfer function and it was mentioned that feedback can enhance the system performance. But on the other hand feedback amplifies noise in the system as well. Feedback is limited by the requirement that the open loop gain should never reach -1, where the feedback becomes a feed-forward and the system starts to oscillate. Therefore, appropriate design is necessary which needs knowledge of the system transfer function. If it is unknown, it must be measured.

2.3.2 Measuring the transfer function

Measuring the transfer function of the system $G(s)$ can be done in several ways. One can simply put a sinusoidal signal on the input and measure the output amplitude and phase with an oscilloscope. This is very tedious and time consuming. The work is simplified by using a lock-in amplifier which directly gives the gain and phase of the output signal versus the input signal. One only has to step through the frequencies of the input signal (manually or if possible by computer control) and record the result. Using a network analyzer would be even more comfortable since this automatically scans over a wide range of signal frequencies and gives directly the Bode plot of the signal. A very different approach to measure the transfer function is to use a step signal as the input and record the time response of the output. By Fourier transformation (see section 6.3) one can obtain the transfer function of the system in the frequency space from the time space response. This method is very elegant since it is easily applied and very fast.

All of these methods are not applicable when the system which one wants to control is not stable without the feedback. In other words, problems arise when the system changes its output faster than the timescale of the measurement. For example, if one wants to balance a plate on a stick it will immediately fall down

[19] Sometimes there are even higher harmonics on the noise spectrum.

before any measurement could be done. In this case the measurement could be done in-loop, i.e. within the feedback loop. This of course requires that some feedback loop is already controlling the system, which may seem nonsense since we want to design the feedback loop by the result of the measurement. But often one can assume a transfer function for the system, or one tries a control loop which holds the system in a more or less stable region. In this case one can perform the measurements within the preliminary feedback loop and will obtain the transfer function. With this information the optimized feedback loop can be designed.

Such an approach was used for optimizing the control loop of the laser linewidth reduction. For doing this the block diagram of the real PID is shown in figure 2.20. We find additional features besides the already known elements from

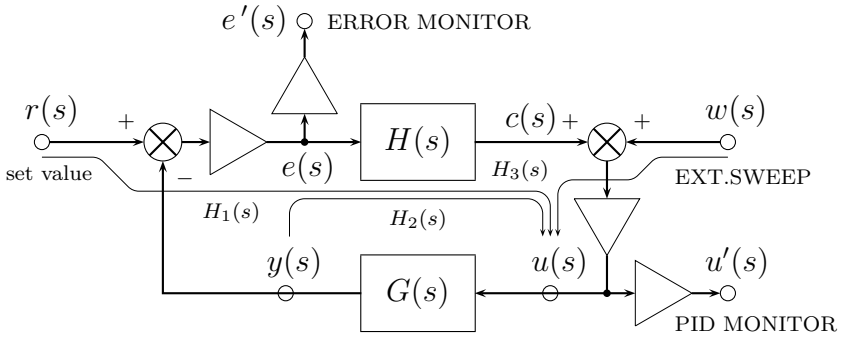

Figure 2.20: Feedback loop for in-loop measurement of the transfer function. The triangles depict amplification of the corresponding signal. The circles symbolize connectors, where the signals can be monitored or fed in. In the actual setup the input "set value" did not exist and was set per default to zero.

figure 2.19. There is another input signal $w(s)$ which is the "EXT.SWEEP" input of the PID controller. This signal is added to the output of the PID $c(s)$ and gives $u(s)$ after amplification. A "PID MONITOR" output monitors the signal $u(s)$ on the input of the system. The output "ERROR MONITOR" is used for monitoring the error signal. Equation (2.133) must be modified for the new situation. For this the new transfer functions $H_m(s)$, with $m = \{1, 2, 3\}$, according to figure 2.20 will be used.

$$y(s) = \big(r(s)\,H_1(s) + y(s)\,H_2(s) + w(s)\,H_3(s)\big)\,G(s) \tag{2.134a}$$

$$y(s) = \frac{r(s)\,H_1(s) + w(s)\,H_3(s)}{1 - H_2(s)\,G(s)}\,G(s) \tag{2.134b}$$

$$\Rightarrow \qquad G(s) = \frac{y(s)}{r(s)\,H_1(s) + y(s)\,H_2(s) + w(s)\,H_3(s)}\ . \tag{2.134c}$$

The $H_m(s)$'s can be measured with the previously described methods. If the in-loop response of the system $y(s)$ to a signal $r(s)$ or $w(s)$ is measured, the system transfer function $G(s)$ can be calculated with equation (2.134c).

One problem still remains. If the used test PID contains an integral part (I), any DC offset of the error signal will bring the PID into saturation after some time, depending on the response time of the I part. Therefore, if it is possible, no I part should be used, or the response time should be set as large as possible while still achieving locking. This way the integrator will not saturate during the measurement time.

2.3.3 Piezo resonances and time-lag

In this section we want to briefly mention piezo (PZT = piezo ceramic transducer) resonances and how they can be controlled by a PID controller or a notch filter. For a thorough treatment of this problem see [HTY99]. The transfer function of a piezo can be modelled by[20]:

$$G_{PZT} = \frac{G_{max}\,\eta\,f_0^2}{f_0^2 - f^2 + i\,\eta\,f\,f_0} \quad \text{with} \quad \eta \equiv \frac{1}{Q} = \frac{\text{FWHM}}{f_0}\ , \tag{2.135}$$

where f_0 is the resonance frequency in Herz, G_{max} is the maximum gain at the resonance frequency, Q is the quality factor with $Q \equiv \frac{f_0}{\text{FWHM}}$ and FWHM is the full-width-half-maximum of the resonance. In figure 2.21 we show a typical Bode plot of such a piezo resonance. The problem with such a resonance is, that at low frequencies the gain is small, while it is large around the resonance. But one wants to have a large gain at low frequencies and at the resonance the gain should be as small as possible.

For doing this one can use a pure integral controller and adjust the gain in such a way, that, when the phase approaches 180° it is smaller than one. But the integral controller adds a phase of $-\pi/2$, which requires that the controller bandwidth has to be reduced well below the resonance frequency. Therefore, the gain of the controller at small frequencies may not be sufficient. One can add another integrator in series with the first, which allows to increase the gain at low frequencies, since the slope of the gain of both controllers is twice the slope of one controller. The PI^2 stage, described in section 3.3.4, is such a solution. But the phase is still a problem.

[20]The transfer function given in [HTY99] is incorrect. The imaginary number is missing and the sign in front of ω must be negative. Here the given transfer function includes the peak maximum G_{max} which can be set to $G_{max} = \frac{1}{\eta} = Q$ which gives the same scaling as in [HTY99], where the DC gain is one.

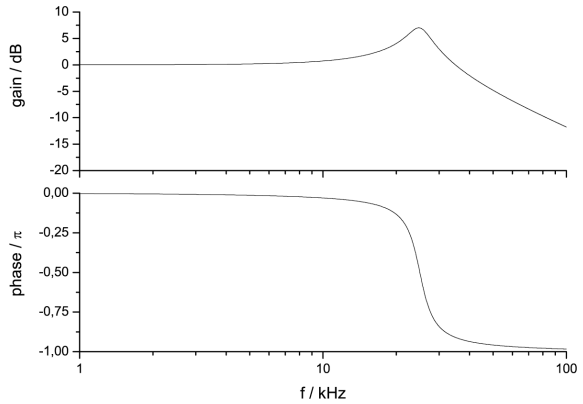

Figure 2.21: Bode plot of a piezo resonance at 25 kHz with $Q = 5$ and $G_{max} = 1/\eta = Q$.

One way out is to add a derivative part into the controller which adds a phase of $+\pi/2$. By careful adjustment of the gains and frequencies, the bandwidth can be increased until the resonance frequency or even above. In our special case this solution was not applicable, since the gain of the system depends on the laser power, which may change. Therefore, an adequate setting for the derivative part could not be found.

In order to overcome this problems one can insert a so-called notch filter. This is a band-gap filter which is composed of one or several L-C circuits, described in the appendix, section 6.5. This is the solution which was finally used for our setup. Nevertheless, also the notch filter adds a phase which has to be included in the considerations as well.

Another problem is time-lag. If there is a component inside the system which causes a time-lag τ (as it is the case for the HV amplifier in our system), the corresponding phase-lag is $\Delta\varphi = -\omega\,\tau$. This means that for increasing frequencies the phase-lag is increasing linearly with slope τ. Therefore, a time-lag can be expressed in the transfer function by:

$$G(\omega, \tau) = G(\omega)\, \boldsymbol{e}^{-i\,\omega\,\tau}. \tag{2.136}$$

The minus sign comes from the common definition of the phase which is negative for lagging phase and positive for advancing phase[21].

Time-lag is present in all systems, but often the bandwidth of the components in the system is much smaller than that related to the time-lag. If time-lag causes problems one should first try replacing the component causing the time-lag by a faster one. If this is not possible, one could try using a derivative part in the controller which adds $+\pi/2$ to the phase and increases the bandwidth.

[21] A capacitance has a phase-lag of -$\pi/2$ and an inductance has an advancing phase of $+\pi/2$.

We have in this section given a brief introduction into feedback. The transfer function was introduced and some methods of measuring this were presented. Difficulties may arise if the transfer function needs to be measured in-loop and a possible way out was discussed. Piezo resonances and time-lag were briefly discussed and some solutions were presented, how systems with such behavior may be controlled.

2.4 Intensity and phase noise

Intensity and phase noise of the laser used as a dipole trap (see section 1.2) are of great interest, because they cause heating of the atoms, which in consequence will increase the loss rate of the atoms from the trap. Phase noise is related to the linewidth of the laser. Both types of noise must be below certain values and we will give an estimation of those values here. If a Fabry-Perot type resonator (see chapter 2.2) is used, as in our case, the linewidth must be below a certain value in order to ensure that the coherence time of the laser is larger than the time each photon travels inside the cavity (equation (2.100) in section 2.2.2).

If one wants to calculate certain values of the noise and wants to compare them with specifications, or with values obtained from measurements one will observe difficulties: there exist different definitions and units and moreover they are often not specified explicitly. This can cause a lot of confusion and we have to admit that we are not sure if we present the considerations here properly. We have used mainly [GOST98, MJM+01, Tha99, MW95] here and in section 2.4.2 additionally [Rau00, Roh06, Wol95, Sch94].

The values of intensity and phase noise are estimated in the first section 2.4.1. The requirement of coherence and of low phase noise both lead to a linewidth specification for the laser. The requirement is more stringent than the linewidth provided by the laser as delivered from the manufacturer so that a laser linewidth stabilization was necessary, which is described in section 3.3. The estimation of the resulting linewidth, presented in section 3.3.9, showed that this specification could be fulfilled. The measurement of the intensity noise is discussed in detail in section 2.4.2. It turned out to be more problematic as one might suppose. With the presented procedure the measurement of the intensity noise in section 3.2.3 was performed. The result is that the intensity noise is larger than the requirements, which might cause problems. But measurements of loss rates of atoms from the resonator optical dipole trap were not performed, since the setup is not yet completed. In the final setup an intensity noise reduction will be implemented, which might help to reduce this noise.

The laser intensity at time t is modelled as the mean intensity $\bar{I}$ plus the

intensity fluctuation $\Delta I(t)$:

$$I(t) = \bar{I} + \Delta I(t) = \bar{I}\Big(1 + \epsilon(t)\Big) \quad \text{with} \quad \epsilon(t) \equiv \frac{\Delta I(t)}{\bar{I}} \ , \tag{2.137}$$

where we have introduced the fractional intensity fluctuation $\epsilon(t)$[22]. Since the fluctuations are a statistical process we do not know the fluctuations at time t, but we can assume that the mean fractional fluctuations $\bar{\epsilon}$ are zero, while the rms fractional fluctuations $\Delta\epsilon$ are nonzero[23]:

$$\begin{aligned} \bar{\epsilon} &\equiv \lim_{T\mapsto\infty} \frac{1}{T} \int_0^T \epsilon(t)\, dt = 0 \\ \Delta\epsilon &\equiv \lim_{T\mapsto\infty} \sqrt{\frac{1}{T} \int_0^T \big(\epsilon(t) - \bar{\epsilon}\big)^2\, dt} = \lim_{T\mapsto\infty} \sqrt{\frac{1}{T} \int_0^T \epsilon(t)^2\, dt} \ . \end{aligned} \tag{2.138}$$

The intensity noise of a laser is measured by a spectrum analyzer, giving the (one-sided[24]) power spectrum $S(f)$ of the photodiode voltage[25]:

$$S(f) \equiv \frac{\Delta\epsilon(f)^2}{\mathrm{BW}} \ , \tag{2.139}$$

with $\Delta\epsilon(f)^2$ the squared rms fractional intensity fluctuation at the bandwidth of BW around frequency f. In order to understand this, we consider following[26]: the spectrum analyzer measures the power applied to the input resistor, which is usually $50\,\Omega$. The current of the photodiode is proportional to the intensity, resulting in a power of $P = I^2\, R$ on the resistor of the spectrum analyzer. Therefore, the measured power spectrum is defined as the square of the rms fractional fluctuations $\Delta\epsilon(f)$. If a transimpedance amplifier with $U \propto I$, is used for amplification, the definition is still valid, since $P = U^2/R$. The division by the bandwidth BW ensures, that the power spectrum is independent of the bandwidth used in the measurement. In order to obtain the rms fractional fluctuations from the power spectrum one has to calculate:

$$\Delta\epsilon(f) = \sqrt{S(f)\,\mathrm{BW}} \ , \tag{2.140}$$

where sometimes the bandwidth is omitted, resulting in a peculiar unit of $1/\sqrt{\mathrm{Hz}}$.

[22] Since the intensity noise increases often linearly with intensity, it makes sense using fractional fluctuations in order to be independent of the mean intensity.

[23] $\Delta\epsilon$ seems to be called relative intensity noise (RIN), but the precise definition is unclear.

[24] The measurement can not distinguish between positive and negative frequencies.

[25] The power spectrum is the fourier transform of the autocorrelation function [GOST98] $S(f) = \frac{2}{\pi} \int_0^\infty \cos[\omega\tau] \langle \epsilon(\tau)\epsilon(\tau + t) \rangle$, which is a consequence of the Wiener-Kinchin theorem, mentioned in section 6.3 in the appendix.

[26] We are not sure about this explanation, but it seems reasonable.

The power spectrum is usually given in units of dB/Hz, which is in logarithmic scale. This is defined as follows:

$$P_{log} \equiv 10 \log_{10}\left[\frac{P}{P_0}\right] \qquad \begin{array}{lll} P_0 & \text{not specified} & \text{unit dB} \\ P_0 & = 1\,\text{mW} & \text{unit dBm} \end{array} , \tag{2.141}$$

where the P's refer to power and P_0 is a reference power value. If a relative value for P/P_0 is inserted the unit of the scale is given in decibel (dB). If one of the predefined reference powers are used, a suffix to the dB is chosen: dBm for P_0=1 mW for example. One can also express voltages in the logarithmic scale by simply using $P = U^2/R$ in the previous definition with R being the resistance:

$$U_{log} \equiv 20 \log_{10}\left[\frac{U}{U_0}\right] \qquad \begin{array}{lll} U_0 & = 1\,mV & \text{unit dBmV} \\ U_0 & = 1\,\mu V & \text{unit dB}\mu\text{V} \end{array} . \tag{2.142}$$

The intensity noise of lasers is sometimes specified by a rms value given for a specific frequency range f_1 to f_2. This value can be calculated from the power spectrum as:

$$\Delta\epsilon\Big|_{\{f_1,f_2\}} \equiv \sqrt{\int_{f_1}^{f_2} S(f)\,df} \ . \tag{2.143}$$

The rms value obtained corresponds to the rms fluctuations which one would measure, with a detector which has a bandwidth of the specified range. This equation was used in order to compare the measured power spectrum with the specification of the laser (section 3.2.3).

We hope we could give the necessary definitions in a clear and correct way. In the following two sections and the measurement of the intensity noise of the laser, described in section 3.2.3, theses definitions are used.

2.4.1 Requirements for our experiment

During the course of this diploma thesis the decision had to be taken which laser to buy. This is discussed briefly in section 3.2. One of the uncertainties was the requirement concerning the noise stability of the laser. Therefore, we have estimated which specifications of intensity and phase noise we need for our experiment. This will be discussed here.

First we want to consider the requirement on the intensity noise of the laser. We are mainly concerned about the heating of the atoms being trapped in a potential whose trap depth is fluctuating by intensity noise. This situation is described in [GOST98], where intensity fluctuations are modelled as fluctuations

of the spring constant (k) of a harmonic oscillator. The authors derive a heating rate of the atoms along one dimension x of the trap:

$$\langle \dot{E}_x \rangle = \Gamma_x \langle E_x \rangle \quad \text{with} \quad \Gamma_x = \frac{1}{T_x} = \pi^2 f_x^2 S_k(2f_x) \ , \tag{2.144}$$

where $\langle E_x \rangle$ is the average energy of the atoms, Γ_x is the heating rate, T_x is the time during which the average energy of the atoms inside the trap increased by a factor of $\boldsymbol{e} \approx 2.7$. The trap frequency is f_x and $S_k(2f_x)$ is the one-sided power spectrum of the fractional fluctuation in the spring constant (k) at the double trap frequency. It is well known, that only frequencies in the range of twice the trap frequency can cause significant heating. Here we encounter one big disadvantage of the resonator enhanced dipole trap. In such trap, the trap frequencies are much higher than in dipole traps formed by focussing a laser beam[27]. For a resonator we have a tight confinement on the range of half a wavelength along the beam axis (see section 2.2.3). This causes the trap frequencies to be much higher along the beam axis. For our resonator the trap frequencies are in the MHz regime. Reducing intensity noise at such high frequencies becomes more and more difficult or even impossible. Therefore, we have to rely on the intrinsic stability of the laser in this region. Luckily the noise power is usually lowest for high frequencies. We need a specification for the noise in the region of the trap frequencies. For this we use the result form [GOST98] again. They calculate the time evolution of the energy distribution inside the trap by solving the Fokker-Planck equation numerically. They obtain that, if the trap was loaded with an initial mean energy of 80 % of the trap depth, the atoms escape the trap with approximately two times Γ, where Γ is now the average of the heating rates over the spatial coordinates $\Gamma = \frac{\Gamma_x+\Gamma_y+\Gamma_z}{3} \approx \frac{\Gamma_{ax}}{3}$, where we have neglected contributions in radial direction, since the heating rate in axial direction Γ_{ax} is much larger due to the large axial trap frequency. For an estimation we require that our atoms shall stay longer than 1 second inside the trap and drop the factor 1/3 of the spatial averaging. Using equation (2.144) with a trap frequency of f_{ax}=1 MHz (see section 3.4.5) we obtain that the power spectrum must be lower than:

$$2\Gamma \stackrel{!}{=} \frac{1}{1\,s} \quad \Rightarrow \quad S_k(2f_{ax}) \leq \frac{\Gamma}{\pi^2 f_{ax}^2} = 5 \times 10^{-14}\mathrm{Hz}^{-1} = -133\,\mathrm{dB/Hz} \ . \tag{2.145}$$

This is a very low value which corresponds for a constant $S_k(2f_{ax})$ over a 50 kHz bandwidth to $\sqrt{S_k(2f_{ax})\,50\,\mathrm{kHz}} = 5 \times 10^{-5}$ rms fractional fluctuations. In [MJM+01] it is specified that the used laser source ("Mephisto", see section 3.2) has a $S_k(2f_{ax}) \leq 10^{-14}\mathrm{Hz}^{-1}$ at twice the trap frequencies ($f_{ax} = 2\pi\,1.4\,\mathrm{MHz}$), where a long trapping time in the order of 10 s was achieved. The measurement of the intensity noise, presented in section 3.2.3, gave about 2 times larger value

[27] In a focussed beam dipole trap the trap frequencies are given by the Rayleigh range along the beam axis and the waist of the focus.

than we estimated here. We hope that this will not cause too much heating of our atoms, but we could not perform any measurements with the atoms so far.

The linewidth of the laser is related to the phase noise of the laser. From the linewidth one can derive the (longitudinal) coherence length[28] of the laser. For this we suppose the laser light having a central frequency ω_0 and a linewidth $\Delta\omega$. We want to calculate for which length of propagation the two spectral frequencies $\omega_0 + \Delta\omega/2$ and $\omega_0 - \Delta\omega/2$ show a phase difference of $\Delta\varphi = 2\pi$:

$$\begin{aligned} 2\pi \stackrel{!}{=} \Delta\varphi &= (\omega_0 + \Delta\omega/2)\,\Delta t - (\omega_0 - \Delta\omega/2)\,\Delta t = \Delta\omega\,\Delta t = \Delta\omega\frac{\Delta l}{c} \\ \Rightarrow \quad \Delta l &= \frac{2\pi\,c}{\Delta\omega} = \frac{c}{\Delta f} \qquad \text{and} \qquad \Delta t = \frac{1}{\Delta f}\ , \end{aligned} \tag{2.146}$$

where we introduced the coherence time Δt. The speed of light is c and f is the frequency in Hertz. We rewrite Δf and the linewidth in terms of the wavelength λ_0 and $\Delta\lambda$ respectively:

$$\begin{aligned} \Delta f &= \left(\frac{c}{\lambda_0 - \Delta\lambda/2} - \frac{c}{\lambda_0 + \Delta\lambda/2}\right) = c\,\frac{(\lambda_0 + \Delta\lambda/2) - (\lambda_0 - \Delta\lambda/2)}{\lambda_0^2 - \Delta\lambda^2/4} \\ &= \frac{c\,\Delta\lambda}{\lambda_0^2 - \Delta\lambda^2/4} \approx \frac{c\,\Delta\lambda}{\lambda_0^2}\ . \end{aligned} \tag{2.147}$$

We assumed that $\Delta\lambda \ll \lambda_0$. This result inserted into the previous relation for the coherence length and obtain [MW95]:

$$\Delta l = \frac{c}{\Delta f} = \frac{\lambda_0^2}{\Delta\lambda}\ . \tag{2.148}$$

This means that if in an interference experiment the path length difference between the two arms is larger than Δl, no interference fringes will be visible. In our experiment the resonator is using interferences to build up the standing wave with its power enhancement capability (see section 2.2.3). Therefore, during the time the light stays inside the cavity it should always be able to maintain the interference pattern. From equation (2.100) and (2.102) derived in section 2.2.2 we know the mean decay time of the cavity and the path length that the photon travels inside the cavity:

$$\bar{T} = \tau = \frac{L\,F}{\pi\,c} \qquad \text{and} \qquad \Delta l = c\,\tau = \frac{L}{\pi}F\ , \tag{2.149}$$

with F the finesse of the cavity and L the distance of between the mirrors. The coherence length of the laser must be at least equal to this length. We can give

[28] Here we are dealing with temporal coherence which gives the longitudinal coherence length. To the spatial coherence a length can be attributed which is then called the transversal coherence length [MW95].

an upper boundary for the laser linewidth, which we give in terms of Δf:

$$\Delta l = \frac{L}{\pi} F \stackrel{!}{\leq} \frac{c}{\Delta f} \qquad \Rightarrow \qquad \Delta f \leq \frac{\pi\, c}{L\, F} \,. \tag{2.150}$$

For our cavity, which has a maximum distance of L=0.7 m between the mirrors (see section 3.4.6), and a maximum finesse of about F=1700 (see section 3.4.4) we obtain:

$$\tau = 1.3\,\mu\text{s} \quad , \quad \Delta l = 380\,\text{m} \qquad \text{and} \qquad \Delta f \leq 792\,\text{kHz} \,. \tag{2.151}$$

The linewidth of the purchased laser is about 2 MHz, see section 3.2.2, which is definitely too large for our purpose. Therefore, we need to reduce the laser linewidth below the 800 kHz. We should even reduce this, since the calculation was done with the mean time each photon stays inside the cavity. In order to estimate by how much we should reduce this requirement we can calculate the fraction of photons that are still inside the cavity after a time equal the coherence time of the laser:

$$\frac{N_{cav}}{N_0} = \boldsymbol{e}^{-\Delta t/\tau} \stackrel{(2.146)}{=} \boldsymbol{e}^{-\frac{1}{\Delta f\,\tau}} \,, \tag{2.152}$$

which gives for Δf=800 kHz 38% remaining photons, for Δf=100 kHz only 0.05% of the photons and for Δf=10 kHz a negligible fraction of photons which are left inside the cavity. Therefore, our linewidth should be less than 100 kHz, in order for having a large coherent fraction of the light inside the cavity.

Phase noise itself causes heating of the atoms since it is related to position noise of the maxima and minima of the standing wave inside the resonator. In section 2.2.3 we have calculated the position of the maxima of the standing wave in equation (2.110). If we add the phase ϕ to the round trip phase $\delta = \frac{\omega L}{c} + \phi$ we obtain the position of the maximum intensity z_{max}:

$$\begin{aligned} &\delta\Big(1 - \frac{z_{max}}{L}\Big) = \Big(\frac{2\pi L}{\lambda} + \phi\Big)\Big(1 - \frac{z}{L}\Big) \stackrel{!}{=} \frac{\pi}{2}\Big(2\,m + 1\Big) \\ &\Rightarrow \quad z_{max} = L - \frac{\lambda}{4}\,\frac{2\,m+1}{1 + \frac{\lambda}{2\pi L}\phi} \\ &\frac{dz_{max}}{d\phi}\Big|_{\phi=0} = \frac{\lambda^2}{8\pi L}\frac{2\,m+1}{(1+\frac{\lambda}{2\pi L}\phi)^2}\Big|_{\phi=0} = \frac{\lambda^2}{8\pi L}(2\,m+1) \,. \end{aligned} \tag{2.153}$$

From the position of the atoms in the center of the resonator $z_{max} = L/2$ we see:

$$\frac{2\pi L}{\lambda}\Big(1 - \frac{1}{2}\Big) \stackrel{!}{=} \frac{\pi}{2}\Big(2\,m+1\Big) \quad \Rightarrow \quad \Big(2\,m+1\Big) = \frac{2L}{\lambda} \,, \tag{2.154}$$

which we substitute into equation (2.153) and obtain the position change Δz_{max} as a function of the phase change $\Delta\phi$:

$$\Delta z_{max} = \frac{dz_{max}}{d\phi}\Big|_{\phi=0}\Delta\phi = \frac{\lambda^2}{8\pi L}\frac{2L}{\lambda}\Delta\phi = \frac{\lambda}{4\pi}\Delta\phi \,. \tag{2.155}$$

In a similar way or by substitution of $\Delta\phi = \frac{L}{c} 2\pi\Delta f$ we obtain the position change as a function of frequency change Δf:

$$\Delta z_{max} = \frac{\lambda}{4\pi}\Delta\phi = \frac{\lambda}{4\pi}\frac{2\pi L}{c}\Delta f = \frac{L\lambda}{2\,c}\Delta f = \frac{L}{2f}\Delta f \ . \tag{2.156}$$

The heating rate of the atoms by position noise is treated as well in [GOST98], again along the x axis:

$$\frac{\dot{Q}_x}{\langle E_x(0)\rangle} = \frac{1}{T'_x} = \pi^2\, f_x^2\ \frac{S'_x(f_x)}{\langle x^2\rangle}\ , \tag{2.157}$$

with $\dot{Q}_x$ the heating rate, $\langle E_x(0)\rangle = m\,\omega^2\langle x^2\rangle$ the mean energy and $\langle x^2\rangle$ the mean-square position of the atoms in the trap. T'_x is the energy doubling time and $S'_x(f_x)$ is the one-sided power spectrum of position fluctuations. Here the relevant frequency is the trap frequency f_{ax}. From the numerical solution of the Fokker-Planck equation for initially 80 % mean energy of the atoms and a 40 % remaining fraction of atoms in the trap (corresponds to the same loss as for the intensity noise) a loss rate of $0.1\ \frac{\dot{Q}_x\, t}{\langle E_x(0)\rangle}$ is obtained. This means that the heating rate due to position noise is much larger than due to intensity noise. Again we require the atoms to stay inside the trap for 1 second and we use the confinement of the atoms within the standing wave to be $\langle x^2\rangle \approx (\lambda/2)^2 = (0.5\mu\mathrm{m})^2$. We obtain the position noise for 1 MHz trap frequency:

$$\begin{aligned} 0.1\ \frac{\dot{Q}_x}{\langle E_x(0)\rangle} &\stackrel{!}{=} 0.4\frac{1}{1\,s} \quad \Rightarrow \\ S'_x(f_{ax}) \ &\leq \frac{\dot{Q}_x}{\langle E_x(0)\rangle}\ \frac{\langle x^2\rangle}{\pi^2\, f^2} = 1\times 10^{-25}\,\mathrm{m^2Hz^{-1}} \\ \Rightarrow \quad \Delta z_{max} &= \sqrt{S'_x(f_{ax})} = 3\times 10^{-7}\mu\mathrm{m}/\sqrt{\mathrm{Hz}}\ . \end{aligned} \tag{2.158}$$

With equation (2.155) and λ=1030 nm, we obtain the phase noise of:

$$\Delta\phi = \frac{4\pi}{\lambda}\sqrt{S'_x(f_{ax})} = 4\times 10^{-6}\,\mathrm{rad}/\sqrt{\mathrm{Hz}}\ , \tag{2.159}$$

and with equation (2.156) and L=0.5 m we obtain the frequency noise:

$$\Delta f = \frac{2\,c}{L\lambda}\sqrt{S'_x(f_{ax})} = 371\,\mathrm{Hz}/\sqrt{\mathrm{Hz}}\ . \tag{2.160}$$

If we assume the phase noise to be White noise (i.e. constant power spectrum with Gaussian statistics) until the cutoff frequency f_{ax}=1 MHz, and the laser linewidth much smaller than the cutoff frequency, then we can use equation (10) from [ERS82] for the laser linewidth Δ_{FWHM}[29]:

$$\Delta_{\mathrm{FWHM}} = \pi D^2\langle V^2\rangle/B\ , \tag{2.161}$$

[29] See also [Cha73] and [Tha99] for similar considerations.

where the noise was considered to stem from a voltage controlled oscillator (VCO) which modulates an AOM. The tuning sensitivity of the VCO is denoted as D in units of Hz/V, the rms Voltage of the noise on the VCO is $\langle V^2 \rangle$ and the cutoff frequency is B. In our case the power spectrum is:

$$D^2 \langle V^2 \rangle / B = (\Delta f)^2 \ , \tag{2.162}$$

and we obtain the maximum laser linewidth in order to have low phase noise:

$$\Delta_{\mathrm{FWHM}} = \pi (\Delta f)^2 = 432\, kHz \ . \tag{2.163}$$

We see that if we have a linewidth of below 100 kHz, as was required above for the coherence length, simultaneously the phase noise and the resulting position noise will be sufficiently low such that small heating rates can be expected.

We obtained in this section requirements of the intensity noise and laser linewidth in order to avoid heating and for keeping the coherence time longer than the time each photon stays inside the cavity. Due to the very high trapping frequencies along the resonator axis we obtained a very low intensity noise requirements of -133 dB/Hz, which is difficult to be fulfilled. The linewidth should be below 100 kHz which is lower than the linewidth of the laser. Therefore, a linewidth stabilization of the laser is necessary, but which should not be problematic.

2.4.2 Measurement of intensity noise

We have seen in the previous section that the intensity noise of the laser is a crucial parameter since it causes heating of the atoms which will be lost from the trap in consequence. We have derived a specification of the maximum intensity noise which can be tolerated. We needed a measurement of the intensity noise in order to check if this specification can be fulfilled. But it turned out that such a measurement is not trivial, therefore we will discuss it here in detail.

The experimental setup for this measurement is very simple. One detects the laser light with a photodiode and a spectrum analyzer. One has to take care of several things. First the photodiode has to be fast enough to detect the noise in the range of interest. The sampling theorem states that the bandwidth of the detector must be at least double the bandwidth of the signal. Second the intrinsic noise of the whole detector circuit including the spectrum analyzer has to be taken into account. We do this by measuring the background noise without the laser shining onto the photodiode. This background noise is subtracted from the signal with the laser light on. Third, the settings of the spectrum analyzer are very important when doing such a measurement and one has to do some corrections according to the setting. Finally, one has to plot the measurement

in the appropriate units and with a normalization which makes it possible to compare different measurements with each other. For doing this, the DC signal level of the photodiode must be measured simultaneously with the AC noise measurement. The steps necessary for a reliable intensity noise measurement are described here.

The spectrum analyzer used was a Rhode&Schwarz (R&S) FSP 7 GHz and all settings are for this specific type of analyzer. But other analyzers should have equivalent settings. Most of the information here can be downloaded from the homepage of R&S [Roh]. As for example the application notes [Wol95, Sch94], and the manuals [Roh06] of the spectrum analyzer. Additional information was obtained from the customer service of R&S, as for example the book [Rau00][30].

Table 2.5 gives the steps (or a checklist) for performing an intensity noise measurement with the spectrum analyzer. The details will be discussed below.

Table 2.4: Settings of the spectrum analyzer for the measurement of intensity noise of a laser. For details see text.

	button	remarks
1.	PRESET	reset the analyzer to default settings
2.	DETECTOR	select SAMPLE, AV or RMS DETECTOR[a]
3.	VBW=0.1 RBW	video bandwidth for SAMPLE DETECTOR
	VBW=3 RBW	video bandwidth for AV and RMS DETECTOR
4.	TRACE AVERAGE	if wanted, only SAMPLE DETECTOR
5.	FREQ	select the center frequency
6.	SPAN	select the frequency span
7.	RBW,SWT	select resolution bandwidth or the sweeptime
8.	ATT	select the smallest possible attenuation
9.	REF LEVEL	select the smallest possible REFERENCE LEVEL
10.		check intrinsic noise of spectrum analyzer[b]
11.		make a background measurement
12.		perform the measurement
13.	ASCII FILE EXPORT	save to ASCII file
14.		measure the signal level on the oscilloscope
15.		apply corrections according to table 2.6

[a]The RMS DETECTOR is the ideal detector for noise measurements.
[b]See discussion on the background measurement.

First we will give a brief description of how a spectrum analyzer works. This will clarify the used settings. A very simplified block diagram of a spectrum analyzer is shown in figure 2.22. The input signal is mixed with the local

[30]We would like to thank Andreas Kühne from R&S for his support.

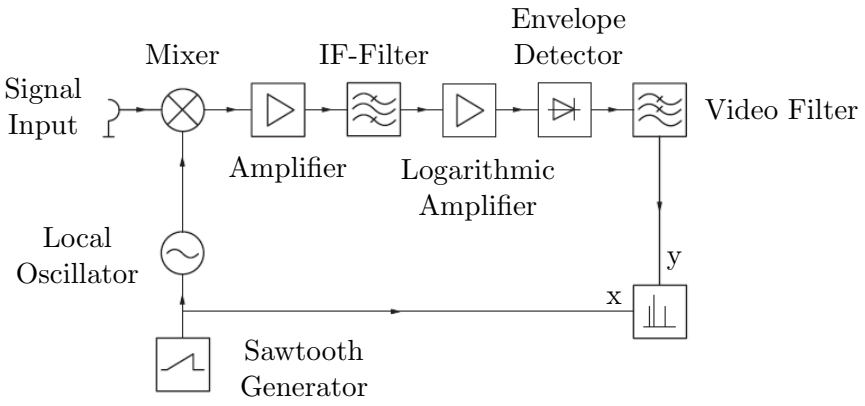

Figure 2.22: Simplified block diagram of spectrum analyzer (from [Rau00]).

oscillator (LO) frequency in the mixer. After amplification the signal is filtered by the intermediate frequency (IF) filter[31] at a fixed frequency of 20.4 MHz and an adjustable resolution bandwidth (RBW). The resolution bandwidth is defined as the frequency difference of two adjacent signals having the same amplitude and showing exactly a 3 dB dip between of them on the spectrum analyzer. The filtered signal is then compressed in a logarithmic amplifier which allows simultaneous treatment of signals having different levels over several orders of magnitude. Then, in the envelope detector, the signal level is detected (like an AM demodulation). The signal goes through a low pass "video" filter with adjustable video bandwidth (VBW) before it is displayed. A sawtooth generator creates the control voltage for the local oscillator and the x axis of the display. In modern spectrum analyzers the signal is converted to digital signals whenever possible. For RBW ≤ 100 kHz therefore the IF filter and following sections are realized in digital form and for higher RBW the analog signal is digitalized after the envelope detector. The LO is usually realized as a phase locked loop (PLL) locked to a stable reference frequency of 10 MHz and therefore no analog sawtooth generator is necessary. Also the signal is usually not directly downconverted to the IF but this is done in several steps in order to reduce crosstalk (by higher harmonics intermodulation products) from the high signal frequency to the low IF frequency.

The maximum signal level on the input must not exceed +30 dBm (1 W), otherwise the input gets destroyed. The signal can be attenuated before the mixer by the internal RF ATTENUATOR which can be set from 0 dB[32] up to 70 dB. The attenuation should be as small as possible since the signal to noise is increasing for lower attenuation. The signal level at the mixer is simply $P_{mixer} =$

[31] In German ZF filter, standing for "Zwischenfrequenz Filter".

[32] The 0 dB RF attenuation can only be entered manually on the keyboard and is not accessible with the spinning wheel.

$P_{input}-$ATTENUATION in units of decibel. It is usually in the range of -40 dBm (low distortion) to -20 dBm (low noise) and can be set automatically by the RF ATTEN AUTO selection. One can manually select the RF attenuation in the RF ATTEN MANUAL mode. When the mixer level exceeds a certain value then distortions from intermodulation products of higher harmonics become significant in the measurement (see manual [Roh06] page 2.21ff). Therefore, if one wants to minimize such distortions one reduces the mixer level. But here we are measuring noise and want to minimize the influence of internal noise. Therefore, we increase the mixer level to about -20 dBm. Probably, it is necessary to increase the mixer level even more if the signal is too close to the noise level or if one wants to measure the carrier to noise ratio on a large dynamic range as presented in [Wol95]. To do this one can reduce the RF attenuation until the spectrum analyzer indicates overload OVL and increase it by one step again.

The gain of the amplification after the mixer and therefore the signal level at the IF filter can be influenced by setting the REFERENCE LEVEL. It should always be a little larger than the measured signal. This ensures that the full dynamic range of the A/D conversion or logarithmic amplifier is used. Also a small REFERENCE LEVEL gives larger signal to noise due to the larger signal amplitude. If the signal exceeds the REFERENCE LEVEL the IF filter is overload and IFOVL is displayed. This should be avoided. Nevertheless, if the analog filter is used, smaller signals than the REFERENCE LEVEL are still measured correctly. On the contrary, if the digital filter is used (for RBW $\leq$ 100 kHz) the measurement becomes distorted due to higher mixing products in the A/D conversion. Therefore, with the digital filter the REFERENCE LEVEL should always be higher than the signal level.

On the display of the spectrum analyzer only a certain number of pixels can be displayed, but the detected signal contains much more information[33]. Therefore, the signal after the video filter must be processed in some way and this can be chosen by selecting a detector. There are several possibilities like SAMPLE DETECTOR, MINIMUM- and MAXIMUM-PEAK DETECTOR, AVERAGE DETECTOR and RMS DETECTOR. For the measurement of noise only the SAMPLE DETECTOR, AVERAGE DETECTOR and RMS DETECTOR give the right result. Do not use the other detectors for a noise measurement.

The SAMPLE DETECTOR is the default setting and takes the signal value at the time when the pixel is displayed. All the information about the signal in the time until the pixel is refreshed is lost. This does not matter for a noise measurement since the statistics about the signal is still preserved if one picks parts of the sample randomly. Therefore, this detector can be used. For a measurement

[33]Usually also the number of datapoints which are exported to the file is exactly the number of pixels displayed on the screen, which is 501 in the case of the R&S spectrum analyzer. With the setting SWEEP POINTS it is possible to change the number of exported datapoints.

with this detector the video bandwidth should be much smaller than the resolution bandwidth, i.e. VBW $\leq$ 0.1 RBW, which effectively gives an averaging of the signal. The (linear) averaged value is 1.05 dB lower than the RMS value for a signal having Gaussian (white) noise. In addition, if the signal is displayed on a logarithmic scale, the averaging gives 1.45 dB attenuation. In total the signal of the SAMPLE DETECTOR is 2.51 dB[34] lower than the RMS value. It is possible to activate TRACE AVERAGING to stabilize the output[35]. The sweep time does not affect the result, allowing to select a small sweep time. The problem with the SAMPLE DETECTOR is, that if the noise is not Gaussian, then the given corrections are not true anymore. In such a case only the RMS DETECTOR gives the correct results.

The RMS DETECTOR displays the root-mean-square of the signal:

$$U_{\mathrm{RMS}} = \sqrt{\frac{1}{N}\sum_{i=1}^{N} U_i^2} \ . \tag{2.164}$$

In contrast to the SAMPLE DETECTOR no information is lost. Moreover the measurement is directly related to the power spectral density by $S(\omega) \propto U_{\mathrm{RMS}}^2/R$ with R the resistance over which was measured (50 Ω usually). This is true regardless of the statistics of the noise. No additional corrections (except the noise bandwidth, see later) are necessary and therefore this detector should be the natural choice for a noise measurement. Averaging is not allowed with the RMS DETECTOR. To avoid averaging by the video filter it should be set to VBW $\geq$ 3 RBW. A large sweep time (SWT) is favorable since this increases the calculation time for each pixel = sweeptime/501.

The AVERAGING DETECTOR (AV DETECTOR) can also be used for a noise measurement. The average is taken over the envelope voltage resulting in a 1.05dB correction. The video bandwidth should be set to VBW $\geq$ 3 RBW as in the case of the RMS DETECTOR. The sweep time gives the averaging time and should be as long as possible.

Generally, the RMS DETECTOR is the best choice since the result is directly related to the spectral noise density. If there are time constrains on the measurement then one can use the SAMPLE DETECTOR, since the sweep time

[34]The sum of the corrections is 1.45 dB+1.05 dB=2.50 dB, which is given in [Rau00] with only one digit precision. The manual [Roh06] gives 2.51 dB in several places. It seems that rounding errors make the difference.

[35]This is written in the manual [Roh06] on page 4.13-2, but in [Rau00] on page 75 one reads, that with linear scale and the video bandwidth set to VBW $\geq$ 10 RBW, the true average is obtained. But this setting is completely the opposite to the one usually used for the SAMPLE DETECTOR. The manual [Roh06] does not mention that the video bandwidth should be changed when TRACE AVERAGING is used. In the same reference just some lines above there is another inconsistence. There it says that averaging with the SAMPLE DETECTOR does not converge, but right below the opposite is stated.

does not affect the quality of the measurement and can be kept small. The AV DETECTOR does not have advantages over the other detectors.

In order to reduce the influence of other sources of noise on the measurement one makes a background measurement. This is done by setting the laser emission to zero (or blocking the beam) and measuring the background signal. The noise within the detector circuit and the spectrum analyzer is measured and can be corrected for by subtracting the background signal from the measured signal. This must be done while using the linear scale. The measured signal is usually given in logarithmic scale, i.e. in dBm and has to be converted. From the definition of the logarithmic scale, equation (2.141), we can calculate a background correction C_{BG} that corrects for the difference between the measured signal power (S) and the real signal which has the background noise (BG) subtracted[36]:

$$\begin{aligned} C_{\mathrm{BG}} &\equiv S - 10\,\log_{10}\left[10^{S/10} - 10^{\mathrm{BG}/10}\right] \\ &= S - 10\,\log_{10}\left[10^{S/10}(1 - 10^{(\mathrm{BG}-S)/10})\right] \\ &= -10\,\log_{10}\left[1 - 10^{(\mathrm{BG}-S)/10}\right] \\ &= +10\,\log_{10}\left[(1 - 10^{(\mathrm{BG}-S)/10})^{-1}\right] \\ &= +10\,\log_{10}\left[\frac{10^{(S-\mathrm{BG})/10}}{10^{(S-\mathrm{BG})/10} - 1}\right]. \end{aligned} \tag{2.165}$$

All numbers are inserted in decibels. It is important to note, that the background signal and the measured signal must have the same corrections applied. Otherwise, the result is wrong. For simplicity we always perform the background correction before any other corrections. In this case we do not need to correct the background signal at all.

For example, if we have a signal level which is 10 dB above the noise level equation (2.165) gives a correction of C_{BG}=0.5 dB. This is a quite large contribution of the noise. Therefore, we suggest having at least 10 dB signal to noise spacing in all measurements. Even though we can correct for the background noise, if the signal is too close to the noise, information gets lost. One can test before any measurement if the noise level is small enough by unplugging the signal from the spectrum analyzer and check for the intrinsic noise of it. If it is smaller than 10 dB below the signal the measurement should not be influenced by the noise.

Otherwise, the signal to noise must be increased. This can be done by

[36]Equation (2.165) is exactly the same result as in [Rau00], equation (5-55) on page 166. Do not be confused by the nomenclature there, $\frac{S+N}{N}$ is simply equivalent to $S - \mathrm{BG}$ in the notation here. The notation in [Rau00] comes from the fact that a subtraction in logarithmic scale corresponds to a division in linear scale.

reducing the RF ATTENUATION and reducing the REFERENCE LEVEL, while one has to be careful not to overload the input mixer or the IF filter. If this is not sufficient one can reduce the resolution bandwidth, where one has to find a good compromise versus the measuring time. It is also possible to reduce the video bandwidth with the SAMPLE DETECTOR, or with the RMS DETECTOR, the sweep time in order to increase the signal to noise. The last possibility is to amplify the signal before the spectrum analyzer or reducing the ambient noise level by shielding, etc.

It is important to know, that the power spectrum measured by the spectrum analyzer is always given relative to the selected resolution bandwidth (RBW). Therefore, the obtained result has to be divided by the resolution bandwidth in order to be independent of the bandwidth used during the measurement. But this is only part of the truth, since the shape of the IF filter is also affecting the bandwidth of the noise. This is called the noise bandwidth (NBW) and is defined as the width of a square-filter having the same area as the integrated power transfer function of the IF filter [Rau00]:

$$NBW \equiv \frac{1}{H(\mathrm{IF})^2} \int_0^\infty H^2(f)\, df \ . \tag{2.166}$$

Here $H(f)$ is the transfer function of the IF filter in units of volt and $H(\mathrm{IF})$ is the transfer function at the central frequency of the filter. For the different types of filters the noise bandwidth has to be calculated with the result obtained from [Rau00] for the R&S FSP spectrum analyzer, which is given in table 2.5.

Table 2.5: Noise bandwidth for the R&S spectrum analyzer FSP as a function of the selected resolution bandwidth RBW. Numbers from [Rau00].

filter type[a]	RBW range[a]	NBW/RBW
digital	$\leq 100\,\mathrm{kHz}$	1.065
analog (4 filter)	$\geq 300\,\mathrm{kHz}$	1.129

[a]The type of IF filter is automatically selected by the spectrum analyzer according to the selected RBW. The RBW is switched in steps with no step lying between 100 kHz and 300 kHz.

As was mentioned before, the measured signal must be divided by the noise bandwidth. The division can simply be expressed as a subtraction of the logarithmic noise bandwidth from the measured power (S):

$$S_{\mathrm{dBm/Hz}} = S - 10\,\log_{10}\big[\mathrm{NBW/Hz}\big] \ . \tag{2.167}$$

Finally, the result must be normalized by the signal level of the photodiode, since the laser power, different photo detectors and also the gain of the amplifier,

if existent, give different signal levels, causing different noise levels. For doing this, the mean signal level $\bar{U}_{DC}$ must be measured at the entrance of the spectrum analyzer. This is easily done by using an oscilloscope. The input resistance of the spectrum analyzer has usually R=50 Ω with which the total signal power can easily be calculated by $P = \bar{U}_{DC}^2/R$. This number converted into the logarithmic scale must simply be subtracted from the measured signal:

$$S_{\mathrm{dB/Hz}} = S - 10\,\log_{10}\left[\frac{\bar{U}_{DC}^2}{RP_0}\right]\,, \tag{2.168}$$

where P_0 is the reference power for the used unit, i.e. 1 mW for the unit dBm.

Now we have all information at hand for doing the corrections of the noise measurement and summarize them in table 2.6.

Table 2.6: Corrections for noise measurements. The given corrections must be added to the measured signal.

condition	correction	remarks
always to do:	$-C_{\mathrm{BG}}$ see (2.165)	subtract background[a]
	$-10\,\log_{10}[\frac{\bar{U}_{DC}^2}{P_0 R}]$	normalization
filter type:		
digital (RBW ≤ 100kHz)	$-10\,\log_{10}[1.065\frac{\mathrm{RBW}}{Hz}]$	noise bandwidth
analog (RBW ≥ 300kHz)	$-10\,\log_{10}[1.129\frac{\mathrm{RBW}}{Hz}]$	noise bandwidth
detector:		
RMS DETECTOR:	–	no corrections
SAMPLE DETECTOR:		
lin. scale	+1.05dB	rms correction
log. scale	+2.51dB	rms- & log. correction
AV DETECTOR:	+1.05dB	rms correction

[a]The background signal must have the same corrections as the measured signal when the subtraction is done. We suggest doing the background subtraction first, then the background signal needs not be corrected.

At the end of this section it should not be left unmentioned, that modern spectrum analyzers often have a marker function that allows to measure noise power. The resulting noise value is automatically calculated with the considerations from before taken into account. We will briefly discuss this feature for the R&S FSP spectrum analyzer (see manual [Roh06] page 2.28ff. and 4.13-2ff.). When the NOISE MEAS function is switched on, the SAMPLE DETECTOR and VBW=0.1 RBW are selected automatically. At the actual marker position the fully corrected value of the spectral noise density is displayed in units of dBm/Hz (if the logarithmic scale is selected) It is important to know that the given value is an average over 17 adjacent pixels symmetrically chosen around the

marker position. Alternatively the RMS DETECTOR and VBW=3 RBW can be selected manually and the spectrum analyzer gives the correct result, averaged over 3 pixels. The AV DETECTOR can also be used for the noise measurement, but it is not clear over how many pixels the average is calculated.

Unfortunately, there is a discrepancy of the automatically calculated result to the manually obtained one with previous corrections. For the SAMPLE DETECTOR the spectrum analyzer always gives a value 1.21 dB lower than the manually calculated one. The given value for the RMS DETECTOR is also different, but without a constant offset. The reason for this could not be evaluated[37].

One has to be careful when trying to measure with the NOISE MEAS function on peaks. The real peak value could be much higher than displayed, since 17 pixels are averaged. Also per default the SAMPLE DETECTOR is selected which is not always the best choice as was discussed above.

We have seen in this section that the measurement of intensity noise is not a trivial task and one has to consider several things before a measurement can be done in a reliable way. We have also performed an estimation of the allowed intensity and phase noise of $\leq -133\,\mathrm{dB/Hz}$ and $\leq 4 \times 10^{-6}\,\mathrm{rad}/\sqrt{\mathrm{Hz}}$ respectively. The requirement of the coherence of the laser light, together with the phase noise, led to a maximum linewidth of 100 kHz of the laser. The measurements of the actual laser noise and linewidth show, that a linewidth reduction is necessary and, that the intensity noise could be a problem. These measurements and the linewidth reduction, among with the setup of the resonator, are presented in the experimental part.

[37] R&S did not explained, why there is a difference.

Chapter 3

Experimental part

In the theoretical part, we have discussed many aspects of a Fabry-Perot interferometer (FPI). The applications of the obtained knowledge in order to design a resonator enhanced dipole trap (see introduction) will be presented in detail here.

The resonator is nothing else than a FPI, which is designed in such a way that the power enhancement (section 2.2.3) is maximized. The resonator is built around a glasscell which is part of the ultra-high-vacuum (UHV) chamber, where the atoms are trapped in the maxima of the standing wave (see section 3.4.5). This glasscell induces losses of the resonator. In order to minimize these losses, the glasscell is designed with a special shape (see section 3.4.1) and the losses are measured (see section 3.4.3). With this the optimum reflectivity of the resonator mirror is calculated (see section 3.4.4).

In section 2.4.1 we have estimated requirements about the laser linewidth and the intensity and phase noise. We will see from the characterization of the laser (see section 3.2), that a laser linewidth reduction is necessary. The linewidth reduction needs another cavity which will give a stable frequency reference, since its linewidth only depends on the geometry and mirror reflectivity. Therefore, we will name this cavity as the "reference cavity". The linewidth reduction will be discussed in section 3.3.

3.1 The setup

A commercially available high power laser is stabilized by the Pound-Drever-Hall (PDH) locking scheme to the reference cavity [DHK83]. We will see that the laser linewidth can be reduced by more than two orders of magnitude. This

stabilized laser is then used as the seeding laser for the resonator, where the power enhancement is used to build up an extremely deep dipole trap for the atoms. The resonator is kept in resonance with the laser light by means of the Hänsch-Couillaud locking scheme [HC80]. In our research group a setup of an optical resonator has already been designed for the lithium experiment. For details see the PhD thesis [Joc04, Bar05] and in particular the diploma thesis [Mor01, Els00]. The articles [GWO00, MJM+01] give a good overview of such traps.

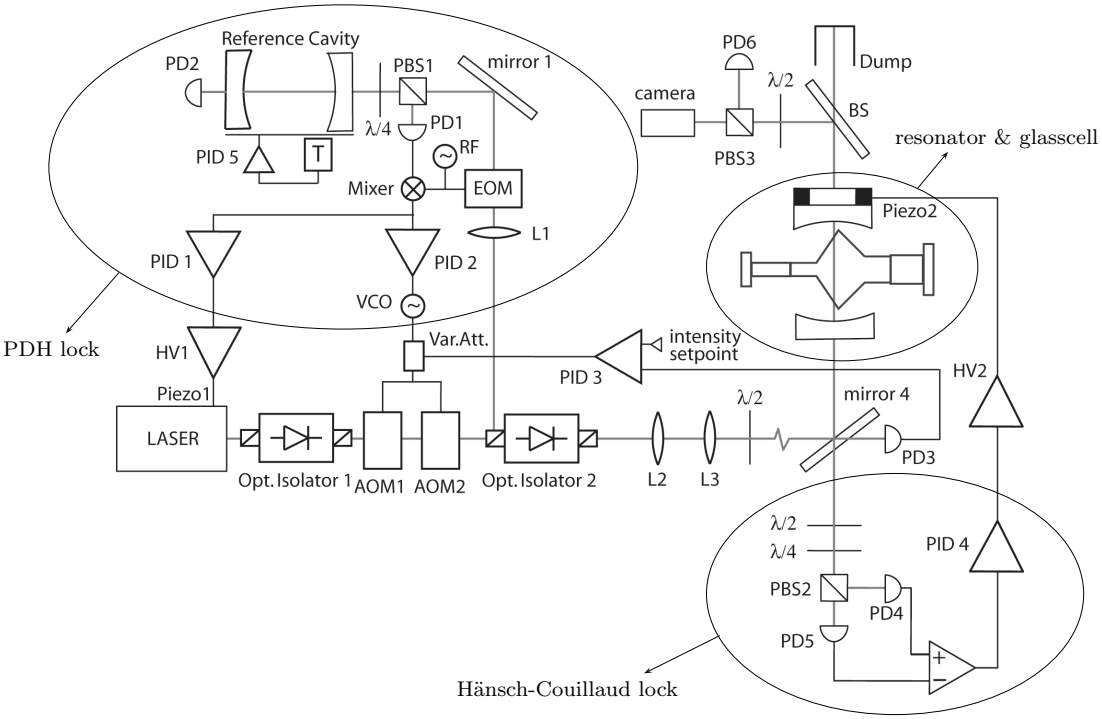

Figure 3.1: Complete setup of the resonator enhanced optical dipole trap.

The setup is shown in figure 3.1 and we will discuss it here briefly before going into details in further sections. The laser source (ELS Versadisk) provides up to 25 W single mode light at a wavelength of 1030 nm. It is stabilized to the reference cavity by changing the internal cavity length with a piezo. After passing the first Faraday isolator (likewise named optical isolator, or sometimes optical diode) the laser light is passing two acousto-optical-modulators (AOM), with the first order used on each. For both AOMs the frequency and the driving power are controlled. This allows stabilization of the laser frequency and intensity simultaneously. The AOMs are turned by 180° relative to each other, such that it compensates for the deviation in angle when the RF frequency is adjusted. On the incoupling cube of the second Faraday isolator the small fraction of deflected light is used for generation of the Pound-Drever-Hall locking signal controlling the piezo of the laser and the frequency of the AOMs. The stabilized laser light passes then one or several lenses for mode matching (see 2.2.4) and is coupled via

three mirrors[1] into the resonator cavity. A halve-waveplate ($\lambda/2$) is inserted in the pathway after the first steering mirror such that the polarization on the mirrors is always s-polarized[2], where the reflectivity of the mirrors is larger. This way also the polarization on the input to the glasscell is automatically p-polarized[3], which is necessary for the Brewster's angle to be effective. On the last mirror the intensity of the incoming light is measured with a photodiode (PD3). At this point an error signal for the intensity stabilization is generated, which goes to a variable attenuator controlling the RF power of the AOMs. The resonator cavity length is stabilized with a piezo, controlled by the Hänsch-Couillaud locking scheme. For this, the ellipticity of the reflected light from the resonator is detected by two photodiodes (PD4 and PD5). Behind the resonator there are a camera and a photodiode for observing the alignment of the beam. A beam dump is needed for deposition of the transmitted power.

3.2 The ELS laser

The used laser is the Yb:YAG disklaser Versadisk ("versatile disklaser") from the German company ELS (Elektronik Laser System [ELS]). It has a wavelength of 1030 nm and a maximum output power of 25 W single mode. The design principle of this laser is shown in figure 3.2. A water cooled pump diode provides the pump

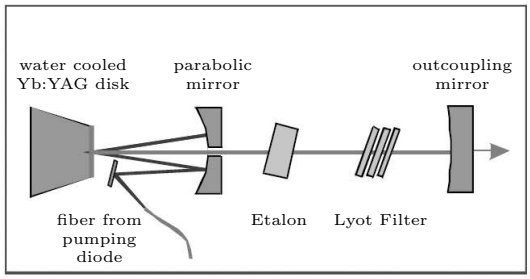

Figure 3.2: Design principle of the Versadisk disklaser, excerpt with permission of ELS.

light via a fiber onto the Yb:YAG disk (⌀10 mm, 240 μm) which is water cooled as well. The pump light traverses the Yb:YAG disk several times due to the parabolic mirror and the high reflectivity coating on the back of the Yb:YAG

[1]Mirrors 2 and 3 are not shown in figure 3.1 for simplicity. In reality, mirror 2 changes the beam direction horizontally by 90°. Mirror 3 directs the beam vertically onto mirror 4, which couples it into the resonator.

[2]The symbol "s" comes from German "senkrecht", meaning "vertical" with respect to the plane of incidence-reflection of the mirror.

[3]The symbol "p" refers to "parallel" which is the same in German and English.

disk. The high reflection side of the disk is also representing one mirror of the laser cavity.

The free spectral range (FSR, see section 2.2.2) of the laser cavity is about 200 MHz, as can be seen from $L \approx 0.75$ m with equation (2.79). ELS specifies the linewidth to be $\leq$ 2 GHz [ELS], which is larger than the FSR. This might be surprising at first sight (c.f. definition of the finesse, equation (2.85)), but the simple explanation is, that about 10 longitudinal modes of the laser cavity are simultaneously emitted. In order to have single mode operation an etalon is inserted into the cavity, which gives a single-mode linewidth of less than 5 MHz. The etalon has a relatively large FSR, which we estimate to be around 10-100 GHz for L=15-1.5 mm. Therefore, it is likely that the transmission maximum of the etalon does not coincide with that of the laser cavity which would cause that the laser does not lase. In order to avoid this, a Lyot filter [KS92] is added into the cavity, which allows to tune the emitting wavelength into and within the range of the etalon. The etalon is provided with a Peltier element and a stepper motor turns the Lyot filter, both are required for fine-tuning the emitting wavelength of the laser. But in our experiment we do not need a certain wavelength, therefore both options are not activated so far. Probably, in the future we need to stabilize the temperature of the etalon in order to cancel temperature drifts and subsequent mode jumps of the laser.

A very thin outcoupling mirror is mounted on a piezo (PICA-Thru piezo stack, P-016/00H from the German company Physikalische Instrumente [PIh, ELS]), which allows to change the length of the laser cavity. This feature is used together with two AOMs for stabilizing the laser and reducing its linewidth, which will be discussed in section 3.3.

During the diploma thesis a decision had to be taken concerning which laser to buy to act as the source for the resonator. Therefore, we defined requirements on the laser stability and output power (sections 2.4.1 and 3.4.5). The linewidth should be less than 100 kHz and the intensity noise should not exceed -133 dB/Hz at twice the trap frequencies of about 1 MHz. The laser power should be larger than 7 W on the input of the resonator. At that time (spring 2006), there were only two alternatives to the ELS Versadisk. One of them was the "Mephisto 2000" from the German company Innolight [Inn], which is an ultrastable diode pumped Nd:YAG ringlaser with wavelength of 1064nm. It has single frequency 2 W power output and a linewidth of less than 1 kHz (100 ms). This laser served already in the lithium experiment as a reliable laser source, but the 2 W of power are not sufficient for our purpose. We would have had to construct a fiber amplifier on our own in order to use this laser. The second option was a single mode fiber laser from the German company IPG [IPG]. This laser has a linewidth of less than 100 kHz, a wavelength of 1064 nm and output power of 20 W which would have met our expectations. But this product was quite new

on the market and, moreover, it did not allow improving its stability by locking it to an external cavity. Therefore, we decided to buy the Versadisk from ELS, which had already been on the market for some time. For example in the group of Klaus Sengstock in Hamburg it is used for the generation of an optical lattice (see diploma thesis [Wil05]). In the lithium experiment the same laser is used for a focussed dipole trap, but there only the intensity is stabilized externally.

In table 3.1 the specifications of the Versadisk laser are given, which will be discussed below. The specification is found in [ELS], and additional information is obtained from ELS per email[4].

Table 3.1: Data for the ELS Versadisk. Check marks show parameter which were measured and agree with the specification. The intensity noise does not fulfill the specification.

wavelength	1030 nm	
power output	27 W[a] (25 W)	✓
beam diameter in waist	0.68 mm ± 2 %[a] (0.7 mm)	✓
mode structure	TEM_{00}, M^2=1.00 ± 5 %[a] (<1.1)	
beam divergence (full angle)	1.72 mrad ± 5 %[a]	✓
beam asymmetry in waist	1.01[a]	
waist position	5 mm ± 8 %[a b]	
polarization	linear, horizontal, >100:1	
linewidth 50 ms	<5 MHz	✓
intensity noise 20 Hz - 100 MHz	<0.04 % rms	↘
beam pointing drift (after warmup)	< 2 μrad/° C	
amplitude instability (after warmup)	< ± 1 %	

[a]These parameters are measured by ELS at 27 W power output. The percentages are given by ELS for the beam parameter. Numbers in brackets give the specification.

[b]The distance is given relative to the laser housing and corresponds to 61 mm to the outcoupling mirror. This means that the waist lies outside the laser cavity, even though the outcoupling mirror is planar. According to ELS this comes from the fact that the laser is not an ideal resonator, the calculated stability is about 90 %.

3.2.1 Laser power and waist

In figure 3.3a) we see the optical power output for different diode pumping currents. The measurement was made right after installation of the laser. The power increases approximately linearly with $(1.40 \pm 0.01)\,\frac{\mathrm{W}}{\mathrm{A}}$ and has at the maximum pump current of 31 A a power of 28.8 W. This is clearly better than the specifica-

[4]Thanks to Sascha Häuser and Matthias Rösch for their support.

tion[5]. There are also some additional beams (3 at minimum) coming out of the laser, but the strongest of them has less than 10 mW of power. The insert gives the lasing threshold at (10.9 ± 0.3) A[6]. Figure 3.3b) shows the beam diameter

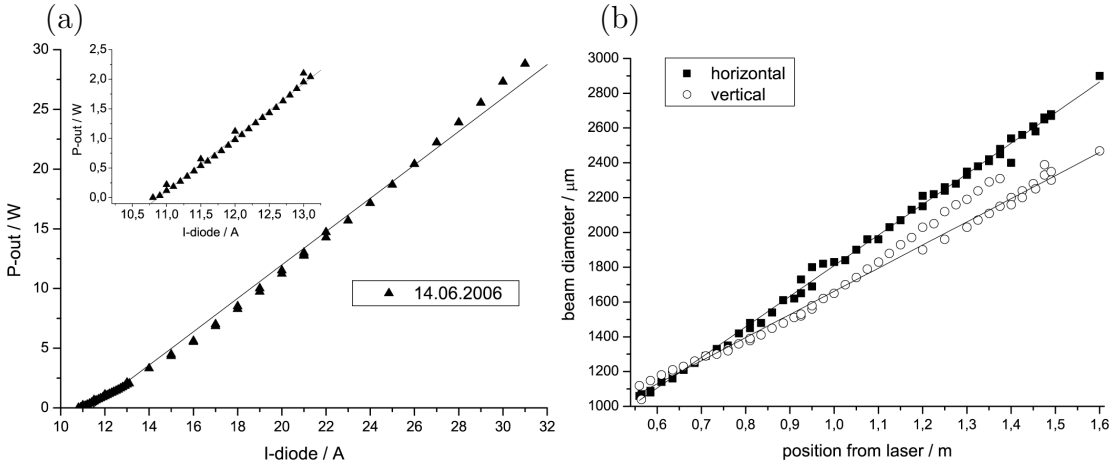

Figure 3.3: a) Pumping diode current vs. output power of ELS Versadisk. b) Beam diameter of ELS laser.

as a function of the distance from the position where the laser beam exits the housing of the ELS laser. The given directions, horizontal and vertical, refer to the measurement axis parallel or orthogonal to the optical table respectively. The pump current was 12 A which gives 680 mW of output power. The measurement was done with a commercial waistmeter (Thorlabs omega meter MW-100[7]) where the beam was mirrored into a dump and only the residual transmitted light was measured. Probably, the beam could have become astigmatic by this mirror, as one can see from the graph. In the vertical direction the beam diameter jumped between two extremes. Therefore, only the horizontal measurement is used for the calculation of the divergence angle of $\Theta_{div} = \frac{dw(z)}{dz} = (0.880 \pm 0.005)$ mrad, where one has to take into account that the beam diameter is measured instead of the radius. This result agrees very well with the given specification from ELS. With equation (2.26e) we calculate the beam waist: $w_0 = \frac{\lambda}{\pi\,\Theta} = (373 \pm 2)\,\mu$m. This agrees not so badly with the 0.68 mm given for the waist diameter by ELS. We have to check if we correctly used the approximation for the far field of the focus by looking if we measured far enough outside the Rayleigh range. This range is, according to equations (2.26), $z_0 = \frac{\pi\,w_0^2}{\lambda} = \frac{\lambda}{\pi\,\Theta^2} = (0.423 \pm 0.005)$ m, which shows that we were still close to the focus, but the measurement should be sufficiently accurate as the linearity was good. Nevertheless, we can improve this by fitting the data directly to equation (2.26b) with a nonlinear fit. For this

[5]A later measurement gave a maximum power of 25.6 W, which is still above specification.

[6]At 11.5 A one starts seeing the laser light on the infrared cards.

[7]The adequate infrared sensor MW-100B was not available, but the used sensor MW-100, works up to 1000 nm and the deviation should not be too bad.

we replace $z \mapsto z - z_{focus}$ to get the position of the focus as well. We obtain a waist $w_0 = (343 \pm 3)\,\mu$m and the position of the focus is $z_{focus} = (133 \pm 7)\,$mm measured from the laser housing. The waist matches exactly the measurement of ELS, but the position of the focus does not agree with the 5 mm provided by ELS. The deviation can be explained by regarding that the measurement did not involve the focus position itself. Therefore, small deviations of the measurement can easily lead to large errors when calculating the position of the focus. The given errors for the fit are only errors calculated from the small sample size which is not really representative.

With equation (2.27), which describes the total power of a Gaussian beam, we can calculate the peak intensity of the laser beam. For 25 W optical power and a waist of 0.7 mm/2 a peak intensity of I_0=130 MW/m^2=13 kW/cm^2 is obtained.

There is a problem with the beam diameter and divergence angle measured by ELS (see table 3.1). They do not match for a TEM_{00} beam. Equation (2.26e) gives for a waist of w_0=0.68 mm/2 a full angle of 2Θ=(1.93 ± 0.04) mrad, which is (0.21 ± 0.10) mrad larger than the measured value. The calculated M^2 factor, see section 2.1.2, for the measured waist and angle of divergence gives, according to equation (2.44), $M^2 = \tilde{w}_0\tilde{\Theta}\frac{\pi}{\lambda} = 0.89 \pm 0.05$, which is 2σ[8] smaller than one. This is definitely not physically possible[9]. The difference is too large to be explained by measurement errors only. We did not measure the beam waist directly, so that it was not possible to check the M^2 factor.

3.2.2 Laser linewidth

The next parameter to check was the linewidth of the laser. For this purpose a scanning Fabry-Perot Interferometer (FPI-100-980-2.0, 825 nm-1200 nm, from Toptica) was used so that the linewidth of the transmitted light could be measured. The length of the FPI is 75 mm and gives a FSR of 2 GHz. The reflectivity of the mirrors is R $\geq$ 99.7 % and the finesse is larger 600 which gives a linewidth of $\delta_A \equiv 3.3$ MHz. See section 3.3.7 for details. A measurement with the FPI is shown in figure 3.4.

In order to measure the linewidth, the FPI was adjusted in a near-confocal configuration. This is necessary because in confocal configuration the higher modes overlap, leading to a broader linewidth than the Gaussian TEM_{00} mode (see discussion in section 2.2.5). We pick out the highest peak, assume it is the TEM_{00} peak, and fit a Lorentzian profile. The Finesse is 668 ± 190 (out of 6 spectra), which gives a linewidth of $\delta_{conv} \equiv (3 \pm 1)$ MHz. For this calculation

[8]The standard deviation is commonly named σ.

[9]ELS explained this by measuring errors and gave the percentages cited in table 3.1. They calculated a M^2 value of 0.98 and rounded up to 1.00.

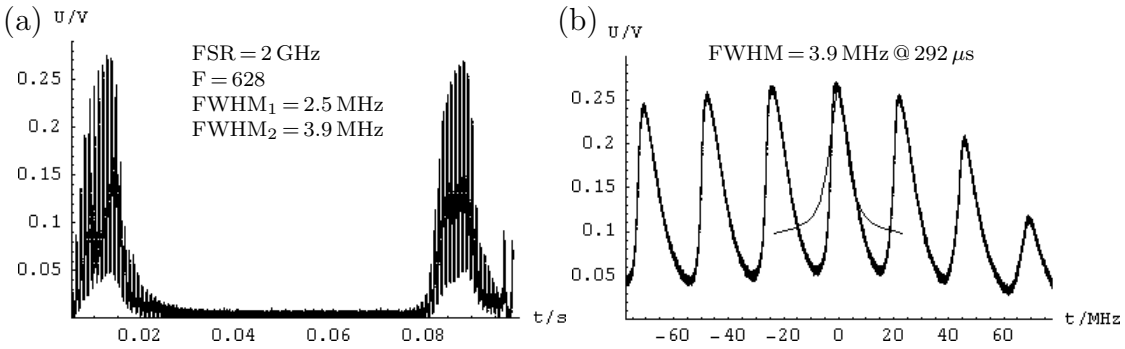

Figure 3.4: a) FPI spectrum near-confocal and b) linewidth.

we used half of the FSR, since in the near-confocal configuration the even and odd TEM-modes form two lines, separated by FSR/2 (see figure 2.17). From figure 3.4b) we see that the fit does not overlap well with the measured line: the lines are all asymmetric. It was not possible to align the FPI in such a way that the lineshape became better. Probably, either there is still some misalignment of the beam or of the mirrors of the FPI, or the photodiode is too slow. The third possibility, the scanning speed being faster than the cavity decay time (see section 2.2.2), can be ruled out by calculating the decay time from equation (2.99), giving $\tau \equiv \frac{L}{c(1-Z)} = 83\,\text{ns}$. The $290\,\mu$s taken for scanning over the linewidth is much larger than the decay time of the cavity, so that this can not be the reason for the asymmetry in this case. It should be mentioned that, due to the asymmetric lineshape, the fitting did not work very well and gave quite often a too small linewidth. But for a large linewidth, as in figure 3.4b), the fitting seems to give a better result. We have to include the contribution of the linewidth of the FPI to this measurement since both linewidths are on the same order of magnitude. The numerical calculation of the convolution of a Gauss distribution with the Airy function of the FPI was already done in section 2.2.2. The result is plotted in figure 2.9. We find for $\delta_{conv}/\delta_A = 0.9 \pm 0.3 \leq 1.2$ that the linewidth of the laser is FWHM $\leq 0.35\,\delta_A = 1.2\,$MHz. This was only measured at lower power (approximately 5 W). In an earlier measurement it was observed that the linewidth gets broader by about 60 % at high power. Therefore, we estimate the laser linewidth to be $\leq 2\,$MHz. This is well below the specification of ELS. Nevertheless, we have anyway to make a linewidth reduction in order to fulfill the linewidth requirement derived in section 2.4.1.

3.2.3 Laser intensity noise

Another crucial parameter of the laser is the intensity noise which was another issue when the laser was bought. An estimation of the maximum allowed intensity noise is made in section 2.4.1. The way of measuring intensity noise is

described in section 2.4.2 in full detail. The laser was reflected into a dump by a mirror. The small fraction of transmitted light was sent to a photodiode. It was a Hamamatsu S5971 PIN photodiode, having its signal amplified with the transimpedance amplifier SA5211 from Philips. The bandwidth of the photodiode is about 100 MHz, that of the amplifier circuit is 180 MHz, which should be more than sufficient. The used spectrum analyzer was a Rhode&Schwarz (R&S) FSP 7 GHz, with the SAMPLE DETECTOR (see section 2.4.2) selected[10]. A background measurement was done after every measurement and the DC voltage at the entrance of the spectrum analyzer was recorded by an oscilloscope. In

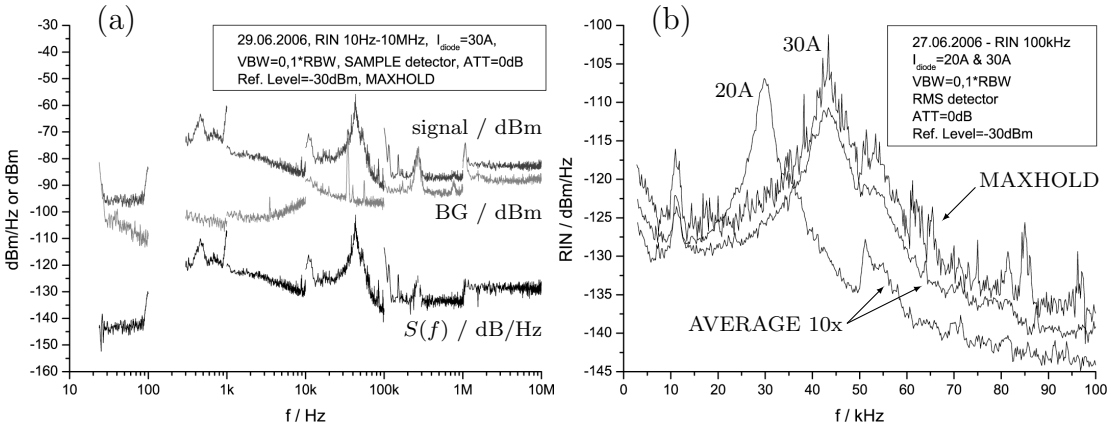

Figure 3.5: Power spectrum $S(f)$ of the ELS laser. a) Combination of 6 measurements with measured and background signal (BG) in dBm and $S(f)$ in dB/Hz b) $S(f)$ in 100k range with relaxation oscillation peak for 20A and 30A.

figure 3.5a) we put 6 measurements together in one plot. At frequencies below 100 Hz the power spectrum is with -140 dB/Hz surprisingly low. In the 100 Hz to 1 kHz range it increases up to -110 dB/Hz. Unfortunately, from 100 Hz to 300 Hz no data was obtained[11]. At 1 kHz the signal rises right at the edge of the measured range, but in the next measurement no peak appeares at this point. From 1 kHz on, the power spectrum mainly decreases to around -130 dB/Hz at 1 MHz. There it jumps up to -128.5 dB/Hz (see mean value below). The big peak between 10 kHz and 100 kHz is enlarged in figure 3.5b), where it is plotted for two different pump currents. For 20 A it appears at 29.8 kHz and has a value of -107 dB/Hz. At 30 A it is shifted to 43.4 kHz and has a value of -111 dB/Hz. When instead of the TRACE AVERAGING the MAXHOLD function is activated, the measured power spectrum increases to -101 dB/Hz at 30 A. Such a peak is known as relaxation oscillation of the laser. It is the (damped) frequency

[10] At the time of the measurement only the calculation of the power spectrum with the SAMPLE DETECTOR was clear, but showed the already mentioned offset of 1.21 dB.

[11] The RBW was set too large for the 1 kHz range which resulted in a broad artificial peak for the lower frequencies which had to be clipped away from the data.

at which the intensity oscillates after a disturbance of the laser. Further peaks arise at 11 kHz (-116 dB/Hz) and at 51 kHz (-128 dB/Hz). Another peak is found at exactly 100 kHz (-113 dB/Hz) and a smaller one at 274 kHz (-124 dB/Hz). The last one might not be noise of the laser because at that point the background level is increased as well. We are generally interested in the power spectrum in the frequency regime larger than 10 kHz since for larger frequencies it becomes more and more difficult to reduce the noise level by intensity stabilization. In section 2.4.1, equation (2.145) we came to a requirement that the intensity noise should not exceed the value of -133 dB/Hz for frequencies twice the trap frequencies which are around 1 MHz (see section 3.4.5). This requirement is by more than 3 dB (factor of 2) not fulfilled.

Finally, we want to compare the measured power spectrum with the specification of ELS. It should be smaller than 0.04 % rms = 4×10^{-4} for the intensity noise in a range from 20 Hz to 100 MHz (see table 3.1). With equation (2.143), derived in section 2.4, we calculate from our measurement the rms fractional noise $\Delta\epsilon|_{\{20,100\times10^6\}\mathrm{Hz}}$ in this range. Since the spectrum is measured in discrete intervals, we have to replace the integral with a sum:

$$\Delta\epsilon\Big|_{\{f_1,f_2\}} \equiv \sqrt{\int_{f_1}^{f_2} S(f)\,df} = \sqrt{\sum_{m=1}^{N} 10^{S_m/10}\,\mathrm{BW}_m}\ . \tag{3.1}$$

The summation goes over all measurement points S_m within the relevant range, where we have taken into account the definition of the logarithmic scale, equation (2.141). The bandwidth BW_m for each measurement point is calculated by $\mathrm{BW}_m = (f_{m+1} - f_{m-1})/2$, where the frequencies of the preceding and the following measurement points, f_{m-1} and f_{m+1} respectively, were inserted. Since we did not measure up to 100 MHz, we used for the calculation of frequencies larger 10 MHz the mean value, calculated from 1 MHz to 10 MHz:

$$\bar{S} = 10\log_{10}\Big[\frac{1}{N}\sum_{m=1}^{N} 10^{S_m/10}\Big]\ . \tag{3.2}$$

We obtain $\bar{S} = -128.5\,\mathrm{dB/Hz}$, which is used for frequencies larger 10 MHz in equation (3.1). The result of the relative rms fluctuations is $\Delta\epsilon|_{\{20,100\times10^6\}\mathrm{Hz}} = 3.8\times10^{-3}$. This means, that the measured value is one order of magnitude larger than the specification of ELS.

We have seen that nearly all of the tested values of the ELS laser fulfill the specifications given from the company. Nevertheless, we are concerned about the intensity noise, since it neither fulfills the specification of ELS, nor our requirement. Since the complete experimental setup is not finished yet, we could not perform experiments on atoms and therefore we still lack the information on how well the laser and resonator work.

3.3 Reducing the linewidth of the laser

In this chapter the setup for reducing the linewidth of the laser by means of the Pound-Drever-Hall (PDH) locking scheme will be described. We have two possibilities of controlling the frequency of the laser. The outcoupling mirror of the laser is mounted on a piezo (see section 3.2), which allows adjustment of the laser cavity length. The very thin outcoupling mirror, together with the low capacitance of the piezo of 42 nF, allow modulation into the few 10 kHz regime. The second possibility for controlling the frequency is realized externally by two AOMs. From the first AOM the -1st order is fed into the second AOM. That one is rotated by 180° and its -1st order is passed on to the experiment. The second AOM is turned by 180° because this way the frequency of the AOMs does not affect the angle at which the beam goes to the experiment. Only the beam is shifted parallel, but this is not a problem (see section 3.3.6). Besides this, we want to ramp down the intensity passing to the resonator with the AOMs over several orders of magnitude, which is only achievable with two AOMs in series.

3.3.1 EOM and error signal

In figure 3.1 we see all the necessary parts for the locking scheme. We use the PDH lock [DHK83]. Sidebands on the laser light are created with an EOM. This light is coupled into a reference cavity, see figure 3.7b). The reflected light from the cavity is detected by a photodiode and the resulting photodiode signal is mixed with the RF signal of the EOM. After passing a low pass filter the mixed signal gives the error signal which is sent to a proportional-integral (PI) controller. It mainly consists of a fast and a slow component. The control signal of the slow PI is amplified by a high voltage (HV) amplifier and drives a piezo which moves the output coupling mirror of the ELS laser and adjusts in this way the frequency at which the laser emits. The fast PI stage adjusts the driving frequency of the two AOMs simultaneously and shifts therefore the frequency of the light in -1st order, which is passed then to the experiment.

First the EOM capacitance was measured with the circuit shown in figure 3.6a). A signal (1 dBm) of the function generator (FG) passed through a power splitter (ZSC-2-1W from Minicircuits) and goes via a 10 μH inductance into the EOM. The power splitter was connected in such a way that the reflected signal from the EOM could be measured on an oscilloscope, which was terminated with 50 Ω in order to avoid backreflection of the signal. When the inductance and the capacitance of the EOM are on resonance, then nearly all the power is coupled into the EOM. We expect a sharp dip on resonance as can be seen in

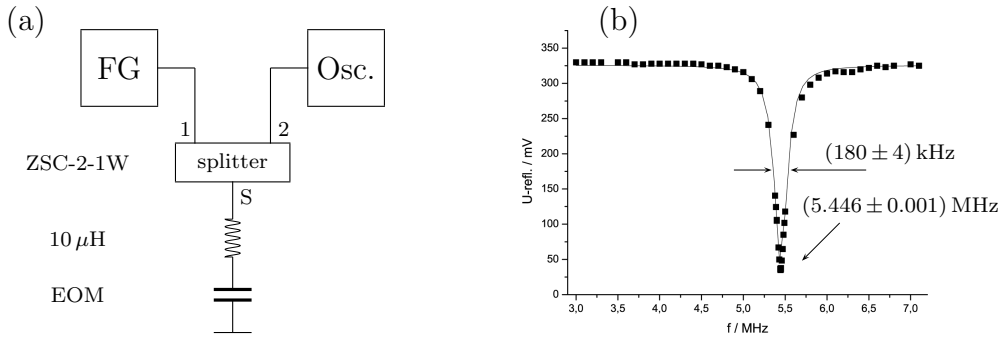

Figure 3.6: a) The circuit for measuring the EOM resonance. b) The reflected signal from the EOM measured on the oscilloscope.

figure 3.6b). The resonance frequency of a serial L-C circuit is:

$$f_{res} = \frac{1}{2\pi\sqrt{L\,C}}\ , \tag{3.3}$$

with L the inductance and C the capacitance of the EOM. The resonance is fitted by a Lorentz curve and it is found at (5.446 ± 0.001) MHz. This corresponds to a capacitance of (17.08 ± 0.06) pF. The full-width-half-maximum (FWHM)[12] is (180 ± 4) kHz. We wanted to have a larger locking range of our PID, and therefore we inserted $5\,\mu$H which gives a theoretical resonance frequency of 17.22 MHz. Finally, by optimizing the error signal we came to 15.71 MHz for the optimum driving frequency of the EOM.

The driving circuit of the EOM for obtaining the PDH error signal is shown in figure 3.7a). A function generator (FG_1) gives maximum 10 Vpp=24 dBm output. The signal has to be attenuated by -24 dB in order not to give more than 0 dBm to the following amplifier (ZHL-42W from Minicircuits), which otherwise would be destroyed. The signal is amplified by +30 dB, passes the inductance of $5\,\mu$H and is fed then to the EOM. The same photodiode and amplifier as in the intensity noise measurement is used (Hamamatsu S5971 and SA5211 from Philips). A second function generator (FG_2) is needed in order to adjust the phase of the mixer signal relative to the signal of the EOM. This is necessary to optimize the error signal, since it depends on the phase between mixer signal and the signal on the EOM [DHK83]. The function generators are linked by the 10 MHz synchronization input, which ensures that both give signals with a constant phase relation. The signal level of the second function generator is optimized by the error signal and is found to be about -10 dBm. This signal is mixed with the signal from the photodiode in the mixer (ZAD-1-1 from Minicircuits) and is passed through two low-pass filters. The first one is a commercial 2.5 MHz filter (BLP-2.5 from Minicircuits) and the second one is a home-made 300 kHz filter. Both were necessary in order to give the good error signal seen in figure 3.7c).

[12] In this case FWHM is the full width at half the depth of the dip.

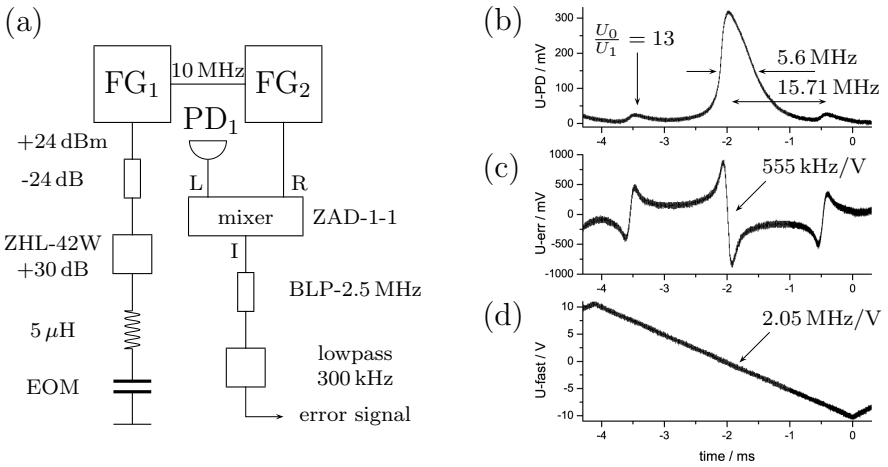

Figure 3.7: (a) The circuit for driving the EOM and mixing the error signal. (b) The transmission signal through the FPI and (c) the corresponding error signal on the error monitor and (d) the scan voltage on the "HV fast" output.

In figure 3.7b) we see the signal of the transmitted light on the photodiode, when the piezo is scanned over the resonance. The signal is quite broad, which comes from the convolution of the laser linewidth and the linewidth of the Fabry-Perot. This was already discussed in section 3.2.2. Here the Fabry-Perot is used in confocal configuration which makes a broader line, as discussed in section 2.2.5. As was mentioned before, the asymmetry in the lineshape could not be removed by a better alignment. The ratio of the carrier (320 mV) to the sidebands (25 mV) is 13, which is not so good, but it was sufficient to get an error signal of 1.8 Vpp with 20 mVpp noise. It has a slope of 18.7 kV/s, which corresponds to 555 kHz/V as seen in figure 3.7c). Figure 3.7d) shows the scan voltage on the "HV fast" output (see section 3.3.2 below) which is directly connected to the piezo. From the slope of 5.06 kV/s we see that with the piezo a 2.05 MHz/V frequency change of the laser is obtained. The axis calibration for these calculations is obtained by figure 3.7b). We know the frequency offset of the sidebands which is 15.71 MHz. Comparing this with the time difference in the scan we get 10.37 GHz/s.

In the future, the complete mixer and EOM setup will be replaced by an electronic box containing all the necessary parts, like amplifier, mixer and phase shifter in discrete elements.

3.3.2 HV amplifier

As already mentioned a fast and a slow PI circuit are used to stabilize the laser frequency. The slow PI drives the piezo and the fast drives the AOMs. More

precisely, we used two slow PI circuits for the piezo. One is connected via the HV amplifier to one side of the piezo (IN1, HV slow) and the other one is directly connected to the piezo from the other side (IN2, HV fast) as is shown in figure 3.8a). The whole circuit "HV fast" is built-in within the PI controller and

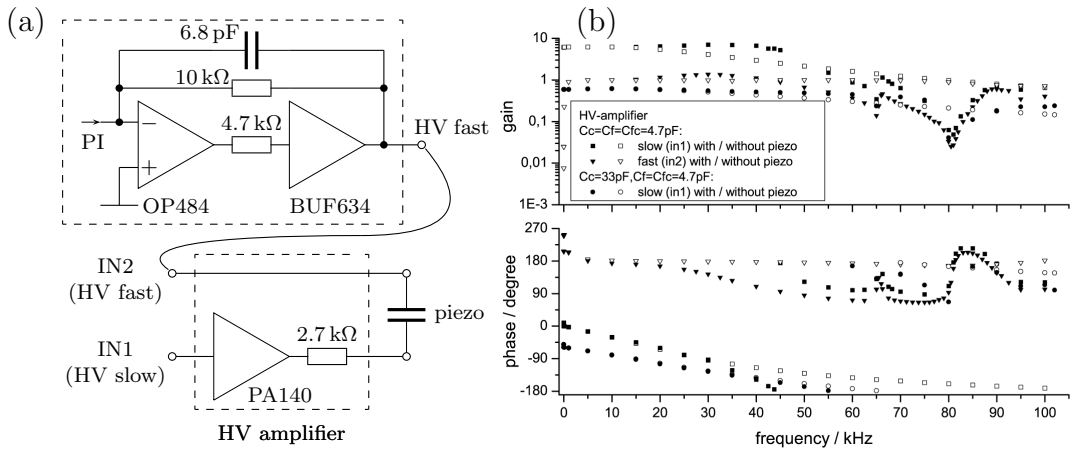

Figure 3.8: a) Circuit of piezo driver. b) HV amplifier transfer function for the different inputs and two different configurations.

is connected to "IN2, HV fast" on the front plane of the HV amplifier, which is internally connected to the piezo. The output "HV slow" of the PI controller must be connected to the "IN1 HV slow" connector on the front plane of the HV amplifier, driving the piezo via the HV amplifier. The gain of the HV amplifier can be adjusted by a potentiometer. This setup was necessary since the HV amplifier was the limiting factor in driving the piezo, which will be discussed below. The used HV amplifier (PA140 from Apex) has a voltage range of +300 V to -20 V. It can only drive 60 mA (120 mA peak) and has a bandwidth of 26 kHz for 280 V swing, according to the datasheet. Both the low bandwidth and the small current driving capabilities imposed constraints. In the chosen setup the HV amplifier is controlled by an integral part only[13], which has a frequency of f_I=9 kHz[14]. For this bandwidth the HV amplifier works properly. For the higher frequencies the piezo is driven from the other connector by a buffer (BUF634) which can deliver up to 250 mA at a bandwidth of 30 MHz. The buffer has gain 1 and is inserted in the last stage (OP484) of the PI controller, as is shown in figure 3.8a). The feedback node is connected at the input of the last PI stage. For the low voltage swing of ± 15 V the HV amplifier has a bandwidth of approximately 300 kHz which should be sufficient. But the problem here is still that the HV amplifier has to deliver or dump the current to drive the piezo. In order to limit the maximum current the 2.7 kΩ is inserted. This way it will not exceed

[13]The P part has gain smaller 1.

[14]Position of servo bump, measured with spectrum analyzer and photodiode. When the gain is increased, the controller starts oscillating at 19 kHz.

I=U/R=300 V/2.7 kΩ=110 mA. Together with the 42 nF capacitance of the piezo this gives, with equation (3.3), a -3 dB frequency of 1.4 kHz[15].

A similar setup as described in [HTY99] was also considered. There it is suggested to use a capacitor from the piezo on the HV side to ground, which should buffer the current. Calculations showed that for frequencies below 40 kHz (C_{shunt}=100 nF, R_{HV}=2.5 kΩ) this strategy makes the system even slower, since a large fraction of the current is necessary to charge the additional capacitor. For higher frequencies the AOMs will play anyway the major role. Hence, this approach was abandoned.

The transfer function of the HV amplifier shown in figure 3.8b) was measured with a lock-in amplifier as described in section 2.3.2. The two inputs of the HV amplifier labelled "slow" and "fast" are shown, each with and without load, i.e. the piezo. In this measurement the 2.7 kΩ resistor was not inserted. It is clearly visible, that there are two resonances which are related to the piezo. One is around 65 kHz and the other one is around 80 kHz. The measurement is given for two different configurations of the HV amplifier, with the given C's referring to internal capacitors. The one with C_f=33 pF was an earlier configuration, and the final configuration has all the C's set to 4.7 pF. The older configuration was included since with this the transfer function of the system (see below) was measured. Nevertheless, there is not a big difference, except for the phase at small frequencies, which was -45° in the old configuration. We see that the HV amplifier on the "slow" input limits the performance since already around 40 kHz the phase is approaching -180°. This is not the case for the "fast" input which it is directly connected to the piezo.

In the first measurements (not plotted) the HV amplifier had a tendency to oscillate with 35 kHz, even without load. Therefore, the internal capacitors were exchanged several times, but without success. The original configuration was: C_c=33 pF, C_f=22 pF and C_{fc}=18 pF. Later it turned out that the negative supply voltage was not soldered properly, which could have caused this problem. But after fixing this problem the phase behavior was still not better. According to the datasheet of the HV amplifier, the phase should stay nearly constant from 10 Hz up to 100 kHz at around -90°. In no configuration this was the case. The observed linear increase of the phase could be related to a time-lag in the system, as was mentioned in section 2.3.3. This seems to coincide with the fitted transfer function of the piezo shown below. There we get a time-lag of 7.0 μs corresponding to a bandwidth of about 150 kHz. This is half the bandwidth of the HV amplifier for the ± 15 V swing, mentioned earlier. But it is not clear how these quantities should be related. Obviously, the phase given in the datasheet

[15]Nevertheless, it seems that the piezo still can be modulated up to 20 kHz, which is surprising. Unfortunately, the transfer function was measured before the resistor was inserted.

is definitely different from the measured one. Probably, the HV amplifier did not caused the problem, but one of the other components of the HV circuit. Nevertheless, we achieved together with the AOM a good linewidth. Maybe we should despite of that consider improving the HV amplifier or using a different one, since it is still a limitation for the performance of the linewidth reduction scheme.

3.3.3 System transfer function

After setting up the PDH locking scheme we measured the system transfer function in order to optimize the PID controller. We already saw from the transfer function of the HV amplifier, that there are piezo resonances and that the HV amplifier produces a phase-lag. One can suppose that both of these components give the final limitation of the performance of the linewidth reduction, since the other components, like the photodiode, the reference cavity, etc. all have a much higher bandwidth. At the beginning of the optimization process of the PI controller it was hard to adjust it in such a way that it was locking nicely. Therefore, we decided to measure the entire system transfer function to be able to design the PI controller in an optimum way. Since the laser must be on resonance with the reference cavity during this measurement, there was no other way than measuring in-loop, as it was described in section 2.3.2. In equation (2.134c) we showed how to calculate the system transfer function. We set the PI controller so that it locked the laser sufficiently[16]. In the used PID controller the set value can not be adjusted and is always zero. Therefore, we had to bring in the additional signal for the measurement of the transfer function via the external sweep input. This required that the transfer function $H_3(s)$ was measured instead of $H_1(s)$. In any case the in-loop response $y(s)$ has to be measured, as well as the transfer function of the PID controller $H_2(s)$. In figure 3.9a) we see the result. These measurements were performed with a lock-in amplifier. The data points labelled "inloop" correspond to the in-loop data $y(s)$. "P only" represents $H_2(s)$, but there the integral part was switched off, since otherwise it would saturate too fast. The data points "ext. sweep" correspond to $H_3(s)$, and $G(s)$ is the calculated system transfer function. In the measurements of $H_2(s)$ and $H_3(s)$ a 20 mV sinus was inserted on the "error in" or "external sweep" input respectively and on the PID out (slow) the resulting signal was measured by the lock-in amplifier. The system transfer function was measured by inserting also 20 mV into the "external sweep" input and measuring the response of the whole loop on the

[16]The error signal during lock was around 600 mV_{pp} on the "error monitor" output of the PID. The open loop error signal was between 0.8 V_{pp} to 1 V_{pp}, giving a linewidth of about 200 kHz (322 kHz/V; c.f. section 3.3.9). The Buffer BUF634 and the 2.7 kΩ resistor were not yet inserted. Only one PI drove the HV amplifier and the piezo, which was grounded on the other side. No AOMs were used.

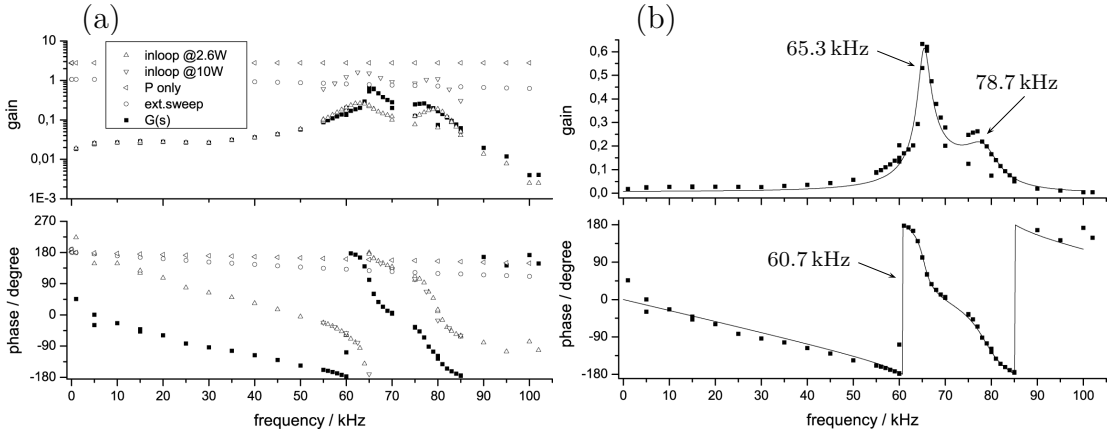

Figure 3.9: a) Measurement of the transfer function of the PDH lock of the laser. b) Fit of the transfer function gives position and width of two piezo resonances.

"error in" input, while the PI controller was locking. For locking properly, the integrator had to be switched on. Since only the P part could be measured in $H_2(s)$ for small frequencies the result is not reliable at low frequencies, where the gain of the integrator plays a major role. Probably, this is the reason why in the resulting transfer function the first data points show positive phase.

Again, we clearly see the two resonances, here around 63 kHz and at 80 kHz. In order to see if one of the resulting peaks is related to the laser relaxation oscillation (see section 3.2.3) we have measured for two different values of the laser power (2.6 W and 10 W). Despite the larger gain, the peaks and the phase stay the same, indicating that the peaks stem from the piezo and not from the laser. We know this already from the measurement of the HV amplifier.

From the measured data the system transfer function $G(s)$ was calculated with equation (2.134c) and it is plotted for the measured points in figure 3.9a) for comparison with the measured data. We plotted it also in figure 3.9b), but there in linear scale. We fitted the measured system transfer function with a model transfer function containing two piezo resonances and a time-lag, according to equations (2.135) and (2.136), section 2.3.3:

$$G_{system} = \frac{G_1\,\eta_1\,f_1^2}{f_1^2 - f^2 + i\,\eta_1\,f\,f_1}\,\frac{G_2\,\eta_2\,f_2^2}{f_2^2 - f^2 + i\,\eta_2\,f\,f_2}\,\boldsymbol{e}^{-i\,\omega\,\tau}\ , \tag{3.4}$$

with $\eta_i \equiv \frac{1}{Q_i} = \frac{FWHM_i}{f_i}$ and $i = \{1, 2\}$ the labels of the resonances. It was very surprising that the measured data corresponds so well to the model transfer function as can be seen in figure 3.9b). The obtained fit parameters are given in table 3.2. The method used for fitting the complex transfer function is briefly explained in the appendix, section 6.4.

Table 3.2: Result of the model system transfer function (3.4) fitted to the measured data shown in figure 3.9b). The R's and C's for the notch filter with L=660 μF are also included (see section 3.3.5).

resonance	f_i	G_i	Q_i	FWHM$_i$	τ	R	C
1	65.3 kHz	0.17	23.3	2.8 kHz		3.6 kΩ	9 nF
2	78.7 kHz	12.5	10.9	7.2 kHz	7.0 μs	2.1 kΩ	6.2 nF

We have obtained the transfer function of the complete system and could model it with two piezo resonances and a time lag. With this information it was possible to understand the system much better and to design an appropriate control system for reducing the linewidth of the laser.

3.3.4 PI for driving the piezo

With the exact information on the system transfer function, and the knowledge of the resonance frequencies and their widths it was possible to understand the behavior of the system much better. The limitations due to the HV amplifier with its associated time-lag were already discussed above. The "HV fast" and "HV slow" PI stages with the buffer IC were built. It turned out that they should not overlap in frequencies too much, since otherwise the integral parts could bring each other to saturation. Therefore, the faster I stage was limited in gain by inserting a resistor (R_{29}, see table 3.3a)) in parallel to the capacitance. After optimization the locking of the laser worked well. The slow PI shows a servo bump (see section 2.3.1) at 9 kHz, the fast one at 29 kHz for the P part and the two stages together show a servo bump at 20.5 kHz. When the laser is locked, the error signal shows 90 mVpp excursions and with the PI^2 stage (see below) even only 70 mVpp, but then the lock is more instable. The sidebands, generated by the EOM in the PDH setup (see figure 3.7 in section 3.3.1), could be increased by a factor of 2 by using the ZHL-42W amplifier. This resulted in 1.8 Vpp on the error monitor when one scanned over the resonance. See the estimation of the linewidth in section 3.3.9. The noise level of the signal is about 20 mVpp. The used resistors and capacitances are given in table 3.3b). Nevertheless, the locking was still very sensitive concerning disturbances. If one knocks on the experiment table, it falls out of lock easily. For low frequencies it seems that the gain is still not sufficient. This can be explained by the very low gain of the system for small frequencies as can be seen in figure 3.9. Therefore, a second PI stage, called PI^2, for the slow lock (HV slow) was built. This is another PI which is in series with the first PI. It is designed to increase the gain for low frequencies, as described in section 2.3.3. It was difficult to adjust so that it does not interfere with the other two PI controllers. After the AOMs were installed it turned out that the AOMs

were locking the laser better. Therefore, at the moment it is not used anymore.

Table 3.3: a) Typical PID cirquit. b) Resistors and capacitors to reduce the linewidth of the laser. No derivative part was used.

(a)

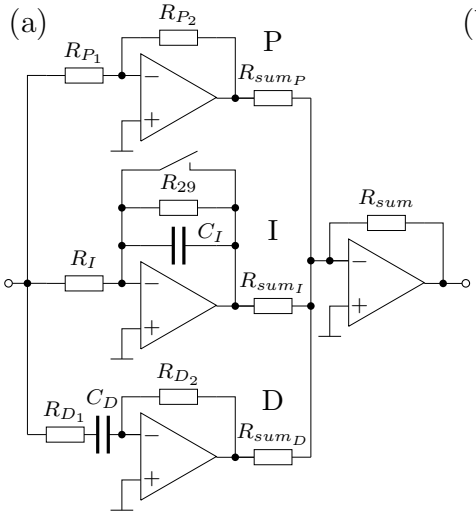

(b)

item	slow[a]	PI[2]	fast	AOM
R_{P1}	10k	10k	1k	10k
R_{P2}	4.33k	10.85k	4.51k	10k poti
R_I	-	-	17.9k	5k poti
C_I	15nF	15nF	2.2nF	1nF
R_{sumP}	-	10k	10k	10k
R_{sumI}	-	10k	10k	10k
R_{sum}	-	10k	10k	10k
R_{29}	-	-	100k	-

[a]Built with only one operational amplifier.

To overcome the piezo resonances a derivative (D) part was tried. It should help bringing the phase back to a value around 90° but this did not work so well. The problem with this approach is, that the settings of the D part depend on the output power of the laser. This is not very comfortable and therefore a notch filter was built instead, as was suggested in section 2.3.3.

3.3.5 Notch filter

We built two notch filters with discrete elements as is shown in figure 3.10a)[17]. The transfer function can be found in the appendix section 6.5, equation (6.30). From the equations of the resonance frequency (6.31c) and the width of the resonance (6.33), we calculated the necessary resistor and capacities by using the largest inductance available in the workshop, which was 2x330 μH. We already have given the result in table 3.2. For both notch filters only one resistor is necessary, since when one filter is on resonance, the other one is not and has nearly gain 1. This of course is only true as long as the resonances do not overlap. If the two resistors from table 3.2 had been used, the maximum current through the resistors would have been higher since they would effectively be in parallel to ground. Therefore, we only use one resistor which consists of a 1.5 kΩ

[17]In the PID controller circuit the filter UAF42 could be inserted, but for high frequencies and large Q values it does not work. It can also only suppress one resonance.

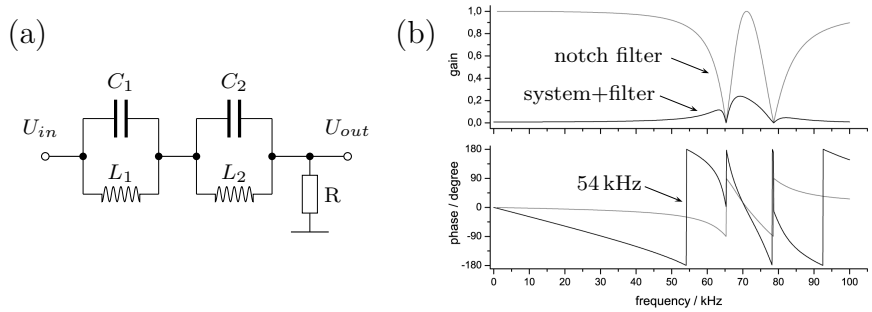

Figure 3.10: a) Notch filter circuit and b) transfer function of notch filter and system together with notch filter. Calculation from fitted model (3.4) with parameters according to table 3.2 and R=2 kΩ.

resistor in series with a 5 kΩ potentiometer. This allows for the adjustment of the widths of both resonances, but only simultaneously. The transfer function of the notch filters and that of the combined system is plotted in figure 3.10b). The system transfer function which was fitted in section 3.3.3 was used for the calculation. We see that the high gain is significantly reduced by the filters, whereas the phase becomes even worse. This has always been the problem when we tried inserting elements that should suppress the resonances: they always made the phase worse. Nevertheless, the notch filter was inserted, but we could not quantify if the performance was improved. Oscillations on the resonances seem to be suppressed, but the phase still is a problem that does not allow for a higher bandwidth than about 50 kHz.

3.3.6 AOM

As was mentioned in the introduction to this chapter, two AOMs (type 3080-197 from Crytal Technology) are used. They provide the fast frequency modulation for the linewidth reduction. Additionally, with the amplitude of the RF power the intensity is stabilized and can be ramped down over several orders of magnitude. Both AOMs are controlled by the same signal. A RF frequency of 80 MHz is generated by a voltage controlled oscillator (VCO, POS-100 from Minicircuits) and is fed into two of our RF amplifier boxes[18]. In each of them the signal can be attenuated by a variable RF attenuator (RVA-2500 from Minicircuits) before it is amplified (MHW9267 from Motorola). In figure 3.11 a schematics is shown. The tuning voltage V_T which is provided by the PI controller "AOM" defines the frequency of the VCO. The center frequency of the AOM is 80 MHz and it is adjusted by the offset of the PI controller to be 9.4 V. The tuning range of the VCO goes from 65 MHz to 95 MHz (30 MHz bandwidth) which perfectly matches

[18]Can be found on `http://www.nintaka.com/schreck`.

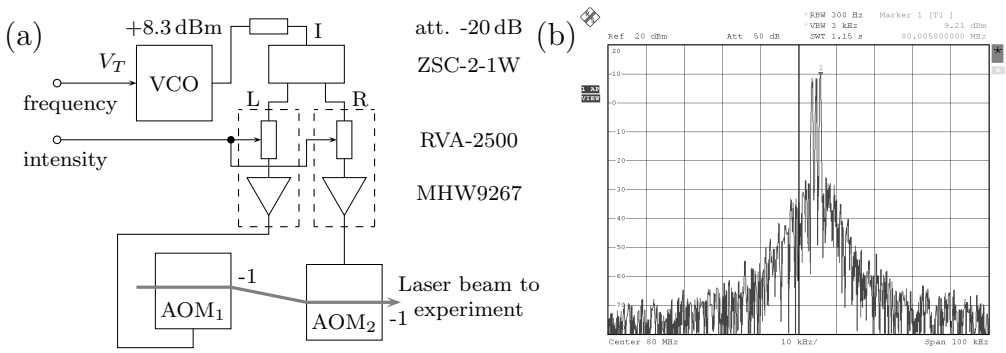

Figure 3.11: a) AOM driving circuit and b) POS-100 noise spectrum.

the bandwidth of the AOM. In order to avoid negative voltages on the VCO input a diode was inserted into the summation operational amplifier (OPA). The noise spectrum of the VCO is given in figure 3.11, which shows three carrier frequencies of the VCO. They are spaced by 1.1 kHz and the outer two have approximately equal levels of $(+8.6 \pm 0.4)$ dBm (+8.3 dBm given on datasheet) while the central peak is 1 dBm smaller at $(+7.6 \pm 0.7)$ dBm. The carrier to noise is about -40 dBc at 3 kHz frequency offset. It was also tried to use a capacitance of 10 μF on the supply voltage of the VCO in order to avoid this behavior but it did not change anything. It seems that this is noise on the V_T input. According to the datasheet the tuning sensitivity is 4.5 MHz/V. Therefore, the 1.1 kHz sidebands would correspond to a tuning noise in the range of 0.24 mV. One could try to insert a lowpass filter into the tuning circuit for filtering out high frequencies (a few 100 kHz), but this was not tried so far since the AOMs locked the laser in a very stable manner. The in-lock error signal (with piezo lock) was limited by noise to 20 mVpp. See linewidth estimation in section 3.3.9 below.

The coupling efficiency through the AOMs has not been measured so far, since the setup needs to be realigned and optimized later, when it is installed on the experiment. The efficiency depends on the beam waist, which should be as large as possible, but simultaneously the larger the beam, the more power might get clipped away when the beam passes the AOMs aperture of 1mm. This leads to an optimum beam diameter of about 700 μm, estimated from the efficiency curve in the datasheet of the AOM[19]. This is approximately the diameter of the laser beam coming from the laser. Therefore, the AOMs were inserted without focusing lenses. But if they were needed, there would be enough space to insert one lens in front of and another behind the AOMs.

It was necessary to place the AOMs in a sufficiently large distance behind each other so that the 0^{th} and -1^{st} order are sufficiently separated. In this way it is guaranteed that the 0^{th} order can be mirrored into a beam dump. To calculate

[19]This is actually the largest beam diameter which is given in the datasheet.

this the Bragg formula is used:

$$\sin[\alpha/2] = \frac{m\,\lambda}{2\,\Lambda}\ , \tag{3.5}$$

where α is the deflection angle of the beam, m is the order of the beam (0^{th} order meaning no deflection), λ is the optical wavelength and $\Lambda = \frac{v_s}{f_0}$ is the acoustic wavelength, with v_s the speed of the sound inside the crystal and f_0 the acoustic frequency which is 80 MHz in our case. The speed of sound is, according to the datasheet, v_s=4200 m/s, which gives for the optical wavelength of λ=1030 nm a deflection angle of the first order of 19.6 mrad. The Bragg angle is defined as $\Theta \equiv \alpha/2$ and is therefore 9.8 mrad (in the datasheet it is given with 10.1 mrad for 1064 nm wavelength). We want to have a beam separation of 4 times the beam radius, since within an area of twice the beam radius of a Gaussian beam there is >99.9 % of the power (see equation (2.27)). Therefore, at the entrance of the second AOM we want to have a beam separation of $\Delta x = 4 \times 700\,\mu$m/2=1.4 mm. This gives a minimum distance between the two AOMs of $\Delta z = \Delta x/\tan[\alpha] \approx \Delta x/\alpha$=71 mm.

Another consideration is by how much the angle changes when the RF frequency is changed. Using the Bragg formula again we get:

$$\begin{aligned} \delta\alpha &= \frac{\partial}{\partial f_0}\alpha \approx \frac{\partial}{\partial f_0}\frac{m\,\lambda\,f_0}{v_s} = \frac{m\,\lambda}{v_s} = 0.25\,\text{mrad/MHz} \\ \delta x &= \delta\alpha\,\Delta z = 18\,\mu\text{m/MHz}\ , \end{aligned} \tag{3.6}$$

where the approximation for small angles $\sin[\alpha/2] \approx \alpha/2$ was used. This means that for a modulation of 1 MHz the position of the 1^{st} order is changed only by 18 μm on the second AOM. This is much smaller than the beam radius, so that this deviation in angle should not affect the coupling of the beam through the second AOM. Within the 30 MHz bandwidth of the AOM the angle of the beam would change by 540 μm, which is a factor 1.5 larger than the beam radius. Since the aperture of the AOM is 2.5 mm in the plane in which the beam is deflected, despite such a big modulation the beam can still pass the second AOM when aligned properly. Otherwise, the high power of the laser beam could damage the second AOM, if it is hit by the beam.

3.3.7 Reference cavity

The reference cavity for the generation of the error signal for reducing the linewidth of the laser is not built so far. Instead a scanning Fabry-Perot (FPI-100-980-2.0, 825 nm-1200 nm, from Toptica) is used. In this section the final cavity and the scanning Fabry-Perot will be briefly described. For the discussion of the general properties of such a cavity refer to section 2.2.

The reference cavity should give a stable and narrow frequency reference in order to lock the laser. Therefore, it should have a high finesse and good mechanical stability. The cavity will consist of two equal mirrors (HR1020-1100/AR SM05-0.15C, BK7, from Laser Components) with a radius of curvature of 150 mm and a thickness of 2.5 mm. They will be glued[20] onto a low expansion spacer (Zerodur, 30 mm×30 mm×100 mm) with 95 mm distance between the mirrors. This gives a free spectral range of FSR=1.58 GHz. In figure 3.12a) the spectrum of the reference cavity is plotted for the length of the cavity changed by a distance of dL. In figure 3.12b) the calculated spectrum is shown, with L=95 mm. The "intensities" are chosen arbitrarily. The radius of curvature was chosen so that

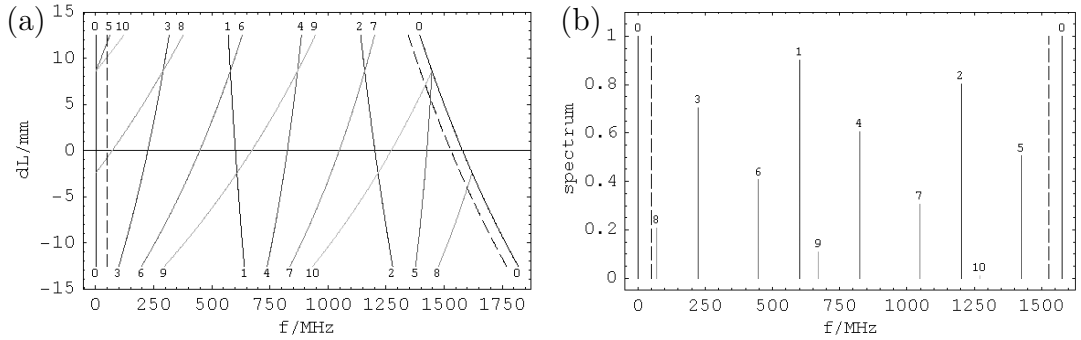

Figure 3.12: Frequencies of the first 10 transversal TEM_{mn} modes of the reference cavity. The numbers correspond to m+n. One FSR=1.58 GHz is drawn with L=95 mm, r=150 mm. a) The mirror distance is varied by dL. b) Transmission spectrum at dL=0 mm, with arbitrary intensities.

no transversal mode smaller than m+n=10 is within a range of 50 MHz (dashed lines in plot). We see that the distance of the mirrors could be enlarged by about 5 mm but should not be smaller. This allows insertion of a piezo in case it is needed[21].

The reflectivity of the mirrors is $\geq 99.8\,\%$ which will give a finesse from equation (2.88) of $F \geq 1500$ and a linewidth of FWHM ≤ 1.0 MHz from equation (2.89). The cavity waist is, according to equation (2.119), $w_{FPI} = 151\,\mu$m, which gives a Rayleigh range of z_0=70 mm from equation (2.26a). The waist at the mirrors is therefore, using equation (2.26b), $w_1 = 183\,\mu$m. The mode matching lens (see section 2.2.4; fused silica lenses from Laser Components) is chosen to be one of the lenses given in table 3.4. In the final setup the used lens will be chosen depending on the available space. The virtual focus of the lens has, from equations (2.121), a waist of $w_{focus} = 127.7\,\mu$m and is shifted by

[20] In ultra-high-finesse cavities the mirrors are optically contacted onto the spacer material, but for the stability required here gluing should be sufficient.

[21] We ordered the same mirrors for other experiments too and if they use the same spacer they have a free choice using a piezo or not.

$\Delta_{focus} = -2.7\,\text{mm}$. The negative sign means that the virtual focus is further away from the incoupling mirror than the real focus of the FPI. The refractive index n=1.507 was used here for the BK7 glass of the cavity mirrors. This value is interpolated from the datasheet of lenses from Laser Components.

With the knowledge of the virtual focus the position and waist at the lens are calculated using the lens equations (2.54). The result is given in table 3.4. The nominal focal lengths of the plano-convex lens f_{nom} are given there also. The exact focal lengths at 1030 nm f_{1030} are calculated with equation (2.60c). They are only marginally different from those given for 1064 nm. The radius of curvature of the lenses r are taken from the datasheet of the lenses from Laser Components. The refractive index for the lenses made of fused silica glass is n=1.450, which is interpolated for 1030 nm from the same datasheet. Furthermore, in the table the propagation distances from the focus of the laser to the lens z_{lens} and that from the lens to the cavity waist z_{FPI} are given, as well as the waists at the lens w_{lens}. For the calculation of z_{lens}, the measurement of the waist w_0=343 μm, discussed in section 3.2.1, is used.

Table 3.4: Lenses for Reference cavity. Details see text.

f_{nom}	r	f_{1030}	z_{lens}	w_{lens}	z_{FPI}
mm	mm	mm	mm	μm	mm
150	77.3	171.8	462	559	209
200	103.0	228.9	728	776	295
300	154.5	343.3	1193	1190	458

For the presently used scanning Fabry-Perot the radius of curvature is r=75 mm and the distance between the mirrors is L=75 mm, meaning that it is in confocal configuration. The free spectral range is FSR=2 GHz[22]. The reflectivity of the mirrors is R>99.7 %, which gives a finesse of F>1000 (datasheet F>600) and a FWHM $\leq$ 2 MHz[22]. A mode matching lens with f=50 mm is already mounted within the Fabry-Perot. In the manual it is said that the incoupling beam should be collimated, but the beam waist is not specified.

In order to get a good long-term stability it will be necessary to temperature stabilize the final cavity and shield it from acoustic noise. This will be done by placing it into an air-tight container with an appropriate design to reduce coupling to external noise. Evacuating the cavity is probably not required. None of this has been done so far, but is on the agenda for the near future.

[22]In the manual the free spectral range is given as 1 GHz, but there the definition FSR=$\frac{c}{4\,L}$ is used. This corresponds to the frequency spacing between the longitudinal and the transversal modes for the confocal configuration, being half the spacing between the longitudinal modes (see section 2.2.5). The same problem arises with the FWHM when calculated from the FSR.

3.3.8 The Faraday isolator

Since there was a problem with one of the two Faraday isolators it is necessary to mention this here in the case further problems arise in the future. The isolators protect the laser from back reflections likely to destabilize the laser in an unpredictable way. Problems due to back reflections were observed during the first measurements of the losses of the glasscell, made with a different laser source and isolator and are discussed in section 3.4.3. Even with 30 dB isolation back reflections significantly influenced the result of the measurement. In the lithium experiment an isolation of approximately 90 dB is used. Therefore, we decided to buy two 40 dB isolators (HP-04-I-1030, 40 dB version[23], from EOT, represented in Germany by Soliton) giving 80 dB isolation against back reflection. If this is still not sufficient we will buy another isolator, but so far for the ELS laser we had no sign that back reflections could cause problems. In section 3.2.1 we calculated the maximum intensity of the laser beam to be $13\,\mathrm{kW/cm^2}$. This is quite a large value, excluding many isolators from other companies. Therefore, besides the large isolation, the decision was made in favour of the EOT isolator because it has a maximum cw intensity damage threshold of $1\,\mathrm{MW/cm^2}$ (given by EOT per email). It has also a high transmission of $> 92\%$. The shipping time of 2 weeks and the very good price were further advantages.

One of the two isolators (serial no. 04-00294) which we bought had an isolation and transmission clearly below the specifications. It turned out that one of the polarizer cubes caused the problem. Visually one could not perceive anything and also when the isolator was tested by EOT, the isolation and transmission seemed to be good. But EOT could only measure with a wavelength of 1055 nm instead of the 1030 nm which we use and finally EOT agreed to replace the bad cube. In table 3.5 the measured transmission and isolation are given for both isolators, where for the bad isolator the data is given before and after the replacement of the cube.

After the replacement of the bad cube the isolation and transmission was good. Obviously, the coating did not work properly with our wavelength. A measurement showed that always a significant amount of light ($\approx 27\,\%$) was steered to the side port regardless of the polarization. When the light propagated in a tilted angle through the cube, the transmission could be increased up to $\approx 85\%$. Therefore, it looks as if that the coating had a local wavelength dependent defect.

[23] This isolator has a standard isolation of 30 dB, but on request EOT can manufacture it with up to 40 dB isolation.

Table 3.5: Isolator transmission and isolation. The specification gives transmission $\geq 90\,\%$ and isolation $\geq 40\,\mathrm{dB}$.

isolator serial no.	transmission %	isolation dB	remark
04-00293	93 ± 2	41 ± 2	good
04-00294	90.3 ± 0.4	41.1 ± 0.3	good[a]
04-00294	56 ± 8	32 ± 9	bad

[a]After the outcoupling cube was replaced. Only two measurements were made.

3.3.9 Estimation of the linewidth

In the final section about the laser linewidth reduction we want to verify the obtained performance of the used locking scheme and estimate the resulting linewidth of the laser. Several methods to measure the linewidth of a laser are known. The easiest of them is to couple the laser beam into a Fabry-Perot interferometer (FPI) and measure the linewidth of the transmitted light. But the light is broadened by the linewidth of the cavity as was discussed in 2.2.2. Therefore, this method is only applicable for a broad laser linewidth, as was done for the not-stabilized laser in section 3.2.2. For a narrow laser linewidth one would need a narrow linewidth of the cavity too, which is difficult. Another method to obtain the laser linewidth is by making a self-heterodyne measurement [Yar89], but also this method is limited to larger linewidths, since it uses an interferometer with one path delayed by more than the coherence time, giving long pathways (often done with fibers). For very narrow linewidths the beat-note of two independent lasers is measured. Or the Allan variance (see for example [Tha99]) has to be measured, which is not so easy. An interesting and easy-to-use way of obtaining the linewidth is by scanning fast over the resonance of a FPI. From the transmitted intensity, measured for different scanning speeds, one can obtain the laser linewidth [KHY+99].

Here we make an estimation of the linewidth by measuring the fluctuations of the error signal while the laser is locked. The error signal can be calibrated to the linewidth by scanning over the resonance of the reference cavity. This gives an estimation of the order of magnitude of the laser linewidth. This is only an approximation because it is an indirect method of measurement. The error signal is derived from the PDH lock [DHK83]. This error signal is used to lock the laser and is small when the laser linewidth is small. But it can show measurement errors and offsets.

The calibration of the error signal is made with the data already presented in section 3.3.1 treating the EOM and the error signal. From figure 3.7c) we have obtained the slope of the error signal to be 555 kHz/V. With this information one has just to measure the largest fluctuations of the error signal during lock and directly relate this to the linewidth of the laser. In table 3.6 the measured in-lock error signals are given for the different locking stages.

Table 3.6: Estimation of laser linewidth by measuring the in-lock error signal of the different locking stages. The error signal U_{err}^{pp} is always the maximum peak-to-peak fluctuation which is recorded over several seconds. The voltage to frequency calibration is 555 kHz/V and gives the FWHM of the laser by multiplication with U_{err}^{pp}.

stage	U_{err}^{pp} mV	FWHM kHz	remark
piezo[a]	90	50	
piezo & PI^2 [b]	70	40	
AOM[c] & piezo	20	10	noise limited

[a] "HV fast" and "HV slow" together. See section 3.3.4
[b] Additional PI in series to "HV slow". See section 3.3.4.
[c] The AOM controller. See section 3.3.6

Another method to obtain the linewidth from the error signal is by using equation (2.161) in section 2.4.1. Here we replace the VCO tuning sensitivity D by the slope of the PDH error signal of 555 kHz/V. The rms noise voltage $\langle V \rangle$ corresponds to the rms noise of the error signal. We did not measured this, but for an estimation half the peak noise of 20 mV/2 will be sufficient. The only remaining unknown is the bandwidth of the measurement. For this we should in principle use the bandwidth of the cavity, which we could estimate to be the inverse of the cavity decay time (see section 2.2.2). But the true bandwidth is reduced, since the error signal passed the lowpass filter after the mixer, which has a bandwidth of about 300 kHz, which we assume to be the bandwidth of the measurement. With this numbers we obtain from equation (2.161) a linewidth of $\Delta_{\mathrm{FWHM}} \approx 300\,\mathrm{Hz}$. This is a very low value, but here we have used very uncertain numbers. Especially the bandwidth of the measurement is not very reliable. A better way of doing this would be to measure the power spectrum of the error signal, which should reveal the true bandwidth of the measurement by a sudden decrease in noise power at a certain frequency. Also from the spectrum one could obtain the rms noise voltage directly by simply integrating over the spectrum (equivalent to section 3.2.3).

We assume the previously estimated linewidth of 10 kHz to be more reliable, which is nevertheless a very good result. In section 2.4.1 the requirement for the laser linewidth of below 100 kHz was derived which seems to be fulfilled easily. At the moment the limit is given by the noise.

For further improvement the signal to noise (S/N) must be increased. At the moment it is S/N=1.8 Vpp/20 mVpp=90 on the error monitor output. An earlier measurement showed that significant noise is added in the mixing and amplification stages for obtaining the error signal. The first will be replaced by the mixing box (mentioned at the end of section 3.3.1) and the noise in the amplification seems to stem from the quite high noise level of the whole PI stage. In particular the scan generator makes some additional spikes whenever the ramp direction is reversed. The signal level could be increased by increasing the modulation index of the sidebands for example. The final reference cavity shall bring a much higher slope of the error signal. The linewidth of the final cavity will be reduced by a factor of at least 2 (see section 3.3.7), which gives a slope twice as steep. Also the PI controllers can be optimized further. On the other side the stability of the system must be improved, maybe at the cost of a larger linewidth. The long-term stability of the system, like mode jumps and drifts of the laser must be recorded in detail. When the new temperature stabilized reference cavity is put into usage, the drifts should be reasonably low, so that locking over several hours should be possible. Already at present, if the laser is not disturbed and the ambient temperature is stable, the laser holds the lock for approximately one hour after warming up, which itself takes one hour. The reason why it falls out of lock, seems to be mode jumps when the laser drifts too far.

In section 3.4.3 we will describe oscillations of the transmitted intensity of the resonator with a high finesse. It is not clear what causes them, but one explanation could be sidebands on the laser light with a frequency spacing of about 80 kHz. These could be caused by the piezo resonance at 80 kHz or by servo bumps of the AOM PI controller. If this is the case something should be visible in the noise spectrum of the error signal, which was not measured for the final setup so far.

We have seen that the laser linewidth is already below the aimed value of 100 kHz (see section 2.4.1). With the piezo controller alone, the linewidth could be reduced from approximately 2 MHz to 50 kHz (a factor of 40). The AOMs reduce the linewidth to 10 kHz (a factor of 5). Now we are limited by noise, allowing us to reduce the linewidth only by a factor of 200. This limitation shall be overcome when the new reference cavity is built[24].

[24]From experience of other groups we know that a factor of 1000 should be feasible.

3.4 Building the resonator

We discussed in the introduction that we have to cool our atoms to very low temperatures which are well below the temperatures in the MOT. Therefore, we use evaporative cooling for a further decrease of temperature. This process is enhanced by a large collision rate among the atoms which drives rethermalization. This can be reached by Feshbach resonances, which require that the magnetic field can be adjusted to a specific value. In order to do so easily, the atoms are loaded into a dipole trap, where they are trapped in an all-optical way.

This dipole trap consists of an optical resonator, which is the heart of the whole setup shown in figure 3.1, and in more detail in figure 3.13. It is a Fabry-

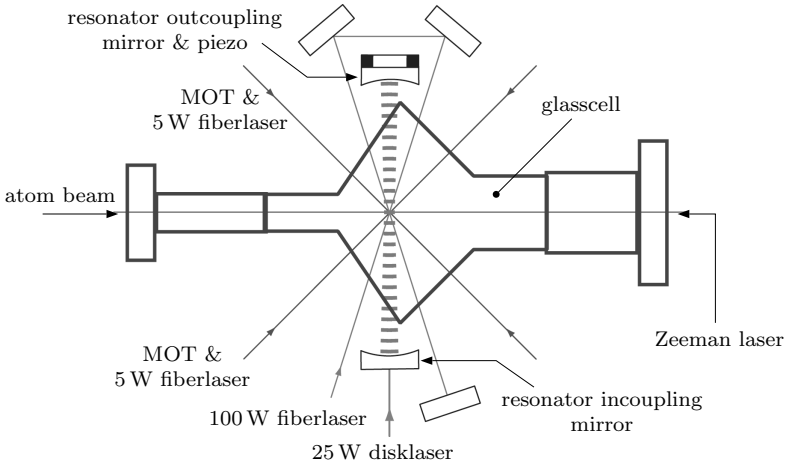

Figure 3.13: Resonator with glasscell and beam paths.

Perot type cavity built around a glasscell. The glasscell is part of the ultra high vacuum (UHV) chamber where our atoms are trapped in a magneto-optical trap (MOT).

The resonator produces a standing wave dipole trap with a large power enhancement, discussed in section 2.2.3. This allows to select a much larger resonator waist than for single focussed beams while the trapping potential is still deep enough to trap the atoms from the MOT. Therefore, the spatial overlap of the resonator with the MOT is large, which results in many atoms to be trapped in the resonator. In a first evaporative cooling stage the intensity of the resonator is ramped down adiabatically.

Using the resonator has some disadvantages. The atoms are divided by the standing wave potential into many thin "slices", also called "pancakes", which are separated by $\lambda/2$. Bulk properties of an atom or molecule cloud can not be studied with this configuration. The transmission through the glasscell is done in Brewster's angle (see section 3.4.1), which causes aberrations of the beam inside

the glasscell making it difficult to characterize the trapping potential. In order to become degenerate the intensity must be ramped down by more than a factor of 1000 in a controlled manner, which needs a large dynamic range for the intensity stabilization to work properly. Also we saw in section 2.4.1, that heating of the atoms by intensity and phase noise is most efficient in a frequency range of the trapping frequencies. But these are very high in the resonator (in the order of MHz, see section 3.4.5), which makes it difficult to reduce the noise actively. Therefore, the noise stability of the laser becomes crucial for the resonator.

In order to avoid these problems we use another dipole trap, which is formed by the focus of a 100 W fiberlaser (from the company IPG). It is used in a crossed configuration, as shown in figure 3.13. The crossed configuration ensures good axial and radial confinement to a size of the beam waist of about 30 μm. But the beams are only crossed twice, since if we overlapped all 4 beams we observed large losses from the dipole trap, which is not understood so far. In the actual setup the atoms are trapped in the crossing of the 1^{st} and 3^{rd} beam, which have orthogonal polarization and nearly parallel propagation directions. Even shifting the beam frequencies of crossing beams by 80 MHz did not help. Also if the beam propagation was opposite the losses were increased.

The 100 W fiberlaser has to be aligned nearly in parallel to the resonator in order to overlap well with the many pancakes of the standing wave. But the aberrations of the beam are still present. Therefore, after performing further evaporative cooling with the 100 W fiberlaser the atoms will be trapped in two 5 W fiberlasers, which are orthogonal to each other and pass the glasscell walls nearly perpendicularly, as can be seen in figure 3.13. Also the intensity at low trap depth is much better controllable in this trap than with the other two traps. Using the 5 W fiberlasers allows to characterize the trap parameters very well, since nearly no aberrations change the position and waist of the focus.

In this section we will discuss the design of the relevant parts used to build the resonator. In order to get the maximum power enhancement the losses which are caused by the glasscell needed to be measured, which is described here in detail. From the losses of the glasscell the optimum mirror reflectivity could be chosen and the mirrors could be ordered. From the measurements we obtained theoretical trap parameters, which we could not verify so far, since the setup is not completed yet.

3.4.1 Custom designed glasscell

The losses of a Fabry-Perot interferometer have a significant influence on the linewidth and the power enhancement, a fact that was discussed in sections 2.2.1, 2.2.2 and 2.2.3. We will present the measurement of the losses of the glasscell in

section 3.4.3. This allowed to choose the optimum incoupling mirror reflectivity, as was described in section 3.4.4.

The easiest way to avoid losses due to the glasscell is by designing the resonator beam to pass the glasscell walls at Brewster's angle α_B:

$$\tan \alpha_B = \frac{n_2}{n_1} \,, \tag{3.7}$$

with n_1 and n_2 the refractive index of air (or vacuum) and the glasscell walls respectively. This equation was derived in appendix 6.2, equation (6.12). It should be mentioned that this approach of avoiding losses has the disadvantage that the resonator beam experiences aberrations by passing the glasscell walls at an angle. In the lithium experiment the resonator was tilted by the Brewster's angle relative to a rectangular glasscell [Joc04, Bar05, Mor01, Els00]. But this design gives limitations for the optical access of the other laser beams and cameras. Therefore, a new design of the glasscell was developed, which led to the kite shape. A photo of the glasscell is shown in figure 3.14, where also the test resonator can be seen. The shape of the glasscell is schematically shown in figure 3.13. The

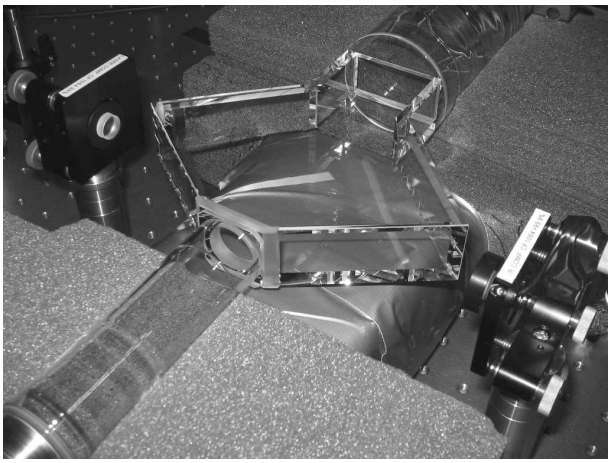

Figure 3.14: Photo of glasscell with testing resonator.

advantages of this shape are:

- resonator perpendicular to glasscell axis
- six orthogonal beam axes with following properties:
  * four beams pass perpendicularly (0°) through the glass
  * two beams pass at only 11° through the glass
  * numerical aperture $f/_{\#} = 2.6$ or better for lenses

The so-called f-number is defined as $f/_{\#} \equiv \frac{f}{D}$, with f the focal length and D the (useable) diameter of the lens [ST91]. The glasscell was manufactured by the German company Hellma. The refractive index is n=1.4496 ± 0.00005 (error estimated), giving a Brewster's angle of α_B=$(55.4003 \pm 0.0009)°$ from equation (3.7).

The measurements in section 3.4.3 show that the losses are indeed minimum for the resonator beam passing perpendicular to the glasscell axis. The only requirement is that the incoming light is p-polarized, which is adjusted by a $\lambda/2$ waveplate.

The resonator will be stabilized using the Hänsch-Couillaud locking scheme, which requires a polarizer within the resonator [HC80]. The glasscell itself acts as a polarizer, since for p-polarized light the losses of the cavity are minimum. Therefore, no additional polarizer is needed, which was one of the reasons why this stabilizing method could be used.

3.4.2 Measuring mirror reflectivity & photodiode voltage

In section 3.4.3, the measurement of the losses of the glasscell will show that the used mirrors have a much higher reflectivity than the minimum specification of the company. Since the measurement of the finesse did not give clear results, we tried to determine the mirror reflectivity in a different way.

The mirrors are borrowed from the lithium experiment. According to the company, they are specified as listed in table 3.7.

Table 3.7: Specified and measured data of the mirrors used for the measurement of the losses of the glasscell.

name	R_{spec}[a]	R_{meas}[b]	r.o.c.	I_{max}	thickness	L[c]	$T_i(y)$
	%	%	m	kW/cm^2	mm	mm	%
1^{st} incoupler	98 ± 0.5	99.04 ± 0.01	0.15	$\geq$1000	3.9 ± 0.1	196 ± 1	99.953 ± 0.008
2^{nd} incoupler	99.4 ± 0.1	99.67 ± 0.01	0.15	$\geq$1000	11 ± 0.5	190 ± 1	99.87 ± 0.02
outcoupler	$\geq$ 99.9[d]	99.9934 ± 0.0004	0.15	100	4.5 ± 0.5	–	99.95 ± 0.01

[a] Specified for 1064 nm.
[b] Measured at 1064 nm from transmission.
[c] Cavity length in combination with outcoupler.
[d] $R = (99.95 \pm 0.05)\,\%$ used in calculations. Small scratch.

For the $\geq 99.9\,\%$ mirror, a small scratch was found on the high reflectivity side, close to the center. Therefore, the alignment during this, and the consecutive measurements, has always been in such a way that the beam does not hit the scratch. Nevertheless, this scratch could have caused some problems as will be discussed in the next section.

First a cavity ring-down (CRD, see section 2.2.2) measurement was performed. The cavity decay time is, according to equation (2.99), with $L = (0.196 \pm 0.001)\,\mathrm{m}$ and for a combination of the outcoupler with either the first incoupler $\tau = (63 \pm 16)\,\mathrm{ns}$ or the second incoupler $\tau = (201 \pm 35)\,\mathrm{ns}$, which is

quite low in both cases. The theoretical finesse for previous combinations is, from equation (2.88), F=303 ± 75 and F=964 ± 166 respectively. Only with the first combination of mirrors a result was obtained, since for the higher reflectivity of the incoupling mirror, the transmitted intensity was so low that we had a signal to noise of about 2. Under these conditions no reliable results could be acquired.

The input light was switched off with the setup shown in section 3.4.3, figure 3.17, but the cavity was not in off-axis configuration. The AOM was frequency modulated (FM) by a 10 Hz square function at 70 MHz+10 MHz. Despite the AOM being used in double-pass configuration, the FM modulation led to a sufficient beam deviation so that the beam did not pass the isolator anymore. Amplitude modulation did not allow to switch off the intensity fast enough. In figure 3.15a) we plot the measured signal of the laser after the laser was switched off, as well as the corresponding ring-down signal of the cavity.

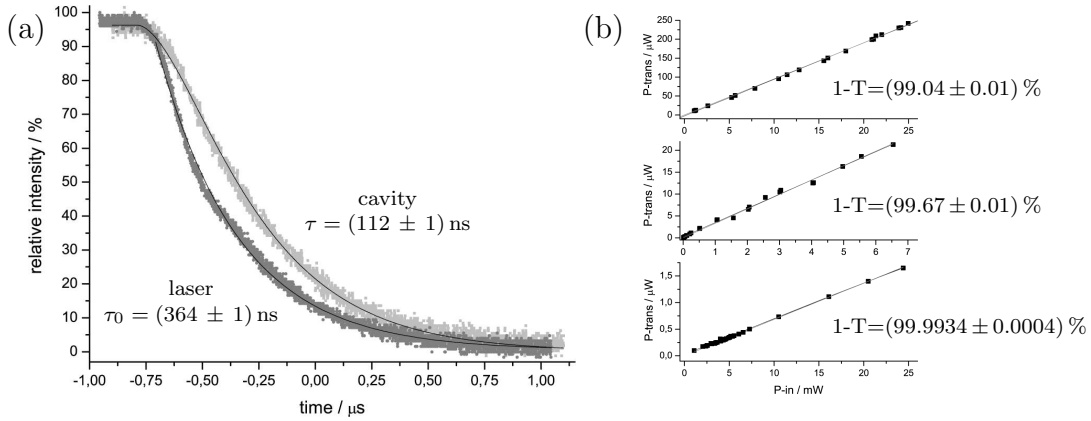

Figure 3.15: Measurement of the test mirror reflectivity. a) Cavity ring-down measurement. b) Mirror transmittance.

We see that input light is switched off nearly exponentially. Fitting the measurement with an exponential decay results in $\tau_0 = (364 \pm 1)$ ns for the switch off time. The CRD measurement treated in section 2.2.2 assumes that the laser light is switched off fast, i.e. $\tau_0 \ll \tau$, which is not the case here. Therefore, a theory for the cavity decay had to be developed for the input beam is switched off slowly. This is done in the appendix, section 6.6. The result is equation (6.47):

$$I_t(t) = \begin{cases} I_t^{(0)} & \text{for t}< t_0 \\ I_t^{(0)} \left| \dfrac{1}{\tau_0 - \tau} \left(\tau_0 \, \boldsymbol{e}^{-(t-t_0)/(2\tau_0)} - \tau \, \boldsymbol{e}^{-(t-t_0)/(2\tau)} \right) \right|^2 & \text{for t} \geq t_0 \end{cases} . \quad (3.8)$$

which we have modified slightly to take into account non zero starting times by introducing a time-offset defined by $t \mapsto t - t_0$. For negative values of $t - t_0$, the fitting function value was set to $I_t^{(0)}$, i.e. constant. We used this function to fit the

measured ring-down signal shown in figure 3.15a). The previously obtained value for the switch off time τ_0 was first fixed in the fitting procedure. We obtained a cavity decay time of $\tau = (112 \pm 1)$ ns. The error had to be calculated separately, which was done by fitting with the program Origin. The result of τ was slightly different, since the negative values of $t - t_0$ needed to be excluded manually, which is not so precise. From the cavity decay time we calculated the finesse of the cavity using equation (2.100) and obtained a finesse of F=539 ± 5. It was also tried to include τ_0 into the fitting procedure. We obtained $\tau_0 = (408 \pm 2)$ ns and $\tau = (73 \pm 1)$ ns. This tells us that the fitting seems to be sensitive enough to distinguish the result for a pure exponential decay from a decay given by equation (3.8). On the other hand, the finesse calculated from this decay time is F=351 ± 5, which shows that the result is strongly dependent on the way the fitting is done. Therefore, we take the mean value of both fits F=445 ± 99 as our result, with the error having a width such that both fits are included. This is about one σ above the finesse calculated from the specification of the mirrors (see above). The "effective reflectivity" for this finesse is with equation (2.91) Z=(99.3±0.2) %, which is one σ larger than the (99.0±0.3) % obtained from the specification of the mirrors.

Since the error is so large, we can not conclude about the mirror reflectivity definitely. We only observe that the reflectivity of the mirrors has a tendency towards larger values than specified, which will be confirmed by the measurement of the mirror transmission below. Nevertheless, the obtained finesse for the cavity ring-down measurement is included in table 3.8 (labelled "CRD") in the next section. A decomposition of the finesse into the different mirror reflectivities was not possible. To do this, at least three different combinations of mirrors need to be measured, which was not possible due to the small signal level for the high reflectivity mirrors.

In general, this method of measuring the finesse should have some advantages, compared to the method used in section 3.4.3. Since the laser light is anyway switched off, back reflections, laser drifts, intensity noise and coupling efficiency are no problems. The cavity is not changed during the measurement and therefore only the stability of the cavity affects the measurement. Ideally, the transmitted intensity is monitored and as soon as the intensity is maximum, the input light is switched off. In order to improve this measurement, one would need to switch off the light faster. Even with the theory taking into account that the input light is switched off exponentially, there remain some sources of uncertainties. The major difference from a pure exponential decay is the smooth starting of the decay seen in figure 6.2a) in the appendix. But from the measurement it is obvious that the laser beam when switched off shows as well a smooth decay instead of a sharp edge as a it would be if switched off exponentially. Therefore, we must assume that the result obtained may be biased by this

feature. An additional error may be introduced by the FM modulation used to switch off the input beam. In equation (6.47), the frequency is assumed to be constant and on resonance with the cavity. With FM modulation this assumption is not true anymore. Therefore, either the case of FM modulation would have to be introduced into the theory or the input light must be switched off without changing the frequency. A suggestion to do so would be: using an EOM in one path of a Mach-Zehnder interferometer and sending one output into the cavity. By switching the phase of the light with the EOM, the light to the cavity could be switched off very fast by interferences without changing the frequency.

In a second measurement, the mirror transmission of the three mirrors in table 3.7 was measured directly. We brought some light onto the mirror and measured the incoming and the transmitted intensity for a range of different light intensities to reduce the influence of incorrect powermeter calibration (see figure 3.15b). For the incoupling mirrors, two linear fits were made. For one fit, the line was fitted through zero (i.e. the slope is fitted, while the offset is set to zero), and for the other one, it was done without this constraint (i.e. slope and offset are fitted). For the outcoupling mirror, the same procedure was done twice, since we had two independent measurements (the different fitting lines are too close to each other to be distinguished in figure 3.15b). The slope in these fits corresponds to the transmission. From the results the mean is taken and the error is set to include all fits. From the transmittance, we can give an upper boundary for the reflectivity of the mirror R $\leq$ 1-T. If losses are present, they reduce the reflectivity. The result is included in table 3.7.

We want to estimate the order of magnitude of the absorbtion losses of the mirror substrates. From [Sch06b] we obtain the internal transmission (transmission inside the glass, T_i) of BK7 glass for a thickness of (25 ± 0.5) mm and a wavelength λ=1060 nm: $T_i(25\,\mathrm{mm})$=(99.7 ± 0.05) % (error estimated). We rewrite the Beer-Lambert law for absorbtion of a medium [EFK+93]:

$$\begin{aligned} I = I_0\, \boldsymbol{e}^{-\alpha\, x} \equiv I_0\, T_i(x) \quad &\Rightarrow \quad \alpha = -\frac{\ln[\,T_i(x)\,]}{x} \\ \text{and} \quad T_i(y) = \boldsymbol{e}^{-\alpha\, y} = \boldsymbol{e}^{-\ln[\,T_i(x)\,]\, y/x} &= \big(T_i(x)\big)^{y/x}\ , \end{aligned} \tag{3.9}$$

with α the absorbtion coefficient, x=25 mm and y corresponding to the thickness of the mirror, according to table 3.7, where we have included the resulting internal transmission $T_i(y)$. The transmission T measured before is related to the T_i by $T = (1 - R)T_i$. With this, the reflection of the mirrors $R = 1 - T/T_i$, compensated for substrate losses, can be calculated. The resulting reflectivities are exactly the same as without these losses. Therefore, transmission losses of the substrate are negligible within the errors. The obtained reflectivity of the two incoupling mirrors, given in table 3.7, are well above the specification. For the second incoupler we obtained from the company a measurement of R=99.5 %,

which does not match with our result. The reflectivity of the outcoupling mirror is within the specification, but it seems as well to be quite high. The company which manufactured the mirrors (Laser Components) claimed that previous customers measured it to be R=99.97 %. Nevertheless, we used the reflectivity we measured in the considerations of the losses of the glasscell in the next section, keeping in mind that especially the errors might be larger than calculated here. The "effective reflectivity" for the first incoupler and the outcoupler is with equation (2.68) Z=(99.516±0.005) % which is about one σ larger than the result obtained from the cavity ring-down measurement.

One uncertainty remains. Transmission losses when passing the coating of the mirror could be significant, even though the thickness of such coatings is very small. We do not know how the coating of the mirrors is designed[25], and therefore we can not include these losses into our calculation.

Finally, we want to report another measurement, which is not related to the mirrors, but, since it was measured simultaneously with the previous measurement, it fits here. For two of the mirrors the transmitted intensity was sent onto a photodiode, and the output voltage was recorded. With this measurement we were able to calibrate the photodiode signal which will be needed in section 3.4.3 for the "Aπ" measurement. The result is shown in figure 3.16. The the data-

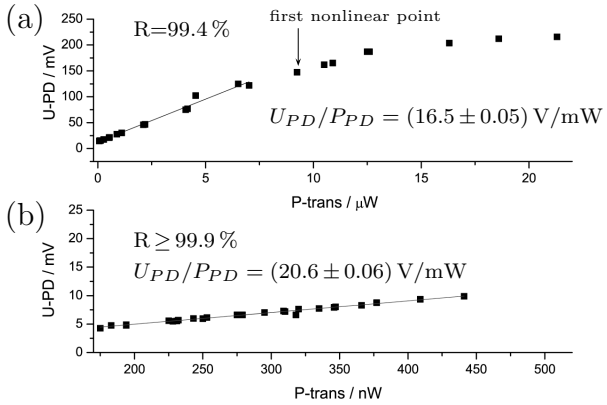

Figure 3.16: Calibration of photodiode, performed with a) the 2^{nd} incoupling mirror and b) the outcoupling mirror.

points in the figure 3.16a), where the photodiode started to become nonlinear were excluded in the fitting.

We obtained slightly different results for the two mirrors. Therefore, we took the mean and enlarged the error so that both results are within. Doing so yields $U_{PD}/P_{PD} = (19 \pm 2)$ V/mW.

[25]The company did not provide the information. Interestingly, to specify their mirrors they make a transmission measurement and suppose zero losses. They claim that transmission losses are on the order of a tenth of a percent and therefore negligible.

3.4.3 Measuring the losses of the glasscell

As we have learned in section 2.2.3, the power enhancement depends on the losses 1-T_3 of the cavity. An optimum reflectivity of the incoupling mirror exists, given by the "impedance matching condition" 2.116. Therefore, the losses caused by the glasscell had to be measured.

To obtain the losses of the glasscell a test resonator was built (see figure 3.17, a photograph is shown in 3.14 and for spectrum see figure 2.16) and the finesse with and without the glasscell was measured. From the difference the loss coefficient 1-T_3, caused by the glasscell, is obtained (see equation (2.68), section 2.2.1):

$$Z_{gc} = T_3\sqrt{R_1\,R_2} = T_3\,Z_0 \quad \Rightarrow \quad T_3 = \frac{Z_{gc}}{Z_0}\ , \tag{3.10}$$

with Z_{gc} and $Z_0 \equiv \sqrt{R_1\,R_2}$ the Z of the cavity with and without the glasscell respectively. Whenever it was possible, Z_0 was not calculated from the reflectivity of the mirrors, but rather from the measured finesse of the cavity.

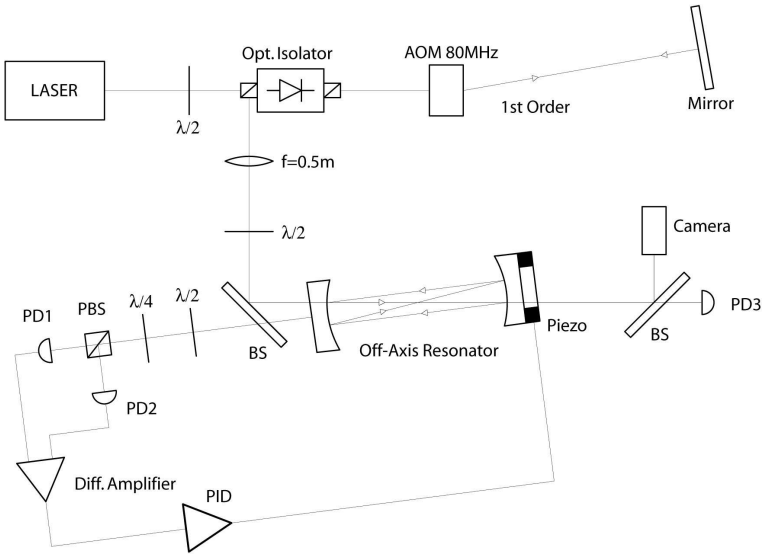

Figure 3.17: Setup for measuring the losses inside the resonator.

In order to obtain the finesse, the cavity length is scanned by a piezo[26] over at least two free spectral ranges (FSR) and the width of the peak (FWHM) is obtained by fitting a Lorentz curve to each peak. The finesse is simply F=$\frac{\text{FSR}}{\text{FWHM}}$.

[26]The HV amplifier used was different to the one used in the final setup. The elements for locking the resonator to the laser, which are shown in figure 3.17 detecting the polarization of the reflected light, were never used during the measurement. They were only used for testing.

In order to obtain a reliable result, the calculated finesse of at least 10 measurements were averaged[27] and the standard deviation of this average is given as the error.

For the first 14 measurements the setup in figure 3.17 was used, for which the mirrors and the cavity length are given in table 3.7, section 3.4.2. The laser source was a single mode (SLM) Nd:YAG/YVO4 laser with 100 mW output power from the company CrystaLaser. It has a wavelength of 1064 nm and its linewidth is <10 kHz, according to the datasheet. The beam diameter ($1/e^2$) is 0.45 mm and the divergence is 3.6 mrad (full angle).

There were several reasons why for the first 14 measurements the setup was chosen to be the one of figure 3.17. In a first attempt, only the Faraday isolator was inserted and the beam was directly coupled into the cavity. The isolator was different from the final chosen one, with about 28 dB isolation at 1064 nm. If a glassplate was inserted into the cavity, the result looked like figure 3.18a).

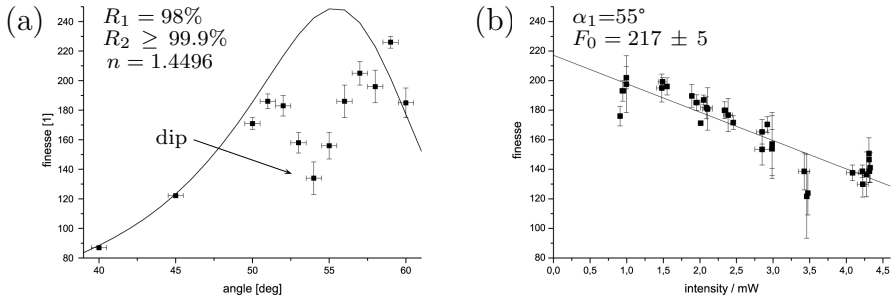

Figure 3.18: First measurements with glassplate showed signatures of back reflections. a) The finesses is decreased at Brewster's angle and b) it is a function of the intensity of the incoming light.

There appeared a dip, clearly visible where one expects the maximum finesse. A similar behavior was observed in [Els00]. It is not completely clear what causes such a dip, but it seems reasonable that it could be caused by back reflection of light into the laser. As long as the laser light is not resonant with the cavity, the light is rejected from the cavity and propagates back into the laser, where it forces the laser to emit at a certain frequency and phase. This effect is often used to stabilize diode lasers [WH91, DHD87]. But here the phase and amount of light which is reflected back into the laser changes significantly if the laser light is on resonance with the cavity. From equation (2.73b) and figure 2.6 we see that, on resonance, no light is reflected and from equation (2.69) it is obvious that the phase is zero on resonance, whereas off resonance it is not. The difference of intensity and the slope with which the intensity and phase changes, when one scans over a resonance, depends on the finesse F. The higher the finesse

[27]The averaging was performed in most cases by weighting with the individual error of the measurements, which is the standard deviation of several (mostly 2) FSR.

the more light is reflected and the steeper is the slope. Therefore, it seems logical that, with back reflections, the laser reacts differently if the finesse is high or low. Since the speed of scanning the cavity is much slower than the dynamics of the laser, it is clear that such an instability of the laser caused by back reflections could affect the measurement. Therefore, back reflections must be avoided.

Several approaches were tried. Together with the optical isolator, an AOM was inserted in double-pass configuration as is shown in figure 3.17. This setup shifts the light which is reflected back into the laser by 4×80 MHz=320 MHz. In combination with the AOM, the Faraday isolator was passed two times, which gives twice the isolation, as described in [Mor01]. It turned out that the AOM and the isolator in double-pass configuration helped reducing the dip, but back reflection still seemed to cut-off the maximum finesse. The next approach was to use the cavity in an off-axis configuration, as was shown in figure 3.17. Such a setup was used by [HC80] as well. This configuration definitely improved the stability of the laser (c.f.#5 and #6 in table 3.8). Therefore, the first measurement of the losses of the cavity were done this way, with the AOM and the isolator used in a double-pass configuration as well.

In figure 3.18b) we see another hint for back reflections. Here the AOM and isolator was used in double-pass configuration and the intensity was adjusted by a combination of a $\lambda/2$-waveplate and a polarizing beamsplitter in front of the cavity (not shown in figure 3.17). Obviously, the measured finesse depends on the intensity of the light going into the cavity. In this example a clear linear dependency is visible, but sometimes the slope looks more exponential. For the off-axis resonator it was not so significant anymore, but still visible. In order to account for this, the finesse was measured for different intensities. The obtained data was fitted linearly or exponentially, according to the column "info" in table 3.8, with the extrapolated finesse at zero intensity to be assumed the true one.

In figure 3.18a), we plotted a theoretical curve for a glassplate inserted into the cavity for comparison. It is turned by an angle α_1, which is defined such that it is zero if the beam passes perpendicular to the glassplate. To calculate the finesse we use equation (2.88) and calculate the transmission T_3 through the glassplate. This transmission we obtain from the Fresnel equation for p-polarized light (6.6a), see appendix 6.2, where we have to take into account both boundaries when the beam enters and leaves the glass. On leaving the glassplate (gp) the angles are just exchanged:

$$\begin{aligned} T_3^{gp}[\alpha_1] &= \Big(1 - \frac{\tan^2[\alpha_1 - \alpha_2]}{\tan^2[\alpha_1 + \alpha_2]}\Big)\Big(1 - \frac{\tan^2[\alpha_2 - \alpha_1]}{\tan^2[\alpha_1 + \alpha_2]}\Big) \\ \text{with} \quad \alpha_2 &= \arcsin\Big[\frac{n_1}{n_2}\sin\alpha_1\Big] \ . \end{aligned} \tag{3.11}$$

The mirror reflectivities were $R_1 = 98\,\%$ and $R_2 = 99.9\,\%$ and the refractive index of the glassplate is n=1.4496 (the same as that of the glasscell).

It is convenient to calculate the transmission for the glasscell (gc) at this point, which we model by two glassplates. The two glassplates are positioned in Brewster's angle α_B to the incoming beam. If the glasscell is turned by an angle α in clockwise direction, the beam on the entering side has an insertion angle of $\alpha_1 = \alpha - \alpha_B$ and the exiting beam has an angle of $\alpha_1 = \alpha + \alpha_B$. This gives for the transmission coefficient of the glasscell:

$$T_3^{gc} = T_3^{gp}[\alpha_B - \alpha]\, T_3^{gp}[\alpha_B + \alpha] \;, \tag{3.12}$$

which is expressed as the transmission coefficient of two glassplates (3.11), for the appropriate angles. The resulting curve of the finesse of the glasscell for different turning angles looks very similar to a Lorentzian curve and therefore such a curve was fitted to the measured data[28]. The maximum of this curve represents the angle of minimum losses.

Table 3.8: Results for the measurement of the losses of the glasscell.

#	R_1 %	R_2 %	L mm	gc.	name	finesse 1	1-T_3 %	info	file *.obj
1	98	≥ 99.9	196	✓	G1&G2	276 ± 5	0.5 ± 0.3	Lorentz&lin.	glasscell98
2					G3	329 ± 31	0.2 ± 0.1	exponential	glasscell98
3					G3	287 ± 14	0.04 ± 0.06	linear	glasscell98
4					G3	317 ± 43	0.1 ± 0.1	mean	glasscell98
5					G4-lowR	188 ± 21	$F_{gc} > F_0$	on axis, lin.	g4
6					G4-lowR	235 ± 17	$F_{gc} > F_0$	off axis, lin.	g4
7	99.4	≥ 99.9	190		G4-highR	401 ± 19	$F_{gc} > F_0$	linear mean	g4
8					G4-highR	365 ± 20	$F_{gc} > F_0$	linear all	g4
9					G4-highR	383 ± 38	$F_{gc} > F_0$	mean	g4
10				✓	G5&G6	526 ± 2	0.4 ± 0.1	Lorentz&lin.	g5 & glasscell994
11	98	≥ 99.9	196		CRD	539 ± 5	0.55 ± 0.02	fixed τ_0	CRDS
12					CRD	351 ± 5	0.24 ± 0.02	not fixed τ_0	CRDS
13					CRD	445 ± 99	0.4 ± 0.2	mean	CRDS
14	99.4	≥ 99.9	190	✓	G6 Aπ	409 ± 8	0.6 ± 0.1	Lorentz&lin.	glasscell994
15	98.58	≥ 99.8	500		res1	514 ± 13	0.06 ± 0.02	lock	
16					res1	465 ± 11	-	unlock	
17				✓	res1	471 ± 4	0.0 ± $\{^{0.4}_{0.0}$	lock	
18	99.4	≥ 99.9	≈ 200		res1	558 ± 5	0.3 ± 0.1	lock	
19	≥ 99.8	≥ 99.8	500		res2	1675 ± 20	$F_{gc} > F_0$	≈ 55 Hz, lock	
20					res2	2232 ± 40	0.02 ± 0.02	21 Hz, lock	
21					res2	3404 ± 87	0.03 ± 0.02	5 Hz, lock	
22					res2	3213 ± 19	-	5 Hz, unlock	
23	≥ 99.8	≥ 99.8	500		res2	2670 ± 78	0.06 ± 0.02	5 Hz, lock	
24				✓	res2	1941 ± 178	0.01 ± $\{^{0.04}_{0.01}$	5 Hz, lock	
25	98.58	98.58	500		res3	295 ± 2	0.00 ± $\{^{0.04}_{0.00}$	10 Hz, lock	
26				✓	res3	295 ± 2	0.00 ± $\{^{0.04}_{0.00}$	10 Hz, lock	

In table 3.8 the results for different measurements of the losses of the glasscell are given. If the entry "gc." has a check mark, the measurement is made with

[28]This was not verified mathematically. One could directly fit equation 3.12 to the data, but the deviation to the Lorentzian curve is very small. Therefore, we decided not to do this.

the glasscell, otherwise it is made without the glasscell. For the measurements without the glasscell the loss coefficient 1-T_3 is calculated from the difference of the finesse with and without the glasscell. For some measurements labelled $F_{gc} > F_0$ this was not possible since the finesse with the glasscell was larger than without it. Besides the large spread of the measurements which might have caused this result, one could imagine that the glasscell acts as a filter which cancels disturbing effects, like a fraction of s-polarized light. It is not clear if this filtering could have such a big effect to outweigh the losses of the glasscell.

The calculation of the finesse and error bar was done under the condition given in the column "info". As discussed above, the finesse depends on the input intensity. Therefore, either a linear or an exponential fit was done in each measurement and the finesse was extrapolated for zero intensity. For the later measurements, starting at measurement number (abbreviated by the symbol "#") #15 no intensity dependence was observed. Therefore, the intensity was not changed anymore, which made fitting obsolete.

In the "G3" measurement, the finesse labelled with "mean" (#4) is obtained from the mean of the two finesses of the exponential (#2) and linear fit (#3). The error bar was enlarged to include both fits. In the measurement "G4-lowR" the difference of the finesse "on axis" (#5) to "off axis" (#6) was measured, both using linear fit of the intensity. The measurements #6 to #10 and #14 were done in the "off axis" configuration. For "G4-highR", either the mean of the finesse for each intensity was taken and afterwards a linear fit was done (#7), or a linear fit from all the measurements was calculated (#8). The finesse labelled with "mean" (#9) is again the finesse and error obtained from the two fits.

In the measurements with the glasscell (#1 and #10) a linear fit for the intensity was done. The result for different angles of the glasscell is shown in figure 3.19a). Two theoretical curves are included in the graph (dashed lines). They are calculated with equation (3.12), using the corresponding mirror reflectivity with zero losses (R_2=99.95 %, T_3=1). The measurement "Aπ" will be explained below. For each measurement Lorentzian curves were fitted and the maximum finesse is given in table 3.8. For the "G5&G6" measurement the maximum finesse is at an angle of $(0.00 \pm 0.02)^\circ$ and for the "G1&G2" measurement the maximum is slightly shifted to $(0.13 \pm 0.04)^\circ$. This means that the input and output windows of the glasscell are within the specification of the glasscell (α_B=$(55.4 \pm 0.25)^\circ$, see section 3.4.1). In measurement "G1&G2" the dip caused by back reflection is visible. This measurement was performed with the AOM and optical isolator in double path, but not in the "off-axis" configuration, as the other measurement "G5&G6". This shows a much larger variation of the result than "G1&G2", which can be explained by the fact that for higher finesse, losses and instabilities have a larger impact than for low finesse (see sections 2.2.1, and 2.2.2). It seems that in nearly all the measurements, there are some reductions of the finesse at

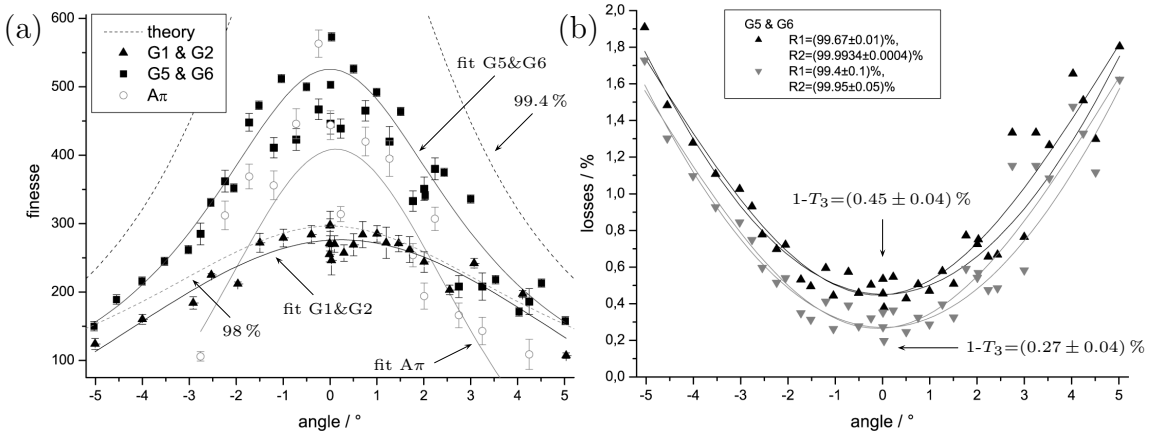

Figure 3.19: Measurement of the losses of the glasscell. a) Finesse and b) calculated loss coefficient.

an angle of about $\pm 2°$. For this, no obvious explanation was found. Possible explanations would be: shifted resonance frequencies due to different cavity length, different focus position and waist, influence of astigmatism, the scratch on the 99.9 % mirror could be hit by the beam at this angle, etc.

In figure 3.19b) the obtained loss coefficient 1-T_3 of the "G5&G6" measurement is plotted. For the calculation of this, either the specified reflectivity of the mirrors or the measured reflectivity was used, see table 3.7 in previous section. This was done in order to get an upper and a lower boundary for the losses. The specification gives a lower boundary and the measured reflectivity gives an upper boundary. Two Lorentzian curves were fitted to the obtained datapoints, where one uses weighting of the errors of the datapoints and the other not. The result is not very different. From the fit we obtained the angle of minimum losses at $(-0.05 \pm 0.03)°$, which is not very different than before.

We obtained $1 - T_3 = (0.45 \pm 0.04)\,\%$ and $1 - T_3 = (0.27 \pm 0.04)\,\%$ for the upper and lower boundary. This is nearly the same result as when we took the fit for the "G5&G6" measurement in figure 3.19a) directly. Again we take the average of the obtained boundaries and we enlarge the error in such a way that it encloses both boundaries. From this we conclude the losses of the glasscell to be $1 - T_3 = (0.4 \pm 0.1)\,\%$. This result was included in table 3.8 for the "G5&G6" measurement (#10) and was used in order to calculate the optimum incoupling mirror for maximizing the power enhancement (see section 3.4.4). In a similar way the "G1&G2" result in table 3.8 was obtained (#1), but instead of fitting the loss coefficient, the fit of the finesse was directly used and the corresponding boundary was calculated, giving the mean and error.

The measurements #1 to #10 in table 3.8 show big variations. Therefore, we decided to make different kinds of measurements in order to verify these

results. The measurement labelled with "CRD" is obtained from the cavity ring-down experiment, described in section 3.4.2. The loss coefficient $1 - T_3$ is calculated by comparing the finesse from the CRD measurement with the finesse obtained in "G1&G2" (#1), using equation (3.10). Taking the mean result from this measurement, $1 - T_3 = (0.4 \pm 0.2)\,\%$ (#13), we can say that it matches the other measurements very well, but due to the large error, we do not gain new information.

An alternative way to obtain the finesse is to measure the power enhancement which gives the finesse with equation (2.114), derived in section 2.2.3. The result is labelled "Aπ" (#14) in table 3.8. We solve equation (2.114) for the finesse and insert the definition of the power enhancement, equation (2.105):

$$F \approx \frac{A\pi}{4} = \frac{\pi}{T_2}\frac{I_t^{max}}{I_0} \; . \tag{3.13}$$

We see that we need to record the input intensity and the transmitted intensity of the cavity. The transmission of the outcoupling mirror has to be known as well. We have measured the voltage of the photodiode during scanning over the resonance. In order to obtain the maximum transmitted intensity we needed to know the relation of the intensity to the output voltage of the photodiode. In section 3.4.2 this was done and the result was $U_{PD}/P_{PD} = (19 \pm 2)\,\mathrm{V/mW}$. We fitted a Lorentzian curve to the measured data and calculated maximum transmitted intensity. The measurement of the transmission coefficient T_2 of the outcoupling mirror was already described in section 3.4.2, and resulted in $T_2 = (6.6 \pm 0.4) \times 10^{-3}\,\%$ from the reflectivity given in table 3.7 ("outcoupler")[29]. When this calculation was made, the fit through zero was not included in the mirror transmission. Therefore, for this calculation only the result of the fit not going through zero, $T_2 = (6.19 \pm 0.02) \times 10^{-3}\,\%$, was used. Since the whole measurement was meant as verification of the previous results, and since it takes quite some time to redo the calculation, we will be satisfied to use the old value. For each measurement point, the input and transmitted intensity of the cavity were measured for different intensity levels and the finesse was calculated. A linear fit was done to obtain the finesse at zero intensity, since again the finesse showed an intensity dependence. In figure 3.19a) the finesse obtained by this procedure is included. The Lorentz curve fitted to this data has a maximum of $F = 409 \pm 8$, which we included in table 3.8 (#14). We see that the finesse obtained has the same order of magnitude as "G5&G6" (#10), but it is generally a little lower. This is not really surprising, since in above considerations we have neglected the coupling efficiency of the input light into the cavity. Actually, we can obtain this by using the difference of the two finesse:

$$F_\eta \approx \frac{\pi}{T_2}\frac{I_t^{max}}{I_0\,\eta} = \frac{1}{\eta}\,F_0 \quad \Rightarrow \quad \eta = \frac{F_0}{F_\eta} \; , \tag{3.14}$$

[29] The transmission was measured directly, while R=1-T is given in the table.

with F_η the real finesse and F_0 the finesse measured without taking into account the coupling efficiency η. Setting $F_\eta = 526 \pm 2$, i.e. the result from measurement "G5&G6" (#10), which was at the same time recorded as "Aπ" (#14), we obtain the coupling efficiency $\eta = (78 \pm 2)\,\%$. This is not so bad.

Summarizing measurements #1 to #14, we obtained a loss coefficient of $1 - T_3 = (0.4 \pm 0.1)\,\%$, which is mainly the result from measurement "G5&G6" (#10). From this the ideal incoupling mirror was calculated to maximize the power enhancement (see section 3.4.4). The company where we ordered the mirrors made a wrong coating for the incoupling mirror with the reflection maximum at 1080 nm instead of 1060 nm. This gave us the opportunity to measure the losses of the glasscell again, but now with the new mirrors and with the ELS laser, which had been delivered at that time. These measurements are labelled #15 to #26 in table 3.8 and will be discussed in the following.

In none of these measurements a fit was necessary for the intensity, since no effects of back reflections was observed. The ELS laser and only one isolator (40 dB from EOT, see section 3.3.8) was used. The measurements were performed with the new mirror with radius of curvature r=0.75 m and cavity length of L=0.5 m, except #13 (see below). The finesse was again obtained with the same procedure as described above.

In two measurements the influence of the laser was measured, when it was in-lock (#15 and #21) or out-of-lock (#16 and #22). The finesse out-of-lock is in both measurements slightly decreased versus that in-lock, but the linewidth of the laser seemed not to have a big influence on the result. Probably, this has something to do with the fact that the scanning speed over the resonance was quite fast, as is discussed below further.

The loss coefficients obtained by comparing the results with the glasscell with those without the glasscell (using equation (3.10)) gave consistent results. Only for the measurement "res3" with low finesse the error is so large that no difference with and without glasscell could be measured.

During the measurements of the finesse with the two high reflectivity mirrors "res2", we observed some interesting lineshapes of the transmitted intensity. Figure 3.20a) shows a typical lineshape for a 4 μs scanning time over the full-width-half-maximum (FWHM) of the peak (#19). The lineshape looks Lorentzian, except for the decreasing intensity which shows some oscillations. The direction of scanning does not affect the appearance of these oscillations.

For a finesse around F=2000 and a length of the cavity of L=0.5 m, we calculate with equation (2.100), derived in section 2.2.2, a cavity decay time of $\tau = 1\,\mu$s. This shows that we are scanning the cavity resonance over the laser frequency during a time interval corresponding to the cavity decay time. The

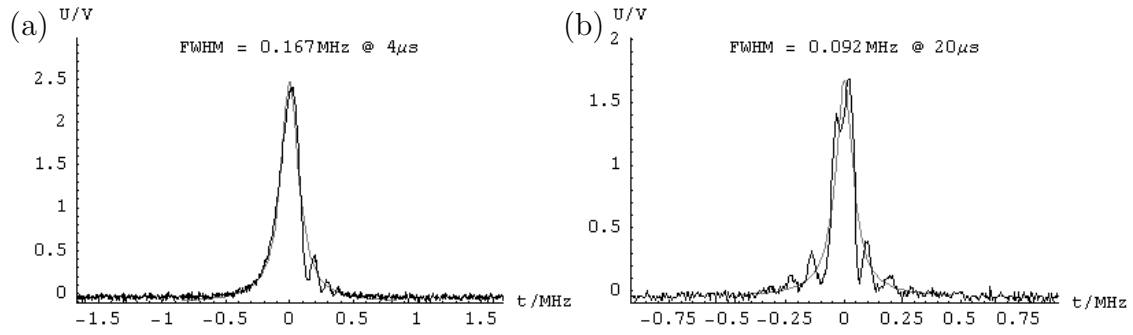

Figure 3.20: Scanning the cavity fast with respect to cavity-decay time. a) ≈ 55 Hz, b) 5 Hz scanning frequency, both with laser locking.

increasing slope corresponds to "filling" the cavity. According to equation (2.99), it should increase exponentially (same as decreasing), but here we change the resonance frequency as well, which is modifying the shape to give it a Lorentzian curve. The decreasing slope is a combination of the decaying cavity with the frequency scanning as well. It seems reasonable that this could cause interferences (see appendix 6.6 and [RESKB02]) during the decay of the cavity. The asymmetry may be explained by the different starting conditions: no light or full light in the cavity, but this should be checked by a theory or simulation. In the same theory one must calculate by how much the measured linewidth is affected by such interferences. Probably, the measured linewidth becomes smaller than the true linewidth. Maybe this is why we measured such a high finesse.

In order to check if the oscillations are interferences, the scanning time was increased to 20 μs per FWHM (#21). No oscillations were expected, but on the contrary, strong oscillations appeared, even on the increasing side of the intensity, as can be seen in figure 3.20b). The finesse increased in this measurement to more than F=3000. The oscillations were spread out over the whole transmission line, often dividing the central peak into two. It is not certain if the positions of the peaks change. Both measurements shown in figure 3.20 were made with the laser locked, having a linewidth FWHM $\approx$ 10 kHz (see section 3.3.9). If the laser was not in lock, the lineshape looked again as in figure 3.20b), with the linewidth just slightly increased (#22), as discussed before. This is surprising as well, but could be explained by the fact that the laser has a good stability on a 20 μs timescale.

From these measurements it is not clear what causes the oscillations. Besides interferences of the decaying cavity with the frequency scanning, several other possibilities exist: the photodiode and electronics are too slow or oscillate, but one has to note that the measurement was done with a 125 MHz photodiode, giving a time resolution of about 10 ns. The oscillations have a frequency of about 80 kHz, which corresponds to the second resonance frequency of the piezo (see section 3.3.2 and 3.3.3). This could give a hint that the piezo resonances are not

cancelled completely by the notch filter (section 3.3.5), such that the piezo still changes the cavity length with this frequency. Another possibility is that mechanical instabilities of the setup were measured. The cavity with 50 cm length is definitely very sensitive to any disturbance, but one would assume that the disturbing frequencies are lower. The intensity noise, measured in section 3.2.3, shows the relaxation oscillation peak in the range of 30 kHz to 40 kHz. The largest oscillations in figure 3.20 are about 20 % of the amplitude of the central peak, which is quite large in comparison to the rms fluctuations of about 0.4 % (20 Hz to 100 MHz) of the intensity noise. Another possibility is that the oscillations could be sidebands (servo bumps) on the laser which become visible when the laser is in lock. But in section 3.3.4 we mentioned that the servo bumps of the slow PI are between 20 kHz to 30 kHz, which is by a factor of more than 2 lower than the observed oscillations. The servo bumps of the AOMs were not measured and we assume them to be around 100 kHz (because of the modulation bandwidth of the AOMs is in that range). Therefore, the oscillations could come from the fast PI of the AOMs. The fact, that the oscillations were still visible when the laser was not locking, indicates that the oscillations are not servo bumps. Also the asymmetry and that there are multiple sidebands seems not to coincide with servo bumps[30]. These oscillations could cause heating of the atoms and in consequence larger loss rates. Therefore, we have to investigate them further.

Summarizing the measurements obtained with the new mirrors (#15 to #26, except #18), we have obtained a loss coefficient of $1 - T_3 = (0.06 \pm 0.02)\,\%$. This result was used in the calculation of the optimum incoupling mirror reflectivity, for the second order from the company (see next section). Obviously, this result is very different from the old one. The errors of the old measurement were quite high, but the new result is about $3\,\sigma$ below (c.f. #10 and #23), which is a quite deviation to be explained by measurement uncertainties. One explanation could be that the back reflections were causing problems in the old measurements and were biasing the result, even with the efforts made to avoid them. In order to have a direct comparison to the previous results, measurement #18 was done with the old mirrors and 0.2 m cavity length. We obtained, as in the old measurements, a high loss coefficient, which could mean several things.

The first implication could be that back reflections seem not to cause the observed difference in the results, since in the new measurements we had no sign of back reflections at all. Further, we know that on the outcoupling mirror which was used in the old measurement there is a small scratch. Probably, this could cause such a behavior. It was tried to align the mirror in a way that the laser beam did not hit the scratch, but maybe this was not sufficient, since the beam falls off exponentially, having a non-zero intensity beyond the beam radius. But

[30] Multiple servo bumps are possible, but in this case the gain must be very large, such that the phase would be 3π with gain larger one, which seems not to be reasonable.

we have calculated the losses from the difference of the finesse with and without glasscell which should compensate (in first order) for such an effect. Another possibility could be, that the observed interferences due to the fast scanning of the cavity led to a smaller linewidth than the one obtained for slow scanning of the cavity. With the old mirrors, and the smaller distance between them, the scanning was always fast with respect to the cavity decay time. Therefore, no interference effects played a role in the old measurement, while we can not be sure of that for the new measurement. This question should be evaluated further. Our last explanation could be that in the off-axis configuration the TEM_{01} mode was optimized to have the largest intensity. But the largest mode was used for the calculation of the finesse. Maybe this mode has a larger linewidth than the Gaussian mode and we were biased in the off-axis configurations by this effect. The linewidth was calculated by assuming a Gaussian mode, but for higher modes we did not calculate the linewidth. Therefore, we are not sure what to expect[31]. Measurement #18, which was performed on the TEM_{00} mode, suggests that the result is not affected by using a higher mode.

3.4.4 Resonator mirrors and power enhancement

In the previous section we have obtained the losses of the cavity introduced by the glasscell to be $1-T_3=(0.4 \pm 0.1)\,\%$ in the first measurement. From this knowledge the optimum reflectivity of the incoupling mirror was chosen, according to the treatment given in section 2.2.3 to maximize the power enhancement.

We decided to buy the mirrors from the German company Laser components. Since the power inside the cavity will be much higher than the damage threshold of the low power coating, which is $100\,\mathrm{kW/cm^2}$, we needed a high-power coating with specification $\geq 1\,\mathrm{MW/cm^2}$ (see discussion below). The maximum obtainable reflectivity for this (standard) coating is 99.8 %. We will use this mirror as the outcoupling mirror, and calculate the incoupling mirror, giving the maximum power enhancement from the loss coefficient. In figure 3.21a) we plot the power enhancement factor inside the glasscell (equation (2.112c), section 2.2.3) using the loss coefficient from the first measurement and the outcoupling mirror reflectivity of $R_2 = (99.85 \pm 0.05)\,\%$. The three black curves correspond to the mean and error of the loss coefficient and are labelled accordingly. The gray lines take into account the corresponding uncertainty of the outcoupling mirror. The line "A_{max}" shows the maximum possible power enhancement, obtainable from the corresponding R_1 (i.e. equation (2.112c) with $T_3 = \sqrt{R_1/R_2}$ inserted).

[31] In equation 2.42, section 2.1.2, we saw that the waist of the beam increases, but this does not mean that the linewidth increases as well. In contrary, the linewidths in figure 2.16a) seem to scale with the intensity, which is by itself an unexpected result.

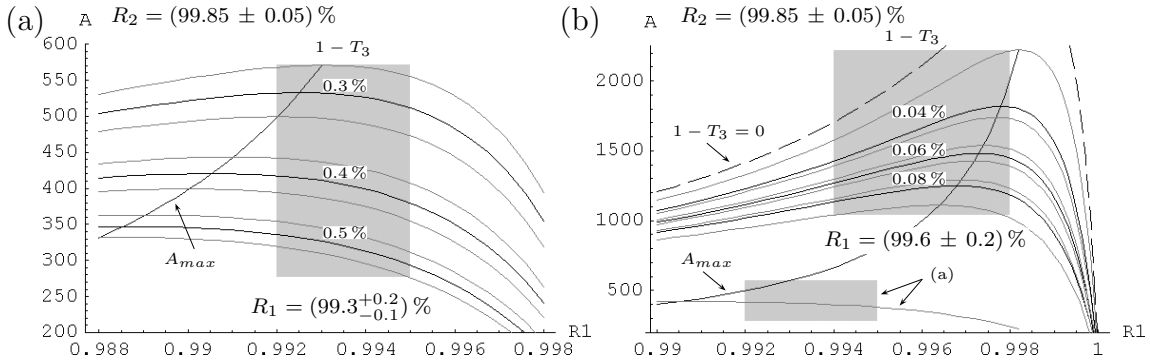

Figure 3.21: Power enhancement for a) first measurement and b) second measurement of the losses of the glasscell.

With the help of figure 3.21a) we decided to order mirrors with reflectivity of $R_1 = (99.3^{+0.2}_{-0.1})\,\%$ in a wavelength range of 1030 nm to 1080 nm. This was chosen, because the results of the losses of the glasscell, obtained from the measured curves, seemed to be more reliable than those obtained from the specification of the mirror reflectivity. Therefore, the ordered reflectivity R_1 was shifted slightly towards a higher reflectivity. The boundaries were chosen according to the capabilities of the company. The wavelength range was chosen so that the mirrors could be used for the fiberlaser wavelength of up to 1080 nm as well. This 100 W fiberlaser is at the moment used for the dipole trap.

The shaded area corresponds to the resulting power enhancement, taking the uncertainties of the mirrors into account. We obtain A=424 ± 148. As the error indicates, this result is very imprecise. Nevertheless, it should be possible to obtain a power enhancement of more than 300.

We purchased the mirrors according to this specification, but the company made a mistake and produced the coating for the wrong wavelength range of 1050 nm to 1120 nm, resulting a mirror reflectivity of R_1=$(98.58 \pm 0.06)\,\%$ at 1030 nm (obtained from a transmission curve of the company). Therefore, the incoupling mirror had to be manufactured again. This gave us the opportunity to measure the losses of the glasscell again, now with the ELS laser and the new mirrors. As described in the previous section we obtained $1-T_3$=$(0.06 \pm 0.02)\,\%$, which is much smaller than the first result. The power enhancement calculated for the first measurement, is shown in figure 3.21b). The optimum coating was chosen to be now $R_1 = (99.6 \pm 0.2)\,\%$ in a wavelength range of 1030 nm to 1080 nm. The decision was made so that the upper boundary is at the maximum possible power enhancement and the lower boundary is on the "left" side of the maximum, where the slope is not as steep as on the other side. This time the reflectivity was within the specification and is, according to a measurement of the company, $R_1 = (99.72 \pm 0.01)\,\%$ (error estimated), which is precisely what we needed. The shaded area corresponds again to the range of the power enhancement obtained

from the specification of the mirrors. We get A=1628 ± 588, i.e. A ≥ 1040.

With equation (2.114) (section 2.2.3) we obtain a finesse of F=1278 ± 462, or F ≥ 800 for the resonator. This corresponds to a linewidth of 1 MHz to 250 kHz for a resonator length of 0.2 m to 0.7 m (FSR=750 MHz to 200 MHz) respectively.

This result is much better than the power enhancement of A=600 from the lithium experiment (see section 3.4.5). But it is concerning, since the optical power inside the cavity is much higher than expected and could damage the mirrors and more problematically, the glasscell as well. In the next section, figure 3.22a), we plot the ratio of the intensity to the total power $\frac{I}{A\,P_0}$. The upper and lower thick lines correspond to the intensity at the focus of the resonator and at the glasscell walls (distance between walls L ≈ 0.17 m), respectively. The thin lines correspond to the intensity at the mirrors, which we have plotted for different distances between the mirrors (L=0.2 m ... 0.7 m). The mirror damage threshold is ≥ 1 MW/cm^2 and that of the glasscell is unknown. We see that in the region of our waists of $w_0 = 100\,\mu$m ... $400\,\mu$m, the damage threshold could be exceeded if the input power and the power enhancement is W_0=10 W and $A = 1000$ respectively (i.e. intensity/power ratio 10^2, dotted line). Therefore, we have to test how much the mirrors and the glasscell can stand and ensure that in no case this maximum is reached. Another issue to think about is the small fraction of light which is scattered from the glasscell. It can be in total quite large in intensity and we have to dump all such beams so that no damage of the other elements of the experiment can happen and that the staff can work safely.

3.4.5 Trap parameters

In the section above we have obtained the power enhancement to be A ≥ 1000. Here we want to calculate the parameters of the dipole trap formed by the resonator. These are the trap depth and the trap frequencies in radial and axial directions. The axial direction is defined to be along the connection line between the mirrors and the radial direction is perpendicular to the axial direction. The equations in this section are not derived here, but can be found for example in [MvdS99]. In table 3.9 the data concerning our atoms are listed.

If laser light interacts with an atom, the energy levels of the atom are displaced by the Stark shift

$$\Delta U = \frac{\hbar\,\Omega^2}{4\,\delta}\ , \tag{3.15}$$

with $\hbar$ the Planck constant and $\delta \equiv \omega_L - \omega_A$ the detuning of the laser frequency ω_L to the atom transition frequency ω_A. The Rabi frequency Ω is related to the

intensity of the laser I by:

$$\Omega = \gamma_A \sqrt{\frac{I}{2\,I_s}} \quad \text{with } I_s \equiv \frac{2\,\pi^2\,\hbar\,c\,\gamma_A}{3\,\lambda_A^3}\ . \tag{3.16}$$

The saturation intensity I_s, the wavelength λ_A and the linewidth γ_A of the transition of the atom are used.

We see that the Stark shift depends on the intensity. Therefore, if the intensity is space-dependent, the Stark shift is space-dependent, too. We know that a conservative force F is related to a potential $F = -\nabla U_{pot}$, with U_{pot} the potential. Since the Stark shift is nothing else than a potential difference, we immediately understand that the atoms will be accelerated by this force. The force and the potential created by the laser are called dipole force and dipole potential $U_{dip} \equiv \Delta U$:

$$U_{dip} = \frac{\hbar\,\Omega^2}{4\,\delta} = \frac{\hbar}{4\,\delta}\,\gamma_A^2 \frac{I}{2\,I_s} = \frac{\hbar}{4\,\delta}\,\gamma_A^2 \frac{I}{2}\,\frac{3\,\lambda_A^3}{2\,\pi^2\,\hbar\,c\,\gamma_A} = \frac{3\,\gamma_A\,\lambda_A^3}{16\,\pi^2\,\delta\,c}\,I\ . \tag{3.17}$$

The name dipole potential comes from an alternative picture: the laser light induces a dipole moment on the atom and the induced dipole moment then interacts with the light in such a way that the atom experiences a force. The sign of the potential can be chosen by the detuning δ. For red-detuned light ($\delta < 0$) the induced dipole moment can follow the direction of the laser electric field and forces the atoms towards the intensity maximum. For blue-detuned light ($\delta > 0$) the induced dipole moments direction lags behind the electric field direction by a phase of π, resulting in a a force towards the intensity minimum. From equation (3.17) one might assume that for small detuning the dipole force becomes very large which is favorable. But for small detuning the probability of absorbtion becomes larger, leading to unwanted heating. Therefore, there exists an optimum value of the detuning, which is usually far-detuned from the transition of the atom. In our case we use laser light of λ_L=1030 nm.

The intensity in the standing wave of a Fabry-Perot interferometer (FPI) is derived in equation (2.107), section 2.2.3[32], and we see that, on resonance and in the waist of the resonator, it scales with $A\,I_0\,\cos^2[k\,z]$ along the axis. The power enhancement A was defined in section 2.2.3 and the peak intensity of a Gaussian beam is related by equation (2.27), section 2.1.1, to the laser power P_0:

$$I_0 = \frac{2\,P_0}{\pi\,w_0^2}\ . \tag{3.18}$$

In radial direction the intensity falls off like the Gaussian beam $A\,I_0\,\exp[-2\rho^2/w_0^2]$, which is found in equation (2.25), section 2.1.1.

[32]The δ here is different to the one defined in section 2.2.3.

In order to obtain the axial and radial trap frequencies we perform a Taylor expansion of the intensity profiles in axial and radial direction:

$$\begin{aligned} U_{axial} &= U_0 \cos^2\Big[k\,z\Big] = U_0\left(1 - k^2\,z^2 + \mathcal{O}[k\,z]^4\right) \\ U_{radial} &= U_0 \exp\Big[-\frac{\rho^2}{2\,w_0^2}\Big] = U_0\left(1 - 2\frac{\rho^2}{w_0^2} + \mathcal{O}[\frac{\rho}{w_0}]^4\right) \\ \text{with} \qquad U_0 &\equiv \frac{3\,\gamma_A\,\lambda_A^3\,A\,P_0}{8\,\pi^3\,\delta\,c\,w_0^2}\ , \end{aligned} \tag{3.19}$$

where we have defined the potential maximum U_0 using equation (3.17) and (3.18). The constant part of the potential can be neglected since it cancels when the gradient is taken to calculate the force. This corresponds to a redefinition of the energy scale. Assuming small deviations of the atoms from the trap center we can approximate the potential by a harmonic potential $U = \frac{1}{2}\,m\,\omega^2\big|\vec{r}\big|^2$ and obtain the axial and radial trapping frequencies:

$$\begin{aligned} \omega_{axial} &= k\sqrt{-\frac{2\,U_0}{m}} = \frac{2\,\pi}{\lambda_L}\sqrt{-\frac{2\,U_0}{m}} \\ \omega_{radial} &= \frac{2}{w_0}\sqrt{-\frac{U_0}{m}}\ . \end{aligned} \tag{3.20}$$

We see that only with red-detuned light atoms can be trapped.

The data of our atoms are summarized in table 3.9, where we give as well an example of the trap parameter for an input power of 10 W into the resonator and a power enhancement of A=1000. We see that a remarkable trapping depth of more than 2.8 mK is reached for all of our species.

Table 3.9: Data of our atoms and of the resulting dipole potential for λ_L=1030 nm, P_0=10 W, A=1000 and $w_0 = 300\,\mu$m.

atom	m	λ_A	γ_A	U_{dip}	ω_{axial}	ω_{radial}
	AMU[a]	nm	2π MHz	mK	MHz	kHz
^{6}Li	6	671	6	-3.8	3.1	2.4
^{40}K	40	767	6	-8.8	1.9	1.4
^{87}Sr	87	461	32	-2.8	0.7	0.6

[a] AMU=1.660 538 86$\times 10^{-27}$ kg

In figure 3.22 we plot the resulting trap parameter as a function of the beam waist. We have normalized them by the laser power. The plotted intensity (observe the logarithmic scale) in figure 3.22a) is larger than the damage threshold specified for the mirrors, which is $\geq 1\,\mathrm{MW/cm^2}$ (dotted line for $A\,P_0 = 10^4$). The

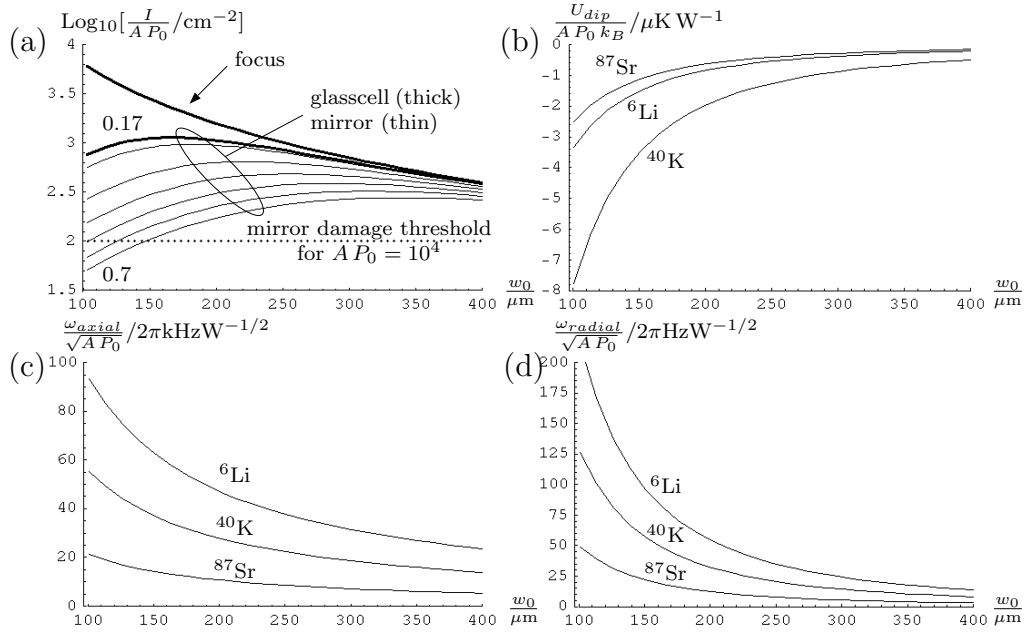

Figure 3.22: a) Intensity (logarithmic scale) in focus, on glasscell (L=0.17 m) and on mirrors for different distances of mirrors from L=0.2 m to L=0.7 m in steps of 0.1 m. b) Trap depth, c) axial trap frequencies and d) radial trap frequencies. All normalized by total power.

maximum power which can stand the glasscell is unknown. Probably, we have to reduce the input power in order not to harm one of these components (see discussion at the end of section 3.4.4). The potential depth shown in figure 3.22b) for ^{40}K is by more than two times deeper than that of ^{6}Li and ^{87}Sr, which experience approximately the same potential depth. The axial trap frequencies in figure 3.22c) can become very large, in the range of MHz (the frequencies scale with the square root of the power, c.f. equations (3.19) and (3.20)), which could be a problem concerning the intensity fluctuations of the resonator laser (see section 3.2.3). In figure 3.22d) the radial trap frequencies are plotted, which are by a factor of 1000 smaller than the axial trap frequencies.

In order to put these results into perspective, we compare them with the ones obtained with the resonator used in the lithium experiment which is described in [Joc04, MJM$^+$01]. There a 2 W laser is used, which has a power enhancement of A=4×150=600[33]. This means that the power in the maxima of the standing wave is 600×0.8×2 W=960 W, with 80 % power coupled into the cavity. The waist of the resonator is 160 μm, which gives a maximum intensity of about 2.4 MW/cm^2, obtained from equation (2.27). The trap depth for lithium becomes, with equation (3.19), 1.3 mK[34]. We know that about 8×10^6 atoms of

[33]The factor 4 comes from the interference of the retroreflected beam, see section 2.2.3.

[34]In [MJM$^+$01] an older configuration is cited with a 1.2 W laser and a power enhancement

^{6}Li can be loaded into the resonator. In the new setup we want to achieve at least the same trap depth but with a waist which is two times larger. This will increase the trapping volume and therefore the number of trapped atoms considerably. The larger waist, together with the same power enhancement, requires at least 4 times more laser power which is about 7 W on the input of the resonator.

Our trap depth is by a factor of two better than in the lithium experiment. Together with the large volume obtained from the large waist of the resonator we can expect to trap a large number of atoms. Ramping down the intensity will allow evaporative cooling already in the resonator stage. When the atoms are loaded afterwards into a focussed-beam dipole trap, they will be cold enough in order to obtain a high transfer fraction.

3.4.6 Resonator waist and mode matching lenses

In a procedure similar to the one for choosing the incoupling lens for the reference cavity (see section 3.3.7), we calculated the necessary lenses for mode matching into the resonator (see section 2.2.4). The difference for the resonator is that the position of the focus has to be exactly at the position of the atoms. This requires using a second lens, i.e. a telescope for mode matching. We have to calculate the parameters of the lenses for all the possible resonator configurations, since we want to be able to adjust the waist of the resonator arbitrarily. We plot the result in figure 3.23 and for specific resonator waists we give the parameter in table 3.11, with the lenses listed in table 3.10.

The resonator was assumed to be symmetric (z=L/2) and the laser waist was assumed to be w_0=343 μm, as measured in section 3.2.1. The propagation distance from the laser to the focus of the resonator is z_{FPI}=1810 mm, which was determined from the available space on the experimental table, which could be occasionally changed in the future. The distances of the mirrors can be varied from 0.2 m to 0.7 m, which is given by the size of the glasscell and breadboards.

We have to consider the effect of the glasscell on the resonator. It introduces a different path length for each half round trip δ defined in equation (2.61). It is $\delta = k\,z = \frac{\omega}{c}$(L+2d(n-1)), with d=6.074 mm (=5 mm/sin[α_B]) the thickness and n=1.4496 the refractive index of the glass. Since δ is larger than without the glasscell, the free spectral range, defined in equation (2.79), becomes smaller:

$$\mathrm{FSR} = \frac{c}{2\mathrm{L}(1+\frac{2d}{\mathrm{L}}(n-1))} = \frac{c}{2\mathrm{L'}} \quad \text{with L'}\equiv\mathrm{L}+2\mathrm{d(n\text{-}1)}\ . \tag{3.21}$$

We defined the effective cavity length L', which we have to use for the transversal modes as well. The cavity length seems to be increased by 2d(n-1)=5.462 mm.

of A=4×130, giving 0.8 mK trap depth.

In order to obtain the waist of the resonator, we can write down the ABCD matrices (table 2.2) for one round trip of the beam inside the resonator. With equation (2.122) we can calculate the complex radius of curvature q_{rt}, which does not change after one round trip. From this we obtain the waist of the resonator with the glasscell inserted. But this is not necessary, since we know the effect of a glassplate to a Gaussian beam, as discussed in section 2.1.3. Equation (2.53) showed that, if the beam passes through a glassplate, it behaves as if the propagation distance was reduced by $\Delta z = d(1-\frac{1}{n})$, which is $\Delta z = 1.88\,\text{mm}$ for the glasscell. The waist of the resonator is obtained from the fact that the radius of curvature (equation (2.26c)) of the mirror is equal to that of the Gaussian beam:

$$\begin{aligned} r[z-\Delta z] &= (z-\Delta z)\Big(1+\frac{z_0^2}{(z-\Delta z)^2}\Big) \quad \text{with } \Delta z \equiv d\Big(1-\frac{1}{n}\Big) \\ z_0 &\equiv \frac{\pi\, w_{FPI}^2}{\lambda} = \big|z-\Delta z\big|\sqrt{\frac{r}{z-\Delta z}-1} \qquad (3.22) \\ \Rightarrow \quad w_{FPI} &= \sqrt{\frac{\lambda}{\pi}\sqrt{(z-\Delta z)(r-z+\Delta z)}}\,. \end{aligned}$$

Without the glasscell, i.e. for $\Delta z = 0$, this equation is the same as (2.119). With the glasscell the waist can be either increased or decreased, depending on the fact whether z is larger or smaller than the confocal length ($2z = r + \Delta z$). Comparison between this result and equation (2.119) shows that we could have replaced the cavity length by $L \mapsto L'' \equiv L - 2\Delta z$ and would have obtained the same result. This effectively shows a reduction of the cavity length, which seems to be in contradiction with the increased L' defined above. So far we have not found a good explanation for this. With these considerations, the waist of the resonator w_{FPI} is calculated. The result is plotted in figure 3.23 and the waists, marked as dots in figure 3.23a) and drawn as lines in figure 3.23b), are listed in table 3.11.

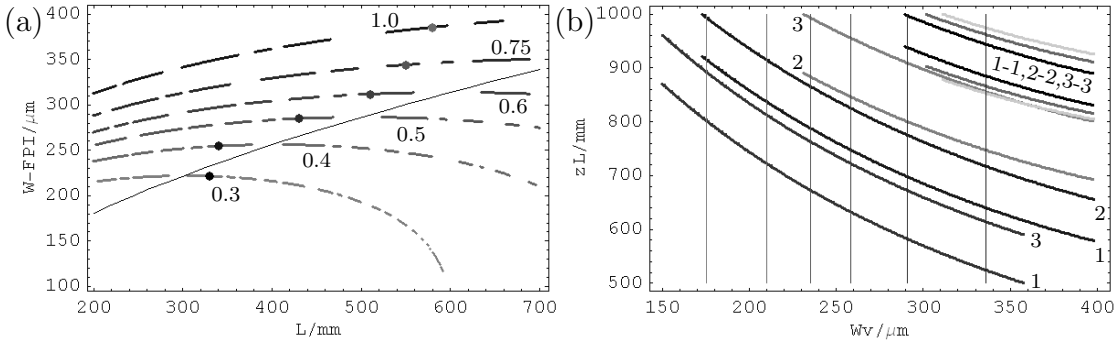

Figure 3.23: a) Resonator waist for different radius of curvature given in m. b) Incoupling lens positions. Numbers refer to lenses in table 3.10.

The resonator waist is plotted as a function of the real distance between the mirrors L. The curved lines correspond to different radii of curvature of the

mirrors, which are indicated by the numbers in meter. We plotted the lines with gaps, because we have only drawn them for the case that no TEM_{mn} until m+n=10 falls within a range of ± 10 MHz from the Gaussian (TEM_{00}) mode. The condition of this 10 MHz minimum spacing comes from the fact that the resonator linewidth is in the range of a few MHz (see section 3.4.4). The minimum spacings Δf and the mode numbers (m+n, in column "#"), which are closest to the Gaussian mode, are included in table 3.11.

In order to design the telescope, the virtual focus parameters for the incoupling mirror were calculated with equation (2.121), section 2.2.4, and are listed in table 3.10. The lenses in table 3.10 are used for the telescope. The focal length for λ=1030 nm was calculated in the same way as were the lenses for the reference cavity, section 3.3.7. No analytical solution for the positions of the lenses of the

Table 3.10: Lenses for Resonator.

#	f_{nom} mm	r mm	f_{1030} mm
1	25	12.9	28.7
2	40	20.6	45.8
3	50	25.8	57.3

telescope could be obtained. Therefore, the solution was calculated numerically. Figure 3.23b) shows the result. For certain waists it is given as well in table 3.11. There the position of the first lens was set fixed and the second lens was placed in such a way that the resulting focus overlaps with the virtual focus. The virtual waist of the focus is plotted as the x-axis for each datapoint. From figure 3.23b) one can immediately get the position of the lenses in order to obtain a certain virtual waist w_v. The lines correspond to the waists listed in table 3.11, where the corresponding positions z_{Li} and beam radius w_{Li} of the lenses are given. The column "L#" contains the number labelling of the lens from table 3.10.

We have presented in this section the calculations of the positions and focal lengths of the mode matching lenses for the resonator. In the measurements described earlier, different lenses and positions were used, where mostly no optimization of the coupling efficiency was done. Nevertheless, a coupling efficiency of about 80 %, was measured in section 3.4.3. In the final setup the calculated lenses will be used and the efficiency will be optimized by maximizing the transmitted intensity, which should result in an even better coupling efficiency.

In previous sections we explained the geometry and the resulting properties of the resonator. As every Fabry-Perot cavity it has to be on resonance with the laser light in order to work optimally. The laser linewidth is stabilized to a linewidth of about 10 kHz, as described in section 3.3. The resonator itself has

Table 3.11: Parameters used for mode matching lenses of resonator.

w_{FPI} μm	r mm	L mm	Δf MHz	#	z_v mm	w_v μm	z_{L1} mm	w_{L1} μm	z_{L2} mm	w_{L2} μm	L#
221	300	340	34	2	1792	175	904	930	982	1528	1-2
							791	830	881	1714	1-3
254	400	340	38	2	1806	210	832	866	910	1412	1-2
							717	767	808	1570	1-3
285	500	430	28	2	1804	235	783	824	861	1338	1-2
							668	725	759	1479	1-3
							879	908	988	1163	2-3
312	600	510	26	2	1805	258	744	790	822	1278	1-2
							629	692	719	1406	1-3
							843	875	952	1116	2-3
344	750	550	22	5	1817	291	940	962	999	967	1-1
							699	751	776	1210	1-2
							583	654	673	1323	1-3
							802	840	911	1063	2-3
385	1000	580	23	8	1836	336	896	923	955	924	1-1
							649	709	726	1135	1-2
							532	613	621	1233	1-3
							877	906	973	907	2-2
							757	801	866	1006	2-3
							864	895	986	896	3-3

to be stabilized to the laser frequency by means of the Hänsch-Couillaud locking scheme [HC80], which is not finished at the moment. The advantage of using this scheme, in comparison to the Pound-Drever-Hall scheme [DHK83], is that no sidebands have to be generated. They would disturb the interferences in the resonator. The glasscell acts as the polarizer needed for the Hänsch-Couillaud scheme. The ellipticity of the reflected light is obtained with the difference signal of two photodiodes detecting the difference of polarization after a quarter wave-plate and a polarizing beamsplitter. A detuning of the resonator from resonance introduces a phase shift of the light reflected from the cavity versus the light reflected on the input mirror. This causes the reflected light to become elliptical. On resonance both components are in phase, causing the reflected light to become linear. This can be seen in section 2.2.1, equation (2.69). An error signal was obtained, but the signal to noise was not good enough for locking the resonator so far. This has to be done in the future.

We have shown in the experimental part how a resonator enhanced optical dipole trap is built. We have implemented a linewidth reduction of the resonator laser and obtained a linewidth of 10 kHz. The losses due to the glasscell were measured with which the optimum reflectivity of the incoupling mirror could be chosen. We expect a power enhancement of $A \geq 1000$, and a very deep trapping potential of more than 2.8 mK. This is a very good result, but we have to be careful, since the intensity exceeds the mirror specifications. We measured the intensity noise of the laser to be larger than the specification and the requirements for our experiment, which could cause heating of the atoms inside the trap. The resonator is not finished yet, therefore we could not measure heating rates so far.

Chapter 4

Summary and outlook

In this thesis the design of a resonator enhanced optical dipole trap was described. We discussed theoretical and practical issues concerning Fabry-Perot type cavities. The two main features of such a setup, namely the frequency selectivity and the power enhancement, were considered in detail, allowing for the optimum design. In the experimental part, the ELS laser was characterized and its linewidth reduction was described. This is necessary to ensure that the light is coherent during the cavity decay time. A linewidth of 10 kHz relative to the cavity was measured. With the measurement of the glasscell losses, the coating of the resonator mirrors could be adjusted for maximum power enhancement, leading to a theoretically possible power enhancement factor of $A \geq 1000$ and resulting in a theoretical trap depth of $U_{dip} \geq 2.8\,\mathrm{mK}$.

The requirements for the laser linewidth are fulfilled and the obtained power enhancement factor is larger than expected. Therefore, the intensity within the resonator could reach the damage threshold of the mirrors and we have to be very careful not to harm the glasscell. The noise stability of the laser might not be sufficient and could cause unwanted heating of the atoms. Measurement of loss rates or other parameters of the resonator could not be performed, since the resonator has not been entirely built so far.

For the future the new reference cavity must be built. With this the signal-to-noise of the laser linewidth error signal will be increased, which will result in a better performance of the AOMs and an even narrower linewidth. The resonator setup and the locking of the resonator to the laser must be finished. An intensity stabilization scheme will be applied by controlling the rf power of the AOMs. This shall reduce the intensity noise of the laser and give the opportunity to ramp down the intensity of the light coupled into the cavity by several orders of magnitude, allowing evaporative cooling already during the resonator stage.

The achieved results look very promising. The obtainable trap depth will allow a large transfer fraction of atoms from the MOT into the resonator. Ramping down the laser intensity will decrease the temperature already at this early stage. By doing this a large fraction of cold atoms can be transferred to the final scientific traps. This will be the starting point at which, with an ultracold sample of high atom number, very exciting new experiments can be performed. Different kinds of fermionic, bosonic, fermi-bosonic, homo- and heteronuclear mixtures will be trapped simultaneously in an all-optical way. This allows to use Feshbach resonances and sympathetic cooling of the species. The BEC-BCS crossover region for these mixtures can be explored, molecules formed and BEC of heteronuclear molecules achieved. In the next step loading into lattices will reduce many body losses and ground state molecules could be generated.

In the current state of our experiment, we use for the dipole trap a 100 W fiberlaser in a crossed configuration, as is shown in figure 3.13. With the present setup we could already reach degeneracy for ^{6}Li molecules, see figure 4.1. Sympathetic cooling of ^{40}K and ^{39}K with ^{6}Li in the dipole trap works well. Features of enhanced loss rates of the ^{6}Li-^{40}K mixture were observed at certain magnetic fields. Measurements are currently under way to improve these results. The future is very promising.

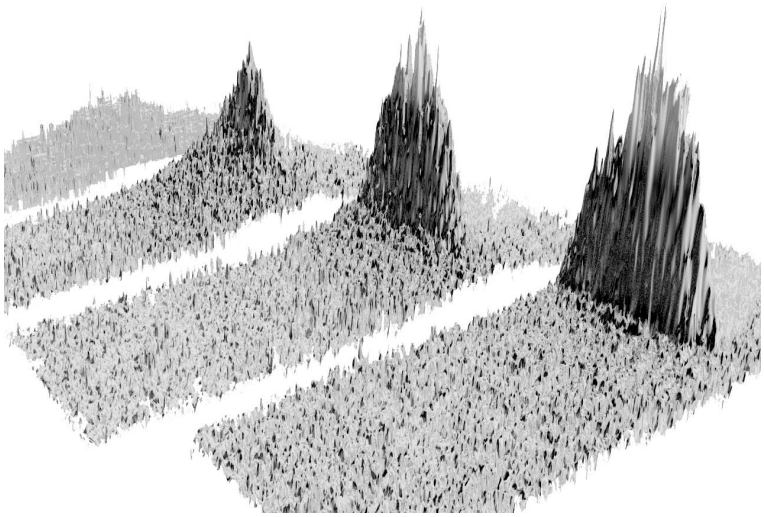

Figure 4.1: First molecular $^6Li_2$ BEC at the FeLiKx experiment.

Chapter 5

Acknowledgements

I am very thankful to many people, having helped to answer questions, having lend equipment or having been present just for a relaxed talk. So many that I will not be able to mention all of them.

First of all, I want to thank Rudi Grimm for giving me the opportunity to work in such a great group and for having supervised this thesis. It was a big challenge to work on the FeliKx experiment, but it was also a fantastic time in which I could gain insight into exciting new physics. Rudi gave me the opportunity to take part in the DPG and ICAP conferences, in the Greenhorn meeting and in the predoctoral school in Les Houches. All of them enlarged my view of the field and I gained important background knowledge. He was patient with the finishing of this thesis, allowing me to do it in my way, even if it may not reflect his preferred appearance. I am looking forward to stay in the FeLiKx team and to do research on one of the frontiers of modern science.

Many thanks to Florian Schreck who always had an open ear for questions and discussions. He gave me the freedom to take many decisions and was a great help with difficulties, having a clear and intuitive way of solving problems. He was very kind to proofread this thesis, which took him a whole bunch of time that he could have definitely spent on much more important subjects.

Clarice Aiello helped a lot to improve the English of this thesis. I hope I did not upset her too much with my bad English. Also many thanks to Bettina Fischer, my external reader, who was a great friend when the motivation was low.

It was always a great pleasure to talk to the other people in the FeLiKx experiment. With Gabriel Kerner I enjoyed sharing the office and he enlarged my sight of things in many aspects - even if I don't share always his opinion. Eric Wille knows everything about the experiment and he answered many technical questions. Frederik Spiegelhalder always reminded me when its lunch time.

Devang Naik I'm looking forward to work with you in the lab and greetings to Raquel Chulia-Jordan. Gerhard Hendl helped with all the electronics. Either physics or non physics discussions with all of you were very helpful in many respects. Also I want to mention the other members of our research group, who helped with particular problems and provided us with many cakes and parties on the weekends. Christine Götsch-Obmascher was always the first contact person for administrative questions.

I enjoyed a lot the numerous discussions about cavities and laser locking that I had with the members of the Blatt group: Gerhard Kirchmair, Jan Benhelm and Christian Roos helped with advice and provided me with unavailable papers and new ideas.

The staff in the IQOQI building deserve a great thank you. The secretaries, Elisabeth Huck and Doris Corona, for their help with any question, Thomas Mayr for solving computer problems, Michael Jäger for helping ordering things and Mr. Knabl for keeping the house working and well in order. Without the people in the mechanical workshop, Stefan Haslwanter and Andreas Strasser, not very much of our experiment would have come to reality. They know how to machine difficult parts, like the oven, and give excellent advise on any practical issue.

I thank all my friends for interrupting me on the weekends and reminding me that there is a life besides physics. My family supported my decision of starting to study after some years of working. They give me the love needed in many hard times.

Finally, I have to express my hope that there are not too many errors in this thesis and that I could give the reader some useful information. An up-to-date version of this thesis will be available on the ultracold homepage (`http://www.ultracold.at`), to which I will add notes and comments at the very end, in case there are important updates. If you find some errors or need additional information, don't hesitate to contact me via the provided email address on the same homepage.

Chapter 6

Appendix

6.1 Gouy phase difference

Here we will rewrite the Gouy phase difference $\Delta\zeta \equiv \zeta(z_2) - \zeta(z_1)$, stated in equation (2.130) section 2.2.5, which leads to the result (2.131). The Gouy phase at the mirror positions z_i from equation (2.26d) are $\zeta(z_i) \equiv \arctan\left[\frac{z_i}{z_0}\right]$. Here the sign convention is, that the position of the incoupling mirror has a negative sign when it is to the left of the focus of a beam propagating towards the right.

Inserting equations (2.128) into the definition of $\zeta(z_i)$ given in equation (2.26d) yields:

$$\begin{aligned} \tan[\zeta(z_1)] &= \frac{z_1}{z_0} = -\frac{(1-g_1)g_2}{\sqrt{g_1\, g_2(1-g_1\, g_2)}} \\ \tan[\zeta(z_2)] &= \frac{z_2}{z_0} = \frac{(1-g_2)g_1}{\sqrt{g_1\, g_2(1-g_1\, g_2)}}\ . \end{aligned} \tag{6.1}$$

The functions arctan and arccos are related by:

$$\tan^2[x] = \frac{\sin^2[x]}{\cos^2[x]} = \frac{1-\cos^2[x]}{\cos^2[x]} = \frac{1}{\cos^2[x]} - 1 \quad \Rightarrow \quad \cos[x] = \pm\frac{1}{\sqrt{1+\tan^2[x]}}$$

$$z \equiv \tan[x] \overset{\cos[x]}{\downarrow} \tan\Big[\arccos\Big[\pm\frac{1}{\sqrt{1+\tan^2[x]}}\Big]\Big] \overset{\text{def. of } z}{\downarrow} \tan\Big[\arccos\Big[\pm\frac{1}{\sqrt{1+z^2}}\Big]\Big]$$

$$\Rightarrow \quad \arctan[z] = \pm\arccos\Big[\frac{1}{\sqrt{1+z^2}}\Big]\ . \tag{6.2}$$

The plus and minus sign correspond to the sign of z. The tangent of a sum can

be written in the following way:

$$
\begin{aligned}
&\boldsymbol{e}^{i(x\pm y)} = \boldsymbol{e}^{ix}\boldsymbol{e}^{\pm iy} \\
&\Rightarrow \quad \cos[x \pm y] + i\sin[x \pm y] = (\cos[x] + i\sin[x])(\cos[y] \pm i\sin[y]) \\
&\qquad = (\cos[x]\cos[y] \mp \sin[x]\sin[y]) + i(\sin[x]\cos[y] \pm \cos[x]\sin[y]) \qquad (6.3a) \\
&\Rightarrow \quad \tan[x \pm y] = \frac{\sin[x]\cos[y] \pm \cos[x]\sin[y]}{\cos[x]\cos[y] \mp \sin[x]\sin[y]} = \frac{\tan[x] \pm \tan[y]}{1 \mp \tan[x]\tan[y]} \; . \qquad (6.3b)
\end{aligned}
$$

We define $a \equiv \tan[x]$ and $b \equiv \tan[y]$ and insert them into the previous relation:

$$
\begin{aligned}
\tan[x \pm y] &= \frac{a \pm b}{1 \mp a\,b} \\
\Rightarrow \quad x \pm y = \arctan[a] \pm \arctan[b] &= \arctan\Big[\frac{a \pm b}{1 \mp a\,b}\Big] \\
&\overset{\arccos}{=} \pm \arccos\Big[\frac{1}{\sqrt{1 + (\frac{a \pm b}{1 \mp a\,b})^2}}\Big] \; .
\end{aligned} \qquad (6.4)
$$

With $a \equiv \frac{z_1}{z_0}$, $b \equiv \frac{z_2}{z_0}$ and (6.1) we obtain $\Delta\zeta$ [Dem96, HW92, Sie86]:

$$
\begin{aligned}
\frac{a-b}{1+a\,b} &= \frac{-(g_2 - g_1\,g_2) - (g_1 - g_1\,g_2)}{\sqrt{g_1\,g_2(1-g_1\,g_2)}} \frac{g_1\,g_2(1-g_1\,g_2)}{g_1\,g_2(1-g_1\,g_2) - (g_2 - g_1\,g_2)(g_1 - g_1\,g_2)} \\
&= \frac{(2g_1\,g_2 - g_2 - g_1)\sqrt{g_1\,g_2(1-g_1\,g_2)}}{g_1\,g_2(1-g_1\,g_2) - g_1\,g_2(1 - g_1 - g_2 + g_1\,g_2)} \\
&= \frac{(2g_1\,g_2 - g_2 - g_1)\sqrt{g_1\,g_2(1-g_1\,g_2)}}{-g_1\,g_2(-g_1 - g_2 + 2g_1\,g_2)} = \sqrt{\frac{1-g_1\,g_2}{g_1\,g_2}} \qquad \Rightarrow \\
\frac{1}{1 + (\frac{a-b}{1+a\,b})^2} &= \frac{g_1\,g_2}{g_1\,g_2 + (1 - g_1\,g_2)} = g_1\,g_2
\end{aligned}
$$

$$
\Rightarrow \qquad \Delta\zeta \equiv \zeta(z_2) - \zeta(z_1) = \arccos\Big[\pm\sqrt{g_1\,g_2}\Big] \; . \qquad (6.5)
$$

The positive sign is applied for the upper right quadrant of the q_i's (q_1 and $q_2 \geq 0$), whereas the negative sign for the lower left quadrant[1].

6.2 Derivation of Brewster's angle

In section 3.4.1, equation (3.7) for the Brewster's angle was given and here we will verify this result. The Fresnel formulas for calculating the reflectivity of a

[1] In [Sie86] the ± sign is included, while in [HW92, Sie86] it is not.

boundary between two different media (see for example [EFK+93]) are:

$$R_p = \frac{\tan^2[\alpha_1 - \alpha_2]}{\tan^2[\alpha_1 + \alpha_2]} \tag{6.6a}$$

$$R_s = \frac{\sin^2[\alpha_1 - \alpha_2]}{\sin^2[\alpha_1 + \alpha_2]} \ , \tag{6.6b}$$

for p- and s-polarization respectively. The angles α_i of the beam in medium $i = \{1, 2\}$ are measured relative to a line perpendicular to the surface of the boundary. The angle after the boundary α_2 is related to the incidence angle α_1 by the Snellius law:

$$n_1 \ \sin \alpha_1 = n_2 \ \sin \alpha_2 \ , \tag{6.7}$$

with n_i the refractive index of the medium i. The Fresnel equation for the p-polarization does not become zero for $\alpha_1 - \alpha_2 = 0$, since together with the Snellius law this is only fulfilled for $\alpha_1 = \alpha_2 = 0$, which gives by taking the limit:

$$R_p(0) = \lim_{\alpha_1 \to 0} R_p(\alpha_1) = \frac{(n_1 - n_2)^2}{(n_1 + n_2)^2} \ . \tag{6.8}$$

But if the denominator in equation (6.6b) becomes infinite the reflection for p-polarized light becomes zero, since the numerator is finite. This case fulfills the condition:

$$\alpha_B + \alpha'_B \stackrel{!}{=} \frac{\pi}{2} \ , \tag{6.9}$$

where we have introduced the Brewster's angle α_B, and α'_B as the angle of the beam inside the medium. The angle α'_B is related to the Brewster's angle by Snellius law, which we insert into the condition:

$$\alpha_B + \arcsin\left[\frac{n_1}{n_2} \sin \alpha_B\right] \stackrel{!}{=} \frac{\pi}{2} \ . \tag{6.10}$$

Taking the cosine and using equation (6.3a), derived in section 6.1, we obtain:

$$\begin{aligned}
\cos\left[\frac{\pi}{2}\right] = 0 &= \cos\left[\alpha_B + \arcsin\left[\frac{n_1}{n_2} \sin \alpha_B\right]\right] \\
&= \cos \alpha_B \ \cos\left[\arcsin\left[\frac{n_1}{n_2} \sin \alpha_B\right]\right] - \sin \alpha_B \ \sin\left[\arcsin\left[\frac{n_1}{n_2} \sin \alpha_B\right]\right] \\
&= \sqrt{1 - \sin^2 \alpha_B} \sqrt{1 - \frac{n_1^2}{n_2^2} \sin^2 \alpha_B} - \sin \alpha_B \frac{n_1}{n_2} \sin \alpha_B \\
\frac{n_1^2}{n_2^2} \sin^4 \alpha_B &= (1 - \sin^2 \alpha_B)(1 - \frac{n_1^2}{n_2^2} \sin^2 \alpha_B) = 1 - \sin^2 \alpha_B (1 + \frac{n_1^2}{n_2^2}) + \frac{n_1^2}{n_2^2} \sin^4 \alpha_B \\
\sin^2 \alpha_B &= \frac{1}{1 + \frac{n_1^2}{n_2^2}} \ .
\end{aligned} \tag{6.11}$$

With the help of the relation between tangent and sine this yields:

$$\tan^2\alpha_B = \frac{\sin^2\alpha_B}{\cos^2\alpha_B} = \frac{\sin^2\alpha_B}{1-\sin^2\alpha_B} = \frac{1}{\frac{1}{\sin^2\alpha_B}-1} \overset{(6.11)}{\downarrow} = \frac{1}{1+\frac{n_1^2}{n_2^2}-1} = \frac{n_2^2}{n_1^2}$$

$$\Rightarrow \quad \tan\alpha_B = \frac{n_2}{n_1} \ . \tag{6.12}$$

This is our expression for the Brewster's angle, stated in equation (3.7).

6.3 Fourier transform and convolution

This section summarizes the Fourier transform and convolution which are used in the main text for calculating the linewidth of the laser (section 2.2.2) and for the noise considerations (section 2.4.2). The treatment here can be found in many books of mathematics with different notations and definitions. Therefore, we collect the formulas used in this thesis, following mainly [LP98].

The Fourier transform $F(\omega) \equiv FT[f(t)]$ of a function $f(t)$ is defined as:

$$F(\omega) \equiv FT[f(t)] \equiv \frac{1}{\sqrt{2\pi}} \int_{-\infty}^{\infty} f(t)\, \boldsymbol{e}^{-i\,\omega\,t} dt \ , \tag{6.13}$$

and the inverse Fourier transform is:

$$f(t) \equiv FT^{-1}[F(\omega)] \equiv \frac{1}{\sqrt{2\pi}} \int_{-\infty}^{\infty} F(\omega)\, \boldsymbol{e}^{+i\,\omega\,t}\, d\omega \ . \tag{6.14}$$

The Fourier transform maps the function from one space to another. In the previous case, it maps from the time space into the frequency space. This is very useful when one knows the time evolution of, for example, an electronic signal and one wants to know which frequencies are related to this signal, or vice versa[2]. Another application of the Fourier transform is the solution of differential equations or to recover filtered signals, for example when the bandwidth of a detector affects a measurement. Mathematically, this is called the convolution $f(t) * g(t)$ of the two functions $f(t)$ and $g(t)$ and is defined as:

$$f(t) * g(t) \equiv \int_{-\infty}^{\infty} f(t')g(t-t')\, dt' \ . \tag{6.15}$$

[2]The Fourier transform of a measured signal can be evaluated numerically with the method of fast Fourier transform (FFT) which is implemented in many mathematics programs.

If both of these functions have a Fourier transform $F(\omega) \equiv FT[f(t)]$ and $G(\omega) \equiv FT[g(t)]$, we can write:

$$F(\omega)\,G(\omega) = \frac{1}{2\pi}\int_{-\infty}^{\infty} dt' \int_{-\infty}^{\infty} dt\, f(t')\,g(t)\,\boldsymbol{e}^{-i\,\omega(t+t')}\ .$$

Substituting $\tau \equiv t + t'$ for t:

$$\begin{aligned} F(\omega)\,G(\omega) &= \frac{1}{2\pi}\int_{-\infty}^{\infty} dt' \int_{-\infty}^{\infty} d\tau\, f(t')\,g(\tau - t')\,\boldsymbol{e}^{-i\,\omega\tau} \\ &= \frac{1}{2\pi}\int_{-\infty}^{\infty} d\tau\, f(\tau) * g(\tau)\,\boldsymbol{e}^{-i\,\omega\tau} \\ \Rightarrow \quad FT\big[f(t) * g(t)\big] &= \sqrt{2\pi}\,FT[f(t)]\,FT[g(t)]\ . \end{aligned} \tag{6.16}$$

In the line before the last line, the integrals were exchanged and the definition of the convolution was inserted. In the last line the variable was changed to t again. We see that the Fourier transform of the convolution of two functions is the product of the Fourier transforms of the individual functions. This is known as the convolution theorem. Therefore, when we know one function, e.g. the transfer function of the detector $g(t)$, one can recover the other function by inverse Fourier transform of the convolution of both signals[3]:

$$f(t) = \frac{1}{\sqrt{2\pi}}\,FT^{-1}\Big[FT\big[f(t) * g(t)\big]/FT[g(t)]\Big]\ . \tag{6.17}$$

The cross-correlation $f(t) \star g(t)$ of the two functions $f(t)$ and $g(t)$ is defined as:

$$\begin{aligned} f(t) \star g(t) \equiv f^*(-t) * g(t) &= \int_{-\infty}^{\infty} f^*(-t')\,g(t-t')\,dt' \\ &= -\int_{\infty}^{-\infty} f^*(t'')\,g(t+t'')\,dt'' \quad \text{with } t'' \equiv -t' \\ &= \int_{-\infty}^{\infty} f^*(t')\,g(t+t')\,dt'\ . \end{aligned} \tag{6.18}$$

Observe the changed sign and the complex conjugate in the definition of the

[3]Some problems may arise when one tries this, since small uncertainties in the measurements may have big effects on the result. Therefore, one usually prefers to fit the obtained convolution signal by a least squares method.

cross-correlation. By a similar derivation as before we get:

$$F^*(\omega)\,G(\omega) = \frac{1}{2\pi}\int_{-\infty}^{\infty} dt' \int_{-\infty}^{\infty} dt\, f^*(t')\,g(t)\,\boldsymbol{e}^{-i\,\omega(t-t')}$$

subst. $\tau \equiv t - t'$ for t:

$$\begin{aligned} F^*(\omega)\,G(\omega) &= \frac{1}{2\pi}\int_{-\infty}^{\infty} dt' \int_{-\infty}^{\infty} d\tau\, f^*(t')\,g(\tau+t')\,\boldsymbol{e}^{-i\,\omega\tau} \\ &= \frac{1}{2\pi}\int_{-\infty}^{\infty} d\tau\, f(\tau)\star g(\tau)\,\boldsymbol{e}^{-i\,\omega\tau} \end{aligned} \tag{6.19}$$

$$\Rightarrow \quad FT\big[f(t)\star g(t)\big] = \sqrt{2\pi}\,FT^*[f(t)]\,FT[g(t)]\ .$$

If the two functions are equal one obtains:

$$FT\Big[\int_{-\infty}^{\infty} f^*(t')\,f(t+t')\,dt'\Big] = \sqrt{2\pi}\,\big|FT[f(t)]\big|^2\ , \tag{6.20}$$

which is known as the Wiener-Kinchin theorem[4]. It states that the Fourier transform of the so-called autocorrelation function $f\star f$ is proportional to the modulus square of the Fourier transform of the function f. This theorem is very useful, since the right-hand side of the equation represents the power spectrum of a laser (see section 2.4).

In equation (6.15) we have defined the convolution of two functions. We want to consider here some examples of the convolution. The Gaussian and Lorentzian[5] curves. They are good approximations for the frequency distribution of a laser, and the Lorentz curve also approximates well the transmission of a Fabry-Perot cavity (Airy function, see equation (2.73)). Thus, when laser light is transmitted by such a cavity, we effectively measure the convolution of the laser frequency distribution with the transmission curve of the cavity. The (normalized) Gaussian and Lorentzian curves are defined as follows:

$$\begin{array}{lll} G(x) & \equiv \frac{1}{\sigma\sqrt{2\pi}}\,\exp\Big[-\frac{(x-\mu)^2}{2\,\sigma^2}\Big] & \text{with FWHM} \equiv 2\sigma\sqrt{2\log[2]} \\ L(x) & \equiv \frac{1}{\pi\,\gamma}\,\frac{1}{1+(\frac{x-x_0}{\gamma})^2}\ , & \text{with FWHM} \equiv 2\,\gamma\ , \end{array} \tag{6.21}$$

where μ and σ^2 are the mean and the variance of the Gaussian. For the Lorentzian, neither a mean nor a variance is defined, but x_0 is the x-value of the peak and γ is the half width of the maximum (HWHM). The FWHM denote the full-width-half-maximum. Without going into the mathematical details, the convolution of

[4]Named after Norbert Wiener and Aleksandr Yakovlevich Khinchin. Sometimes it is also spelled Wiener-Kinchine theorem.

[5]Also known as Cauchy distribution or Breit-Wigner distribution.

two Gaussian curves is:

$$\begin{aligned} G_1 * G_2 &= \frac{1}{2\pi\,\sigma_1\,\sigma_2}\int_{-\infty}^{\infty}\exp\Big[-\frac{(\omega-\omega_2-\Delta)^2}{2\,\sigma_1^2}\Big]\,\exp\Big[-\frac{(\omega-\omega_2)^2}{2\,\sigma_2^2}\Big]\,d\omega = \cdots \\ &= \frac{1}{\sqrt{2\pi}\sqrt{\sigma_1^2+\sigma_2^2}}\exp\Big[-\frac{\Delta^2}{2(\sigma_1^2+\sigma_2^2)}\Big]\,, \qquad \text{with } \Delta \equiv \omega_2-\omega_1, \end{aligned} \tag{6.22}$$

where we have defined the frequency difference Δ. This result shows that the convolution of two Gaussian curves leads to another Gaussian curve with a mean of $\Delta = 0$ and a variance given by the geometric mean of the two original Gaussian curves:

$$\sigma_{G_1*G_2} \equiv \sqrt{\sigma_1^2+\sigma_2^2}\,. \tag{6.23}$$

The convolution of two Lorentzian curves gives:

$$\begin{aligned} L_1 * L_2 &= \frac{1}{\pi^2\,\gamma_1\,\gamma_2}\int_{-\infty}^{\infty}\frac{1}{1+(\frac{\omega-\omega_2-\Delta}{\gamma_1})^2}\frac{1}{1+(\frac{\omega-\omega_2}{\gamma_2})^2}\,d\omega = \cdots \\ &= \frac{1}{\pi\,(\gamma_1+\gamma_2)}\,\frac{1}{1+(\frac{\Delta}{\gamma_1+\gamma_2})^2}\,. \end{aligned} \tag{6.24}$$

We get for the convolution of two Lorentzian curves another Lorentzian, with peak at the frequency $\Delta = 0$ and a HWHM of the sum of the original HWHM:

$$\gamma_{L_1*L_2} \equiv \gamma_1+\gamma_2\,. \tag{6.25}$$

Finally, we want to discuss the convolution of a Lorentzian and a Gaussian curve. The result is known as the Voigt profile. There is no analytical solution for the resulting linewidth, but one can numerically perform the integration:

$$\begin{aligned} L * G &= \int_{-\infty}^{\infty}\frac{2}{\pi\delta_L}\,\frac{1}{1+(2\,\frac{\omega-\omega_G-\Delta}{\delta_L})^2}\,\frac{2}{\delta_G}\sqrt{\frac{\log[2]}{\pi}}\boldsymbol{e}^{-4\log[2](\frac{\omega-\omega_G}{\delta_G})^2}\,d\omega = \cdots \\ &= \frac{4}{\pi\delta_G}\sqrt{\frac{\log[2]}{\pi}}\int_{-1}^{1}\frac{1}{1+t^2}\,\exp\Big[-\frac{4\log[2]}{\delta_G^2}\big(\delta_L\frac{t}{1-t^2}-\Delta\big)^2\Big]\,dt\,, \end{aligned} \tag{6.26}$$

where we defined for simplicity $\delta_G \equiv \mathrm{FWHM}_G$ and $\delta_L \equiv \mathrm{FWHM}_L$, and introduced again the frequency difference $\Delta \equiv \omega_L - \omega_G$. To get this integral, we made the substitution $\omega - \omega_G \equiv \frac{t}{1-t^2}$, which makes the boundaries finite[6]. In figure 2.9, section 2.2.2, different line profiles and widths are plotted.

[6]By doing this, the integration time should be shorter according to [Tat06], but with Mathematica this integral took 50 % longer than the integral with infinite boundaries. Probably, the computation of the large number inside the exponential close to the boundaries ± 1 caused additional computations. One could try to use boundaries which are sufficiently close to ± 1. In this way one would not loose accuracy, while no large numbers would be generated.

6.4 Fitting complex functions

In section 3.3 we measured the transfer function of the laser PDH lock with the piezo and wanted to fit a model function (3.4) to this data. But this requires fitting a complex function to the two independent variables, gain and phase. Since it was not clear from the beginning how to do this, we will present it here.

Basically, we can see the complex function as a vector having two entries, gain and phase, or a real part and an imaginary part. But none of the computer programs which we used, Mathematica and Origin, has an available function to fit a complex function or vectors. Nevertheless, Mathematica has a function that can minimize an arbitrary function by variation of different parameters. This is exactly what we need, when we define the cost function χ^2, which should be minimized:

$$\chi^2 \equiv \sum_{m=1}^{N} \left\| \vec{f}(x_m, p_1, \ldots, p_N) - \vec{y}(x_m) \right\|^2 \quad \rightarrow \quad \text{Minimum} \ . \tag{6.27}$$

Here the summation is done over the measured data points $\vec{y}(x_m)$, with x_m the independent variable (ω in our case), and $\vec{f}(x_m, p_1, \ldots, p_N)$ is the function to fit with the parameters $p_1, \ldots, p_N$, which should be varied. These are the parameters we are searching for, like frequency, width, etc. of the piezo resonances. The previous definition of the cost function corresponds to the definition used for the commonly known least-squares method, but here it is defined for vectors. χ^2 is the sum of the (squared) distances between the two vectors in the vector space spanned by all possible vectors $\vec{f}(x_m, p_1, \ldots, p_N)$. For this vector space two definitions have to be made. The first concerns which norm to use. We use the Euclidean norm:

$$\left\| \vec{f}(x_m) \right\|^2 \equiv \sum_{i=1}^{d} f_i(x_m)^2 \ , \tag{6.28}$$

where the summation is performed over the dimensions i of the vector, i.e. 2 in our case. The $f_i(x_m)$ are the components of the vector in dimension i. The second definition we have to make is related to the components of the vector: either gain and phase, or the real and the imaginary parts of the complex function. It seems more reasonable to use the real and imaginary parts, since both of these have the same order of magnitude. Therefore, when calculating the cost function χ^2, they will be equally weighted. Otherwise, if we used the gain and the phase, the gain might for example range from 0 to 100, while the phase has values from 0 to 2π, leading to a result mainly focussing on the gain.

The Mathematica function for minimization is "FindMinimum" and we give here the code to call this function:

$$res = FindMinimum[\, \chi^2, \{\{p_1, p_1^0\}, \ldots\}] \ ,$$

with χ^2 the cost function defined before. The list $\{\{p_1, p_1^0\}, \ldots\}$ are the parameters for variation, with p_1^0 the starting value of the variation. The result is stored as a list of replacement rules $\{p_1 \mapsto \ldots\}$ in res. The starting values play a crucial role, since the variation can only find local minima. Therefore, it is necessary to use starting values which are already close to the final result. Sometimes it is necessary to vary them until the result is satisfactory. This is best seen, when plotting the data with the fitting function.

In general one can say that this scheme of fitting a complex number can be expanded for arbitrary vectors. In this case, only the norm must be adapted and the entries in the vector have to be considered. Maybe some weighting has to be applied in order to account for non-equal ranges. Measurement errors could as well be included in these weighting factors. For our purpose the fitting worked well with the given scheme, as can be seen in figure 3.9b). For further information, see for example [PTVF02].

6.5 Notch filter

In section 3.3.5 we described how two notch filters were built in order to overcome the resonances of the piezo. Here in this section the transfer function of one notch filter will be presented. From this we will calculate the resonance frequency and the full-width-half-maximum. The notch filter is built of a L-C combination in parallel, with a resistor, according to figure 6.1a). The transfer function is simply

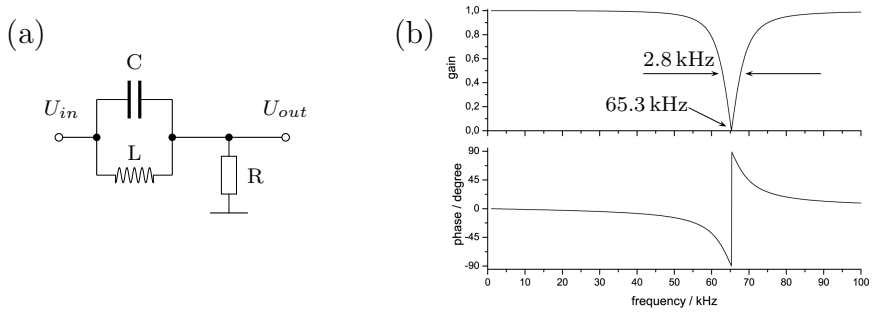

Figure 6.1: a) Notch filter circuit and b) transfer function. The parameters are L=660 μH, C=9 nF, R=3.6 kΩ giving f_0=65.3 kHz and FWHM=2.8 kHz (Q=f_0/FWHM=23.3).

obtained by recognizing the notch filter as a voltage divider with the output voltage:

$$U_{out} = U_{in} \frac{Z_2}{Z_1 + Z_2} \ , \tag{6.29}$$

with Z_1 the impedances from the input to the output and Z_2 the impedance from the output to ground. For the notch filter the first corresponds to L in parallel with C and the second to the resistor R. Therefore, the transfer function $G(\omega) \equiv U_{out}/U_{in}$ is simply [TS02]:

$$\begin{aligned} G(\omega) &= \frac{R}{R + \frac{1}{i\,\omega\,C + \frac{1}{i\,\omega\,L}}} = \frac{R}{R + \frac{i\,\omega\,L}{1-\omega^2\,L\,C}} = \frac{R(1-\omega^2\,L\,C)}{R(1-\omega^2\,L\,C) + i\,\omega\,L} \\ &= \frac{R(1-\omega^2\,L\,C)(R(1-\omega^2\,L\,C) - i\,\omega\,L)}{R^2(1-\omega^2\,L\,C)^2 + \omega^2\,L^2} \\ &= (1-\omega^2\,L\,C)\,\frac{1-\omega^2\,L\,C - i\,\omega\,L/R}{(1-\omega^2\,L\,C)^2 + \omega^2\,L^2/R^2}\ . \end{aligned} \tag{6.30}$$

The gain $\big|G(\omega)\big|$ and the phase $\varphi(\omega)$ of the transfer function are:

$$\big|G(\omega)\big| = \frac{\big|1-\omega^2\,L\,C\big|}{\sqrt{(1-\omega^2\,L\,C)^2 + \omega^2\,L^2/R^2}} = \frac{1}{\sqrt{1 + (\frac{\omega\,L/R}{1-\omega^2/\omega_0^2})^2}} \tag{6.31a}$$

$$\varphi(\omega) = \arctan\left[\frac{\mathrm{Im}\big[G(\omega)\big]}{\mathrm{Re}\big[G(\omega)\big]}\right] = -\arctan\left[\frac{\omega\,L/R}{1-\omega^2/\omega_0^2}\right] \tag{6.31b}$$

$$\text{with} \qquad \omega_0 \equiv \frac{1}{\sqrt{L\,C}} \qquad \text{or} \qquad f_0 \equiv \frac{1}{2\pi\,\sqrt{L\,C}}\ . \tag{6.31c}$$

At the resonance frequency ω_0, the gain is zero ($\big|G(\omega_0)\big| = 0$). Far off-resonance, the gain is one and the phase is zero. We define the full-with-half-maximum (FWHM) as the width of the dip having gain $\big|G(\omega)\big| = \frac{1}{2}$:

$$\begin{aligned} \frac{1}{2} &= \frac{1}{\sqrt{1 + (\frac{\omega\,L/R}{1-\omega^2/\omega_0^2})^2}} \quad \Rightarrow \quad \sqrt{3} = \pm\,\frac{\omega\,L/R}{1-\omega^2/\omega_0^2} \\ 0 &= 1 - \omega^2/\omega_0^2 \pm \omega\,\frac{L}{R\,\sqrt{3}} = -\Big(\frac{\omega}{\omega_0} \mp \frac{L\,\omega_0}{2\,R\,\sqrt{3}}\Big)^2 + \Big(\frac{L\,\omega_0}{2\,R\,\sqrt{3}}\Big)^2 + 1 \\ \frac{\omega}{\omega_0} &= \pm\,\frac{L\,\omega_0}{2\,R\,\sqrt{3}} \pm \sqrt{1 + \Big(\frac{L\,\omega_0}{2\,R\,\sqrt{3}}\Big)^2}\ . \end{aligned} \tag{6.32}$$

We have to consider which of the solutions are positive. These are the following, and the difference of them is our result:

$$\omega_1 = -\frac{L\,\omega_0^2}{2\,R\,\sqrt{3}} + \omega_0\,\sqrt{1 + \Big(\frac{L\,\omega_0}{2\,R\,\sqrt{3}}\Big)^2}\ ,\ \omega_2 = +\frac{L\,\omega_0^2}{2\,R\,\sqrt{3}} + \omega_0\,\sqrt{1 + \Big(\frac{L\,\omega_0}{2\,R\,\sqrt{3}}\Big)^2}$$

$$\Delta\omega = \omega_2 - \omega_1 = \frac{L\,\omega_0^2}{R\,\sqrt{3}} = \frac{1}{R\,C\,\sqrt{3}} \quad \Rightarrow \quad \mathrm{FWHM} = \frac{1}{2\pi\,\sqrt{3}\,R\,C}\ . \tag{6.33}$$

Finally, we consider the current flowing through the filter to ground:

$$I_R = \frac{U_{out}}{R} = U_{in}\,\frac{G(\omega)}{R}\ . \tag{6.34}$$

The current through the resistor is zero at resonance and maximum ($I_R^{max} = U_{in}/R$) far off-resonance.

We have seen how the transfer function of a notch filter looks like, how the inductance and capacitance determine the resonance frequency. The resistor, together with the capacitance, determine the width of the resonance. The current flowing through the resistor must be supplied by the source and is maximum far off-resonance, giving design limitations to the filter.

6.6 CRD for the input beam switched off slowly

In a similar way as the derivation of equation (2.99), in section 2.2.2, we will derive here how the cavity ring-down (CRD) time is affected if the input field to a cavity is switched off slowly. Furthermore, the calculations here include the non-resonant case, leading to interference effects of the input light with the decaying light from the cavity.

We are interested to study the behavior of the electric field, instead of the intensity. The transmitted field of a Fabry-Perot type cavity at time t is a function of the transmitted field before one round-trip $E_t(t-T)$ and the input field before half the round trip time $E_{in}(t-T/2)$, with $T \equiv \frac{2L}{c}$ the round trip time. The relation we write:

$$E_t(t) = E_t(t-T)\,Z\,\boldsymbol{e}^{-i2\delta} + E_{in}(t-T/2)\sqrt{T_1T_2T_3}\,\boldsymbol{e}^{-i\delta}\ , \tag{6.35}$$

with $Z \equiv T_3\sqrt{R_1R_2}$ the remaining fraction of the field after one round trip and $\delta \equiv \frac{\omega L}{c}$ the phase accumulated at half the round trip. We assume the change of the field to be small during one round trip and write down the inhomogeneous differential equation:

$$\begin{aligned}
\dot{E}_t(t) = \frac{dE}{dt} &\approx \frac{\Delta E}{\Delta t} = \frac{1}{T}\big(E_t(t) - E_t(t-T)\big) \\
&= \frac{c}{2L}\Big(E_t(t-T)\big(Z\,\boldsymbol{e}^{-i2\delta} - 1\big) + E_{in}(t-T/2)\sqrt{T_1T_2T_3}\,\boldsymbol{e}^{-i\delta}\Big) \\
&\approx -\frac{1}{2\tau}E_t(t) + \frac{1}{2\tau'}E_{in}(t-T/2) \\
\text{with}\quad \tau \equiv \frac{L}{c}\frac{1}{1-Z\,\boldsymbol{e}^{-i2\delta}} &\quad\text{and}\quad \tau' \equiv \frac{L}{c}\frac{1}{\sqrt{T_1T_2T_3}\,\boldsymbol{e}^{-i\delta}}\ ,
\end{aligned} \tag{6.36}$$

where the two time constants τ and τ' have been defined. The first of them is the same as in equation (2.99), which is the cavity decay time for the input light switched off instantaneously. But here the additional phase factor accounts for non-resonant light and becomes 1 on resonance.

For the steady state case with $\dot{E}_t = 0$ and $E_{in}(t) = E_{in}^{(0)}$, the solution is:

$$0 = -\frac{1}{2\tau}E_t + \frac{1}{2\tau'}E_{in}^{(0)} \quad \Rightarrow \quad E_t = \frac{\tau}{\tau'}E_{in}^{(0)} \equiv E_t^{(0)} \ . \tag{6.37}$$

Comparing this result with equation (2.66), in section 2.2.1, shows that both are exactly the same. We found an alternative way to derive the transmitted field.

The general solution to the previous differential equation (6.36) is:

$$\begin{aligned} E_t(t) &= c(t)\, \boldsymbol{e}^{-t/(2\tau)} \\ \text{and } c(t) &= \int \frac{1}{2\tau'} E_{in}(t - T/2)\boldsymbol{e}^{+t/(2\tau)} dt \ . \end{aligned} \tag{6.38}$$

If the input field is switched off at $t = -T/2$ instantaneously this gives for $c(t)$ and $t \geq 0$[7]:

$$c(t) = \int \frac{1}{2\tau'} E_{in}(t - T/2)\boldsymbol{e}^{+t/(2\tau)} dt = 0 + c \ , \tag{6.39}$$

and from the initial condition we get the integration constant c and the result:

$$E_t^{(0)} \stackrel{!}{=} E_t(t = 0) = c \quad \Rightarrow \quad E_t(t) = E_t^{(0)} \boldsymbol{e}^{-t/(2\tau)} \ . \tag{6.40}$$

This corresponds, not surprisingly, to the result we obtained in equation (2.99), but here given for the electric field instead of the intensity. Moreover, there is a phase factor within τ accounting for non-resonant light. This yields an effective decay time $\tilde{\tau}$, which would be measured from the decay of the intensity with $I(t) = I(0)\boldsymbol{e}^{-t/\tilde{\tau}}$. It is obtained by calculating the intensity from equation (6.40), where we temporarily substitute $\tau \equiv a + ib$ for simplicity:

$$\begin{aligned} \left|\exp\Big[-\frac{t}{2\tau}\Big]\right|^2 &= \left|\exp\Big[-\frac{t}{2(a+ib)}\Big]\right|^2 = \exp\Big[-\frac{t}{2(a+ib)}\Big]\exp\Big[-\frac{t}{2(a-ib)}\Big] \\ &= \exp\Big[-\frac{t}{2}\Big(\frac{1}{a+ib} + \frac{1}{a-ib}\Big)\Big] = \exp\Big[-\frac{t}{2}\frac{2a}{a^2+b^2}\Big] \\ &= \exp\Big[-t\,\frac{\mathrm{Re}\big[\tau\big]}{|\tau|^2}\Big] \quad \Rightarrow \quad \tau \mapsto \tilde{\tau} \equiv \frac{|\tau|^2}{\mathrm{Re}\big[\tau\big]} \ . \end{aligned} \tag{6.41}$$

[7]For times between $t = -T/2$ and $t = 0$, the transmitted field is not changed, since the light needs the time $T/2$ to travel from the input to the output of the cavity. For times $t \leq 0$ the steady state solution is obtained.

By inserting the definition of τ, equation (6.36), and defining again some temporary variables (a_1 and b_1), we find:

$$\begin{aligned}
\tau &= \frac{L}{c}\frac{1}{1-Z\,\boldsymbol{e}^{-i2\delta}} \equiv \frac{L}{c}\frac{1}{a_1+ib_1} = \frac{L}{c}\frac{a_1-ib_1}{a_1^2+b_1^2} \\
|\tau|^2 &= \frac{L^2}{c^2}\frac{a_1^2+b_1^2}{(a_1^2+b_1^2)^2} = \frac{L^2}{c^2}\frac{1}{a_1^2+b_1^2} \quad \text{and} \quad \mathrm{Re}\big[\tau\big] = \frac{L}{c}\frac{a_1}{a_1^2+b_1^2} \\
\Rightarrow \quad \tilde{\tau} &\equiv \frac{|\tau|^2}{\mathrm{Re}\big[\tau\big]} = \frac{L}{c}\frac{1}{a_1^2+b_1^2}\frac{a_1^2+b_1^2}{a_1} = \frac{L}{c}\frac{1}{a_1} \\
&= \frac{L}{c}\frac{1}{1-Z\cos[2\delta]} = \frac{L}{c}\frac{1}{(1-Z)+2Z\sin^2[\delta]} \quad \text{with} \quad \delta \equiv \frac{\omega\,L}{c}\ .
\end{aligned} \tag{6.42}$$

For the resonant case with δ an integer multiple of π, this is the same result as in equation (2.99). Off-resonance, the decay time is reduced.

In the measurement shown in section 3.4.2, figure 3.15, we saw that the light is switched off exponentially. Therefore, we consider this case:

$$E_{in}(t) = \begin{cases} E_{in}^{(0)} & t < -T/2 \\ E_{in}^{(0)}\,\boldsymbol{e}^{-(t+T/2)/(2\tau_0)} & t \geq -T/2 \end{cases}\ , \tag{6.43}$$

with τ_0 the time constant with which the input light is switched off. We perform the integration in order to obtain $c(t)$ for $t \geq 0$[7]:

$$\begin{aligned}
c(t) &= \int \frac{1}{2\tau'}E_{in}(t-T/2)\boldsymbol{e}^{+t/(2\tau)}dt = \frac{1}{2\tau'}\int E_{in}^{(0)}\,\boldsymbol{e}^{-t/(2\tau_0)}\boldsymbol{e}^{+t/(2\tau)}dt \\
&= \frac{\tau}{\tau'}E_{in}^{(0)}\frac{\tau_0}{\tau_0-\tau}\,\boldsymbol{e}^{\,t\frac{\tau_0-\tau}{2\,\tau\tau_0}} + c = E_t^{(0)}\frac{\tau_0}{\tau_0-\tau}\,\boldsymbol{e}^{\,t\frac{\tau_0-\tau}{2\,\tau\tau_0}} + c\ .
\end{aligned} \tag{6.44}$$

For time $t = 0$ the starting condition gives the integration constant c:

$$\begin{aligned}
E_t^{(0)} &\stackrel{!}{=} E_t(t=0) = E_t^{(0)}\frac{\tau_0}{\tau_0-\tau} + c \\
\Rightarrow \quad c &= E_t^{(0)}\Big(1-\frac{\tau_0}{\tau_0-\tau}\Big) = E_t^{(0)}\frac{-\tau}{\tau_0-\tau}\ .
\end{aligned} \tag{6.45}$$

The result for the transmitted electric field becomes:

$$\begin{aligned}
E_t(t) &= c(t)\,\boldsymbol{e}^{-t/(2\tau)} = E_t^{(0)}\frac{1}{\tau_0-\tau}\Big(\tau_0\,\boldsymbol{e}^{\,t\frac{\tau_0-\tau}{2\,\tau\tau_0}} - \tau\Big)\,\boldsymbol{e}^{-t/(2\tau)} \\
&= E_t^{(0)}\frac{1}{\tau_0-\tau}\Big(\tau_0\,\boldsymbol{e}^{-t/(2\tau_0)} - \tau\,\boldsymbol{e}^{-t/(2\tau)}\Big)\ .
\end{aligned} \tag{6.46}$$

Taking the absolute square yields the final result for the transmitted intensity, when the input light is switched off exponentially:

$$I_t(t) = I_t^{(0)}\Big|\frac{1}{\tau_0-\tau}\Big(\tau_0\,\boldsymbol{e}^{-t/(2\tau_0)} - \tau\,\boldsymbol{e}^{-t/(2\tau)}\Big)\Big|^2\ . \tag{6.47}$$

On resonance, the time constant τ is real and the modulus square can be simply replaced by the square. This is the result which is used to fit the measured data given in figure 3.15 in section 3.4.3.

In the case that $\tau_0 = \tau$, the above equation is not valid anymore, and we have to perform the integration of $c(t)$ again, which becomes in this case:

$$c(t) = \frac{1}{2\tau'} \int E_{in}^{(0)}\, \boldsymbol{e}^{-t/(2\tau)} \boldsymbol{e}^{+t/(2\tau)} dt = \frac{1}{2\tau'} E_{in}^{(0)}\, t + c = \frac{t}{2\tau} E_t^{(0)} + c\ . \tag{6.48}$$

From the starting condition we get the result for equal time constants:

$$E_t^{(0)} \stackrel{!}{=} E_t(t=0) = c \quad \Rightarrow \quad \begin{cases} E_t(t) = E_t^{(0)} \big(1 + \dfrac{t}{2\tau}\big)\, \boldsymbol{e}^{-t/(2\tau)} \\ I_t(t) = I_t^{(0)} \left| \left(1 + \dfrac{t}{2\tau}\right) \boldsymbol{e}^{-t/(2\tau)} \right|^2 . \end{cases} \tag{6.49}$$

In figure 6.2a) we give some examples of the decay of the cavity when the input beam is switched off exponentially. The intensity does not decrease immediately, but it decays smoothly. In figure 6.2b) we have plotted the cavity

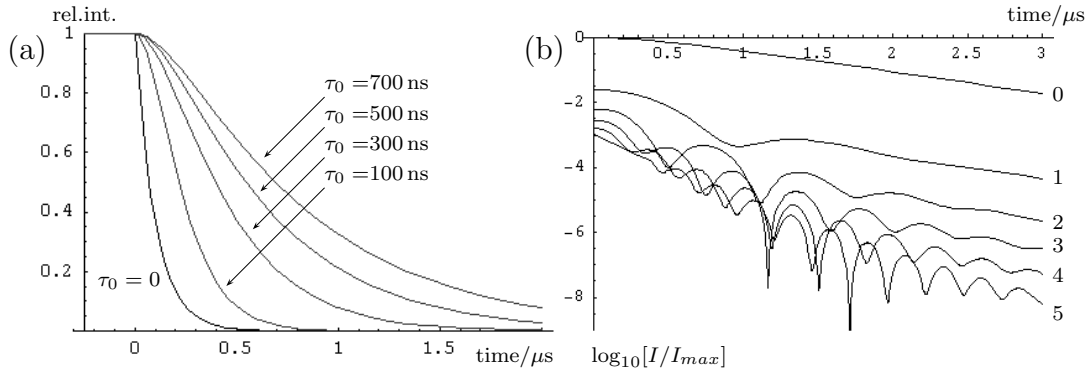

Figure 6.2: CRD with the input field switched off slowly. a) For different τ_0 with $\tau = 100\,\text{ns}$ and δ=0. b) Non-resonant decay with the numbers corresponding δ in units of $\pi/1000$. $\tau = 633\,\text{ns}$ and $\tau_0 = 200\,\text{ns}$.

decay for different δ. Interestingly, the decay time can be even further reduced by setting τ_0 to certain values $\neq 0$. In this case, obviously interferences lead to an oscillatory behavior of the decaying intensity. In [RESKB02] similar interferences were numerically modelled and experimentally the cavity decay time was shortened by applying an appropriate intensity and phase to the input light.

Bibliography

[AEM+95] M. H. Anderson, J. R. Ensher, M. R. Matthews, C. E. Wieman, and E. A. Cornell, *Observation of Bose-Einstein Condensation in a Dilute Atomic Vapor*, Science **269** (1995), no. 5221, 198–201. 2

[AGR81] Alain Aspect, Philippe Grangier, and Gérard Roger, *Experimental Realization of Einstein-Podolsky-Rosen-Bohm Gedankenexperiment: A New Violation of Bell's Inequalities*, Phys. Rev. Lett. **49** (1981), no. 2, 91–94. 1

[AM38] John F. Allen and Don Misener, *Flow of Liquid Helium II*, Nature **141** (1938), no. 3558, 75. 2

[Bar05] Markus Bartenstein, *From Molecules to Cooper pairs: Experiments in the BEC-BCS crossover*, Dissertation, Leopold-Franzens-Universität Innsbruck, 2005. 80, 109

[Bec05] John Bechhoefer, *Feedback for physicists: A tutorial essay on control*, Reviews of modern physics **77** (2005), 783 – 836. 56, 57, 58

[Bel64] John S. Bell, *On the Einstein Podolsky Rosen Paradox*, Physics **1** (1964), 195–200. 1

[Boh35] Niels Bohr, *Can Quantum-Mechanical Description of Physical Reality Be Considered Complete?*, Phys. Rev. Lett. **48** (1935), 696–702. 1

[Bos24] Satyendra Nath Bose, Zeitschrift für Physik **26** (1924), 178. 2

[BSTH95] C.C. Bradley, C.A. Sackett, J.J. Tollett, and R.G. Hulet, *Evidence of Bose-Einstein Condensation in an Atomic Gas with Attractive Interactions*, Phys. Rev. Lett. **75** (1995), no. 9, 1687–1690, see also Phys. Rev. Lett. **75** (1997), 1170. 2

[Cha73] David C. Champeney, *Fourier Transforms and their Physical Applications*, Academic press, inc., 1973, excellent book. 69

[CN04] Roberto Casalbuoni and Giuseppe Nardulli, *Inhomogeneous superconductivity in condensed matter and QCD*, Rev. Mod. Phys. **76** (2004), 263, Review article. 3

[Dar59] Charles Darwin, *On the Origin of Species*, 1st ed., John Murray, October 1st 1859, available online at the Project Gutenberg homepage, `http://www.gutenberg.org/etext/1228`. iii

[Dem96] Wolfgang Demtröder, *Laser Spectroscopy*, Springer, 1996. 28, 52, 140

[DHD87] B. Dahmani, L. Hollberg, and R. Drullinger, *Frequency stabilization of semiconductor lasers by resonant optical feedback*, Optics Letters **12** (1987), 876, `http://tf.nist.gov/timefreq/general/pdf/598.pdf`. 116

[DHK83] R.W.P. Drever, J.L. Hall, and F.V. Kowalski, *Laser Phase and Frequency Stabilization Using an Optical Resonator*, App. Phys. B **31** (1983), no. 2, 97–105. 79, 89, 90, 104, 134

[DMA+95] K.B. Davis, M.-O. Mewes, M.R. Andrews, N.J. van Druten, D.S. Durfee, D.M. Kurn, and W. Ketterle, *Bose-Einstein Condensation in a Gas of Sodium Atoms*, Phys. Rev. Lett. **75** (1995), no. 22, 3969–3973. 2

[DME87] J. Durnin, J.J. Miceli, Jr., and J.H. Eberly, *Diffraction-Free beams*, Phys. Rev. Lett. **58** (1987), no. 15, 1499–1501. 21

[dMJ99] Brian de Marco and Deborah S. Jin, *Onset of Fermi Degeneracy in a Trapped Atomic Gas*, Science **285** (1999), 1703–1706. 2

[EFK+93] H.J. Eichler, A. Fleischer, J. Kross, M. Krystek, H. Lang, H. Niedrig, H. Rauch, G. Schmahl, H. Schoenebeck, E. Sedlmayr, H. Weber, and K. Weber, *Bergmann-Schäfer, Lehrbuch der Experimentalphysik, Optik*, 9th ed., Walter de Gruyter, 1993. 113, 141

[Ein24] Albert Einstein, Sitzber. Kgl. Preuss. Akad. Wiss. (1924), 261. 2

[Ein25] Albert Einstein, Sitzber. Kgl. Preuss. Akad. Wiss. (1925), 3. 2

[ELS] *ELS homepage and Versadisk information*,
`http://www.els.de/`,
`http://www.els.de/PDF/VersaDisk_General.pdf`,
`http://www.els.de/PDF/VersaDisk_Options.pdf`,
`http://www.els.de/PDF/VersaDisk_Data.pdf`. 81, 82, 83

[Els00] Thilo Elsässer, *Optischer Resonator zur Realisierung einer Stehwellendipolfalle für fermionisches Lithium*, Diplomarbeit, Max-Planck-Instiut für Kernphysik, Heidelberg, 2000. 80, 109, 116

[EPR35] A. Einstein, B. Podolsky, and N. Rosen, *Can Quantum-Mechanical Description of Physical Reality Be Considered Complete?*, Phys. Rev. Lett. **47** (1935), 777–780. 1

[ERS82] D. S. Elliott, Rajarshi Roy, and S. J. Smith, *Extracavity laser bandshape and bandwidth modification*, Phys. Rev. A **26** (1982), 12. 69

[FF64] Peter Fulde and Richard A. Ferrell, *Superconductivity in a Strong Spin-Exchange Field*, Phys. Rev. **135** (1964), no. 3A, A550. 3

[GOST98] M. E. Gehm, K.M. O'Hara, T. A. Savard, and J. E. Thomas, *Dynamics of noise-induced heating in atom traps*, Phys. Rev. A **58** (1998), 3914 – 3921. 63, 64, 65, 66, 69

[Gou90] L. G. Gouy, *Sur une propriete nouvelle des ondes lumineuses*, Comptes Rendus Acad. Sci. Paris **110** (1890), 1251–1253 (french). 14

[GRJ03] Markus Greiner, Cindy A. Regal, and Deborah S. Jin, *Emergence of a molecular Bose-Einstein condensate from a Fermi gas*, Nature **426** (2003), 537–540. 3

[GWO00] R. Grimm, M. Weidemüller, and Y. Ovchinnikov, *Optical dipole traps for neutral atoms*, Adv. At. Mol. Opt. Phys. **42** (2000), 95–170. 4, 28, 80

[HC80] T.W. Hänsch and B. Couillaud, *Laser frequency stablilization by polarization spectroscopy of a reflecting reference cavity*, Optics communications **35** (1980), no. 3, 441–444. 80, 110, 117, 134

[HTY99] John L. Hall, Matthew S. Taubman, and Jun Ye, *Laser Stabilization*, OSA handbook **14** (1999), `http://jilawww.colorado.edu/YeLabs/PDFfiles/OSAHandbookfinal.pdf`. 57, 61, 93

[HW92] Norman Hodgson and Horst Weber, *Optische Resonatoren*, Springer, 1992, good and complete reference, also available in english. 8, 15, 20, 21, 23, 25, 28, 53, 140

[Inn] *Innolight homepage and mephisto information*, `http://www.innolight.de/`, `http://www.innolight.de/pdfs/mephisto.pdf`. 82

[IPG] *IPG fiberlaser*, http://www.ipgphotonics.com/products_1micron_lasers_singlefrequency_ylr-lp-sfs.htm, http://www.ipgphotonics.com/. 82

[JBA+03] S. Jochim, M. Bartenstein, A. Altmeyer, G. Hendl, S. Riedl, C. Chin, J. Hecker Denschlag, and R. Grimm, *Bose-Einstein Condensation of Molecules*, Science **302** (2003), 2101–2103, published online 13 November 2003; 10.1126/science.1093280. 3

[Joc04] Selim Jochim, *Bose-Einstein Condensation of Molecules*, PhD thesis, Leopold-Franzens-Universität Innsbruck, 2004. 80, 109, 130

[Kap38] Pyotr Leonidovich Kapitza, *Viscosity of Liquid Helium below the λ-Point*, Nature **141** (1938), no. 3558, 74. 2

[KHY+99] Jae Wan Kim, Jae Won Hahn, Yong Shim Yoo, Jae Yong Lee, Hong Jin Kong, and Hai-Woong Lee, *Measurement of the linewidth of a continuous-wave laser with a cavity-length modulation technique*, Applied Optics **38** (1999), no. 9, 1742–1745. 104

[KL66] Herwig Kogelnik and Tinge Li, *Laser Beams and Resonators*, Applied Optics **5** (1966), no. 10, 1550–1567. 8, 28

[KS92] S.M. Kobtsev and N.A. Sventsitskaya, *Application of birefringent filters in countinuous-wave tunable lasers: a review*, Opt. Spectrosc. **73** (1992), 114–123. 82

[LO64] A. I. Larkin and Y. N. Ovchinnikov, Zh. Eksp. Teor. Fiz. **47** (1964), 1136, [Sov. Phys. JETP 20, 762 (1965)]. 3

[LP98] Christian B. Lang and Norbert Pucker, *Mathematische Methoden in der Physik*, Spektrum, Akademischer Verlag, 1998 (german), very good introduction. 142

[LW03] W. Vincent Liu and Frank Wilczek, *Interior Gap Superfluidity*, Phys. Rev. Lett. **90** (2003), no. 4, 047002. 3

[Mac86] Agnus Macleod, *Thin-film optical filters*, 2nd ed., Adam Hilger Ltd, Bristol, 1986. 29

[MGLW05] Michael McNeil Forbes, Elena Gibankova, W. Vincent Liu, and Frank Wilczek, *Stability Criteria for Breached-Pair Superfluidity*, Phys. Rev. Lett. **94** (2005), no. 1, 017001. 3

[MJM+01] A. Mosk, S. Jochim, H. Moritz, T. Elsässer, M. Weidemüller, and R. Grimm, *Resonator-Enhanced Optical Dipole Trap for Fermionic Lithium Atoms*, Opt. Lett. **26** (2001), no. 23, 1837–1839, found also on arXiv:physics/0105009. 63, 66, 80, 130

[Mor01] Henning Moritz, *Fermionisches Lithium in einer optischen Resonatordipolfalle*, Diplomarbeit, University of Heidelberg, Germany, 2001. 80, 109, 117

[MvdS99] Harold J. Metcalf and Peter van der Straten, *Laser Cooling and Trapping*, Springer, 1999. 4, 5, 127

[MW95] Leonard Mandel and Emil Wolf, *Optical Coherence and Quantum Optics*, Cambridge University Press, 1995. 63, 67

[PIh] *PI homepage and piezo information*, `http://www.physikinstrumente.com/en/products/prdetail.php?sortnr=102800`, `http://www.physikinstrumente.com/en/index.php`. 82

[PTVF02] William H. Press, Saul A. Teukolsky, William T. Vetterling, and Brian P. Flannery, *Numerical Recipes in C: The Art of Scientific Computing*, 2nd ed., Cambridge University Press, 2002. 147

[Rau00] Christoph Rauscher, *Grundlagen der Spektrumanalyse*, Rohde&Schwarz, 2000 (german). 63, 71, 72, 74, 75, 76

[RESKB02] H. Rohde, J. Eschner, F. Schmidt-Kaler, and R. Blatt, *Optical decay from a Fabry-Perot cavity faster than the decay time*, J. Opt. Soc. Am. B **19** (2002), 1425. 123, 152

[Roh] Rohde&Schwarz, *homepage*, `http://www.rohde-schwarz.com/`. 71

[Roh06] Rohde&Schwarz, *Operating Manual R&S FSP, Volume 1 and 2*, Rohde&Schwarz, 2006. 63, 71, 73, 74, 77

[Sak94] J.J. Sakurai, *Modern Quantum Mechanics*, revised ed., Addison Wesley, 1994, very good and modern introduction to quantum physics at an undergraduate level. 1

[Sch52] Erwin Schrödinger, *Are There Quantum Jumps?*, British Journal for the Philosophy of Sciences **3** (1952), *"... we never experiment with just one electron or atom or (small) molecule. In thought experiments we sometimes assume that we do; this invariably entails ridiculous consequences. ... In the first place it is fair to state that we are not experimenting with single particles, any more than we can raise Ichthyosauria in the zoo."*. 1

[Sch94] Herbert Schmitt, *Träger/Rauschmessung mit der Funktion PHASE NOISE*, R&S application note 1EPAN11D (1994) (german), not available anymore on the R&S homepage. 63, 71

[Sch06a] Stefan Schmid, *Long distance transport of ultracold atoms using a 1d optical lattice*, Diplomarbeit, Leopold-Franzens-Universität Innsbruck, 2006. 21

[Sch06b] Schott, *Optical Glass Catalog - Data Table EXCEL*, July 4th 2006, http://www.schott.com/optics_devices/english/download/opticalglassdatasheetsv040706b2.xls. 113

[Sie86] Anthony E. Siegman, *Lasers*, University Science Books, 1986. 8, 14, 15, 18, 20, 21, 22, 23, 28, 53, 140

[SKC+01] F. Schreck, L. Khaykovich, K. L. Corwin, G. Ferrari, T. Bourdel, J. Cubizolles, and C. Salomon, *Quasipure Bose-Einstein Condensate Immersed in a Fermi Sea*, Phys. Rev. Lett. **87** (2001), 080403. 2

[ST91] Bahaa E.A. Saleh and Malvin C. Teich, *Fundamentals of Photonics*, Wiley, 1991. 8, 13, 18, 21, 22, 26, 28, 53, 109

[Tat06] J. B. Tatum, *Stellar Atmospheres*, 2006, chapter 10, Line Profiles, http://orca.phys.uvic.ca/~tatum/stellatm.html. 145

[Tha99] Gregor Thalhammer, *Frequenzstabilisierung von Diodenlasern bei 850, 854 und 866 nm mit Linienbreiten im Kilohertz-Bereich*, Diplomarbeit, Universität Innsbruck, 1999. 63, 69, 104

[TS02] Ulrich Tietze and Christoph Schenk, *Halbleiter-Schaltungstechnik*, Springer Verlag, 2002 (german). 148

[TSM+01] Andrew G. Truscott, Kevin E. Strecker, William I. McAlexander, Guthrie B. Partridge, and Randall G. Hulet, *Observation of Fermi Pressure in a Gas of Trapped Atoms*, Science **291** (2001), 2570–2572. 2

[WH91] Carl E. Wieman and Leo Hollberg, *Using diode lasers for atomic physics*, Rev. Sci. Instrum. **62** (1991), no. 1, 1–20, http://tf.nist.gov/timefreq/general/pdf/739.pdf. 116

[Wik] *Wikipedia*, http://www.wikipedia.org. 9

[Wil05] Oliver Wille, *Aufbau eines 3D-optischen Gitters für quantenentartete Fermi-Bose-Mischungen aus ^{40}K und ^{87}Rb*, Diplomarbeit, Universität Hamburg, 2005. 83

[Wol95] Josef Wolf, *Phase Noise Measurements with Spectrum Analyzers of the FSE family*, R&S application note 1EPAN16E (1995). 63, 71, 73

[Yar89] Ammon Yariv, *Quantum Electronics*, 3rd ed., John Wiley & Sons, 1989. 104

Notes

If there are important things to mention, like errors, notes or clarifications, they will be provided in this section.

end of official thesis